Steps on surfaces: experiment and theory

Hyeong-Chai Jeong, Ellen D. Williams

Materials Research Science and Engineering Center, University of Maryland, College Park, MD 20742-4111, USA

ELSEVIER

Amsterdam–Lausanne–New York–Oxford–Shannon–Tokyo

Contents

1. Introduction 175
2. Background 177
   - 2.1. Representation of surface 178
   - 2.2. Equilibrium thermodynamics 180
     - 2.2.1. Equilibrium crystal shape at zero temperature 180
     - 2.2.2. Vicinal surfaces on the equilibrium crystal shape 184
     - 2.2.3. Faceting and thermodynamics as a function of surface orientation 194
     - 2.2.4. Steps in the thermodynamic formalism 197
   - 2.3. Kinetics of evolution of morphology 201
     - 2.3.1. Mullins continuum description of surface evolution 202
     - 2.3.2. BCF approach to kinetics of morphology 203
     - 2.3.3. Step curvature 209
     - 2.3.4. Kinetic instabilities 209
3. Approaches to surfaces and models for surface dynamics 211
   - 3.1. Atomic scale approaches 212
     - 3.1.1. Discrete models 212
     - 3.1.2. Microscopic models for surface dynamics 214
   - 3.2. Coarse graining and continuum models 216
     - 3.2.1. Coarse graining 216
     - 3.2.2. Phenomenological Hamiltonians in continuum models 218
     - 3.2.3. Surface dynamics in continuum models 219
   - 3.3. Step models 221
     - 3.3.1. Mesoscopic models 221
     - 3.3.2. Effective Hamiltonian for step models 222
       - 3.3.2.1. Step stiffness 222
       - 3.3.2.2. Step interactions 223
       - 3.3.2.3. Step Hamiltonian 226
     - 3.3.3. Step chemical potential 228
     - 3.3.4. Models for step dynamics 229
       - 3.3.4.1. Isolated step 229
       - 3.3.4.2. Steps in a quasi-1D step array 232
         - 3.3.4.2.1. Global movement 234
         - 3.3.2.2.2. Local movement 234
         - 3.3.4.2.3. Finite step permeability 235
       - 3.3.4.3. Fluctuating steps in a 2D step array 236
4. Application of step models for morphology evolution 238
   - 4.1. Determining the energetic and kinetic parameters 238
     - 4.1.1. Spatial correlations of step-edge positions 238
       - 4.1.1.1. Step stiffness and diffusivity 239
       - 4.1.1.2. Step–step interactions 243
     - 4.1.2. Temporal step fluctuations and the kinetic parameters 248
       - 4.1.2.1. Fourier analysis of step fluctuations 249
       - 4.1.2.2. Application to experiment 251
   - 4.2. Relaxation of metastable structures 253
     - 4.2.1. Decay of a step bunch 254

4.2.1.1. Relaxation of step bunches on Si(111) 254
4.2.1.2. Isolated step bunch and shape-preserving ansatz 254
4.2.2. Decay of structure with curvature effects 257
4.2.2.1. Island decay 257
4.2.2.2. Decay of a bi-periodic structure 259
4.3. Faceting transitions 261
4.3.1. Adsorption and reconstruction-induced faceting 261
4.3.1.1. 2D step hamiltonian incorporating reconstruction 262
4.3.1.2. Models for reconstruction and step motion 264
4.3.1.3. Isolated facet growth 265
4.3.1.4. Induced nucleation and 2D pattern formation 267
4.3.1.5. Faceting driven by 7×7 reconstruction on Si(111) 268
4.3.1.5.1. Equilibrium phase diagram 268
4.3.1.5.2. Nucleation and growth, spinodal for Si(111) 270
4.3.1.6. Oxygen adsorption-induced faceting on Ag(110) surface 271
4.3.1.7. Magic vicinals on Pt(0 0 1) 273
4.3.2. Attractive step interactions 274
4.3.2.1. Step doubling on W(4 3 0) 276
4.3.2.2. Faceting of vicinal Si(1 1 3) 277
4.3.2.2.1. Reversible phase separation 279
4.3.2.2.2. Kinetics of phase separation 281
4.4. Current-induced step bunching 283

5. Conclusions 286
Acknowledgements 287
Note added in proof 287
References 287

ELSEVIER

Surface Science Reports 34 (1999) 171–294

surface science reports

www.elsevier.nl/locate/surfrep

Steps on surfaces: experiment and theory

Hyeong-Chai Jeong[1], Ellen D. Williams*

Materials Research Science and Engineering Center, University of Maryland, College Park, MD 20742-4111, USA

Manuscript received in final form 7 January 1999

Abstract

The properties of steps in thermal equilibrium are described in the context of prediction of the stability and evolution of nanostructures on surfaces. Experimental techniques for measuring the appropriate step parameters are described, and simple lattice models for interpreting the observations are reviewed. The concept of the step chemical potential and its application to the prediction of step motion (and therefore surface mass transport) is presented in depth. Examples of the application of this step-continuum approach to experimental observations of evolution of surface morphology are presented for morphological phase transitions, the decay of metastable structures, and the spontaneous evolution of metastable structure due to kinetic instabilities. © 1999 Elsevier Science B.V. All rights reserved.

1. Introduction

In this review, we will attempt to present the state of the art in understanding and predicting the evolution of surface morphology. The practical reasons for wishing to master this problem are compelling: the frontiers in developing novel materials and device properties lie in the realm of the length scale from nanometers to microns. In this size regime, structural evolution involves collective behavior which is strongly influenced by finite size effects occurring at the atomic scale. Thus, neither a description based on continuum mechanics nor one predicated on extrapolation of individual atomic behavior alone provides an adequate approach to the problem. To incorporate the appropriate atomic scale properties, while maintaining the computational ease of a continuum approach, a hybrid approach known as the ''continuum step model'' has proven to be extremely powerful. In this model, illustrated in Fig. 1 [1], evolution of surface morphology is described in terms of motion of steps, which is implicitly connected to atomic motion via the attachment and detachment of atoms at the edges of the steps.

* Corresponding author. Tel.: +1–301–4056156; fax: +1–301–4057993; e-mail: edw@physics.umd.edu

[1] Permanent address: Department of Physics, Sejong University, Kwangjin-Ku, Seoul 143-747, South Korea

0167-5729/99/ – see front matter © 1999 Elsevier Science B.V. All rights reserved
PII: S0167-5729(99)00010-7

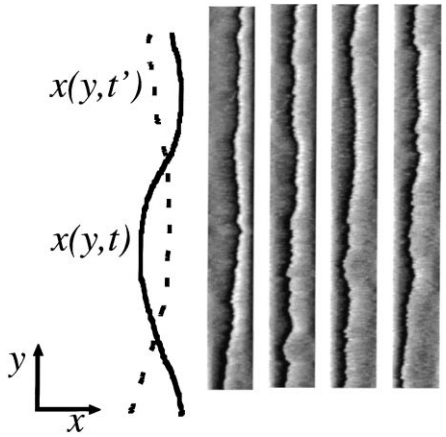

Fig. 1. STM images of a thermally equilibrated step on the Ag(1 1 0) surface [1]. The size of the images is 600 Å × 5000 Å. Each image was acquired in 18 s, and the time increment between images was 30 min. Time-dependent displacements of the steps due to thermal fluctuations are clearly detectable. The schematic illustration at the left shows the description of the step as a wandering line which is used in the continuum step model (figure provided by J. Reutt-Robey, University of Maryland).

In describing the continuum step model, we will use two perspectives. The first is an experimental perspective, in which our experimental system serves as an analog device whose output is dependent on the governing interatomic potentials of the system. We take the philosophy that a relatively small set of experimentally measurable parameters can be used to encapsulate all the details of the atomic behavior of the system needed to predict large scale structural evolution. As we will see later, the key measurables are those concerning the energetics and kinetics of steps on the surface. The second perspective is the theoretical approach, in which we attempt first to justify and understand the relationship between atomic behavior and the key measurables, and secondly to develop methods of using the key measurable to predict the nature and rates of evolution of morphology under a variety of driving conditions. At the atomic scale, very simple models have been used to define and demonstrate the validity of the key measurables to be determined experimentally. At the mesoscopic scale, the results from the simple atomic models are combined with continuum descriptions of mass transport to develop methods of predicting large scale structural changes.

Dynamical studies on crystalline surfaces can be grouped into several different categories depending on the main driving force for the surface motion. The dynamics of a surface under a non-equilibrium growth or evaporation condition is quite different from that of the surface near equilibrium, in which the surface has reached a local equilibrium state. Even when the surface evolves under a near-equilibrium condition, the dynamics of the surface motion can show different characteristic behaviors depending on the initial (out-of-equilibrium) configuration and the final (equilibrium) configuration (e.g., relaxation versus faceting dynamics). Furthermore, depending on whether the surface is above or below its roughening transition temperature, T_R, qualitative differences in dynamical behavior are expected. However, as will be shown, a unified simple thermodynamic approach can be applied for all surfaces under a near-equilibrium condition through the concept of local equilibrium state. For those surfaces, we can define a local chemical potential and describe the dynamics of surface motion in terms of the chemical potential differences as the driving force. These surfaces will eventually go to the complete equilibrium state in which the local chemical potential is essentially the same except for

thermal fluctuations. In this review, we will show that continuum step models, in which individual surface steps are treated as the fundamental objects of interest and mass transport between them is explicitly considered, can be a very efficient approach for describing surface dynamics below T_R.

We will begin with a brief historical review of studies of surface morphology and evolution. In Section 2, thermodynamic approaches to the surface, both equilibrium and kinetic aspects, will be reviewed and re-examined from a step approach point of view. Then, in Section 3, we will briefly review the conventional microscopic approaches and continuum approaches, and discuss the relationship of these approaches and the step approach. The concept of step chemical potential will be introduced and calculated in this section from the effective interactions between steps. We derive the equation of step motion in terms of step chemical potential here. In Section 4, we will discuss how continuum step models have been applied to experimental observations of the dynamics of real surface evolution.

2. Background

A surface is a boundary between two *macroscopic* objects with different phases. For crystalline surfaces, the two phases are the crystalline solid and a fluid phase. We mainly focus on the case when these two phases are near equilibrium, i.e., when the net atomic flux from one phase to the other is zero or near zero. Then, if complete equilibrium is achieved, the solid exists in a history-independent, unique shape called the equilibrium crystal shape (ECS). However, even when the two phases are nearly in equilibrium, in most cases, a solid sample is far from its macroscopic equilibrium shape. The reason for this is that slow relaxation of long wavelength modes of the surface motion makes real solids unlikely to reach their equilibrium shapes. This slow relaxation of the long wavelength modes allows us to apply surface thermodynamics to study surfaces which are not in a complete equilibrium state as shown in Fig. 2. We can apply thermodynamics locally to a ''near equilibrium'' surface which is under slow evolution to the complete equilibrium state. Such systems are rather common, since the short wavelength fluctuations on the surface often can relax faster than the timescale of the experimental observation and each part of the system reaches a local equilibrium state easily, even when long wavelength modes have not been completely relaxed. For such systems, we can define a local chemical potential, $\mu(\boldsymbol{r})$ over a coarse-grained region centered at position $\boldsymbol{r}$ and understand the evolution of surface morphology from the mass transport driven by the chemical potential differences between different regions. In this approach, the problem of the evolution of surface morphology, illustrated in Fig. 3, is reduced to the deceptively simple equation governing mass transport between two regions at positions $\boldsymbol{r}_1$ and $\boldsymbol{r}_2$:

$$j = -\lambda \Delta\mu, \tag{1}$$

where j is the net mass flux between the two regions, $\Delta\mu = \mu(\boldsymbol{r}_2) - \mu(\boldsymbol{r}_1)$ is the difference in chemical potential between them and λ is the linear kinetic coefficient of the mass transport mode between them. The more familiar continuum expression, $j = -D_s \nabla\mu$, with surface diffusion constant D_s is recovered when we consider the flux between two neighboring regions on the surface ($\boldsymbol{r}_2 = \boldsymbol{r}_1 + \delta\boldsymbol{r}$) as will be described in detail in Section 2.3.1.

The proper definition of local chemical potential and the effective modes of mass transport depends on the time and length scale of the surface description. The surface is described by a continuous height (Fig. 3 (a)), if it is coarse grained over several terraces including steps and the chemical potential is

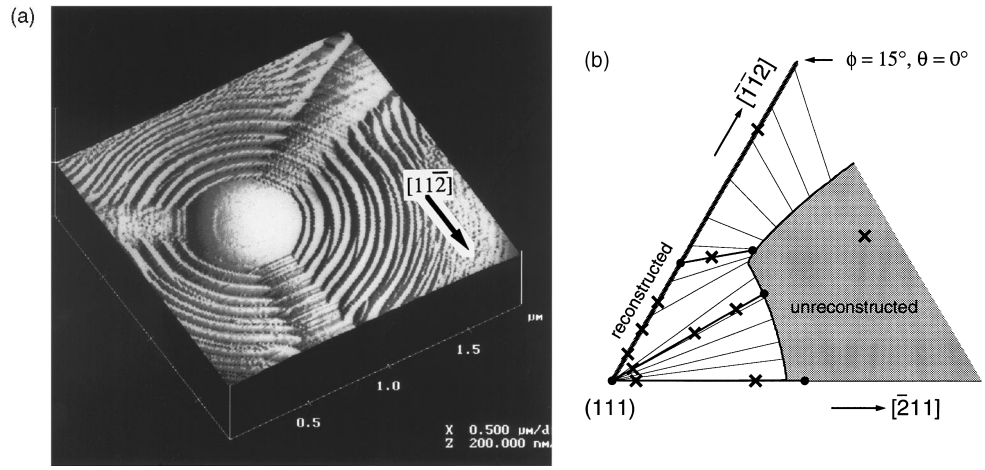

Fig. 2. (a) A standard Si lithographic process was used to create an array of small holes of diameter 1.5 micron and depth 1 micron. The structures were then annealed under clean UHV conditions at 1300°C in time increments of 30 s. After annealing the holes had substantially filled in and formed locally equilibrated structures as shown in the 2 micron × 2 micron AFM image. The 3-fold crystallographic symmetry of the substrate is clearly shown in the morphology of the final structure, and the pattern of step arrangements matches the predictions of the equilibrium phase diagram. Figure provided by Dr. T. Ogino of NTT Basic Research Laboratories (figure from Refs. [212,213]). (b) Orientational phase diagrams of Si near the (1 1 1) orientation at 800°C. Solid lines are calculated using parameters fit to experimental measurements at macroscopic orientations shown by the x's, which determined the phase separation indicated by the heavy lines terminating in solid dots (figure from Ref. [20]). Directly along the [$\bar{1}$ $\bar{1}$ 2] direction, the surface is orientationally stable, and near the [$\bar{1}$ $\bar{1}$ 2] the surface phase separates azimuthally to regions of steps oriented perpendicular to the [$\bar{1}$ $\bar{1}$ 2] and regions in which the steps are rotated to a higher azimuthal angle. This is reflected in (a) by the three smooth trenches running outward from the central pit. Along the [$\bar{2}$ 1 1] orientation and in azimuthal directions up to approximately ±40° away from the [$\bar{2}$ 1 1], vicinal surfaces phase separate into regions of flat (1 1 1) terraces and regions of higher misorientation. This is represented in (a) by the areas of highly corrugated staircase-like structure.

obtained from the local slope of the surface. If instead we separately integrate out the role of kinks on the steps and adatoms on the terraces, we get a chemical potential profile which appropriately represents the discontinuities due to steps as shown in Fig. 3 (b). Using Eq. (1) requires understanding the thermodynamics of the surface since the surface free energy (which also governs the global equilibrium shape of the solid sample) is needed to determine the chemical potential profile for a given surface configuration. We also must consider the kinetic properties of the material since we need to know the allowed effective mass transport modes and their rate to study the actual evolution of the surface morphology. In this paper, we will focus on the cases where the dominant mass transport modes on the surface can be effectively described in terms of the mass transport from/to steps and then describe surface evolution as arising from step motions alone as suggested in Fig. 3(c). The application of these concepts to real experimental structures, as shown in Figs. 1 and 2(a), will be discussed in Section 4.

2.1. Representation of surface

A surface of a real material (at finite temperature) consists of a thermodynamic number of moving particles. How can we represent this in a simple mathematical form? To answer this, we need a precise definition of a surface. Although a surface is a boundary between two objects with different phases, the

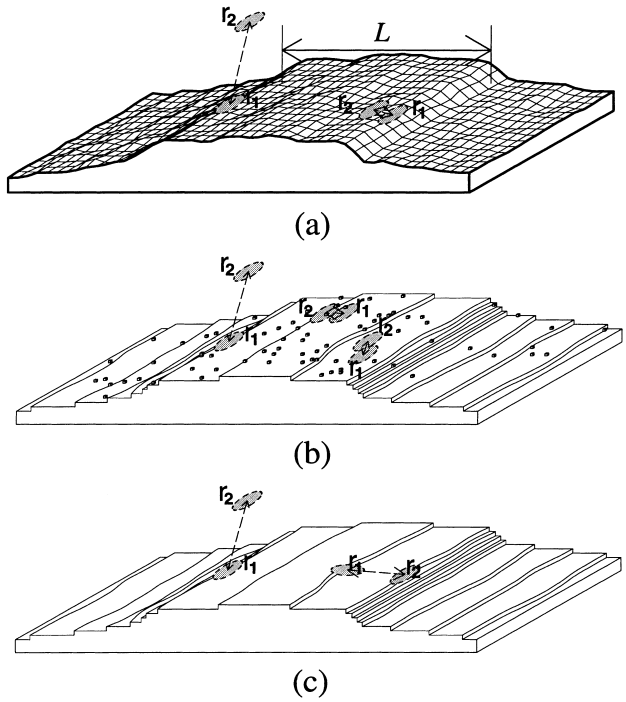

Fig. 3. Schematic illustration of a metastable surface structure of dimension L, which will decay via surface mass transport due to chemical potential differences at different positions on the surface. We can use equilibrium thermodynamics to define the local chemical potentials for regions (shown shaded) much smaller than L, using the assumption that they have relaxed to local equilibrium via fluctuations of wavelength much shorter than L, on a timescale much faster than that required for the equilibration (decay) of the structure of size L. The proper definition of local chemical potential and the effective modes of mass transport depend on the time and length scale of the surface description. The surface is described by a continuous height (a), if it is coarse grained over several terraces including steps and the chemical potential is obtained from the local slope of the surface. If instead, coarse graining is applied separately parallel to the step-edge and over small regions of the surface, we get a chemical potential profile over steps and terraces as shown in (b). In this article, we will mainly focus on the modes of mass transportation from/to steps and will illustrate how mass transport can be described in limiting cases based on step motions alone, as suggested in (c).

change from one phase to the other occurs continuously over the interface region. In other words, the order parameter, which tells the difference between the phases, changes continuously from the bulk value of one phase to that of the other. Thus some arbitrary decision should be made to define the position (or region) of the boundary. A precise definition of a surface as a boundary (with zero volume) between two phases was given by Gibbs a long time ago [2]. (We will not discuss the details of how this "Gibbs dividing surface" can be constructed or the validity of the approximation in representing the interface as a mathematical surface with zero volume. For a recent review on these subjects, see [3].) Once the real surface is mapped to a mathematical surface in d dimensions, it can be specified by a constraint, $S(u_1, \ldots, u_d) = 0$ and the thermodynamic surface functions, such as surface tension, γ, are given as the functional of S in general. The surface can be represented by an explicit solution of the constraint, $u_d = u_d(u_1, \ldots, u_{d-1})$ with $d-1$ parameters, when an appropriate choice for coordinates $u_1, \ldots, u_{d-1}$ is made for a given geometry and the thermodynamic surface functions are useful when

they are represented in the same coordinate system. For example, in three dimensions, a surface of a compact object, e.g., an equilibrium crystal shape, can be specified by the distance from the center $r = r(\phi, \theta)$ with two parameters representing the polar angles. In this case, the surface free energy in terms of its orientation, $\gamma(\phi, \theta)$, is convenient to study the equilibrium crystal shape of an entire sample. For nearly flat surfaces, which one often encounters when a small portion of crystal surface (limited by the range of mass transport) is considered, a surface is properly represented by the height from a reference flat surface, $z = z(x, y)$, where (x, y) is the point in the reference plane. Then the surface free energy is useful when it is expressed in terms of its slope $(\partial z/\partial x, \partial z/\partial y)$. In this paper, we mainly focus on nearly flat surfaces (represented in Monge gauge, $z = z(x, y)$) on a mesoscopic scale. But let us first consider the global equilibrium thermodynamics and equilibrium crystal shape on the macroscopic scale and discuss the relationship between the two.

2.2. Equilibrium thermodynamics

2.2.1. Equilibrium crystal shape at zero temperature

For crystalline materials, the surface free energy depends on the orientation of the surface due to the directional nature of the crystalline lattice. At zero temperature, it is easy to calculate the surface energy of solids described by simple lattice models by simply counting the number of neighbor bonds which are broken for a surface of a given orientation, as illustrated in Table 1 and Fig. 4. One might

Table 1
The surface energies at $T = 0$ K for simple crystalline lattices with nearest neighbor interactions of energy J_1 and second neighbor interactions of energy J_2. The energies are expressed in terms of the surface Miller indices $(h\,k\,l)$, the crystalline lattice constant a. Adapted from Wolff and Gulatieri [258]. The surfaces exposed on the equilibrium crystal shape are listed in the final columns for the case of nearest neighbor interactions only, for the case of first and second neighbor interactions. A tabulation including third neighbor interactions, a large number of crystal habits can be found in [258]

Structure	$\gamma_{h\,k\,l}/[a^2\sqrt{h^2+k^2+l^2}]$	Surfaces on ECS	
		First neighbor interactions only	First and second neighbor interactions
Simple cubic	$\frac{1}{2}(h+k+l)J_1 + (k+2l)J_2$	{0 0 1}	{0 0 1}, {0 1 1}, {1 1 1}
Face centered cubic	$2(h+2l)J_1 + 2(h+k+l)J_2$	{0 0 1} {1 1 1}	{0 0 1}, {0 1 1}, {1 1 1}
Body centered cubic	$2lJ_1 + (h+k+l)J_2$	{0 1 1}	{0 1 1}, {0 0 1}

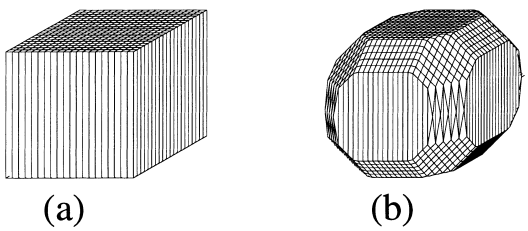

Fig. 4. Calculated equilibrium crystal shapes at $T = 0$ for a simple cubic model (a) with the nearest neighbor interaction only and (b) with both the second nearest neighbor interaction and the nearest neighbor interaction. As the interaction range increases, more facets appear on the ECS.

then expect that only the lowest energy surface orientation would be observed on the equilibrium crystal shape. Fortunately, reality is much more interesting, as the total surface free energy may be minimized by combinations of higher energy surfaces which reduce the overall surface area. To determine which surfaces are displayed on the equilibrium crystal shape one must know the surface free energy as a function of orientation. Then the thermodynamic stability of a surface orientation can be determined by the Wulff construction of the equilibrium crystal shape [4,5]. The Wulff construction gives the solution to the problem of minimizing the overall surface free energy for the given constraint of constant volume. The result basically states that the equilibrium shape is the shape which results from taking the inner envelope of the surfaces perpendicular to the radii of a polar plot of the surface free energy. An intuitively useful result of this construction is that the distance of a facet from the center of the equilibrium crystal shape is proportional to its surface energy

$$R_i = (\text{constant})\gamma_i, \tag{2}$$

where γ_i is the surface free energy per unit area (the surface tension) of the ith facet and R_i is the distance of the ith surface from the center of the crystal shape measured normal to the surface. This geometrical description of the equilibrium crystal shape makes it easy to see that the lowest energy surfaces will also be those with the largest relative areas. As an example, the zero temperature crystal shapes corresponding to a simple cubic lattice with first and second neighbor interactions are shown in Fig. 4(a) and (b). The results listed in Table 1 illustrate how the complexity of the ECS increases with the geometry and range of neighboring interactions in the model.

Real solids are only qualitatively described by lattice models, and real surfaces are likely to bear even smaller resemblance to lattice models due to the possibilities of surface relaxations and reconstructions [6]. Table 2 lists some calculated surface energies ($T = 0$) for different solid materials. It is a useful rule of thumb that surface energies are typically on the order of 0.1 eV/Å^2. Also the differences in energies between different surface orientations are typically much smaller than those of Kossel crystals (see Table 1). As an example of the issues which arise in calculating real crystal shapes, we consider the case of GaAs. Because it is readily possible to change the surface composition of GaAs, the various low-index surfaces can each exist in a number of reconstructions of different relative arsenic content. Moll et al. [7] have recently dealt with this issue by calculating the equilibrium crystal shape as a function of variable surface chemical potential of arsenic. The approach is illustrated in Fig. 5. Based on experimental observations of faceted GaAs samples, a limited number of surface orientations were considered. For each, the surface energies of the most stable reconstructions, illustrated in Fig. 5(a) for the (1 1 0) surface, were each calculated while allowing the surface chemical potential of As to vary compared with that of the bulk, as shown in Fig. 5(b). For non-stoichiometric structures, the resulting surface energies varied significantly with As chemical potential, with the result that different reconstructions may be stabilized at different As chemical potentials. The immediate consequence of this, shown in Fig. 5(c) is that the equilibrium crystal shape is strongly dependent on the surface chemical potential. Less obvious is the fact that different surface orientations present on the same equilibrium crystal shape need not have the same composition. Depending on the specific energetics, structures of quite different composition may be present on different surfaces. Both the sensitivity of the equilibrium crystal shape to chemical composition, and the phenomenon of differential composition on different surfaces, described here for a binary solid, are important in studies of chemical adsorption on surfaces [8–10]. Incorporating the complexity of

Table 2
Selected values of the surface tension determined experimentally and theoretically are shown here to illustrate the range of values observed. The surface tension is a decreasing function of temperature so the experimental values for the melting temperature should be lower than the theoretical values for absolute zero. More complete tabulations of experimental values can be found in [259–261]. Tabulations of theoretical values can be found in [262–264]

Element	Experimental[a] values (meV/Å^2)	Theoretical values; $T = 0$ K		
		Miller index	LAPW[b]	EAM[c] (meV/Å^2)
Al	63.7	(1 0 0)		34.3
Ag	68.0	(1 0 0)	75.5 meV/Å^2	43.7
		(1 1 1)	75.5 meV/Å^2	38.7
Ni	129.8	(1 0 0)		101.7
		(1 1 1)		93.0
		(1 1 0)		111.1
		(3 1 1)		110.5
Pd	108.6	(1 0 0)	116.1 meV/Å^2	90.0
Mo	156.6	(1 1 0)	195.9 meV/Å^2	
		(1 0 0)	219.7 meV/Å^2	
GaAs[d]	54 ± 19	(1 1 0)	52 meV/Å^2 (cleavage surface) 45 meV/Å^2 (As-rich surface)	
		(1 1 0)	65 meV/Å^2 $\alpha(2 \times 4)$ + others depending on As content	
		(1 1 1)	54 meV/Å^2 (Ga vacancy) 51 meV/Å^2 (As-rich surface)	
		$(\bar{1}\,\bar{1}\,\bar{1})$	69 meV/Å^2 (Ga adatom) 43 meV/Å^2 (As-rich surface, As trimer structure)	
Si	77[e] 76[f]	(1 1 1)	(1×1) 0.109[g] eV/Å^2 (adatom 2×2) 0.088[g] eV/Å^2 (2×1) 0.097[h] eV/Å^2 (7×7) 0.092[h] eV/Å^2 (7×7) 0.090[i] eV/Å^2	

[a] Ref. [259] (metals at $T = T_m$) and [269] (GaAs cleavage).
[b] Ref. [263] (metals) and [7] (GaAs).
[c] Ref. [262].
[d] Surface energy depends on arsenic chemical potential, different surface reconstructions are stable at different chemical potentials.
[e] Ref. [270], surface reconstruction is most likely 2×1 following cleavage.
[f] Ref. [271,272].
[g] Ref. [273].
[h] Ref. [274].
[i] Ref. [275].

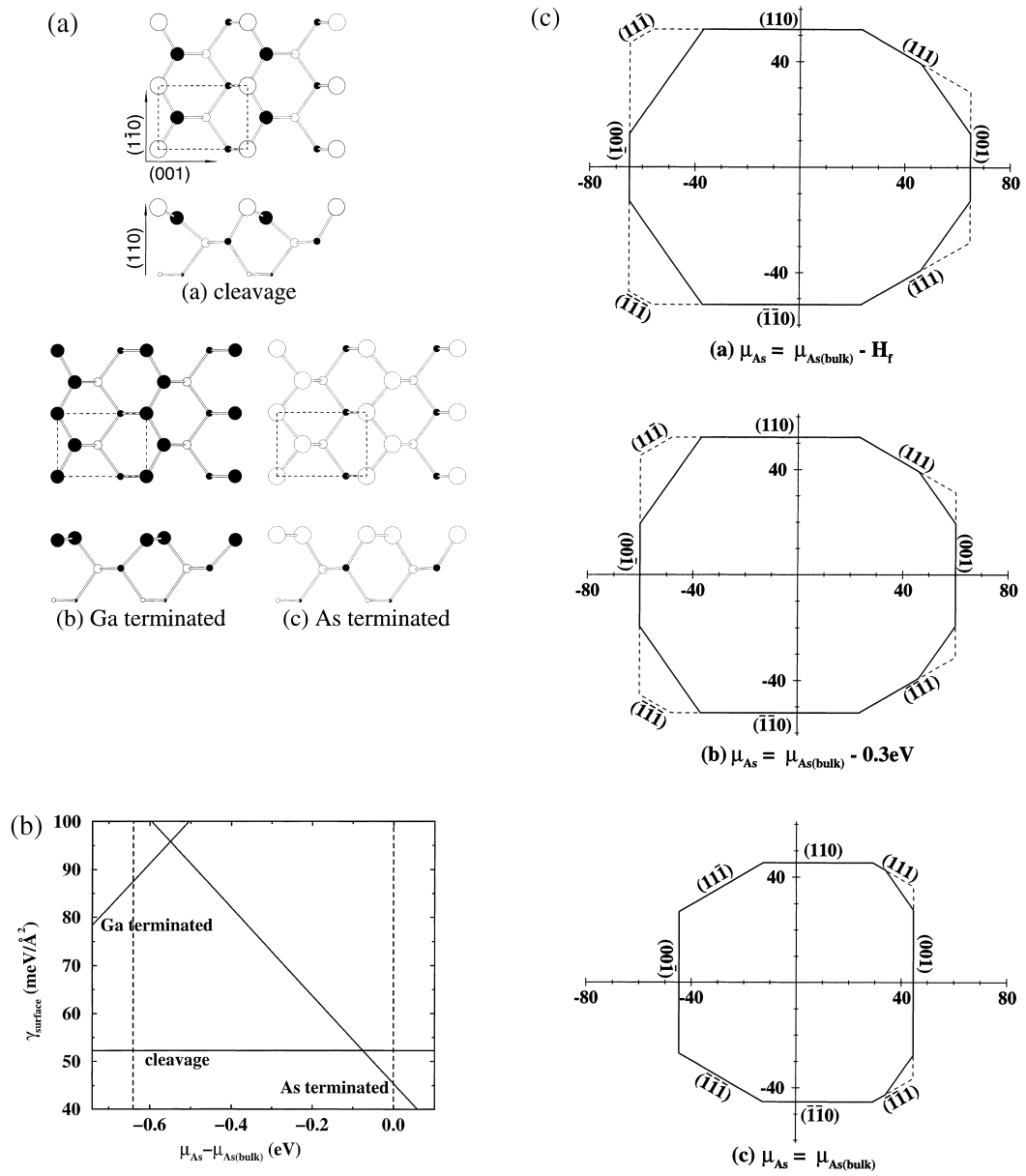

Fig. 5. Calculation of the $T = 0$ equilibrium crystal shape of GaAs [7], (a) the three lowest-energy reconstructions of GaAs(1 1 0) are the cleavage surface, which has the bulk stoichiometry ($\Delta N = 0$), a Ga-rich structure ($\Delta N = -2$), and an As-rich structure ($\Delta N = 2$). (b) The energy of the stoichiometric cleavage structure is independent of the surface As chemical potential, while the Ga-rich structure is de-stabilized by increasing As chemical potential, and the As-rich structure is stabilized by increasing As chemical potential. As shown, the Ga-rich structure is never stable with respect to the other two structures. A crossover in structure from the cleavage surface to the As-terminated surface occurs at an As chemical potential just below that of the bulk. (c) Energy calculations similar to those shown in (b) were also performed for the (1 0 0), (1 1 1), and $(\bar{1}\,\bar{1}\,\bar{1})$ surfaces. Using the calculated values for the surface tension at common values of the As chemical potential allows the strong dependence of the equilibrium crystal shape on As chemical potential to be demonstrated. Note that it is the chemical potential, not the stoichiometry of the different surfaces represented on the ECS which is required to be the same (figures from Ref. [7], provided by M. Scheffler, Fritz-Haber Institut).

compositional effects into the step-based description of surface mass transport is an important challenge.

2.2.2. *Vicinal surfaces on the equilibrium crystal shape*

The discussion above, predicated on the zero-temperature surface energies, focuses attention on the low-index surfaces, which are atomically rather smooth. To obtain higher index surface orientations in the zero-temperature equilibrium crystal shape, it is necessary to introduce longer-range interactions between the atoms in the models used to describe the solid. As the range of the interaction energy is increased to further and further neighbor pairs, more and more facet orientations are stabilized, until finally high-index surfaces which have corrugated surface structures at the atomic level appear. Finally, if the interactions are long range enough, the very high-index surfaces which are called stepped or ''vicinal'' surfaces can be stabilized as facets in the ECS. In this case, the surface will be perfectly ordered as for a $(3, \bar{2}, 16)$ surface illustrated in Fig. 6 [11]. However, such energetic stabilization of stepped surfaces is of far less interest than the ''entropic'' stabilization which occurs at non-zero temperature.

At finite temperature, vicinal surfaces can be stable even in a model based on short ranged energetic interaction and can appear on rounded edges on the ECS. Regardless of the range of the interactions, at zero temperature the equilibrium crystal shape consists of a series of discrete facets separated by sharp edges and corners, but at non-zero temperature the corners and edges of the equilibrium crystal shape can become rounded, exposing a continuum of orientations. As temperature increases, the facets shrink and the rounded regions grow. Each facet fully disappears as the temperature is raised to its ''roughening transition temperature'', T_R [12,13], and the surface is smoothly rounded everywhere for $T \geq T_R$ (which is usually below the melting temperature). Fig. 7 illustrates the equilibrium crystal shapes at finite T for a simple cubic model with the nearest neighbor interaction. Global equilibrium crystal shapes are shown in (a) and (b) for below and above the roughening transition temperature respectively. The local regions, denoted by the squares in (a) and (b), are vicinal

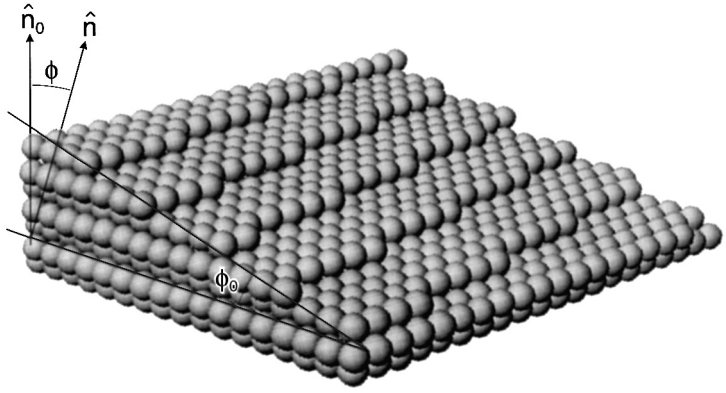

Fig. 6. Structure of an fcc $(3, \bar{2}, 16)$ surface, which is vicinal to the fcc (0 0 1), to illustrate the defect structure in the form of steps and kinks, which occurs on high index (or ''vicinal'') surfaces at zero temperature. The vicinal-surface and terrace normals are $\hat{n} = (3, -2, 16)/\sqrt{269}$ and $\hat{n}_0 = (0, 0, 1)$, respectively. The polar angle ϕ (defined here with respect to the (001) direction) is $\arccos\left(16/\sqrt{269}\right)$, while the azimuthal angle θ, indicating how much $\hat{n}$ is rotated around $\hat{n}_0$ away from the vertical border on which ϕ_0 is marked is clearly $\arctan(1/5)$; $\tan\phi_0 = \tan\phi\cos\theta$ (figure from Ref. [11], provided by T.L. Einstein, University of Maryland).

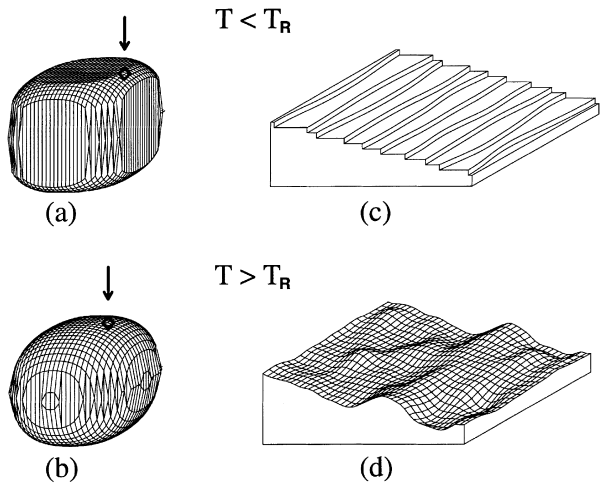

Fig. 7. Schematic illustrations of equilibrium crystal shapes at finite T for a simple cubic model with the nearest neighbor interaction. Equilibrium crystal shape is shown for (a) $T < T_R$ for which the (0 0 1) facets are stable and (b) for $T > T_R$ for which the ECS has become continuously rounded so that no facets are present. The local regions, denoted by the squares under arrows in (a) and (b), are vicinal to the low index (0 0 1) surface. Their characteristic structures on the mesoscopic scale are very different as shown in (c) and (d). See text for details.

to the low-index (0 0 1) surface. Fig. 7(c) and (d) show such regions in a mesoscopic view (see Section 2.2.3 for the details on the viewpoints of different scales). In both cases, the vicinal surfaces themselves are in a rough phase [13,14] but their thermal properties and characteristic structures are very different. This is because the thermal proliferation rates of steps, islands and voids critically depend on whether the temperature is above or below the roughening transition temperature of the neighboring low-index surface. The roughening transition is connected with the disappearance of the cusp in the γ-plot. In the Wulff construction, the cusp in the γ-plot results in the existence of a facet. The cusp in the γ-plot, i.e., the non-analytic term in the surface tension, comes from the finite free-energy cost (β, per unit length) for the formation of a step. Hence, the disappearance of a facet implies that the step free energy, β, vanishes at T_R and free proliferation of steps is expected for $T > T_R$.

For $T < T_R$, a vicinal surface mainly consists of terraces and steps as shown in Fig. 7(c). Though the fractional area of vicinal surfaces on the ECS is relatively small at low temperature, we encounter those surfaces quite commonly in experiments. Experimentally, even serious attempts to prepare extremely well-oriented low-index surfaces inevitably result in surfaces with a small residual miscut (typical value around 0.1°), and thus a low density of steps. Such steps (or alternatively steps which arise via crystal defects such as misfit dislocations) play an important role in allowing growth and sublimation processes to occur at very small supersaturations [15]. Structures with high step densities may occur during growth, or as a result of nano-fabrication processes. Finally, vicinal surfaces are often also prepared experimentally in an effort to change the chemical reactivity or growth properties of a surface by changing its structure.

At low T, below the roughening temperature (of the low-index surface), thermal excitation of islands or voids on the terrace is rare and a vicinal surface has the minimum number of steps (of the same sign; all ascend or descend) which is necessary to satisfy the boundary condition imposed by the macroscopic orientation of the sample. Then, the surface free energy of a vicinal surface can be

estimated by considering the free energy of steps. As a physical illustration, let us consider a simple cubic lattice model in which the surface energy per unit area, or equivalently the surface tension at zero temperature, of a vicinal surface with direction $\hat{r}(\phi,\theta)$ (see Fig. 6) is given by

$$\begin{aligned}\gamma(\phi,\theta) &= \frac{\epsilon_z}{a_x a_y}|\cos\phi| + \frac{\epsilon_x}{a_y a_z}|\sin\phi\cos\theta| + \frac{\epsilon_y}{a_x a_z}|\sin\phi\sin\theta| \\ &= \frac{\epsilon_z}{a_x a_y}|\cos\phi| + \left[\frac{\epsilon_x}{a_y}|\cos\theta| + \frac{\epsilon_y}{a_x}|\sin\theta|\right]\frac{|\sin\phi|}{a_z},\end{aligned} \tag{3}$$

where ϵ_x, ϵ_y and ϵ_z are the energy costs to break a bond and a_x, a_y and a_z are the lattice constants in the x, y and z directions, respectively. For vicinal surfaces ($|\tan\phi| \ll 1$), considering the surface free energy per unit area projected onto the nearest facet orientation ($\theta = 0, \phi = 0$), $f \equiv \gamma/|\cos\phi|$ is convenient to predict the finite temperature form of the free energy. It is also useful to study the thermodynamics of faceting, as will be discussed in Section 4.1, since it allows a direct analogy with the thermodynamics of a liquid–vapor system [16,17]. At zero temperature, from Eq. (3), we have

$$f = \frac{\epsilon_z}{a_x a_y} + \left[\frac{\epsilon_x}{a_y}|\cos\theta| + \frac{\epsilon_y}{a_x}|\sin\theta|\right]\frac{|\tan\phi|}{a_z} = \gamma_0 + \beta_0(\theta)\,|\tan\phi|/h, \tag{4}$$

where $\gamma_0 = \epsilon_z / a_x a_y$ is the energy density of the flat surface, $\beta_0(\theta) = \epsilon_x|\cos\theta|/a_y + \epsilon_y|\sin\theta|/a_x$ is the energy cost per unit length of a step and $h = a_z$ is the height of the step. Real step energies are unlikely to be quantitatively described by a lattice model for the same reasons, relaxation and reconstruction, that real surface energies differ from the predictions of a lattice model. However, calculation of step energies is more difficult than calculation of surface energies due to the lower symmetry of the problem. Thus there is a limited body of information about step energies and their variation with step orientation, which is synopsized in Table 3. Unsurprisingly, step energies tend to be larger on materials with large surface energies, and for step orientations with ''rougher'' crystallographic orientation. A useful rule of thumb for estimating step energies is to take the step energy as the areal cost of creating the surface represented on the step face minus the energy gained by reducing the area of the terraces (if the step face is not perpendicular to the terrace) [11].

The crystallographic variation of step free energy as a function of orientation can be clearly seen in the shapes of equilibrated islands during growth [18]. Such studies can also demonstrate the extremely important consideration that the changes in the chemical properties of the surface, for instance due to chemical adsorption, can have profound effects on the energetic parameters, including the step energy. This result is strikingly illustrated in Fig. 8. The islands shown in the figure show a complete reversal in the relative stability of the $[\bar{2}\,1\,1]$ oriented steps and $[2\,\bar{1}\,\bar{1}]$ oriented steps due to the adsorption of carbon monoxide.

At finite temperature, the steps become wavy and fluctuate due to thermal proliferation of kinks and their motion along the step-edge. Now, we need to consider the configurational entropy of a step, S_0 to calculate the step free energy, β, which is given as

$$\beta = \beta_0 - TS_0. \tag{5}$$

In the simplest case, we can easily estimate the entropy of wandering of an isolated step. Using the simple lattice model of Eqs. (3) and (4), and considering a step along a high symmetry direction for

Table 3
The energies of the three fundamental structural units in defining vicinal surfaces, the terrace energy, the step energy and the kink energy are listed for several different systems. Systems chosen for the table are those for which information about low-symmetric excitations as well as step energies have been calculated. For each system, defined by the material and the orientation of the nearest low-index surface, the results for the energies of the surface, steps of specified orientation, kinks on each type of step are tabulated. The step orientation is indicated by the vector lying in the plane of the terrace and oriented perpendicular to the step-edge pointing in the downhill direction. For high-symmetry steps on a fcc lattice, common orientations are

• fcc (1 1 1) surface: $[\bar{1}\,\bar{1}\,2]$ step, for which the step-edge is parallel to the close packed $[\bar{1}\,1\,0]$ direction, and the vicinal surfaces are located on the stereographic triangle between the (1 1 1) and the (0 0 1) orientation [265]. Another notation for this type of step is $\langle 1\,1\,0\rangle/\{1\,0\,0\}$, where the first term refers to the direction parallel to the step, and the second term is a "micro-facet" orientation which is likely to correspond to the orientation of the step face [266,267].

$[1\,1\,\bar{2}]$ step, for which the step-edge is parallel to the close packed $[\bar{1}\,1\,0]$ direction, and the vicinal surfaces are located on the stereographic triangle between the (1 1 1) and the (1 1 0) orientation. Another notation for this type of step is $\langle 1\,1\,0\rangle/\{1\,1\,1\}$.

• fcc (1 0 0) surface: [1 1 0] step, for which the step-edge is parallel to the close packed $[\bar{1}\,1\,0]$ direction, and the vicinal surfaces are located on the stereographic triangle between the (0 0 1) and (1 1 1) orientations. Another notation for this type of step is $\langle 1\,1\,0\rangle/\{1\,1\,1\}$.

[1 0 0] step, for which the step edge is parallel to the non-close packed [0 1 0] direction, and the vicinal surfaces are located off the high symmetry axes of the stereographic triangle. Another notation for this type of step is $< 010 >/\{1\,1\,0\}$.

The formation energy for each type of structure is listed in the third column. The surface formation energy is the energy cost for creating the surface from a bulk crystal, e.g. it is just the $T = 0$ K surface tension. The step formation energy is the energy increase required to create a surface with one perfectly straight step from a flat surface at $T = 0$ K. The kink formation energy is the energy increase required to create one kink on an otherwise perfectly straight step at $T = 0$ K. The adatom energies, listed in column 4, are the energy change required to move an atom from the bulk to a position on the flat surface, the straight step, or the kink site respectively. The difference in the adatom energies are useful for calculating changes in binding energy as an adatom moves between different types of sites. Similarly, the vacancy energies listed in column 5 are the energy changes when an atom is removed from a site on the flat terrace, the straight step, or the kink site, respectively, to a bulk position.

The calculational approaches used for each result reported are listed in the last column, along with the major reference reporting the results. The abbreviations are: DFT–LDA = density functional theory– local density approximation, EAM = embedded atom method, ECT = equivalent crystal theory, 4th Mom = fourth- moment approximation to tight-binding theory, SW = Stillinger Weber potential, EP = empirical potential other than SW, GGA = generalized gradient approximation

System	Structure	Energy				Technique [reference]
		Formation		Adatom	Vacancy	
Al (1 1 1)	Terrace		0.070 eV/Å^2	1.05 eV	0.67 eV	DFT–LDA
	$[\bar{1}\,\bar{1}\,2]$ Step		0.088 eV/Å	0.25 eV	0.24 eV	[276]
	Kink		$\sim 0.12^a$ eV	–	–	
	$[1\,1\,\bar{2}]$ Step		0.082 eV/Å	0.28 eV	0.21 eV	
	Kink		$\sim 0.12^a$eV	–	–	
Ag(1 1 1)[b]	Terrace	0.039	(0.077) eV/Å^2	0.709 eV	0.549 eV	EAM (ECT)
	$[\bar{1}\,\bar{1}\,2]$ Step	0.065	(0.171) eV/Å	–	–	[11,277]
	Kink	0.102	(0.213) eV		–	
	$[1\,1\,\bar{2}]$ Step	0.066	(0.161) eV/Å	–	–	
	Kink	0.099	(0.255) eV	–	–	
Ag(0 0 1)[b]	Terrace	0.044	(0.099) eV/Å^2	–	–	EAM (ECT)
	[1 1 0] Step	0.036	(0.056) eV/Å	[c]	–	[11,277]
	Kink	0.102	(0.219) eV	–	–	

Table 3 (*continued*)

System	Structure	Energy				Technique [reference]
		Formation		Adatom	Vacancy	
Au(1 1 0)	Terrace		–	–	–	EAM
	$[\bar{1}\,1\,0]$ Step		0.03 eV/Å	–	–	[278]
	Kink		0.002 eV	–	–	
	[0 0 1] Step		0.014 eV/Å	–	–	
	Kink		0.024 eV	–	–	
Cu(1 1 0)	Terrace		–	–	–	EAM
	$[\bar{1}\,1\,0]$ Step		0.05 eV/Å	–	–	[278]
	Kink		0.04 eV	–	–	
	[0 0 1] Step		0.004 eV/Å	–	–	
	Kink		0.13 eV	–	–	
Ni(1 1 0)	Terrace		–	–	–	EAM
	$[\bar{1}\,1\,0]$ Step		0.05 eV/Å	–	–	[278]
	Kink		0.05 eV	–	–	
	[0 0 1] Step		0.01 eV/Å	–	–	
	Kink		0.32 eV	–	–	
Pt(1 1 1)[b]	Terrace	0.09	(0.107) eV/Å^2	–	–	EAM (ECT)
	$[\bar{1}\,\bar{1}\,2]$ Step	0.124	(0.283) eV/Å	–	–	[11,277]
	Kink	0.161	(0.384) eV	–	–	
	$[1\,1\,\bar{2}]$ Step	0.123	(0.274) eV/Å	–	–	
	Kink	0.178	(0.431) eV	–	–	
Pt(0 0 1)[b]	Terrace	0.103	(0.148) eV/Å^2	–	–	EAM (ECT)
	[1 1 0] Step	–	(0.090) eV/Å	–	–	[11,277]
	Kink	–	(0.401) eV	–	–	
	[0 1 0] Step	–	(0.100) eV/Å	–	–	
	Kink	–	(–)	–	–	
Pt(1 1 0)	Terrace		–	–	–	EAM [278]
	$[\bar{1}\,1\,0]$ Step		0.05 eV/Å	–	–	
	Kink		0.005 eV	–	–	
	[0 0 1] Step		0.03 eV/Å	–	–	
	Kink		0.36 eV	–	–	
Si(1 1 1)	(1 × 1) Terrace	0.085	(0.088) eV/Å^2	–	–	SW (KD) [279]
	$[\bar{1}\,\bar{1}\,2]$ Step	0.162	(0.240) eV/Å	–	–	
	Kink	0.220	(0.324) eV	–	–	
	$[1\,1\,\bar{2}]$ Step	~ 0.188	(0.202) eV/Å	–	–	
	Kink	−0.02	(0.987) eV	–	–	
	$[\bar{1}\,0\,1]$ Step	0.188	(0.324) eV/Å	–	–	
	Kink	–	–	–	–	
Si(0 0 1)	Terrace		–	–	–	TB [280,281]
			–	1.34 eV	–	SW [282]
	S_A^{d}		3±3 meV/Å	–	–	TB [283]
			–	1.17 eV	–	SW [284]
	S_B		39±8 meV/Å	–	–	TB [283]
			–	1.17[d] eV	–	SW [284]

Table 3 (*continued*)

System	Structure	Energy			Technique [reference]
		Formation	Adatom	Vacancy	
	$D_A^{(e)}$	140±30 meV/Å	–	–	TB [283]
		–	1.17[h] eV	–	SW [284]
	D_B	13±5 meV/Å	–	–	TB [283]
		–	1.33[h] eV	–	SW [284]
W(1 1 0)	Terrace	0.116 eV/Å^2	–	–	fourth–moment
	$[1\,\bar{1}\,2]$ Step	0.136 eV/Å	–	–	[183]
	Kink	0.349 eV/Å	–	–	
		0.427[g] eV/Å	–	–	
	[0 0 1] Step	0.208 eV/Å	–	–	
	Kink	−0.277[h] eV	–	–	
	$[\bar{1}\,1\,0]$ Step	0.309 eV/Å	–	–	
	Kink	−0.275[h] eV	–	–	
O/Pt(1 1 1)	$[\bar{2}\,1\,1]$ Step	–	$\Delta E = 0.6$[i] eV	–	
	$[2\,\bar{1}\,\bar{1}]$ Step	–	$\Delta E = 0.4$ eV	–	

[a] Not directly calculated. Estimated as approximately one half of the formation energy for an adatom or a vacancy at the step.
[b] The surface energy was calculated as a function of orientation between the (001) and (111). The EAM- and ECT-predicted energy variation was in good agreement with the prediction for near–neighbor interactions for Ag, and in moderate agreement for Pt.
[c] The binding energy difference for an adatom on the terrace and an adatom at the step-edge has been calculated to be 0.43 or 0.32 eV using LDA and GGA methods [285].
[d] The traditional notation for steps on Si(1 0 0) uses S for single–layer high steps and D for double–layer high steps. The subscripts A and B indicate the orientation of the symmetry–breaking 2×1 reconstruction with respect to the step-edge. S_A steps are single-height steps with the dimer rows on the upper terrace parallel to the step-edge.
[e] Experimentally S_A and S_B steps are observed at low step densities ($\phi \leq 2^\circ$) and D_B steps are observed at high step densities. D_A steps are not observed experimentally when surface are clean and well–annealed.
[f] There are a number of binding sites at each step. The numbers listed here are for the most strongly bounded site.
[g] The $[1\,\bar{1}\,2]$ step is the close–packed step-edge on this surface (step-edge is parallel to $[\bar{1}\,1\,1]$, but it does not have mirror symmetry parallel to the step-edge. Thus there are two distinct kink geometries on this step.
[h] The kinks on the two low–symmetry steps can form with the close packed structure of the $[1\,\bar{1}\,2]$ step, and thus kink formation lowers the step energy in spite of the increased length of the step-edge.
[i] Energies quoted are the difference in binding energy between an O–atom at the step-edge site on $[\bar{2}\,1\,1]$ step and upper step-edge for fcc site for $[2\,\bar{1}\,\bar{1}]$ step and the preferred 3–fold fcc site on the terrace.

which $\theta = 0$, we find that the energy for creating the simplest excitation at a step-edge, a kink, is ϵ_y. Then it is possible to find the temperature dependence of the free energy cost for an isolated step by analogy with the Ising model [19]:

$$\beta(T) = \frac{\epsilon_x}{a_y} - \frac{kT}{a_y} \ln\left(\coth\frac{\epsilon_y}{2kT}\right), \tag{6}$$

where k is the Boltzmann constant. The step free energy of the isolated step decreases with increasing temperature due to the configurational entropy generated by thermal kink formation. For the isolated

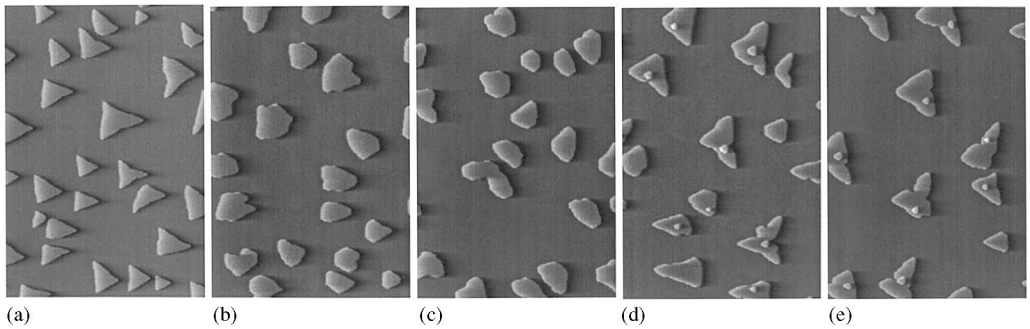

Fig. 8. The influence of chemical adsorbates on the energetics and kinetics of steps is clearly illustrated in this series of 1700 Å× 2500 Å STM topographs measured after deposition of 0.15 ML of Pt on Pt(1 1 1) at 400 K and with different CO partial pressures during growth. (a) $p_{CO} < 5 \times 10^{-12}$ mbar (clean island growth shape), (b) $p_{CO} = 1 \times 10^{-10}$ mbar, (c) $p_{CO} = 4.7 \times 10^{-10}$ mbar, (d) $p_{CO} = 9.5 \times 10^{-10}$ mbar, (e) $p_{CO} = 1.9 \times 10^{-9}$ mbar (figure from Ref. [343], provided by Th. Michely of RWTH Aachen).

step energy, β for non-zero θ, see [19]. Application of this result in terms of the effect of azimuthal misorientation on step interactions and phase separation is discussed in [20].

The configurational entropy of steps on real surfaces is always smaller than that of the hypothetical isolated steps. This is because the steps on real surfaces exist with a non-zero density, and the resulting effect of the no crossing constraint between the steps, which prevents the formation of structures with a prohibitively high overhang energy, reduces the entropy when two steps get close. Therefore, the entropic reduction of free energy depends on the distance between the neighboring steps as well as the temperature. The terrace width dependence of the entropy was first calculated by Gruber and Mullins [21], using a simple model of a wandering step constrained in its motion by the presence of two neighboring fixed walls, as illustrated in Fig. 9. They showed that the configurational entropy of the step trapped between two walls of separation $2w$ is given by

$$S(T, w) = S_0(T) - g'(T)/w^2, \tag{7}$$

where S_0 is the entropy of a free step without walls and g' is a width-independent constant. The entropy reduction of steps on a vicinal surface due to the confinement by the neighboring (fluctuating) steps

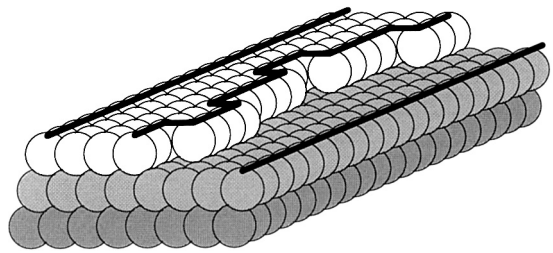

Fig. 9. Gruber and Mullins [21] considered an atomistic model of step wandering via kink formation similar to the illustration here. The position of the step, indicated by a heavy dark line follows the centers of the atoms at the edge. The wandering of the step is constrained by a requirement that it does not pass the two neighboring steps, indicated by the two straight solid lines. In the first approximation, which catches the essential physics of entropic interactions due to step wandering, the neighboring steps are treated as straight walls.

shows essentially the same behavior [22] when w is replaced by the average distance between steps, $h/|\tan\phi|$. Hence, with β of Eq. (5), the projected free energy density, f becomes

$$\begin{aligned} f(T) &= \gamma_0(T) + (\beta_0 - TS_0(T))\,|\tan\phi|/h + (g'(T)T/h^3)|\tan\phi|^3 \\ &= \gamma_0(T) + \beta\,|\tan\phi|/h + g|\tan\phi|^3, \end{aligned} \tag{8}$$

where $\beta = (\beta_0 - TS_0)$ is the free energy cost per unit length to create an isolated, thermally wondering step of height h and $g = g'T/h^3$ is the step interaction parameter. The parameter g considered here is explicitly dependent on the extent of wandering of the step through a parameter known as the step diffusivity, or its inverse, the step stiffness, which in turn is determined by the facility with which thermal kinks are excited on the step-edge. The stiffness $\tilde{\beta}$, as its name suggests, is a measure of a step's tendency to straighten, thus reducing the length and kink density. The stiffness is related to the step free energy by [23–25]

$$\tilde{\beta}(\theta, T) = \beta(\theta, T) + \frac{\partial^2\beta}{\partial\theta^2}. \tag{9}$$

In the case of entropically wandering steps, the expression for the entropic step interaction term g can be expressed in terms of the stiffness as [22, 25–27]

$$g(\theta, T) = \frac{(\pi kT)^2}{6h^3\tilde{\beta}(\theta, T)}. \tag{10}$$

In addition to this entropic effect, step wondering may also be reduced by repulsive energetic terms between neighboring steps on the surface, such as elastic or dipole interactions, which give rise to the same inverse square dependence on terrace width [3]. Hence, in general, the step interaction parameter g must take account of both entropic and energetic interactions between neighboring steps. In the case where there are energetic step–step repulsions which go as $U(w) = A/w^2$, the step interaction parameter g becomes [3,16,26,27]

$$g(\theta, T) = \frac{(\pi kT)^2}{24h^3\tilde{\beta}(\theta, T)}\left[1 + \sqrt{1 + \frac{4A\tilde{\beta}(\theta, T)}{(kT)^2}}\right]^2. \tag{11}$$

Experimental measurements of the form and magnitude of the step interactions will be discussed in Section 4.

The thermal fluctuations of steps have a number of practical consequences for the observation of the structure of vicinal surfaces. One prediction involves the equilibrium crystal shape near the edge of a facet. Based on the expression for the free energy in Eq. (8), where it is implicitly assumed that the neighboring facet is below its roughening temperature, the ECS contains a flat facet whose width is proportional to the step free energy β. The rounded regions at the edge of the facet approach the facet tangentially, with a shape governed by the step interaction term in the free energy, resulting in a shape that goes as $z \sim (x - x_0)^{3/2}$, where z is the height of the surface and x_0 is the x-coordinate of the point at which the rounded region and the flat surface meet. Experimental tests of this prediction have included direct measurements of the shape of equilibrated crystals of He [28] and Pb [29]. Making such measurements is difficult, as the definition of the point at which the rounded region begins, x_0, strongly affects the determination of the exponent [30], and as the scaling prediction is only valid over a small range of angles. However, the results for the rounding of the edge of the Pb crystals are at least

consistent with an exponent of $3/2$, and those for the He crystals confirm the value of $3/2$. More recently, Bonzel and co-workers [31] have used STM to image directly the facet edge of small supported Pb crystallites, as shown in Fig. 10. In this case, the zero of the facet edge can be determined precisely by the position of the first observed step, ameliorating the problems of the experiments mentioned above. To test the form of the exponent in Eq. (8), profiles of the crystallites such as the one shown in Fig. 10 (c) were fit to the expected asymptotic ECS for a surface free energy of the form

$$f = f_0 + f_1 \tan\phi + f_2 \tan^2\phi + f_3 \tan^3\phi. \tag{12}$$

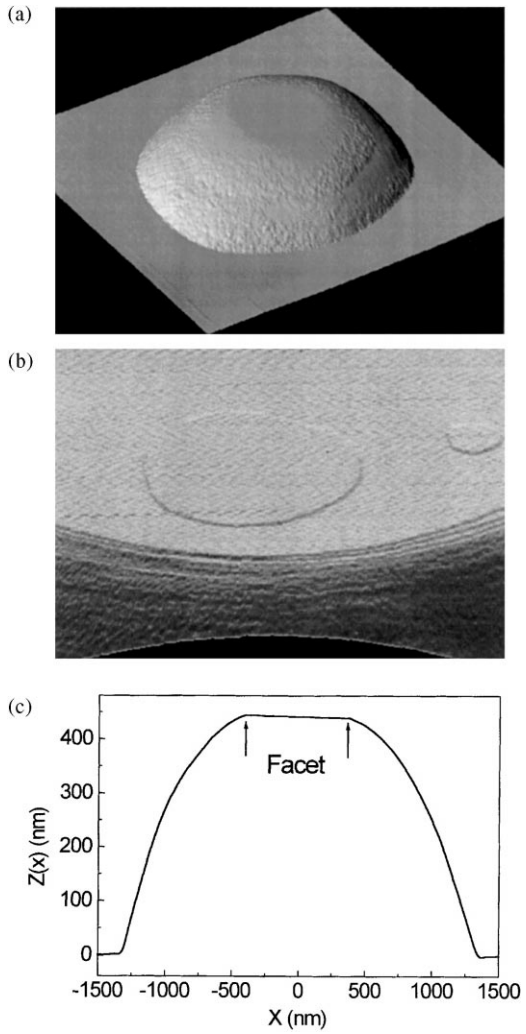

Fig. 10. (a) Three-dimensional view of a STM image of a Pb particle on a Cu(1 1 1) substrate equilibrated at 440 K. The size of the image is 3.5 micron × 3.5 micron. (b) Three-dimensional view of a section of a (1 1 1) facet and the vicinal surface next to the facet. Individual monatomic steps can be recognized as the transition from the facet to the rounded edge. Image size: 775 nm × 527 nm. (c) Line profile across center of a complete Pb particle, annealed at 530 K; arrows indicate facet edge (figures from Ref. [31], provided by H.P. Bonzel of the IGV, Julich).

The parameters determined from the fit were found to depend consistently on the azimuth of the profile, i.e., the crystallographic direction of the cross-section of the crystallite. Specifically, the measured values of f_2 and f_3 oscillate out of phase, with maxima and minima along the high-symmetry directions. However, the amplitude of the variation in f_2 (which varies symmetrically about zero) is approximately 10 times smaller than the maximum value (and three times smaller than the minimum value) of f_3 (for which the value is consistently positive). If the data are fit to the simple form $z \sim (x - x_0)^n$, these variations correlate to a variability in the value of n from 1.4 to 1.7, with the same 3-fold azimuthal symmetry. These results confirm the use of Eq. (8) with only the cubic term as a good approach for describing the behavior of real stepped surfaces. They also raise interesting questions about possible physical mechanisms which might perturb the dominant inverse square interaction.

Another result of the thermal wandering of steps is that the vicinal surfaces are rough. This means that the height–height correlation function should diverge logarithmically [14]. For stepped surfaces, this logarithmic divergence is related to the wandering of the steps, which causes the step-edge correlation function parallel to the average step position to diverge logarithmically as a function of distance parallel to the step [26]. The roughness of a vicinal surface can be measured by measuring the correlation function of the perpendicular step displacements as a function of distance perpendicular to the step-edge. Experimental tests of this idea have been attempted using scanning tunneling microscopy (STM) for the Si(111)-7×7 surface [32], which showed consistency with a logarithmic divergence, and more rigorously using reflection electron microscopy (REM) for the high-temperature Si(111)-1×1 surface [33]. In the latter study, the logarithmic divergence was confirmed, with a physically reasonable prefactor, but only up to distances corresponding to about seven step spacings (average spacing was 29 nm). Beyond that distance the correlation function deviated in a positive sense from the predicted behavior, coincident with the step–step autocorrelation function going to zero. The reason for this observation is as yet unclear. Finally, the diffraction line shapes for step structure on the high-temperature Si(111)-1×1 surface have also been measured [34] showing clearly the expected power law shape characteristic of a rough surface.

The relationships between the step energy, the step stiffness, and the kink energy have been evaluated analytically for a number of simple lattice models as shown in Table 4 [35]. It is possible to use Eqs. (9)–(11) to estimate the terms in Eq. (8) for real surfaces given an estimate of the kink energy and the strength of the energetic step–step interactions. Due to the importance of the problem, an increasing number of calculations of step and kink energies are being performed, as illustrated in Table 3. As will be discussed in Section 4.1.1, experimental approaches to determination of step stiffness and step–step interactions via direct measurement of spatial correlation functions present a powerful and accurate method for determining the terms appropriate to Eq. (8). The experimental approach to measuring the

Table 4
The relationship between the step stiffness $\tilde{\beta}$ and the kink energy for three different models of the energy cost $\varepsilon(n)$ of kink formation with the kink depth n. The table is adopted from Bartelt et al. [35]

Model	$\varepsilon(n)$	$a\tilde{\beta}/kT$
TSK	$\lvert n\rvert\epsilon$	$2\sinh^2(\epsilon/2kT)$
TSK + corner	$\lvert n\rvert\epsilon + (1-\delta(n,0))\epsilon_c$	$2\sinh^2(\epsilon/2kT)[1 + \{\exp(\epsilon_c/kT) - 1\}\tanh(\epsilon/2kT)]$
Restricted	$\varepsilon(\lvert n\rvert \leq 1) = \lvert n\rvert\epsilon, \quad \varepsilon(\lvert n\rvert \geq 2) = \infty$	$1 + \frac{1}{2}\exp(\epsilon/kT)$

quantities follows directly from the formalism of the continuum step model, and obviates the need to make assumptions based on lattice models.

2.2.3. *Faceting and thermodynamics as a function of surface orientation*

Given an understanding of the equilibrium crystal shape, we can make predictions of the stability of surfaces. Herring [4] showed explicitly that only those surfaces which are exposed on the equilibrium crystal shape are thermodynamically stable with respect to faceting. When the surface tension is sufficiently anisotropic, a certain range of macroscopic orientations, known as ''missing angles'', are not represented on the equilibrium crystal shape. This shows up as a sharp edge on the ECS, as in Fig. 4. If a surface of an orientation $\hat{n}$ in the range of missing angles is prepared macroscopically and then allowed to equilibrate, the surface will break up into facets of the neighboring orientations which are represented on the equilibrium crystal shape. To predict the facet sizes and the spatial distribution of the facets, one needs to consider dynamics in general. However, from experimental observations, we know that the entire macroscopic surface never facets into the thermodynamically preferred configuration of two macroscopic surfaces of the allowed orientations. Relaxation of the surface toward equilibrium occurs via faceting on length scales determined by the atomic mobility and usually produces a ''hill-and-valley'' structure as illustrated in Fig. 11. In this case, the net angle of the surface orientation is always conserved and the areas of the facets exposed are determined by this conservation, which can be written as

$$\sum_i A_i \hat{n}_i = A\hat{n}, \tag{13}$$

where the area of the original unstable surface is A and the surface normals of the neighboring faces on the equilibrium crystal shape are $\hat{n}_i$, and their areas are A_i. The free energy of the faceted surface is lowered, even though the area is increased, if the surface tensions of the surface orientations involved obey the relationship [24]

$$\sum_i \gamma_i A_i < \gamma A. \tag{14}$$

These equations serve as the basis of a thermodynamic description of surface stability in terms of surface orientation.

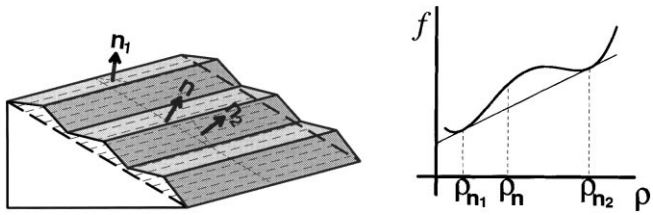

Fig. 11. Orientational phase separation occurs when a ''hill-and-valley'' structure has a lower total surface tension than a flat surface as in Eqs. (13) and (14). This translates into a convexity requirement on the reduced surface tension as a function of either component of the step density ρ_x or ρ_y (Eq. (21)). The figure illustrates schematically a non-convex surface tension curve for the case $\theta = 0$, and thus $\rho_y = 0$. The phase separation occurs between the two points illustrated by the tie bar. The requirement that the slope of the tangent at the two points be equal translates into the equivalence of the intensive parameter P_x (Eqs. (22) and (24)) and the requirement that the tangents at the two points have the same intercept translates into the equivalence of the intensive parameter P_z (Eqs. (22) and (25)).

Up to this point, we have been rather cavalier in using the terms free energy and surface tension. There in fact exists a simple relationship between the surface excess free energies and the surface tension. Many excellent reviews of surface thermodynamics exist in which the formalism of the surface excess quantities are introduced [36,37]. Here we will summarize only the key points needed for the purposes of this review. The surface excess Helmholtz free energy F^s, and the surface excess Grand Potential Ω^s are most directly related to the surface tension

$$F^s(T,A,N^s_{i\neq 1}) = \gamma A + \sum_{i\neq 1}\mu_i N_i^s \quad \text{and} \quad \mathrm{d}F^s = -S^s\,\mathrm{d}T + \gamma\,\mathrm{d}A + \sum_{i\neq 1}\mu_i\,\mathrm{d}N_i^s, \tag{15}$$

and

$$\Omega^s(T,A,\mu_{i\neq 1}) = \gamma A \quad \text{and} \quad \mathrm{d}\Omega^s = -S^s\mathrm{d}T + \gamma\,\mathrm{d}A - \sum_{i\neq 1}N_i^s\mathrm{d}\mu_i^s, \tag{16}$$

where the restriction on the sum in Eqs. (15) and (16) occurs because one independent degree of freedom, the density of one component chosen as N_1, was eliminated in defining the location of the surface. From these equations, we see that the surface tension is the Helmholtz free energy per unit area for a one-component system

$$\gamma(T) = \frac{F^s}{A}. \tag{17}$$

For a multi-component system, the surface tension is equal to the grand potential per unit area regardless of the number of components

$$\gamma(T,\mu_{i\neq 1}) = \frac{\Omega^s}{A}. \tag{18}$$

If we now reconsider Eq. (14), we see that the condition for faceting is simply that faceting is allowed if the excess surface free energy is minimized. This is the same requirement that arises in conventional descriptions of phase separation, and in fact the thermodynamic formalism describing faceting is completely analogous to that of phase separation [16,17,38,39]. In faceting, the phases in equilibrium are surfaces of different orientations, and the conservation requirements, analogous to the volume and number of each of the components in phase separation of fluids, are expressed by Eq. (13). The conserved quantities in this phase separation are the three components of the surface orientation, which in rectangular coordinates can be expressed as

$$A_x = A\sin\phi\cos\theta, \qquad A_y = A\sin\phi\sin\theta, \qquad A_z = A\cos\phi, \tag{19}$$

where the z-direction is most usefully defined as normal to a low-index orientation and the x-direction as a high-symmetry direction within the plane of the low-index orientation. Then the angles ϕ and θ define the miscut angle of the surface, and the rotation angle of the steps with respect to a high symmetry direction, respectively, as illustrated in Fig. 6.

Again in analogy with phase separation of fluids, we can define intensive variables conjugate to the conserved extensive variables of Eq. (19) [40]. The requirement that these intensive variables be the same for the orientations which are in equilibrium on the faceted surface will give us readily usable equations for describing the conditions of coexistence. We obtain the most useful and intuitive forms of these intensive variables, by working with a reduced free energy and orientational ‘‘densities’’ rather

than with the grand potential and areal components of Eq. (19) directly. A full thermodynamic justification of these transformations is given elsewhere [41]. The key point in these transformations is the definition of a reduced surface free energy (as was also done in Eqs. (3) and (4))

$$f = \frac{\gamma(\hat{n}_i)}{\hat{n}_i \cdot \hat{z}} = \frac{\Omega^s}{A_z}, \tag{20}$$

and corresponding areal densities

$$\rho_x = A_x/A_z = \tan\phi\cos\theta, \qquad \rho_y = A_y/A_z = \tan\phi\sin\theta, \qquad \rho = \sqrt{\rho_x^2 + \rho_y^2} = \tan\,\phi. \tag{21}$$

The most useful forms of the intensive variables for orientational phase separation, which we will call P_i, where $i = x, y$ or z, to emphasize their analogy to the pressure in fluid phase equilibrium, take the forms:

$$P_x = \left.\frac{\partial\Omega^s}{\partial A_x}\right|_{T,A_y,\mu_{i\neq 1}} = \left.\frac{\partial f}{\partial\rho_x}\right|_{T,\rho_y,\mu_{i\neq 1}}, \qquad P_y = \left.\frac{\partial\Omega^s}{\partial A_y}\right|_{T,A_x,\mu_{i\neq 1}} = \left.\frac{\partial f}{\partial\rho_y}\right|_{T,\rho_x,\mu_{i\neq 1}},$$
$$P_z = \left.\frac{\partial\Omega^s}{\partial A_z}\right|_{T,A_x,A_y,\mu_{i\neq 1}} = \left.\frac{\partial(f/\rho)}{\partial(1/\rho)}\right|_{T,\theta,\mu_{i\neq 1}} = f - \rho\left.\frac{\partial f}{\partial\rho}\right|_{T,\theta,\mu_{i\neq 1}}. \tag{22}$$

The utility of the orientational intensive variables can be shown by constructing for a hypothetical two-dimensional ($\theta = 0$, so $\rho_x = \rho$) orientational phase separation, the same type of ''tie-bar'' formalism used for fluid phase separation as illustrated in Fig. 11.

Here, the convexity requirement on the plot of the reduced surface free energy vs. areal density shows that a surface of original orientation ρ_0 will phase separate to two neighboring orientations ρ_a and ρ_b with relative areas of the new component phases

$$\frac{A_z^a}{\rho_0 - \rho_b} = \frac{A_z^b}{\rho_0 - \rho_a}. \tag{23}$$

The condition defining the location of the tie bar, and thus the orientations of the two new phases is that the tie bar be tangent to the free energy curve at the points a and b, or mathematically that the slope of the free energy curve be the same at these two points and that the tangents at the two points share a common origin. The mathematical requirement is the same as requiring equivalence of the intensive variables [40]. For the slope,

$$P_x^a = P_x^b, \tag{24}$$

and for the intercept,

$$P_z^a = P_z^b. \tag{25}$$

We can interpret the first of these two equations physically, by imagining the two equilibrated facets fluctuating via the exchange of small increments of slope (or vertical area A_x), while maintaining constant projected areas A_z^a and A_z^b as shown in Fig. 12(a) and (b). For the second equation, we imagine fluctuations in which the projected areas are not conserved, but the total ''rise'' of each of the two facets A_x^a and A_x^b is maintained as shown in Fig. 12(a) and (c). As this suggests, and as we will see later, the intensive parameter P_z of the latter case corresponds to a ''spreading pressure'' which can be used to define the chemical potential gradients governing surface mass transport.

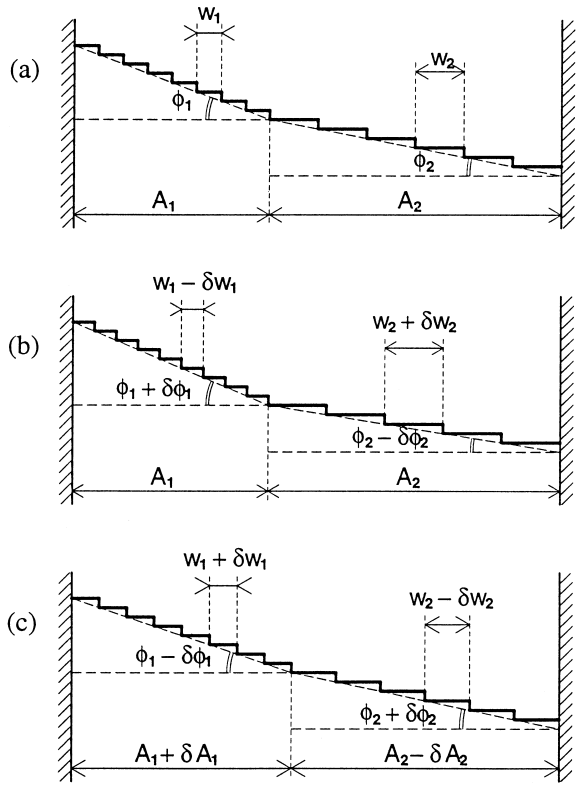

Fig. 12. Schematic illustration of fluctuations in a "hill-and-valley" structure of an equilibrium faceted surface which indicate the physical meaning of the intensive parameters governing equilibrium faceting. (a) Initial structure of a faceted surface with different step densities on each of the facets. (b) Result of a fluctuation of two facets in which step densities change via the exchange of steps between the two regions. The projected area ($A_1 = A_z^a$ and $A_2 = A_z^b$) occupied by each facet remains the same. (c) Result of a fluctuation of two facets in which the step densities change via expansion and compression of the projected areas occupied by the facets. The number of steps in each faceted region remains constant.

2.2.4. *Steps in the thermodynamic formalism*

The thermodynamic formalism presented in the previous section is independent of any assumptions about the form of the surface free energy, or the physical description of the surface itself. We can now specifically incorporate a step-based description of surfaces by reiterating the physical definition of the areal density $\rho = \tan\phi$ as the density of steps (with unit step height), and the ratio of the x and y areal densities, $\tan\theta$ as the density of (non-thermal) kinks on the step-edge, as illustrated in Fig. 6. We can reformulate the reduced surface free energy of Eq. (8) in terms of step density ρ

$$f = f_0 + \beta\rho/h + g\rho^3, \tag{26}$$

where the reduced free energy of the reference plane f_0 is equal to the surface tension of the reference plane γ_0, and where the effect of the azimuthal angle θ is implicitly incorporated in a θ-dependence of step parameters β and g as in Eq. (8). As before, the last term takes into account both entropic repulsion (due to fluctuations along the step-edge) and energetic interactions between neighboring steps. In most cases, the effective (energetic+entropic) interaction between steps of the same sign is repulsive, and

Table 5
Selected experimental observations of equilibrium faceting and step rearrangment. The emphasis in this table is on morphological changes which occur due to thermodynamic effects, e.g. reversible transitions as a function of temperature, surface reconstructive changes, or coverage of an adsorbate or growth material. More extensive compilations of change in surface morphology can be found in Refs. [8,9,10,268]

Material and surface orientation	Conditions for faceting or step rearrangement	Observation Tech. [ref.]
Alumina (0 0 0 1) and (1 0 $\bar{1}$ 0)	Upon extended annealing, the (0 0 0 1) surface facets into a step and facet structure, while the (1 0 $\bar{1}$ 0) surface facets into (1 $\bar{1}$ 0 2) and a complex surface	AFM, SEM [286,287]
W(1 1 1)	Annealing above 700 K in the presence of S, Rh, Ir, Au, Pt, or Pd causes faceting to pyramids with (2 1 1) oriented faces	LEED, STM [288,289]
Mo(1 1 1)	Annealing above 700 K in the presence of Pt or Pd films causes faceting of the surface to pyramids with (2 1 1) oriented faces	LEED [289,290]
Si(1 1 1) vicinal	Vicinal surfaces undergo reversible morphology transitions associated with the 7×7 reconstructive transition, see Section 4.3.1.5	LEED, RHEED, STM, REM, SEM [20,43,108,116, 202–205,291–296]
As/Si(1 1 1) vicinal	Cooling through the As desorption temperature ($\sim$800 °C) in an arsenic overpressure causes the reversible formation of double-layer height steps independent of azimuth on vicinal surfaces	LEED [297,298]
Au/Si(1 1 1) vicinal	Formation of (7 7 5) and (9 9 5) facets upon annealing of a Au-covered Si(1 1 1) surface, dependent on Au-coverage and annealing temperature	REM, STM [299, 300]
Cu/Si(1 1 1) vicinal	Deposition of Cu at 450−650 °C results in step bunching and faceting	REM [301]
As/Si(0 0 1) vicinal	Cooling through the As desorption temperature causes the reversible formation of small facets or (at lower step densities) quadruple-layer height steps on vicinal surfaces.	RHEED, LEED [302,303]
In/Si(0 0 1) vicinal	Annealing an In-covered vicinal Si(100) surface between 250°C and 650 °C causes step bunching at low coverages and faceting at high coverages	STM [304]
Ag/Si(0 0 1) vicinal	Formation of multiple-layer steps upon deposition of Ag at 700 K	SPA-LEED, STM [305]
Au/Si(0 0 1)	Formation of straight 2*n*-height steps upon deposition of Au at 500−700 °C	STM [306]
In/Ge(0 0 1)	Deposition of 2 ML of In followed by annealing at 250−400 °C causes formation of (310) facets.	STM [307]
Si(1 1 3) vicinal	Vicinal surfaces undergo reversible faceting transitions at all measured azimuths, see Section 4.3.2.2	REM, X-ray diffraction, STM [148,149,228,230–233]
Ag(1 1 0) vicinal	Vicinal surfaces undergo reversible faceting to the (110) facet and step bunches upon reaction with oxygen, see Section 4.3.1.6	LEED, STM [192,308,309]
Pt(0 0 1) vicinal	Reversible faceting to the (0 0 1) facet and step bunches of increasing density with decreasing temperature, associated with the reconstructive phase transition, and terminating in the formation of magic vicinals, see Section 4.3.1.7	X-xay diffraction [221]
W(4 3 0)	Step doubling with increasing temperature, See section 4.3.2.1	LEED [225]
Al(1 1 0) vicinal	Melting-induced faceting between the melting (1 1 0) and non-melting (1 1 1) surfaces	MEIS [310]

Table 5 (*continued*)

Material and surface orientation	Conditions for faceting or step rearrangement	Observation Tech. [ref.]
Pb(0 0 1) vicinal	Incomplete surface melting with no associated faceting to 10° of miscut	MEIS [311]
Pb(1 1 1) vicinal	The vicinal surface phase separates to a melted surface with a higher angle of misorientation and a dry surface with a lower angle of misorientation	SEM of ECS [180], X-ray diffraction [312], MEIS [313]
O/Pt(9 9 7)	Oxygen-induced step doubling	He scattering [314]
Pt(9 9 7)	Thermal faceting associated with formation of surface reconstruction.	STM [315]
S/Pt(1 1 1) vicinal	Step doubling in the presence of S, which is changed to single-height steps upon co-adsorption of CO	[316]
O/Ni(9 9 7)	Formation of double layer-height steps over a narrow range of oxygen coverage and temperature	He Scattering [317]
Au(0 0 1) vicinal	Reversible faceting associated with formation of the surface reconstruction	X-ray diffraction [318]
Au(1 1 1) vicinal	Reversible orientational phase separation associated with the formation of the surface reconstruction. Stabilization of a (1 1 1) facets in coexistence with a stepped phase (or (7 5 5) facets) at room temperature	X-ray diffraction, STM [198,319]
K/Cu(1 1 5)	0.2 ML of K causes the surface to form (1 1 4) facets, which are destabilized at higher coverages	He scattering [320]

therefore, the step interaction parameter g is positive. The free energy curve given by Eq. (26) versus slope is convex (downward) and thus all vicinal surfaces described by Eq. (26) will be stable with respect to faceting. Experimentally, deviations from this prediction are myriad, as illustrated in Table 5, which lists a number of observed vicinal surfaces which facet in equilibrium. One way in which the deviations from convexity needed to obtain faceting can arise is if the reference plane can exist in two different structural phases (e.g., due to surface melting or to reconstructions) or compositional phases (e.g., due to growth, adsorption or segregation) [42]. Then each phase may individually be described by a curve of the form of Eq. (26), but with different values of the parameters, resulting in intersecting free energy curves, and a non-convex shape, as shown in Fig. 13(a). As a special example, we consider the case where the reconstruction on a low-index flat face lowers its free energy relative to that of an unreconstructed surface and increases the creation energy of steps (which disturb the reconstruction). To illustrate the point, we can consider a case where Δf_0 is the difference between the free energies of the unreconstructed and the reconstructed flat surface, and $\Delta\beta$ is the difference between the step creation energies on the two surfaces, and the step interaction term g is the same for the two surfaces. Then the two free energy curves cross at $\rho_c \equiv h\Delta f_0/\Delta\beta$ as shown in Fig. 13(a) and (b). The lower envelope of the two free energy curves now loses overall convexity and the ''phase separation'' will occur between the two phases at orientations determined by the usual tie bar construction as illustrated in Fig. 13(c). The step density of the unreconstructed step-bunch region can be obtained from Eq. (25) and given by $\rho_b = (\Delta f_0/2g)^{1/3}$. Such faceting corresponds to the formation of a sharp-edge on the ECS, as shown in Fig. 13(d).

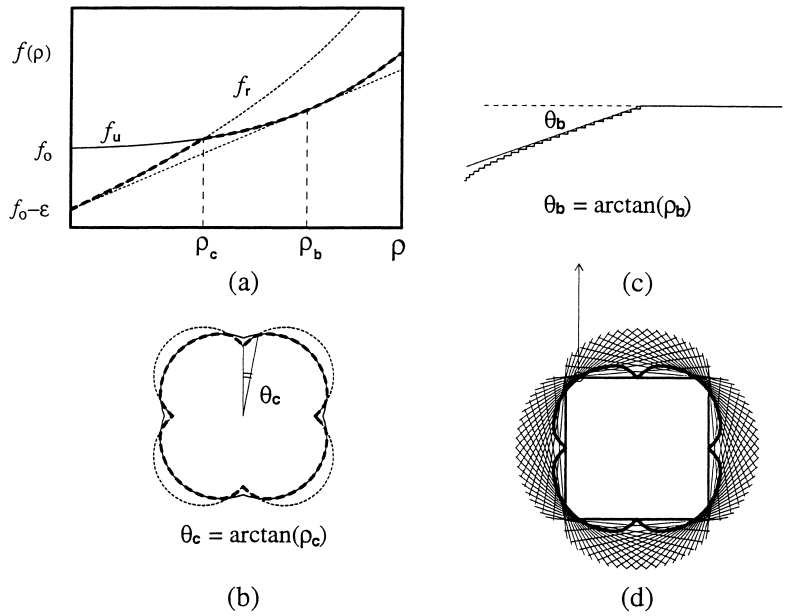

Fig. 13. Schematic illustration of surface free energies of unreconstructed and reconstructed surfaces. (a) Reduced free energies for unreconstructed surface f_u and reconstructed surface f_r verse step density ρ. Each phase can be described by a curve of the form of Eq. (26) but with different values of the parameters. If we assume that the step interaction parameter, g, is the same in the two phases, then the critical slope, ρ_c and the slope of the surface at step bunches, ρ_b are given by $\rho_c = \Delta f_0/\Delta\beta$ and $\rho_b = (\Delta f_0/2g)^{1/3}$ where Δf_0 and $\Delta\beta$ are the differences in free energies and step creation energies between two phases. (b) Schematic representation of crossing gamma-plots constructed from the extension of figure (a) with symmetry consideration. The fine dotted line is for the reconstructed surface and the thin solid line is for the unreconstructed one. The inner envelope of the two curves, shown in thick dashed line determines the ECS through Wulff construction as shown in (d). The edge between the facet and rounded region denoted by a circle in (d) is expected to be sharp (''first order'') with missing angels from $\theta = 0$ to $\theta_b = \arctan(\rho_b)$. This can be easily understood from the free energy of (a) which predicts the equilibrium step configuration shown in (c). This result could be equivalently obtained by calculating the ECS's individually for the reconstructed and unreconstructed surfaces, and then taking the inner envelopes of the intersecting ECS's [42,10].

We have previously tabulated and discussed the types of equilibrium phase diagrams that can arise from intersecting free energy curves of the form of Eq. (26) [29,41], including a treatment of 3D orientational phase separation [20,41,43]. We will not repeat this detailed exposition here, but will present some examples of orientational phase separation and its interpretation in Section 4.

Finally, we note that the parametric form of Eq. (26) gives a way of physically evaluating the significance of the intensive parameters which were introduced in Eqs. (22)–(25). Using Eq. (26) directly in Eq. (22) (we take the case of high symmetry step orientation, $\theta = 0$, the non-zero case is discussed in [41]), we obtain

$$P_x = \beta + 3g\rho^2 \tag{27}$$

and

$$P_z = f_0 - 2g\rho^3. \tag{28}$$

As shown in Fig. 11 and Eqs. (24) and (25), these two intensive parameters must each be equal in the two orientational phases in equilibrium. We can return to considering these two variables as they relate to fluctuations between two equilibrated phases. The x-component of the step pressure p_x relates to fluctuations in which the vertical component of the projected area A_x fluctuates between the two phases while maintaining the projected area in the reference plane, A_z, constant. Eq. (27) allows us to see that these fluctuations are governed by the step free energy β, and a step–step interaction term. We can thus think of these fluctuations as involving the exchange of steps between the two phases with a concomitant change in the step density of the two phases. The z-component of the step pressure p_z relates to fluctuations in which the A_x component or rise of each phase (and thus the total number of steps) remains constant, but the projected area in the reference plane A_z changes. From Eq. (28), we see that these fluctuations are governed by the free energy of the surface in the plane of projection and a step-interaction term. Clearly this involves fluctuations in the step density of the two phases as their relative areas change, simultaneously compressing and expanding the steps in the two phases. The z-component of the step pressure has thus been related to a ''spreading'' pressure of steps, and used to predict the gradients in surface chemical potential which drive mass transport in cases where there is no creation or destruction of steps [40]. This is a key concept in the continuum step model and will be described in detail later.

2.3. Kinetics of evolution of morphology

As discussed above, thermodynamic arguments on the surface free energy provide a relationship between faceting, or orientational phase separation, and the equilibrium slopes of the faceted surfaces. However, this does not explain how new facets start to appear and how their sizes and spatial distributions change with time to the final equilibrium morphology. To understand these questions, we need to study the kinetics of morphology evolution, which in turn forces us to consider the transport mechanism of individual atoms on the surface. In cases where a surface undergoes reversible faceting, the processes of nucleation and evolution of structure can be studied by mechanically preparing an unstable surface, or by making a uniform surface unstable by a sudden change in temperature or chemical composition. Studies of relaxation dynamics, in which the starting configuration is a structural modulation artificially created on a stable uniform surface, allow a controlled approach to specific problems such as the size dependence of the decay exponent. In both cases, the time dependence can be understood by describing the surface motion in terms of mass transport driven by chemical potential differences.

Historically, two very different approaches to describing the evolution of morphology have been used. In both cases, the motions of individual atoms on the surface are considered ''implicitly'' (rather than explicitly as in a molecular dynamics study) through the concept of local chemical potential or local adatom density. In one case (see Fig. 3a), significant physical insight into the evolution of morphology is obtained by considering structures composed of rough surfaces, on which the atomic mechanisms can be considered to be homogeneous. The orientational dependence of the surface free energy, which predicts the final equilibrium morphology, is applied locally to find the local chemical potential of the surface. The evolution of surface morphology in time is achieved by mass transport driven by chemical potential differences. In the other case (see Section 2.3.2) formulated to deal with problems of growth and etching, a local kinetic formalism is considered, and orientational free energy is ignored except through the recognition that steps play an important role in the kinetic processes of

morphological evolution. In this approach, the requirement of the conservation of local mass yields a diffusion equation for adatoms on the surface, which can be solved using proper boundary conditions at the steps. In other words, the morphology changes are derived by the motion of steps as they absorb or release atoms in response to the adatom density changes near the steps. In this section, we will describe each of these approaches briefly, as key aspects of each are incorporated in the continuum step model.

2.3.1. Mullins continuum description of surface evolution

In the late 1950s, Mullins first considered the kinetics of faceting [44] and relaxation [45,46] in a continuum approach. The key to this approach is the ability to define the total surface free energy in such a way that the surface chemical potential can be derived as an analytical function of local surface slope. To accomplish this, it is usually assumed that surface tension can be written as an analytic function of the surface direction $\hat{n}$. The total surface free energy is then obtained by the surface integration of the surface tension, $\gamma(\hat{n})$. The local surface direction, $\hat{n}$, and the surface area elements in the integral can be represented in terms of the local slope $\nabla z = (\partial z/\partial x, \partial z/\partial y)$, and therefore, the total surface free energy of a vicinal surface can be expressed in terms of local slopes

$$F = \int_A \gamma(\hat{n})\, \mathrm{d}S = \int_{A_0} (1 + |\nabla z|^2)^{1/2}\, \gamma(\hat{n}(\nabla z))\, \mathrm{d}x\, \mathrm{d}y, \tag{29}$$

where A and A_0 represent the surface and the projected surface of the system, respectively. When $\gamma(\hat{n})$ is an analytic function of $\hat{n}$ near the reference plane $\hat{n}_0$, as in the case for a rough surface, it can be expanded in a power series of the slope

$$\gamma(\hat{n}) = \gamma_0 + \frac{\gamma_1}{2}|\nabla z|^2 + \cdots, \tag{30}$$

and the free energy can be approximated by

$$F = \int_{A_0} \gamma_0 \; + \; \frac{\sigma}{2}\, |\nabla z|^2\, \mathrm{d}x\, \mathrm{d}y, \tag{31}$$

where $\gamma_0 = \gamma(\hat{n}_0)$ is the surface tension for the reference flat surface and $\sigma = (\gamma_0 + \gamma_1)$ is the surface stiffness.

To study the dynamics of morphology evolution, one needs to consider the chemical potential at the surface since the surface motions are achieved by motions of atoms. An atomic attachment, detachment or movement on the surface creates a small variation of the continuous surface profile, $z(x, y)$. The free energy change due to such changes is proportional to the functional derivative of the free energy. The chemical potential, defined as the average free energy change for removing an atom at position (x, y) on the surface, $\mu(x, y)$ is, therefore, written as

$$\mu(x, y) \equiv \Omega_\mathrm{v} \frac{\delta F}{\delta z(x, y)}, \tag{32}$$

where Ω_v is the volume occupied by an atom ($\Omega_\mathrm{v} = a_x a_y a_z$ for a simple cubic lattice). For the surfaces whose free energy is described by Eq. (31), the chemical potential is given by

$$\mu(x, y) = \Omega_\mathrm{v} \sigma \nabla^2 z, \tag{33}$$

where $\nabla^2 = \partial^2/\partial x^2 + \partial^2/\partial y^2$.

Various transport mechanisms can contribute to the motion of surface and the actual rate of faceting or relaxation depends on the mode of mass transport of the system. Mullins considered three basic cases of mass flow; evaporation–condensation, bulk diffusion and surface diffusion. In the first case, the normal velocity of the local surface is directly proportional to the excess chemical potential and the equation of the surface motion is given by

$$\frac{\partial z}{\partial t} = -\frac{\Gamma_{\mathrm{A}}^{\mathrm{su}}}{\Omega_{\mathrm{v}} kT}\,\mu = -\frac{\Gamma_{\mathrm{A}}^{\mathrm{su}}\sigma}{kT}\,\nabla^2 z, \tag{34}$$

where $\Gamma_{\mathrm{A}}^{\mathrm{su}}$ is known as the surface mobility[2] . Thus, the point on the surface where the curvature is largest will change height most rapidly, with a tendency to flatten the surface overall.

For the surface diffusion case, mass is locally conserved and the normal velocity is given as

$$\frac{\partial z}{\partial t} = \frac{\Gamma_{\mathrm{B}}^{\mathrm{su}}}{a_z kT}\,\nabla^2\mu = \frac{\Gamma_{\mathrm{B}}^{\mathrm{su}}\Omega_{\mathrm{s}}\sigma}{kT}\,\nabla^4 z, \tag{35}$$

where $\Omega_{\mathrm{s}} = \Omega_{\mathrm{v}}/a_z$ is the area occupied by an atom on the surface and $\Gamma_{\mathrm{B}}^{\mathrm{su}}$ is the effective surface mobility for the surface diffusion case, which is given as $\Gamma_{\mathrm{B}}^{\mathrm{su}} = D_{\mathrm{s}}\Omega_{\mathrm{v}} c_{\mathrm{eq}} a_z$, with the surface diffusion constant D_{s}, and the equilibrium adatom density on the flat surface c_{eq}.

With the above equations of surface motion (Eqs. (34) and (35)), Mullins [46] showed that the amplitude, $A(t)$ of sinusoidal modulation decays exponentially with time, $A(t) \sim \exp(-t/\tau)$. The decay constant τ grows as $\tau(L) \sim L^2$ for the evaporation–condensation case and $\tau(L) \sim L^4$ for the surface diffusion case where L is the wavelength of the modulation. (The equation of surface motion for the bulk diffusion case is not as simple as the other two cases. It is given as a non-local function of the surface chemical potential but still the amplitude decay can be studied analytically. $A(t)$ decays exponentially with $\tau(L) \sim L^3$. See Section 3.3.4.) Mullins applied the above continuum equations (Eqs. (34) and (35)) to the problem of faceting dynamics also. He used a one-dimensional model to describe the growth of a single linear facet, and showed that the normal width of the facet grows as $t^{1/4}$ under surface diffusion and as $t^{1/2}$ under an evaporation–condensation mechanism.

The continuum approach with the free energy of Eq. (31) is physically applicable only above the roughening temperature T_{R}. There have been several attempts to extend this continuum approach to the surface below T_{R} using a free energy of Eq. (26) with $\rho = |\mathrm{d}z/\mathrm{d}x|$ [49–51]. One difficulty with doing so is that the free energy is not analytic and the chemical potential given by Eq. (32) is not well defined at $\rho = 0$. Another difficulty with this approach is that it does not account for the different kinetics of mass transport at steps and on terraces. In fact, well below T_{R}, one expects atomic detachment to take place only at steps. Hence, there must be a factor of the local slope (density of steps) in the dynamics. For a recent review on constructing the continuum theory from step dynamics, see [52].

2.3.2. BCF approach to kinetics of morphology

In introducing the concepts in the previous sections we have explicitly begun from a perspective of equilibrium structures. This allows us to formulate powerful expressions for understanding phase

[2] Surface mobility as defined by Spohn [47], m_{s} in their notation, is given by $m_{\mathrm{s}} = \Gamma_{\mathrm{A}}^{\mathrm{su}}/\Omega_{\mathrm{v}} kT$ with $\Gamma_{\mathrm{A}}^{\mathrm{su}}$ in Eq. (34). We call $\Gamma_{\mathrm{A}}^{\mathrm{su}}$ the surface mobility for consistency with the definition of step mobility in Eq. (93) in Section 3.3.4 following the convention of Bartelt et al. [48].

transitions in morphology as well as the kinetics of morphological transformations. However, there is another approach to describing the evolution of morphology which begins explicitly with a kinetic perspective. This is the model of step-flow growth or sublimation originally introduced by Burton et al. [15] and thus known as the BCF model. As originally formulated, this model was designed to deal with situations in which the interface morphology is preserved, and thus does not consider the effect of free energy changes with orientation.

This model is also strictly 1D, and does not incorporate naturally the effects of step wandering and step interactions which are important in describing the evolution of large structures toward the equilibrium state. Approaches to make contact between the most useful aspects of the BCF model and the step-based model using the step chemical potential will be described in Section 4.4. Here we will outline the main aspects of the model, and discuss its consequences for understanding the spontaneous evolution of non-equilibrium structures.

The major physical insight of the BCF model was that sublimation or growth should be strongly mediated by the presence of steps, which are assumed to act as relatively easy sites for the attachment and detachment of adatoms onto the intervening terraces. As illustrated in Fig. 14, the concentration of the adatoms exists in dynamic equilibrium with the step-edges by a balance between the rate of attachment and detachment from the step-edges, κ, their rate of diffusion on the terraces governed by diffusion constant, D_s, by desorption processes with a time constant, τ, and deposition of adatoms with a flux, R. If one looks at an element of the terrace, and balances the rate of diffusion into and out of that element with the rates of sublimation and deposition, one easily derives the differential equation governing the evolution of the concentration profile of adatoms, $c(x)$

$$D_s \frac{d^2 c(x)}{dx^2} - \frac{c(x)}{\tau} + R = 0. \tag{36}$$

Here one is explicitly assuming that the steps are moving slowly enough that the concentration profile is established on the terraces between the steps on a timescale much faster than the motion of the steps.

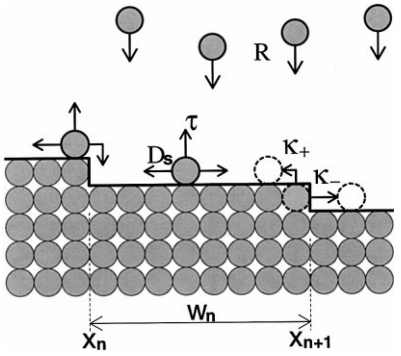

Fig. 14. Schematic illustration of the important parameters in the Burton–Cabrera–Frank kinetic model of step flow under growth. The separation between steps n (at position x_n) and $n+1$ (at position x_{n+1}) is w_n. Atoms impinge with equal probability at all positions on the surface due to an external flux R. Atoms diffuse on the terrace with a diffusion coefficient D_s until they encounter a step-edge and are incorporated with a probability proportional to κ (which may be different for approach from the lower and upper side of the step), or until they desorb with a time constant τ. Under growth, the external flux is greater than the equilibrium flux R_{eq}. Under etching, the position-dependent sublimation rate $(c(x)/\tau)$ is larger than the equilibrium flux.

The boundary conditions for this equation are the relationship between the flux of material toward the two step-edges bounding a terrace and the rate of incorporation (growth) or removal (sublimation) of material at the step-edges, x_n^+ and x_{n+1}^- [53–55]

$$\mp D_s \frac{dc(x)}{dx} = -\kappa_\pm \left[c(x) - c_{eq} \right], \tag{37}$$

where c_{eq} is the equilibrium adatom density and κ_+ (κ_-) is the kinetic coefficient for adatom attachment from the terrace in front of (behind) the step. Here the boundaries correspond to the inner edges of the two steps, step n and step $n+1$, bounding a given terrace. A specific solution to this equation can be readily found when the attachment/detachment rates are very large and are the same at the ascending and descending sides of a step, i.e., when $\kappa_+ = \kappa_- \gg D_s/x_s$, where $x_s = \sqrt{D_s \tau}$ is the diffusion length. In this case, rapid exchange of atoms with the step-edge maintains the concentration at the step-edge at the equilibrium value, and the resulting evolution of the morphology under either growth or sublimation is shape preserving. That is, the original relative configuration of steps remains the same, with the absolute positions of the steps sweeping across the surface at a rate determined by the net rate of growth or sublimation. The steady state solution of Eq. (36) with the boundary condition $c(x) = c_{eq}$ at steps ($x = \mp w/2$) is given by

$$c(x) = (R - R_{eq})\,\tau \left[1 - \frac{\cosh(x/x_s)}{\cosh(w/2x_s)} \right] \; + \; c_{eq}, \tag{38}$$

where

$$R_{eq} = c_{eq}/\tau \tag{39}$$

and w is the average distance between the steps. The mass conservation determines the step velocity [56] as

$$v = \Omega_s D_s \left[\left. \frac{dc}{dx} \right|_{-w/2} - \left. \frac{dc}{dx} \right|_{w/2} \right] = 2\Omega_s (R - R_{eq}) x_s \tanh\left(\frac{w}{2x_s} \right), \tag{40}$$

where Ω_s is the area occupied by an atom on the surface near the step-edge. Here, the contributions to the flow of a step from both bounding terraces are considered; the first term with $x = -w/2$ is the contribution from the terrace in front of the step and the other term with $x = w/2$ is that from the terrace behind the step. When the step separation is much smaller than the diffusion length ($w \ll x_s$), the step velocity takes on an especially easy and intuitive form

$$v = \Omega_s (R - R_{eq})\, w. \tag{41}$$

The physical meaning of this limiting case is (in the case of net growth) that all of the atoms landing on a given terrace are incorporated into the steps on either side. Then the rate of motion of a step is simply proportional to the size of the terraces adjacent to it. This limit has been observed experimentally for sublimation of the Si(1 1 1) surface over a range of temperatures, as illustrated in Fig. 15 [57].

The other limit, in which the diffusion length is smaller than the step separation can be interpreted simply as the point at which the ''step-flow model'' breaks down, and a transition to growth by island formation takes place [58,59]. Alternatively, it can be considered as the case of an ''isolated'' step on the growing surface, where only the material deposited within a diffusion length of the step-edges is incorporated into the growing layer, and the remaining material desorbs instead. In this case (limit of

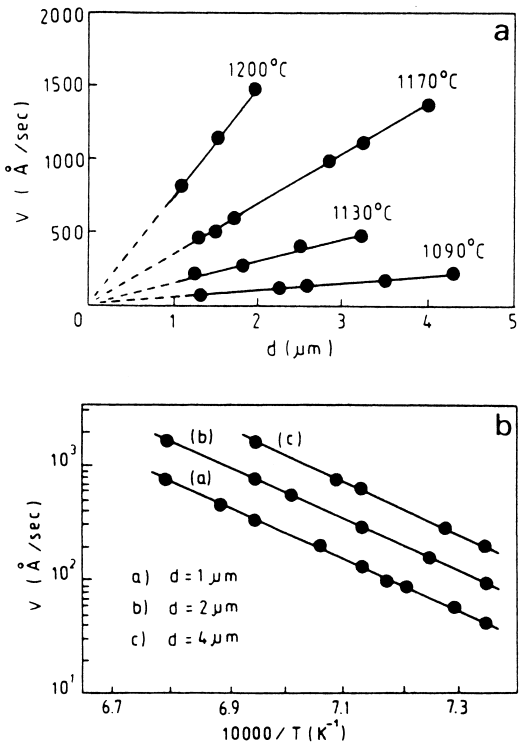

Fig. 15. Direct real time imaging of stepped Si surfaces at elevated temperatures is possible using reflection electron microscopy (REM). (a) The velocity of steps on a Si(1 1 1) surface measured as a function of the width of the adjacent terraces over a temperature range from 1090–1200°C. (b) An Arrhenius plot of the velocities measured for different average step spacings. The apparent activation energy is 4.2 ± 0.2 eV, which is close to the Si sublimation energy (figure from Ref. [57], provided by A.V. Latyshev, Institute of Semiconductor Physics, Novosibirsk).

large step separation, or $w = \infty$), the resulting step velocity is

$$v = 2\Omega_s(R - R_{eq})\, x_s. \tag{42}$$

Quantitative application of the BCF formalism requires knowledge of the surface diffusion coefficients, the attachment/detachment rate coefficients at the step edges, which in a simple atomistic picture can be related to the activation barriers for atoms hopping between terrace and step-edge sites, and the equilibrium adatom density. Diffusion rates on terraces have been measured and calculated, and extensive tabulations exist [60–62]. However, diffusion across step-edges remains very poorly characterized. The results of the small number of calculations relating to diffusion at step-edges are listed in Table 6. One important concept is that attachment and detachment may occur not via a simple site-hopping process, but by much complex correlated motion of atoms in an exchange process, which can lower the activation barrier [63,64]. Relating the attachment barriers shown in Table 6 to the parameters $\kappa_\pm$ of the BCF model for growth require an atomistic understanding of the diffusion path, a value of the frequency factor and knowledge of either the equilibrium adatom concentration on the terraces, or the binding energy for an atom at the step-edge (see Table 3 for this value for Al). A simple example of such an atomistic model is illustrated in Fig. 16. As illustrated in references cited in Table 6,

Table 6
Calculated activation energies for diffusion on stepped surfaces. Values listed are for motion via a hopping motion where no other mechanism is indicated, or via an exchange mechanism [63], were indicated by the word "exchange" following the value. Units are in eV

System	Terrace	Direction	Step			Technique [reference]
			Attachment from upper terrace	Attachment from lower terrace[a]	Motion parallel to step edge	
Al(1 1 1)	0.04	$[\bar{1}\,\bar{1}\,2]$	0.08, exchange		0.32	DFT–LDA
		$[1\,1\,\bar{2}]$	0.06, exchange		0.42, exchange	[276]
		$[\bar{1}\,\bar{1}\,2]$	0.16 ± 0.07			
Si(1 1 1)	0.97 ± 0.07	+ [kink]	[< 0.39, < 0.62][b]			SW
1×1		$[1\,1\,\bar{2}]$	0.61 ± 0.07			[321,322]
		+ [kink]	[0.15, 0.50][b]			
Ag(1 0 0)	0.52 (0.45), hopping	[1 1 0]	0.52(0.45), exchange		0.30(0.27), hopping	LDA (GGA) [285]
Si(0 0 1)	0.67 ± 0.04[c]	S_A	0.50	0.38, (0.84)[e]	0.62 ± 0.05	SW
	0.76 ± 0.04[d]	S_B	0.76	1.0	0.39	[282,284]
Ni(1 1 1)	0.056	$[2\,\bar{1}\,\bar{1}]$	0.55, hopping	0.022, hopping		EAM
		$[\bar{2}\,1\,1]$	0.19, exchange	0.040, hopping		[278]
Ni(1 1 0)	0.41[f]	$[1\,\bar{1}\,0]$	1.34[f], hopping			EAM
	0.49[g]		1.28[g], exchange			[278]
Ni(1 0 0)	0.63	[0 1 1]	0.85, exchange	0.60	~ 0.63	EAM [278]
Pt(1 1 1)	0.16	A-step $[2\,\bar{1}\,\bar{1}]$	0.41	0.12–0.15	0.63–0.45	[165]
		B-step $[\bar{2}\,1\,1]$	0.37, exchange	0.12–0.15	0.63–0.45	
			0.26[h], exchange			

[a] In the absence of other information, it is reasonable to estimate this activation energy as being equal to the activation energy for diffusion on the terrace.
[b] Barrier is reduced when diffusion over kink sites at the step-edge is considered. Multi-atom processes could also reduce the barrier further.
[c] Single adatom diffusion along 2×1 dimer row.
[d] Single adatom diffusion perpendicular to 2×1 dimer row.
[e] Value is for detachment from step edge to lower terrace.
[f] In-channel hops.
[g] Cross-channel hops.
[h] At kink site.

the reality is likely to be much more complex than the simple schematic of Fig. 16. The activation energy for diffusion on the terrace $E_{a,t}$ is related to the terrace diffusion constant via $D_s = a^2 \nu \, e^{-E_{a,t}/kT}$, where ν is the frequency of hopping attempts. It is often suggested that there is an enhanced activation barrier $E_{a,u}$ to attachment to the step from the upper terrace (i.e., an Ehrlich-Schwoebel barrier [65,66]). The barrier to attachment from the lower terrace $E_{a,l}$ is often assumed to be the same as the terrace activation energy. Within this simple atomistic framework, one can estimate values for the step attachment/detachment coefficient $\kappa_\pm$ of Eq. (37) and Fig. 14:

$$c_{eq}\,\kappa_+ = (\nu_+/a)\,e^{-E_{a,u}/kT}, \qquad c_{eq}\,\kappa_- = (\nu_-/a)\,e^{-E_{a,l}/kT}, \tag{43}$$

where c_{eq} is the equilibrium concentration on the terrace and where we have explicitly assumed that the frequency factors $\nu_\pm$ may also be different at the step-edges. In the simplest case, where the diffusion

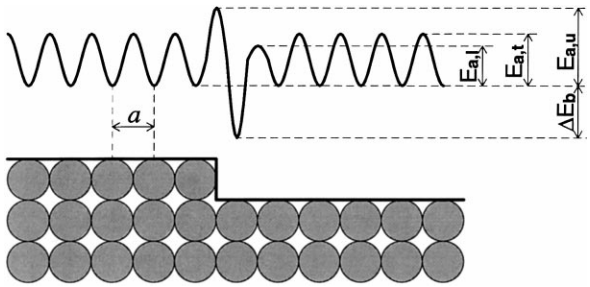

Fig. 16. Simple models of atomistic diffusion are based on the idea of discrete hops between preferred binding sites as shown here. (However, diffusion by an exchange mechanism in which one atom displaces a neighbor is also known to be a lower-energy path in many cases.) On the terraces, the bindings sites might be on-top, bridge or hollow sites. In this illustration, the binding sites are assumed to have the same spatial periodicity as the substrate atoms (which would not be the case for instance for bridge bonding), and a simple activation barrier $E_{a,t}$ for hopping between sites. In moving onto a step binding site (which may have many possible binding configurations), from the upper step–edge, it is physically reasonable to assume that the activation state involves a lower-coordination than for hopping on the terrace, and thus will have a higher activation energy, $E_{a,u}$. It might also be assumed that hopping onto the step from the lower terrace would involve a somewhat more accessible activated state, and thus a slightly lower activation energy $E_{a,l}$. Calculated values of activation energies near steps are listed in Table 6.

properties at the step are the same as on the terrace, the value of the step attachment rate, κ reduces to $\kappa = D_s / a^3 c_{eq}$.

In the continuum step model such atomistic approximation can be avoided, because the parameter κ can be determined experimentally from the equilibrium step fluctuations. As will be shown in Section 3.3.4, the mobility of the step-edge Γ can be determined directly from an experimental analysis of equilibrium step fluctuations and related in turn to the step attachment rate κ.

Knowledge of the equilibrium concentration is also important as it appears in Eqs. (37) and (38). It can also be combined with knowledge of the equilibrium flux to determine the time constant for desorption τ. The equilibrium flux, R_{eq}, can be obtained from the equilibrium vapor pressure, p_{eq}, of the sample [67]

$$R_{eq} = p_{eq}/\sqrt{2\pi mkT}, \tag{44}$$

assuming perfect adsorption on the surface (adsorption coefficient is equal to 1). However, the equilibrium adatom density, c_{eq} is not easily measured [68]. One can obtain a physical feeling for the adatom density by using a simple lattice model. We can consider the problem in two simple cases. One case is where the concentration of adatoms on the terraces is equal to that of vacancies. Mechanistically, this could arise either by excitation of adatoms directly from the terraces or by diffusion of vacancies from step-edges onto the adjoining upper terrace. If we treat both adatoms and vacancies as independent and non-interacting entities (which may be a good approximation at low coverage), we can calculate the fractional coverage of adatoms, $\theta = N/M$, with the number of sites on the terrace, M and the number of adatoms on the terrace, N, on the surface which equilibrate with the bulk using Langmuir adsorption theory

$$\left(\frac{\theta}{1-\theta}\right)^2 = \exp\left(\frac{-\Delta E}{kT}\right), \tag{45}$$

where ΔE is the difference in energy between an atom in a fully coordinated site in a terrace layer, and an adatom on the terrace.

The second case arises if we assume that the adatoms either are created directly from the step-edge without creating a corresponding vacancy, or that any terrace vacancies diffuse to the step-edge and disappear after creation. Then there is no entropy term due to the vacancies, and one obtains

$$\frac{\theta}{1-\theta} = \exp\left(\frac{-\Delta E'}{kT}\right), \tag{46}$$

where $\Delta E'$ is the effective free energy cost to detach an atom from the step-edge. In a square lattice model with near neighbor energy of ϵ, $\Delta E = 4\epsilon$. The use of a single value, $\Delta E'$, for step detachment, is an approximation because of thermal excitation at the step-edge. However, we can reasonably approximate $\Delta E'$ to be around 2ϵ since we can assume that the adatoms are detached from the kink sites on an average. Note that Eqs. (45) and (46) are valid only at low coverage, say $\theta \lesssim 0.2$, or equivalently $kT \lesssim \Delta E/3$. In the high-coverage limit of this range of validity, say $\Delta E/5 \lesssim kT \lesssim \Delta E/3$, the coverage increases roughly linearly with temperature. Thus, it is fairly easy to estimate the adatom density given an estimate of the value of ΔE. However, at lower temperatures ($kT \lesssim \Delta E/6$), uncertainty in the value of ΔE can easily lead to errors of several orders of magnitude in the adatom density since coverages change rapidly with temperature. However, this approach in any case can hardly be used to estimate quantitative values because of both rudimentary statistical mechanical model and because of the limited knowledge of ΔE.

2.3.3. Step curvature

The one-dimensional nature of the BCF formalism implicitly assumes straight steps. The effects of step curvature on step velocity can be included in an ad hoc fashion by the use of the Gibbs–Thompson relationship for the adatom concentration, $c(\boldsymbol{r})$ near a curved step

$$c(\boldsymbol{r}) = c_{\mathrm{eq}}\, \mathrm{e}^{\Omega_s \tilde{\beta} K(\boldsymbol{r})/kT}, \tag{47}$$

where $K(\boldsymbol{r})$ is the curvature of the step at position $\boldsymbol{r}$ [69,70]. By considering the impact of the modified concentration on the rate of incorporation of atoms into the step, as described in Eq. (37), one immediately reaches the physical conclusion that concave steps straighten by moving more rapidly in the downhill direction, while convex steps straighten by moving more slowly in the downhill direction. Quantitatively, this is expressed as [46,71]

$$v = \Omega_s \kappa \left[c(x_{n^+}) + c(x_{n^-}) - 2c_{\mathrm{eq}} \mathrm{e}^{\Omega_s \tilde{\beta} K(\boldsymbol{r})/kT}\right]. \tag{48}$$

The Gibbs–Thomson relationship is a powerful tool in analyzing the rate of evolution of curved structures [72–74]. As we will show in Sections 3.3 and 4.2.2, the physics of the Gibbs–Thomson relationship is naturally incorporated in the continuum step model, allowing the evolution of arbitrarily shaped structures to be addressed within this powerful formalism.

2.3.4. Kinetic instabilities

Because the BCF formalism is 1D, the effects of step wandering and the resulting entropic interactions which govern equilibrium morphologies are neglected. However, because it expressly incorporates the kinetic mechanisms of mass flow via step motion, the BCF approach provides a

valuable tool for investigating the evolution of structures under far-from equilibrium conditions where kinetic factors may drive the qualitative behavior. One particularly interesting phenomenon which can be understood using the BCF formalism is the spontaneous evolution of non-equilibrium morphologies via kinetic ''step bunching''. The qualitative mechanism for an instability can be understood in terms of the step motion via transfer of atoms to and from adjacent terraces. As discussed above, the rate of step flow depends on the size of the adjacent terraces, varying linearly with terrace width when the terrace width is smaller than the diffusion length. An explicit assumption in the solutions leading to Eq. (40) is that the system is isotropic with respect to mass transfer in the direction perpendicular to the step-edges. In other words, it is assumed that mass transfer between a step and its adjacent terraces occurs with equal probability in the step-uphill and step-downhill directions. Kinetic instabilities can arise when this requirement is relaxed, yielding independent contributions to the step flow [75]:

$$v_n = f_+(x_{n+1} - x_n) + f_-(x_n - x_{n-1}). \tag{49}$$

In this case, a vicious cycle of terrace width evolution can arise when $f'_-(w)$ is greater than $f'_+(w)$, where $f' = \mathrm{d}f/\mathrm{d}w$. (Note that the numbering convention for steps, as shown Fig. 14, is reversed for growth and sublimation.) For the case of net sublimation or etching, this cycle will begin when fluctuations of the steps cause a spontaneous displacement of step n such that the terrace behind the step is wider, and the terrace in front of the step becomes narrower than the average step separation w (see Fig. 14). Now step n, whose motion is dominated by transfer of atoms to the wider terrace $n-1$ will move more quickly than step $n+1$ whose motion is dominated by transfer of atoms to the narrower terrace n. As a result, terrace $n-1$ gets even larger, and terrace n gets even smaller, and the velocity differential between steps n and $n+1$ increases even more. Eventually, step n collides with step $n+1$ in an event called step-pairing, which is the first event in the kinetic instability leading to step bunching. In the reverse case, where f'_+ is greater than f'_-, the same type of reasoning shows that kinetic processes oppose fluctuations that make the terraces non-uniform, and uniform step-flow results [76,77].

A number of possible mechanisms have been proposed for the diffusional anisotropy required to cause the step-bunching instability. Frank [78,79] originally proposed a model in which impurities on the terrace causes slow step motion when the terrace becomes very large. Another mechanism for anisotropy involves the barrier to attachment at the step from the upper and lower terraces [65,66]. Since Schwoebel and Shipsey [66] first discussed such an anisotropic barrier as a possible source of a pairing instability, there has been a great deal of interest in this asymmetry [80,81]. The term ''Schwoebel barrier'' is generally used to mean a high activation barrier for an atom to hop down from an upper terrace to the step site, thus causing an instability toward bunching during evaporation. Such a barrier has recently been shown to play a profound role in roughening during growth via island formation [82]. A final mechanism for anisotropy can arise if the actual diffusion on the terraces is biased in one direction. This can occur if diffusion takes place in a potential energy gradient, with a practical example being the case where the diffusing species has a net or effective charge and diffusion takes place in an electric field (or as in field ion microscopy, where a polarizable species diffuses due to horizontal gradients in the applied electric field [83]). Stoyanov [55,84,85] has explicitly modified the BCF formalism of Eqs. (36) and (37) to include the diffusional bias induced by such an effect and Natori [86] has further improved the approach by addressing the effects of step interactions.

3. Approaches to surfaces and models for surface dynamics

Many different approaches, both in experiment and theory, have been employed to understand surface morphologies and their evolution. Recent advances in direct imaging on an atomic scale, such as high resolution scanning tunneling microscopy (STM) [87], allow us to investigate the microscopic properties of steps on surfaces directly. Traditional diffraction methods such as low energy electron and X-ray diffraction techniques provide a direct measure of the average step structure plus some information about the distribution of step spacings. Scanning electron microscopy (SEM), field ion microscopy (FIM), reflection electron microscopy (REM) [88,89], low energy electron microscopy (LEEM) [90], and STM [1] have all been used to investigate the properties of the stepped surface on a mesoscopic scale, in which individual steps are identified as the fundamental objects of interest.

Many different theoretical models can be used for the study of the surface properties and evolution. At the two extremes are atomistic descriptions – either molecular dynamics or kinetic Monte Carlo, and continuum approaches. In a continuum approach, surfaces are described in a coarse-grained scale using surface slopes or step density as a variable as outlined in Section 2.3.1. This approach has been a powerful tool to describe the large scale evolution of the surface, especially above the roughening transition temperature. In this approach, the physical properties of coarse-grained surfaces are investigated with a *phenomenological Hamiltonian* (of a Landau–Ginzburg [91] type). A Landau–Ginzburg [91] type phenomenological Hamiltonian is written in terms of order parameters and their spatial derivatives and constructed by an analytic expansion of those variables with terms allowed by the symmetry of the system. If one could construct a continuum model from a microscopic model by integrating out short-wavelength fluctuations, and obtain an *effective Hamiltonian* in terms of coarse-grained variables, this would be a direct way of testing the validity of the phenomenological Hamiltonian and obtaining physical values for the input parameters. However, this direct construction scheme of a continuum model is difficult to carry out. A non-direct way of obtaining the input parameters is by comparison of the results from a microscopic model (simulation) and the analytical or numerical predictions based on the continuum model.

The continuum surface approach is not adequate for describing surface morphology below the roughening temperature where a simple phenomenological Hamiltonian obtained by an analytic expansion of order parameters is not suitable. A mesoscopic approach known as the ‘‘continuum step model’’ has been proven to be powerful in this case. Although it is still difficult to accomplish a formal derivation (from a microscopic model) of an effective step Hamiltonian for general step configurations, it is quite easy to conjecture its form using known results of simple systems [22,23] and some heuristic arguments [92]. Then, it is not difficult to check the validity of the conjectured step models from simulation results of microscopic models [93]. Furthermore, it does not seem to be necessary to construct a continuum model (from the step model) or perform a long-time simulation to test the validity of the step model experimentally. Today’s advanced surface probe methods allow us to observe the fluctuations and motion of individual steps directly.

Recently, an extensive amount of theoretical work has been devoted to studies of the relationship between microscopic models and step models [93] or on the derivation of continuum models from step models [49–52]. We will not attempt to review these subjects thoroughly here. Rather, in this section, an example or two of each of the microscopic, continuum, and step approaches will be presented and the connection between them will be briefly reviewed.

3.1. Atomic scale approaches

In a microscopic approach, surface properties are investigated from an atomic scale Hamiltonian which assigns a specific energy to each possible atomic configuration at the surface. One, in principle, would like to consider a microscopic model which allows all possible atomic configurations of the real surface with a Hamiltonian which is as close to the true atomic potential as possible, for instance by using the results of first principles calculations. In practice, the utility of this approach to the study of surface morphology changes, which involve the motion of a thermodynamic number of atoms at non-zero temperature, is doubtful. First principles calculations are possible only numerically, and very difficult unless limited to structures with small unit cells. Recently, first principles calculations on steps have been performed, as summarized in Table 3, yielding valuable information on energy scales, preferred configurations and mechanisms for atomic motion at steps. Still the scope of these results is limited and a full understanding of all the relevant atomic interactions at steps remains a challenge. Even if all microscopic energies at the level of detail needed to describe every aspects of atomic motion could be obtained, solving the length-scale bridging problem which is required to predict large scale evolution of structure in a macroscopic system remains a grand challenge of condensed matter physics. Without appropriate length-scale bridging, the motion of all individual particles would be more information than we could deal with; we cannot observe or recognize this in real materials. For macroscopic systems, the experimentally measurable parameters are averaged macroscopic variables and their correlations and fluctuations. Thus, in studies on a macroscopic system, we make progress by concentrating on a particular aspect of the system and defining a simple model Hamiltonian, which considers only the most essential excitations relevant to the changes of the macroscopic variables under consideration. For the study of surface morphology from a microscopic perspective, we consider a model Hamiltonian which simplifies the possible configurations and the interactions of atoms at the surface (so that it can be solved analytically or easily investigated numerically for a system of a large number of atoms). The surfaces in this microscopic approach are usually described by *discrete* variables. The limitation of such discrete models are well understood, but they still remain a powerful source of physical insight.

3.1.1. Discrete models

Depending on the most relevant excitations for the morphology changes, which mainly depend on the temperature, we employ different discrete microscopic models, like a lattice–gas (LG) model, a solid-on-solid (SOS) model or a terrace–step–kink (TSK) model. In these models and many other microscopic models, configurations are usually specified by discrete variables, but the understanding obtained from these models is not restricted to the systems in which atom motions are discrete or close to discrete. Instead we physically understand these models as obtained by integrating out the stages corresponding to the configurations which are not allowed in the models. For instance, in real materials, atoms are constantly moving but if we integrate out the vibrational motion, the averaged position for most atoms can be approximated by lattice sites. Models which restrict atoms to lattice sites may or may not allow configurations which include vacancies and overhangs. As the temperature increases, the number of such defects which are present in the physical system also increases and their role in surface morphology can be important. When these defects take an important role in morphology changes, which might be the case at temperatures near melting, we may have to consider a model which allows such excitations like a LG model [94], while at low temperatures,

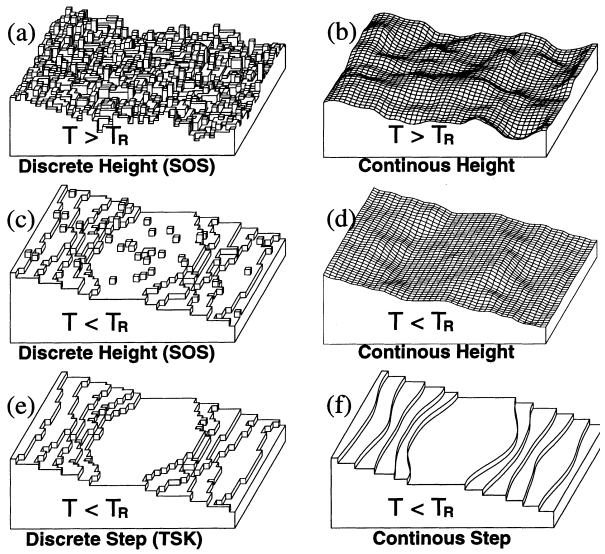

Fig. 17. Schematic surface configurations in different approaches above (a),(b) and below (c)–(f) the roughening transition temperatures, T_R. Surface configurations in a microscopic approach described by a discrete height are shown in (a) and (c), above and below T_R, respectively. Below T_R, the main topological objects on a vicinal surface are steps and adatoms. By integrating out the role of adatoms properly, the surface morphology may be characterized by terraces, steps and kinks (e). For each discrete configuration shown in the left panels, the corresponding continuum configuration is shown in the right panels, which are obtained by integrating out the short-wavelength fluctuations in heights (b),(d) or the positions of steps (f) using a Gaussian smearing kernel (see text).

where overhang structures are rare, a SOS model can be a good model for the study of surface morphology.

In a SOS model, overhang structures are forbidden and the surface profile is described by the discrete height of the kth column h_k, as shown in Fig. 17(a) and (c). The energy of a particular surface configuration (Hamiltonian) in a SOS model is given as a function of the height differences between neighboring columns,

$$E(\{h_k\}) = \frac{J}{2}\sum_{k,\delta(k)} f(h_k - h_{\delta(k)}), \tag{50}$$

where $\delta(k)$ is one of the columns adjacent to the kth one and $Jf(\Delta h)$ is the energy cost when the height difference between adjacent sites is Δh. Again the physical systems which can be studied by this model need not be restricted to surfaces with absolutely no overhang structures. It may be used to describe the surface as long as the excitation to an overhang structure is rare enough that it is not a dominant feature and does not take a significant role in the morphology changes. SOS models have been successful in explaining many properties of crystalline surfaces below the melting temperature including the roughening transition [12].

For surfaces well below the roughening transition temperature, T_R, many excitations considered in a SOS model are suppressed. The main features of low temperature surfaces are the steps and adatoms (and vacancies) as shown in Fig. 17(c) and the properties of these surfaces may be well described by a

terrace–step–kink-adatom (TSKA) model which considers the motions of adatoms (and vacancies) on the terrace and attachments or detachments of adatoms to the steps. When the effects of adatoms are integrated out, we get a TSK model which focuses on the energetics of steps and kinks. The surface is described by the array of non-crossing steps (one-dimensional interfaces) and its profile is specified by the position of steps[3] as illustrated in Fig. 17(e).

3.1.2. Microscopic models for surface dynamics

Evolution of surface morphology is investigated from the motion of individual atoms in microscopic approaches. The most dominant method in this area has been Monte Carlo kinetics, though some important and interesting discoveries have made through Molecular Dynamics [95]. We present a brief review of some microscopic studies of relaxation dynamics in which the connection to the step models is easily checked.

Depending on whether the surface is above or below its roughening temperature, T_R, a qualitative difference in relaxation behavior is expected. Most simulation results on microscopic models for $T > T_R$ [96] are consistent with the predictions of Mullins' continuum model [46]. For $T < T_R$, there is not a well-established unified continuum theory for the relaxation from a general perturbation. One crucial factor which affects the relaxation dynamics toward the uniform equilibrium state is whether the initial perturbed surface has only one sign of slope. This is because in the region where the slope changes sign, there are steps of opposite sign which annihilate upon collision, changing the step density. Fig. 18 shows examples of quasi-1D, non-equilibrium surfaces for two cases; a surface with both signs of steps is shown in (a) and a surface with only one sign of step in (b). Most microscopic studies have been devoted to the case where two different signs of steps are involved (Fig. 18(a)). It is

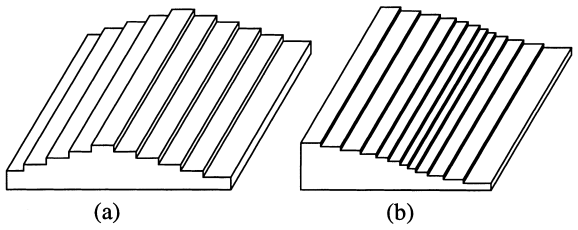

Fig. 18. Quasi-1D perturbed non-equilibrium surfaces. (a) Sinusoidal perturbation on a flat surface with two different signs of steps. (b) Sinusoidal perturbation on a vicinal surface. The amplitude is small enough that the perturbed surface still has only one sign of steps. The relaxation dynamics to the uniform equilibrium state is quite different depending on whether the initial perturbed surface has only one sign of slope or both.

[3] As an operative way to get a TSK configuration from a TSKA, or a low-temperature SOS configuration, one may consider applying the Gibbs dividing-surface construction scheme row by row on the surface. Then, a TSK configuration may need a careful interpretation to avoid an unphysical situation that a motion of adatoms on the terrace results in creating or annihilating a kink at the nearby step. Note that the usual Gibbs dividing-surface construction is applied to a continuum profile. If one integrates out short-wavelength fluctuations on the steps also, up to the length scale on which the fluctuation of adatoms disappears, kinks on the steps are also smeared out and steps become continuous. One other scheme to map a TSKA configuration to TSK configuration is by considering the role of adatoms and vacancies in the neighboring terraces as acting as a reservoir like the atoms in a vapor phase of a SOS model. Motion "in the reservoir" does not effect the step configuration. Fig. 17(e) is obtained from (c), by adopting the latter scheme.

difficult to compare these results with predictions of either the continuum approach or the step approach as both encounter some difficulties associated with the non-analyticity of free energy at zero slope, or in finding an effective interaction between neighboring steps of the opposite signs. As pointed out by Tang [52], these difficulties partially come from the fact that the proper definition of local chemical potential at the top area of the groove strongly depends on the timescale. If we want the local chemical potential at a step to include the effect of step–step interactions, the local equilibration time, τ_l should be considered on the timescale longer than the collision time τ_c between neighboring steps. However, the collision time of steps of opposite sign τ_c^{+-} becomes much larger than that of steps of equal sign τ_c^{++} as the top area gets flat. On the other hand, we should resolve the timescale of order τ_c^{++} to describe the *dynamics of step motion* using the local chemical potential. Several different relaxation behaviors have been predicted [47,49,97,98] due to different definitions of the local chemical potential used at the top area. For some studies [47,98] interactions between neighboring steps of the opposite signs are considered ($\tau_l > \tau_c^{+-}$) while for some others [49], only step–step repulsion between steps of the same sign are considered ($\tau_c^{++} < \tau_l \ll \tau_c^{+-}$). Studies on the dynamics of surfaces with microscopic models have been performed [99] and provided some clues to resolve the issue of finding a proper definition of the chemical potential. However, the size of the systems used in these studies seems to be too small to make a decisive conclusion on the issue. For a review on this subject, see the recent articles by Tang [52] and by Duport et al. [100].

Now let us turn to the simpler case where only one type of step exists as shown in Fig. 18(b). Here, where the nature of the step interaction is reasonably well understood, and one can use microscopic models, such as the SOS or TSK, to check the validity of the equations of motion used in continuum step models. For example, Bartelt et al. [93] used a SOS model with Monte Carlo kinetics to confirm the predictions of the continuum step model for the relaxation dynamics from the step-bunched state to the uniform equilibrium state as shown in Fig. 19. They used one of the simplest SOS models, known as the absolute SOS (ASOS) model, in which the energy assignment between neighboring columns with different heights is proportional to the height difference $|\Delta h|$, that is $Jf(\Delta h) = \epsilon|\Delta h|$ in Eq. (50) with broken bond energy ϵ.

In performing such kinetics simulations with discrete models, the simplest approach is to use the Metropolis Monte Carlo (MC) algorithm [101] without any activation barriers. The time unit is set as the trial event. Then, at each trial, one site on the surface is chosen at random and a random choice to either increase or decrease (biased to increase (decrease) for a growth (evaporation) case) its height by unit length is considered. If the energy of the resultant configuration is equal to or less than that of the original configuration, the height change is made. Otherwise, the attempt is accepted with the usual Boltzmann probability. Since the MC movement trial (height change attempt) site is sampled independently, this kinetics would be appropriate for mass transport by the evaporation–condensation process. If the surface motion is dominated by the adatom movements on the surface (surface diffusion), the decrease (increase) in one site height should be accompanied by an increase (decrease) in a neighbor site. Bartelt et al. [93] used this Kawasaki dynamics [101] between the nearest neighbor sites (surface diffusion) to study surface dynamics at low temperature.

Fig. 19 shows sample configurations of the surfaces at three different times; the initial, a middle, and the final configuration in (a)–(c) and the time dependence of the average step-edge position of the process (d). The time evolution of the average step-edge position is compared with the prediction of the continuum step model of Rettori and Villain [49] which will be discussed later. As shown in Fig. 19(d), the two results are nicely consistent. As mentioned at the beginning of the section, this comparison

between the microscopic model and the step model provides the input parameter of the step model, in this case, the diffusion constant on the surface.

3.2. Coarse graining and continuum models

3.2.1. Coarse graining

Continuum descriptions of surfaces, as schematically shown in the right panels of Fig. 17, are usually obtained by integrating out short-wavelength fluctuations at the atomic scale. For example, a smooth

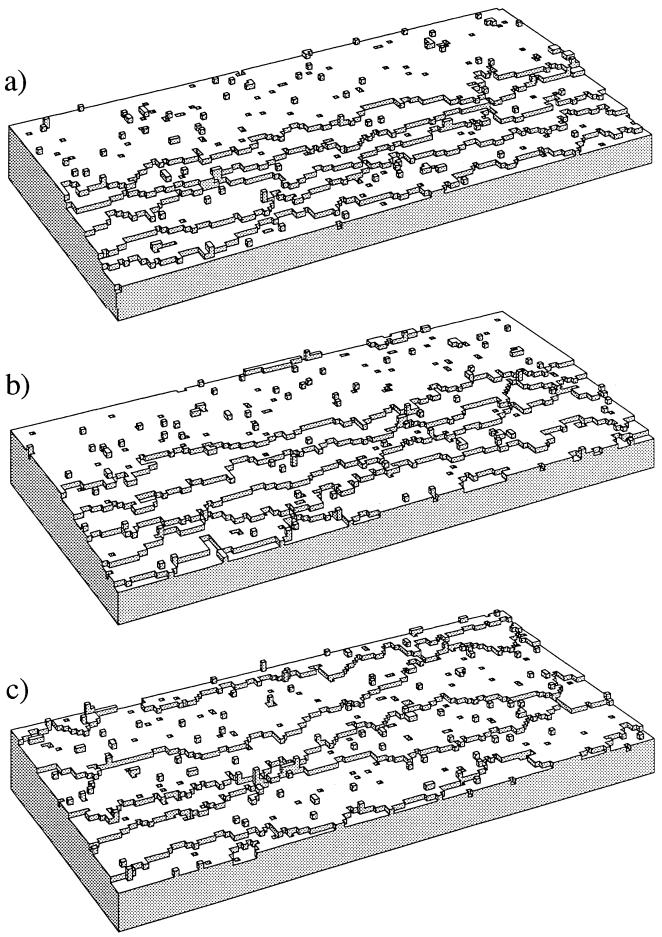

Fig. 19. (a,b,c) Sample configurations of the surfaces used by Bartelt and co-workers to study step motion using an ASOS model set up to display diffusion limited step motion. The lattice size used is $L_x = 60$ units, $L_y = 120$ units with a screw boundary condition applied in the x-direction to introduce steps, and periodic boundary conditions in the y direction. (a) The initial configuration of five steps separated by six lattice constants, (b) The surface after 10^6 Monte Carlo steps per site. (c) The final configuration after 3×10^6 MCS per site. (d) The average step-edge positions were measured as a function of time and are plotted as the jagged lines. The predicted positions of the step-edge using the continuum step model (see Eqs. (113)–(122) are shown as the smooth lines (figure from Ref. [93], provided by T.L. Einstein of University of Maryland).

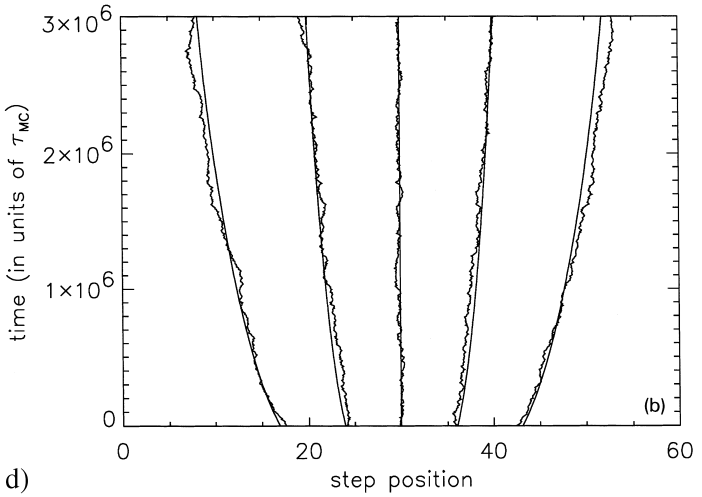

Fig. 19. (*continued*)

continuum surface described by the continuous height variable, $z(x, y)$, can be obtained by

$$z(x, y) = \sum_k K(x - x_k, y - y_k)\, h_k, \tag{51}$$

with a smooth smearing kernel $K(\boldsymbol{r})$, where (x_k, y_k) is the position of the kth column. When a proper[4] smearing kernel is used, the properties of the resultant continuum surface, at least its long-wavelength components are expected to be well described by a phenomenological Hamiltonian. Surface configurations in Fig. 17(b) and (d) are obtained with a Gaussian smearing kernel, $K(|\boldsymbol{r}|) \sim \mathrm{e}^{-(|\boldsymbol{r}|/r_0)^2}$ with the range of the smearing r_0 equal to three atomic units.[5] In a commonly used coarse-graining scheme, we get a continuous surface profile by averaging discrete heights over a coarse-graining area ΔA, i.e. using

$$K(\boldsymbol{r}) = \frac{1}{\Delta A}\Theta(r_0 - |\boldsymbol{r}|), \tag{52}$$

with $\Delta A = \pi r_0^2$ and Heaviside step function Θ. When r_0 is chosen to be much larger than atomic scale, the averages are expected to be smooth. The long-wavelength (say, larger than some cut-off length Λ_0)

[4] No quantitative criterion for a smearing kernel to be "proper" is invoked. We use the term "proper" according to how well the properties of the smeared continuum surface are described by the continuum model. Regardless of implementation of the coarsening, sufficiently long wavelength properties are believed to follow the continuum model. Therefore, any smearing kernel from a coarse-graining scheme would be proper in that sense. On the other hand, with a well-chosen smearing kernel, the (ensemble average) properties of the smoothed surface may be consistent with the continuum model prediction over a wider range of scales than the original discrete surface [102,103]. In this sense, the more proper smearing kernel is that for which the smaller scale properties of the resultant smoothed surface can be described by a continuum model. Also a proper smearing kernel should be localized enough so that the relationship between the actual discrete surface and the derived continuum surface can be seen intuitively.

[5] We choose r_0 to be three atomic units as an example to demonstrate the relationship between the discrete surface and the derived smoothed configuration clearly, not for any particular physical reason.

properties of such smooth surfaces, or equivalently the properties of the rescaled surface (by the inverse cut-off length $1/\Lambda_0$), are assumed to be well described by a continuous model with a phenomenological Hamiltonian of a Landau–Ginzburg [91] free energy type, which can be often investigated analytically. The cut-off length Λ_0, above which a continuous model can be applied safely, may depend on the form of kernel as well as the details of the continuous model [104]. There could be a kernel such that the (ensemble averaged) properties of the resulting surface given by Eq. (51) may be applied to the study of small size patterns (of a few atomic size), but, in general, continuum approaches are suitable for the study of large scale, long-time behaviors.

3.2.2. *Phenomenological Hamiltonians in continuum models*

Continuum approaches have been a major tool in the study of kinetics for large scale surface evolution including surfaces under non-equilibrium growth or evaporation conditions [105–107]. Here, however, we consider only the case where the surface motion can be described by a Hamiltonian approach (through local chemical potential differences) which is applicable to systems in which local equilibrium is achieved. For the dynamics of the surface under far from equilibrium growth conditions, which is also a topic of much current interest, see, for example, a recent review by Krug and Sphon [107].

A phenomenological Hamiltonian for a continuum model is usually constructed from an analytic expansion of order parameters and their spatial derivatives. Since the surface free energy is not analytic below the roughening transition temperature, T_R, strictly speaking, the simple construction scheme for the Hamiltonian with a symmetry argument in this section is only valid for systems above the roughening temperature.

The surface tension $\gamma(\hat{n})$ in Eq. (29) is the surface free energy per unit area of a *macroscopic* flat surface whose normal is $\hat{n}$. However, the expression for the total surface free energy used in Eq. (29) is not accurate when the surface normal changes rapidly on small length scales, which might be the case, for instance, for a surface undergoing faceting through spinodal decomposition [108]. One can approach the problem of incorporating the effects of small scale structural variation into a continuum approach by curvature terms in the expression for total free energy. A general form of the phenomenological Hamiltonian for an arbitrary surface morphology is then given by [109]

$$H = \int_S \left[\gamma(\hat{n}) + 2\kappa\left(\frac{1}{R_c} - \frac{1}{R_0}\right)^2 + \frac{\kappa_G}{2}\frac{1}{R_G}\right] dA, \tag{53}$$

where $1/R_c$ is the mean curvature and $1/R_0$ is that of the preferred surface (the mean curvature of a free surface without any constraint) and $1/R_G$ is the Gaussian curvature. The third term, the Gaussian curvature term is irrelevant here since the topology of a crystal shape is hardly changed[6], and the

[6] The topology of an object can be changed if its surface is allowed to break up into many disjoint parts to generate handles, for example, if it is changed from a sphere (of genus 0) shape to a donut (of genus 1) shape. The surface integration of the Gaussian curvature term is proportional to the Euler characteristic of the surface, $2(1-g)$ where genus g is the number of handles of the object. Here, we consider the evolution of the crystal morphology and never consider the case of the topology change.

Gaussian curvature contribution is always constant due to the Gauss–Bonnet theorem [110]. Also, the mean curvature of the preferred surface, $1/R_0$, is zero for the crystalline surface[7] so that the second term, the mean curvature contribution, is simply proportional to the square of the gradient of the normal vector

$$2\kappa\left(\frac{1}{R_c}-\frac{1}{R_0}\right)^2=\frac{\kappa}{2}(\nabla\cdot\hat{n})^2, \tag{54}$$

and Eq. (53) becomes

$$H=\int_A\left[\gamma(\hat{n})+\frac{\kappa}{2}(\nabla\cdot\hat{n})^2\right]\mathrm{d}S. \tag{55}$$

When the surface tension, $\gamma(\hat{n})$, is sufficiently anisotropic, the surface will have edges and corners. The curvature term reduces the sharpness of these defects (rounding) since the energy cost associated with each defect increases with the sharpness. In a continuum approach for the study of *equilibrium* surface morphology, we usually describe the surface with a scale much larger than the typical core size and the energy cost associated with the defect is negligible compared to the surface energy, which is proportional to area. However, this edge (or corner) energy is essential to many features of the dynamics of morphology changes. For example, it provides a driving force for the coarsening of the surface structure in a faceting process. Also, the curvature term should be considered explicitly to avoid divergences associated with mathematically singular defects when the dynamics is investigated through a Langevin equation.

Since it is a phenomenological Hamiltonian, the input parameters, which are the orientation dependence of the surface tension and the curvature rigidity κ, are not determined by the model itself. As discussed in Section 2, microscopic models have been used to evaluate the orientation and temperature dependence of the surface tension. Recently, Liu and Weeks have developed a scheme for estimating the curvature rigidity κ, or free energy cost for the edge formation in faceting, from a microscopic model by calculating the effective interactions between steps in a non-uniform step arrangement using a simple quantum mechanical approximation [111]. They considered the effects of the edge formation energy in a reconstruction induced faceting process and showed that it causes wider step spacing at the edge of the step bunch, i.e., reduces the surface curvature near the facet edge.

3.2.3. *Surface dynamics in continuum models*

In Section 2.3.1, we considered Mullins' continuum theory for the kinetics of the relaxation [45,46] and faceting, in particular the growth of a *single* linear facet [44]. His result of exponential decay of the modulation amplitude ($A(t)\sim\exp(-t/\tau)$) for the relaxation dynamics of a 1D sinusoidal profile is consistent with experiments [112,113], and predictions from the simulation of microscopic models [114] above the roughening transition temperature. Also, the prediction of the modulation wavelength, L, dependence of the decay time constant, $\tau\sim L^2$, for an evaporation–condensation case

[7] Examples that free surfaces prefer non-zero curvature can be easily found for a surfactant layer separating water from oil in microemulsions but it seems safe to assume that the free crystalline surfaces prefer the flat surfaces.

and $\tau(L) \sim L^4$ for a surface diffusion case, is consistent with simulation results of microscopic models [96,114,115]. For the faceting case, Mullins showed that the normal width of a single linear facet grows as $t^{1/4}$ under surface diffusion and as $t^{1/2}$ under an evaporation–condensation mechanism. In fact, as will be seen in Section 4.3.1, this prediction of $t^{1/4}$ or $t^{1/2}$ growth of the normal width of the linear facet agrees with the results of some recent microscopic or mesoscopic faceting models even below T_R, as well as above T_R [116,117].

A continuum approach incorporating the curvature term of Eq. (55) can be used to address additional questions concerning the size selection in facet growth. Recently, Stewart and Goldenfeld [118] and Liu and Metiu [119] considered some general aspects of faceting dynamics, including propagation along the facet axis and coarsening of the facets in the continuum limit. They applied the theory of dynamics for bulk phase separation of binary systems [120] to faceting problems. The order parameter describing the faceting (orientational phase separation) is the slope of the surface [16]. The surface with a uniform orientation corresponds to a single (supercritical) fluid phase while the faceted surface is analogous to the phase separated state [10]. As mentioned in Section 2.2.3, the driving force for faceting is the anisotropy in the surface tension. The driving force for the coarsening of the surface structure is the curvature term, i.e. the free energy cost associated with the edge formation which corresponds to the interface free energy in liquid–vapor phase separation.

Any surface whose slope is not on the equilibrium crystal shape (ECS) will facet into the surfaces of the ECS. Faceting can occur through two different mechanisms: via nucleation and via spinodal decomposition [108] as in the cases of the phase separations of binary systems [120]. Liu and Metiu [119] studied the growth of the hill-and-valley structures from a flat surface for both cases. For the spinodal decomposition case, they showed that exponential growth of the hill-and-valley structures is expected [120] in the early stage of the faceting. Also, during this stage, there is a specific size of structure which grows faster than any other size. This wavelength selection results from the compromise between energetics, which favors the lowest energy structure, and kinetics, which tends to conserve the order parameter locally. Using Eq. (55) to evaluate the energetics in the spinodal decomposition regime requires the surface stiffness σ of the flat surface to be negative thus favoring hill-and-valley structures with any wavelength to flat ones. However, the curvature term results in a higher energy cost for shorter wavelength fluctuations and, therefore, only hill-and-valley structures of long wavelength are favored from the energetic point of view. To be precise, if one describes the surface in terms of its height variations $z(x, y)$ (e.g., uses the Monge gauge), the curvature term is given by

$$\frac{\kappa}{2}\left(\nabla \cdot \hat{n}\right)^2 = \frac{\kappa}{2}\frac{\left(\nabla^2 z\right)^2}{\left(1 + |\nabla z|^2\right)^3}, \tag{56}$$

and therefore, the Hamiltonian of Eq. (55) is approximated

$$H = \int_{A_0} \gamma_0 + \frac{\sigma}{2}|\nabla z|^2 + \frac{\kappa}{2}\left(\nabla^2 z\right)^2 \mathrm{d}x\,\mathrm{d}y, \tag{57}$$

where A_0 represents the projected surface, γ_0 the surface tension for the reference flat surface, and σ is the surface stiffness as in Eq. (31) and κ is the curvature rigidity. Therefore, even in the spinodal decomposition regime, where $\sigma < 0$, the flat surface is unstable only with respect to the fluctuations with wavelength larger than $\lambda_c = \sqrt{\kappa/|\sigma|}$. All hill-and-valley structures with size larger than some critical size of order λ_c have lower energy than the flat surface and the energy decreases monotonically

with increasing wavelength. On the other hand, mass conservation always makes formation of long-wavelength fluctuations more difficult. The order parameter (slope of the surface) is *conserved locally* for both the global and the local mass transport mechanisms. This local order-parameter conservation makes the rate of growth of long wavelength structures go as q^2 for the evaporation–condensation case and q^4 for the surface diffusion case, as one can see from Eqs. (34) and (35) in Section 2.3.1, where q is the wave vector which characterizes the order parameter fluctuation scale. Competition between the wavelength dependence of mass conservation (q^2 or q^4) and the curvature term ($\sigma + \kappa q^2$) in the early spinodal regime makes a particular wavelength (of order $\sqrt{\kappa/2|\sigma|}$) of the hill-and-valley structures grow fastest. Well-defined periodicity in the pattern of the early facet growth in the ''spinodal'' regime on Si(1 1 1) has been already observed [108].

For the late stage of faceting via spinodal decomposition, Liu and Metiu [119] show that the typical size of the hill-and-valley structures for the late stage grows logarithmically for a quasi-1D system and algebraically for a 2D system with the exponents $n \approx 0.13$ under surface diffusion and with $n \approx 0.23$ under an evaporation–condensation mechanism.

3.3. Step models

3.3.1. Mesoscopic models

We have reviewed the conventional simple continuum approach with a phenomenological Hamiltonian, which is most appropriate for the studies of the surface evolution under a near-equilibrium and when the surface is above the roughening transition temperature of the low index surface, T_R. Considering continuous height variables (Fig. 17(d)) may not be the best continuum description of the surface below T_R. The surface free energy below T_R has a cusp singularity at zero slope and the continuum equations of motion (Langevin equation) in terms of the height variable give rise to mathematical difficulties associated with the singularity. Furthermore, this approach offers no means of incorporating the physical properties of the steps and terraces which are the main features of the surface at low temperature. Here, we thus present a different approach which focuses on the properties of individual steps and their interactions.

Fig. 17(f) shows schematically a surface configuration of a ''continuum step approach'' which focuses on the motion of individual steps. In this approach, the individual steps are identified with a discrete index n, but the behavior of each step is described with a continuum approach. The continuum description of a step is obtained by integrating out microscopic short-wavelength fluctuations in a step such as kinks. For example, the continuum step position $x_n(y)$ shown in Fig. 17(f) is obtained from the discrete step position, $x_{n,j}$ in a TSK model of Fig. 17(e) by

$$x_n(y) = \sum_j K(y - y_j)\, x_{n,j}, \tag{58}$$

with a Gaussian smearing kernel $K(y) \sim \mathrm{e}^{-(y/y_0)^2}$ where y_0 is the range of the smearing which occurs in the direction parallel to the step-edge. Fig. 17(e) was obtained by integrating out the adatom degrees of freedom from Fig. 17(c), hence, Fig. 17(f) can be also directly obtained from Fig. 17(c) by integrating out the effects of adatoms at the terrace and kinks at the step altogether.

To proceed, we need to provide an effective Hamiltonian for coarse-grained steps. There are a couple of formal ways to construct an effective Hamiltonian from microscopic models but, in practice, formal methods are not easy to carry out for general step configurations [92,111]. In the following section, we

introduce a mesoscopic model Hamiltonian for the coarse-grained steps which incorporates the known results for two simpler systems, a 1D interface (an isolated step) [23] and a quasi-1D system (*uniform* straight step array) [21,22] with heuristic arguments to motivate the choice of such model.

3.3.2. *Effective Hamiltonian for step models*

We start with a simple situation that the steps are in an equilibrium state of a vicinal surface with a single orientation. The long-wavelength properties of this stable uniform step configuration are dominated by the effects of step–step repulsions. On an atomic scale, the fluctuations of individual steps are controlled by the microscopic energy cost to form kinks. On coarse-graining, this translates into an effective step *stiffness*,[8] $\tilde{\beta}$ defined in Eq. (9), that tends to keep the step straight.

3.3.2.1. Step stiffness. On a short length scale (shorter than the collision length, l_c-defined below), where the approximation of isolated steps is valid, the step fluctuations are dominantly controlled by this step stiffness. In this case, the continuum step Hamiltonian, which controls fluctuations of the coarse-grained isolated step, is expected to be written as

$$H = \int \frac{\tilde{\beta}}{2} \left(\frac{\partial x}{\partial y}\right)^2 \mathrm{d}y, \tag{59}$$

and can be diagonalized by Fourier transforming

$$H = \frac{1}{2\pi} \int \frac{\tilde{\beta}}{2}\, q^2 |x_q|^2 \,\mathrm{d}q \tag{60}$$

with $x_q = (1/\sqrt{2\pi}) \int \mathrm{d}y\, x(y) \mathrm{e}^{-\mathrm{i}qy}$, where $x(y)$ is the x-coordinate of the step at y (see Fig. 1 for definition of the coordinates). From the equipartition theorem, the equilibrium second moment of a Gaussian random variable, $\langle x_q x_{q'} \rangle$ is given by

$$\langle x_q x_{q'} \rangle = \frac{kT}{\tilde{\beta}\, q^2}\, \delta(q + q'). \tag{61}$$

The mean square displacement along the step-edge [35],

$$G(y) \equiv \langle [x(y) - x(0)]^2 \rangle, \tag{62}$$

increases linear with y

$$G(y) = \frac{1}{2\pi} \int \mathrm{d}q\, \mathrm{d}q'\, \langle x_q x'_q \rangle (\mathrm{e}^{\mathrm{i}qy} - 1)(\mathrm{e}^{\mathrm{i}q'y} - 1) = \frac{kT}{2\pi} \int \frac{2(1 - \cos(qy))}{\tilde{\beta} q^2} \mathrm{d}q = \frac{kT}{\tilde{\beta}}\, |y|, \tag{63}$$

where the brackets denote an ensemble average. This linear increasing $G(y)$ can be checked trivially in a 1D SOS model from the analogy with random walkers. If $E(n)$ is the energy of a kink of size na_x, x changes by na_x upon each "pace" with the probability, $p(n) \sim \mathrm{e}^{-E(n)/kT}$, and the mean-square

[8] Computing $\tilde{\beta}$ from microscopic energy $E(n)$ of a kink of size n can be easily done for various kink Hamiltonians. For details on this calculation, see, for example, Bartelt et al. [35].

wandering is written as

$$G(y) = \frac{b^2(T)}{a_y}\,|y|, \tag{64}$$

with the step-edge "diffusivity" $b^2(T)$ defined by

$$b^2(T) = a_x^2 \sum_{n=-\infty}^{\infty} n^2 \exp[-E(n)/kT] \Bigg/ \sum_{n=-\infty}^{\infty} \exp[-E(n)/kT], \tag{65}$$

since the wandering of an isolated step-edge can be considered as a simple random walk with the averaged "pace width" of each pace, $b(T)$. By comparing Eq. (63) with Eq. (64), we have $\tilde{\beta}(T) = kT/b^2(T)$. Step-edge diffusivity, $b^2(T)$, can be exactly calculated for various forms of kink energies $E(n)$ as described in Section 2.2. The experimental application of Eq. (63) to determine the step stiffness experimentally is presented in Section 4.1.1.

As the distance along the step-edge direction y increases, the root-mean-square displacement, $\Delta(y) = \sqrt{G(y)} \sim \sqrt{y}$, inevitably becomes a significant fraction of the terrace width, w, and the effect of step–step collision must be taken into account. The collision length l_c is defined as the distance y along the average step-edge direction such that $\Delta(y)$ of an *isolated* step would be the half width of the average terrace, $w/2$:

$$l_c(w) = \frac{\tilde{\beta}}{4kT} w^2, \tag{66}$$

from Eq. (63). On an average, a step meets a neighboring step once in every distance l_c along the y-direction but it cannot cross the other step due to the prohibitively high energy cost associated with overhangs. This prohibition reduces the configurational entropy of the step when it is near to the neighboring steps. Hence the "collision" produces an effective repulsion between steps which favors a uniform step spacing at equilibrium. Since the number of collision per unit distance in the y-direction, which is proportional to the inverse collision length,[9] decreases as $1/w^2$ (Eq. (66)), the configurational entropy of a step is expected to decrease as $1/w^2$. With the fact that the step density is given by $1/w$, we now expect that entropic repulsion contribution to the projected free energy density should be proportional to $1/w^3$. Indeed, the standard microscopic 2D models of step arrays, such as the free-fermion model and the terrace–step–kink (TSK) model [121,122], show that the projected free energy density of a uniform vicinal surface of step density $1/w$ is given by the familiar Gruber–Mullins [21] expression

$$f(w) = f_0 + \beta/w + gh^3/w^3. \tag{67}$$

3.3.2.2. Step interactions. The relationship between the step interaction parameter g and the mean-square step wandering $G(y)$ can be easily understood. First, let us consider a quasi-1D system with average terrace width w_a, whose energy is given by

$$H = L_y \sum_{n=1}^{N_s} f_0 w_n + \beta + gh^3/w_n^2, \tag{68}$$

[9] Strictly speaking, this is valid only in average over a scale larger than $l_c(w)$.

where L_y is the length of each (straight) step, w_n the width of the nth terrace and N_s is the number of steps. A vicinal surface described by this Hamiltonian is rough even though it is below the roughening transition temperature of the flat surface because the energy has an analytic expansion in deviations in slope. If u_n denotes the deviation of the nth step position from its average position, $w_a n$,

$$u_n = x_n - w_a n, \tag{69}$$

and u_q is the Fourier component of u_n,

$$u_q = \frac{1}{\sqrt{N_s}} \sum_n u_n e^{-iqw_a n}, \tag{70}$$

the energy difference between a non-uniform and a uniform vicinal system is written as

$$\begin{aligned} H - H_0 &= L_y \sum_n \frac{gh^3}{(u_{n+1} - u_n + w_a)^2} - \frac{gh^3}{(w_a)^2} \\ &= \frac{L_y g h^3}{w_a^2} \sum_n \left[\left(1 + \frac{u_{n+1} - u_n}{w_a} \right)^{-2} - 1 \right] \\ &\simeq \frac{3 L_y g h^3}{w_a^4} \sum_q 2\,(1 - \cos(q w_a)) |u_q|^2 \\ &\simeq \frac{N_y \tilde{\gamma}_x}{2} \sum_q (q w_a)^2 |u_q|^2 \end{aligned} \tag{71}$$

for small q and $|u_q|$. Here, $H_0 = (f_0 + \beta/w_a + gh^3/w_a^3) L_y N_s w_a$ is the energy of the uniform vicinal surface, $N_y = L_y/a_y$ is the dimensionless step length with the unit length in the y-direction a_y, and the effective surface stiffness in the x-direction, $\tilde{\gamma}_x$ is given by

$$\tilde{\gamma}_x = 6gh^3 a_y / w_a^4. \tag{72}$$

Now consider a continuum theory for a 2D vicinal surface of fluctuating steps. Since it is in a rough phase, the free energy cost for long wavelength, small distortions from the uniform system can be written as

$$H = \frac{1}{2} \sum_q \left[\tilde{\gamma}_x (w_a q_x)^2 + \tilde{\gamma}_y (a_y q_y)^2 \right] |u_q|^2, \tag{73}$$

in terms of the Fourier components of the deviations,

$$u_q = \frac{1}{\sqrt{N_s N_y}} \sum_n \int \mathrm{d}y\, u_n(y)\, e^{-i(q_x w_a n + q_y y)}, \tag{74}$$

where $u_n(y) = x_n(y) - w_a n$ is the deviation from the uniform state.[10] Since the equilibrium second moment of a Gaussian random variable, $\langle u_q u'_q \rangle$ is given by

$$\langle u_q u'_q \rangle = \frac{kT}{\tilde{\gamma}_x (w_a q_x)^2 + \tilde{\gamma}_y (a_y q_y)^2}\ \delta_{q',-q}, \tag{75}$$

[10] One could use different normalization for Fourier transforming, for example, $1/\sqrt{N_s L_y}$ instead of $1/\sqrt{N_s N_y}$, which gives additional powers of $N_s L_y$ in quantities in terms of Fourier components. We choose the above normalization to avoid confusion of Fourier components having different dimensions depending on the direction.

the mean square step wandering, $G(y)$, is given by

$$\begin{aligned} G(y) &= \frac{1}{N_s N_y} \sum_{q,q'} \langle u_q u'_q \rangle \, (\mathrm{e}^{\mathrm{i}qy} - 1)(\mathrm{e}^{\mathrm{i}q'y} - 1) \\ &= \frac{kT}{N_s N_y} \sum_{q} \frac{2\,[1 - \cos(q_y y)]}{\tilde{\gamma}_x l^2 q_x^2 + \tilde{\gamma}_y a_y^2 q_y^2} \\ &\simeq \frac{kTla_y}{4\pi^2 \tilde{\gamma}} \int \frac{2\,[1 - \cos(q_y y)]}{\tilde{\eta} l^2 q_x^2 + a_y^2 q_y^2/\tilde{\eta}} \, \mathrm{d}q_x \mathrm{d}q_y, \end{aligned} \tag{76}$$

where $\tilde{\gamma} = \sqrt{\tilde{\gamma}_x \tilde{\gamma}_y}$ is the (geometric) mean surface stiffness and $\tilde{\eta} = \sqrt{\tilde{\gamma}_x / \tilde{\gamma}_y}$ measures the anisotropy in surface stiffness. By introducing variables, p and θ through $p\cos\theta = \sqrt{\tilde{\eta}}\, l q_x$ and $p \sin\theta = a_y q_x / \sqrt{\tilde{\eta}}$, we have

$$\begin{aligned} G(y) &= \frac{kT}{4\pi^2 \tilde{\gamma}} \int \frac{\mathrm{d}p}{p} \int 2\,[1 - \cos(\sqrt{\tilde{\eta}} kp \sin\theta)] \, \mathrm{d}\theta \\ &= \frac{kT}{\pi \tilde{\gamma}} \int \frac{\mathrm{d}p}{p} (1 - J_0(\sqrt{\tilde{\eta}}(y/a_y)p)) \\ &\simeq \frac{kT}{\pi \tilde{\gamma}} \int \frac{\mathrm{d}y}{y} \int_0^{\infty} J_1(x) \, \mathrm{d}x \\ &\simeq \frac{kT}{\pi \tilde{\gamma}} \ln(y/a_y) + \text{const}, \end{aligned} \tag{77}$$

for y much larger than l_c.

Therefore, we expect the mean square step wandering, $G(y)$ to increase linearly for small y but change to logarithmic behavior for large y

$$G(y) \simeq \begin{cases} C_1(T)\, y & \text{for } y \ll l_c, \\ C_2(T) \log(y) & \text{for } y \gg l_c. \end{cases} \tag{78}$$

If one measures the coefficients, $C_1(T)$ and $C_2(T)$, from step configurations, the step stiffness $\tilde{\beta}(T)$ and the step interaction parameter $g(T)$ can be obtained from Eqs. (63) and (77) with Eq. (72)

$$\tilde{\beta}(T) = kT/C_1(T), \qquad g(T) = \tilde{\gamma}_x w_a^4/6 \;=\; \tilde{\gamma}^2 w_a^4/(6\tilde{\gamma}_y) = \frac{1}{6\pi^2} \left(\frac{kT}{C_2(T)/a_x^2} \right)^2 \left(\frac{C_1(T)}{a_x} \right) a_x^2. \tag{79}$$

A mean square displacement difference of step positions, which is defined by

$$G_n(0) = \langle (u_n(y) - u_0(y))^2 \rangle, \tag{80}$$

can be calculated by a similar method to Eqs. (76) and (77). It shows a logarithmic dependence on step index n with the same coefficient[11] as Eq. (77). This logarithmic behavior has been confirmed from a

[11] In general, $G_{n-m}(y - y') = \langle [u_n(y) - u_m(y')]^2 \rangle$ shows logarithmic dependence, $G_n(y) = (kT/\pi\tilde{\gamma}) \ln \rho_{n,y}$ with the rescaled distance $\rho_{n,y} = [\tilde{\eta} y^2 + n^2]^{1/2}$ [14].

STM [32] and a REM [33] measurement. The step interaction parameter $g(T)$ can be also obtained from the correlation of positions of different steps or terrace width distributions [122–124]. The application of measurement of the terrace width distribution to experimental data will be discussed in Section 4.1.2.

3.3.2.3. Step Hamiltonian. The free energy of Eq. (67) has been used to approximate the interaction between steps in quasi-1D step models [49]. In a quasi-1D model, the positions of steps are obtained by averaging the transverse step fluctuations in the 2D TSK model over a distance $L_y \gg l_c$ along the step-edge direction, and the effective interactions between steps are given in terms of the resulting 1D positions of the steps. The Hamiltonian of the entire system can be written as the sum of contributions from each step and terrace

$$H = \sum_{n=1}^{N} V_n^s + V_n^t, \tag{81}$$

where N is the number of steps (or terraces) and V_n^s (V_n^t) is the contribution from the nth step (terrace). If the total projected area, A_0, is conserved and the surface tension for the flat surface, f_0, is the same for all terraces, the total terrace contribution, given as

$$H^t = \sum_{n=1}^{N} V_n^t = f_0 A_0, \tag{82}$$

is constant and can be ignored. This approach can be generalized to cases such as reconstruction or adsorption when the free energy may vary from terrace to terrace. To do so, it is convenient to re-express the free-energy contribution from the nth terrace as the part of the step–step interaction term between the nth and the $(n+1)$th steps [111,117]. Then the free energy contribution from the nth step V_n^s is, in general, a function of all step positions

$$V_n^s = V_n^s(x_n; x_1, \ldots, x_{n-1}, x_{n+1}, \ldots, x_N), \tag{83}$$

but the dominant contributions come from the interactions with the neighboring steps, the $(n-1)$th and the $(n+1)$th steps which directly restrict the motion of the nth step. Therefore, V_n^s can be approximated as

$$V_n^s \approx V_n^s(x_n; x_{n-1}, x_{n+1}). \tag{84}$$

Rettori and Villain [49] used a quasi 1D model for (non-uniform step spacing) surfaces with V_n^s given as the average of the nearest-neighbor *pair* interactions which are functions of the distance between them

$$V_n^s(x_n; x_{n-1}, x_{n+1}) = \tfrac{1}{2}\,[V(x_n - x_{n-1}) + V(x_{n+1} - x_n)], \tag{85}$$

where $V(w)$ is the interaction between the two neighboring steps with distance w. This local interaction is approximated by using the free energy density of a *uniform* vicinal surface with spacing w between neighboring steps

$$V(w) = wf(w), \tag{86}$$

where $f(w)$ is the projected free energy density of a *uniform* vicinal surface with average terrace width w as in Eq. (67). From this, one can define a 1D Hamiltonian given as

$$H = \sum_{n=1}^{N} w_n f(w_n). \tag{87}$$

The approximation of Eq. (85) may fail to capture some essential features in dynamics of surface morphology evolution, especially those with an edge energy associated [111,119]. For example, Eq. (87) does not provide any driving force for coarsening in the faceting dynamics. However, the quasi-1D model of Rettori and Villain of Eq. (87) with various generalizations of the local free energy $f(w)$ (from Eq. (67)) has been used successfully to describe the surface evolution dynamics of a number of different systems which exhibit quasi-1D features [51,117,125,126]. We will review some applications of these quasi-1D models in Section 4.

To describe the dynamics of general surface evolution (including surfaces which show 2D patterns) with a continuum step model, we need to provide an effective Hamiltonian for arbitrary configurations of the coarse-grained steps. We can think of a couple of formal ways to construct the effective Hamiltonian for coarse-grained steps from microscopic models such as a TSK model. We can imagine all microscopic configurations which correspond to a given coarse-grained step configuration $x_n(y)$, following the concept of renormalization, then calculate the logarithm of the partial sum of Boltzmann factors to get the effective Hamiltonian

$$H(\{x_n(y)\}) = -kT \log\left[\sum_{\{x_{n,j}^m\}\in\{x_n(y)\}} \exp\left(-\frac{H^m(\{x_{n,j}^m\})}{kT}\right)\right], \tag{88}$$

where $\{x_{n,j}^m\}$ is a configuration and H^m is the Hamiltonian of the microscopic model. Alternatively, in analogy with density functional methods for inhomogeneous fluids [127], we can consider an auxiliary external field $\{\phi(x,y)\}$ that couples linearly to the step positions such that a given arbitrary step configuration of $\{x_n(y)\}$ be the equilibrium state. The free energy of this system, calculated by taking the trace over all configurations under external fields, will be a functional of $\{\phi(x,y)\}$ and include the direct linear contribution from the external field. If we subtract this linear term in the field we get the intrinsic free energy of the non-uniform system. Technically, this generates a Legendre transform giving the free energy as a functional of the configurations $\{x_n(y)\}$ rather than the field $\{\phi(x,y)\}$.

In practice, both formal methods are difficult to carry out for general step configurations, though the second method has been successfully applied to calculate the edge energy of non-uniform, quasi-1D configurations [111]. We will not review such formal developments, nor attempt to generalize it to 2D configurations. Rather, we consider a mesoscopic model Hamiltonian which incorporates the known results for two simpler systems, a 1D interface [23] and a *uniform* step array [21, 22]

$$H(\{x_n\}) = \sum_n \int \mathrm{d}y \left[\frac{\tilde{\beta}}{2}\left(\frac{\partial x_n}{\partial y}\right)^2 + V(w_n(y))\right], \tag{89}$$

where $w_n(y) \equiv x_{n+1}(y) - x_n(y)$. The first term describes the energetics of distorting an individual step, controlled by a line stiffness $\tilde{\beta}$. Everything else should be incorporated into an effective step interaction, V, where we make an assumption that V can be approximated as a function of local terrace

width $w_n(y)$. Here, we would like to point out the assumptions and approximations made in writing Eq. (89). For the step–step interaction, we first assume that it can be approximated as the two nearest-neighbor pair interactions and given as functions of the distance between the pairs as in Eq. (85). Furthermore, the distances between neighboring steps are evaluated at the same y-position. Hence, Eq. (89) may not be good in describing strongly fluctuating steps. In general, the effective step–step interaction $V(w)$ depends on the coarse-graining size, Δy. As an approximation, the 1D free energy of Eq. (67) has been used (Eq. (86)) for estimating $V(w)$ of the 2D model [92]. This approximation is expected to be reasonable as Δy gets larger than the collision length l_c. We can estimate the range of terrace widths for which this approximation is valid from the requirement that the coarse-graining length Δy be larger than the collision length l_c. Since $l_c(w) = \tilde{\beta} w^2/4kT$, we find that the 1D free energy approximation of Eq. (67) is strictly valid only for local terrace widths $w \lesssim 2\sqrt{\Delta y kT/\tilde{\beta}}$ or, equivalently, the coarse-graining length $\Delta y \gtrsim w^2\tilde{\beta}/4kT$. Typically, $kT/\tilde{\beta}$ will be much less than $10a_y$ and hence Δy should be larger than $w^2/40a_y$ to use Eq. (86) with Eq. (67). On the other hand, physically, the integration length Δy must be much less than the length-scale of the curvature of interest. Thus we can adapt the general rule that the quasi-1D free energy of Eq. (67) can only be used to describe 2D step patterns where the wavelength of the pattern is much larger than the step spacing. As a corollary of this rule, we also conclude that 2D step patterns must reflect configurations with weak curvature (as was also required to use the same y-approximation). We also make a quadratic approximation for the line tension term which is the lowest term in the change in step length. (Note that the step length is given by $\int[1 + (\partial_y x_n)^2]^{1/2}\,dy$.) This quadratic approximation is also reasonable for relatively straight steps.

3.3.3. Step chemical potential

In Section 2.3.1, where the morphology evolution was considered from a continuum perspective, removing (or adding) an atom changes the local height a little bit. Hence, we considered the local *surface* chemical potential, defined as the free energy change due to an atom attachment to the continuum *surface*, which is given as $(\delta H[z(x,y)]/\delta z(x,y))\Omega_v$ with the continuum surface Hamiltonian $H[z(x,y)]$ and the atomic volume Ω_v. Here in the step approach, surface motion results from the step motion, which is invoked by adsorption or emission of atoms at the step-edge. Adatom attachment or detachment at a step corresponds to a small variation of the continuous step position, and therefore, the free energy change due to an atom attachment on the step is proportional to the functional derivative of the effective step Hamiltonian of Eq. (89). We define the step-edge chemical potential [128], $\mu_n(y)$ as the change in the free energy when we remove an atom from the nth step at y. If Ω_s is the *area* occupied by an atom ($\Omega_s = a_x a_y$ for a simple square lattice surface), $\mu_n(y)$ is given by

$$\mu_n(y) \equiv -\Omega_s \frac{\delta H}{\delta x_n(y)} = \Omega_s \left[V'(w_n(y)) - V'(w_{n-1}(y)) + \tilde{\beta}\,\frac{\partial^2 x_n}{\partial y^2} \right], \tag{90}$$

where $V'(w)$ is the derivative of the step interaction energy $V(w)$ with respect to the step spacing w. Since $V(w) = wf(w)$, where f is the free energy density of a surface of uniform step spacing w, and since the step density ρ is given by $\rho = 1/w$, we can rewrite Eq. (90) as

$$\mu_n(y) = \Omega_s \left[\frac{d(f/\rho_n)}{d(1/\rho_n)} - \frac{d(f/\rho_{n-1})}{d(1/\rho_{n-1})} + \tilde{\beta}\frac{\partial^2 x_n}{\partial y^2} \right] = \Omega_s \left[P_z^n - P_z^{n-1} + \tilde{\beta}\frac{\partial^2 x_n}{\partial y^2} \right]. \tag{91}$$

Here we have made explicit connection to the thermodynamic formulation of Section 2.2.3, specifically Eq. (22). As noted before, and illustrated in Fig. 12, the term $V'(w_n)$ has dimensions of force per unit length and can be interpreted as an effective *pressure* on the step associated with terrace n. Thus the local step chemical potential $\mu_n(y)$ depends on the local (linearized) curvature $\partial_y^2 x_n$ of the step and on the difference in pressure from terraces behind and in front of the step.

3.3.4. Models for step dynamics

For describing step motion, we use linear kinetics, i.e., the assumption that the velocity of a step is proportional to the change in free energy produced by its motion.[12] Since the motion of steps results from the movement of atoms at steps, the step kinetics depends on the mechanism of mass transport on the surface. The aim of this section is to introduce simple models for step dynamics for the mass transport modes allowed in 2D step models. We first start with the simplest case, the step dynamics of an isolated step. Then, we consider the dynamics of (straight) steps in a quasi-1D step array and generalize the approach to fluctuating 2D steps. Experimental application of these models through analysis of the time correlation function will be described in Section 4.

3.3.4.1. Isolated step. For the motion of an isolated step, there are three limiting cases of the mass transport, evaporation–condensation (EC), step-edge diffusion (SED) and terrace diffusion (TD) which correspond to EC, surface diffusion and volume diffusion, respectively, for the analogous 1D interface of a genuine 2D system as was discussed in Section 2.3.1. The isolated step limit corresponds to the absence of step–step interaction term ($V(w) = 0$) in Eq. (90). Therefore, the local step chemical potential $\mu(y)$ is given by

$$\mu(y) = \Omega\tilde{\beta}\,\frac{\partial^2 x}{\partial y^2}, \tag{92}$$

where the area occupied by an atom Ω_s is now denoted by Ω. We also dropped the step index n since only a single step is considered.

For an EC case, the local step exchanges adatoms with the vapor which serves as a reservoir of constant chemical potential. The local step thus moves according to the chemical potential difference between the step and the reservoir:

$$\frac{\partial x(y)}{\partial t} = \frac{\Gamma_A}{\Omega kT}\,[\mu(y) - \mu_{res}] = \frac{\Gamma_A\tilde{\beta}}{kT}\,\frac{\partial^2 x}{\partial y^2}, \tag{93}$$

where Γ_A is the mobility of the step-edge, as defined by Bartelt et al. [35,48] and as will be described in Section 4.1.2. The arbitrary zero for the step chemical potential is selected such that a straight line has zero chemical potential. Therefore, for the EC case, μ_{res} is zero when there is no net evaporation or condensation. The reservoir of constant chemical potential, with which the step exchanges adatoms,

[12] Short-wavelength thermal fluctuations are already incorporated into the effective Hamiltonian of Eq. (89), which, in principle, represents the partial sum of Eq. (88). The remaining thermal fluctuations are irrelevant to the dynamic behavior of the surface approaching equilibrium (from out-of-equilibrium) in most cases. When temperature is a relevant variable, thermal noise, whose amplitude is give by the fluctuation–dissipation theorem, should be considered explicitly and the dynamics considered here becomes the Langevin dynamics [48].

need not be a vapor. In fact in most of the cases we consider, the neighboring terrace serves as the reservoir.

Mass transport along the step-edge is completely analogous to the one-dimensinal interface limit of surface diffusion on a two-dimensional interface. This process may be dominant at low temperature where desorption from the step-edge is unlikely and atomic motion occurs along the step-edge. If mass transport through terrace diffusion or vapor is forbidden so that the diffusion along the step-edge is the rate-limiting process in the mass transport, we get the SED limit. The mass (area) of each terrace is locally conserved in this case and the normal velocity of the step is determined by gradients of chemical potentials along the step edge

$$\frac{\partial x(y)}{\partial t} = -\frac{\Gamma_h}{\Omega kT}\,\frac{\partial^2 \mu(y)}{\partial y^2} = -\frac{\Gamma_h \tilde{\beta}}{kT}\,\frac{\partial^4 x}{\partial y^4}, \tag{94}$$

where Γ_h is an effective mobility of the step due to atomic motion along the step-edge.

Deriving the equation of step motion in the TD case is not so simple as the EC or SED case. A TD limit is the case when the step emits atoms to (or adsorbs atoms from) the terrace rapidly but atoms diffuse slowly on the terrace. Therefore, to derive the equation of step motion, we should consider the adatom diffusion dynamics on the terrace as well as attachment/detachment of atoms at the step as illustrated in Fig. 14. Since the step exchanges atoms with the terrace, we can assume that the step moves according to the chemical potential difference between the step and the terrace, providing that the *local terrace* chemical potential near the step is used

$$\frac{\partial x(y)}{\partial t} = \frac{\Gamma_+}{\Omega kT}\,[\mu(y) - \mu_+^{\mathrm{t}}(y)] + \frac{\Gamma_-}{\Omega kT}\,[\mu(y) - \mu_-^{\mathrm{t}}(y)], \tag{95}$$

with

$$\mu_\pm^{\mathrm{t}} = \lim_{\delta x \to 0} \mu^{\mathrm{t}}(x,y)|_{x=x(y)\mp\delta x}, \tag{96}$$

where $\mu^{\mathrm{t}}(x,y)$ is the local chemical potential of an adatom on the terrace which is yet to be calculated. Here Γ_+ (Γ_-) is the mobility of the step-edge from mass exchange with upper (lower) terrace and we ignore the mass transport along the step-edge ($\Gamma_h = 0$). The relationship between Γ and the step attachment rate κ of Fig. 14 and Eq. (37) is simply $\Omega^2\kappa = \Gamma/c_{\mathrm{eq}}$, where c_{eq} is the equilibrium concentration on the terrace far from the step, where chemical potential (which should be equal to the average step chemical potential when there is no overall step movement) is set to be zero.

To obtain $\mu_\pm^{\mathrm{t}}$, the chemical potential on the terrace $\mu^{\mathrm{t}}(x,y)$, which is related to the adatom concentration profile $c(x,y)$ by

$$c(x,y) = c_{\mathrm{eq}} \exp[\mu^{\mathrm{t}}(x,y)/kT], \tag{97}$$

needs to be calculated [129,130]. Recall that, in a step approach, the equation of motion is given in terms of step configurations only. Therefore, one must formally integrate out the role of adatoms on the terrace and find $\mu_\pm^{\mathrm{t}}$, as a functional of the step configuration, $\{x(y)\}$. To do that, we assume that the step movements are slow enough that the concentration profile is established on the terraces much faster than the motion of the steps. In this case, one can use the quasistatic approximation [46,56,131] and write a time-independent diffusion equation on the terrace

$$\nabla^2 c(x,y) = 0. \tag{98}$$

The boundary condition at the step is the same same as in Eq. (37)

$$\mp D_s\left[\frac{\partial c(x,y)}{\partial x}\right]_{x=x(y)\mp\delta x}+\frac{\Gamma_\pm}{\Omega^2 kT}\ [\mu(y)-\mu^t(x,y)]_{x=x(y)\mp\delta x}=0, \tag{99}$$

as $\delta x\to 0$, from the mass conservation in the vicinity of the step.[13] We consider the case where $|\mu^t(x,y)|/kT$, or equivalently, $|c(x,t)-c_{eq}|/c_{eq}$ is small everywhere so that $c(x,t)$ of Eq. (97) can be approximated by

$$c(x,y)=c_{eq}(1+\mu^t(x,y)/kT), \tag{100}$$

i.e.,

$$\mu^t(x,y)=kT\left[\frac{c(x,y)-c_{eq}}{c_{eq}}\right]. \tag{101}$$

Then, the terrace chemical potential $\mu^t(x,y)$ satisfies the Laplace equation

$$\nabla^2\mu^t(x,y)=0, \tag{102}$$

with the boundary condition

$$\mp D_s c_{eq}\Omega^2\left[\frac{\partial\mu^t(x,y)}{\partial x}\right]_{x=x(y)\mp\delta x}+\Gamma_\pm\ [\mu(y)-\mu^t(x,y)]_{x=x(y)\mp\delta x}=0 \tag{103}$$

at the step ($\delta x\to 0$), and

$$\lim_{x\to\pm\infty}\mu^t(x,y)=0, \tag{104}$$

on the terrace far away from the step.

The rate of step flow in the TD case is most readily solved using a Fourier transform technique. Let $x_q(t)$ be the Fourier q-component of the step fluctuation

$$x_q(t)=\frac{1}{\sqrt{L_y}}\int x(y,t)e^{-iqy}dy. \tag{105}$$

Then, the q-component of the step chemical potential μ_q is given by

$$\mu_q=-\Omega\tilde{\beta}q^2x_q \tag{106}$$

from Eq. (92). Now, the q-component of the terrace chemical potential

$$\mu_q^t(x,t)=\frac{1}{\sqrt{L_y}}\int\mu^t(x,y,t)\,e^{-iqy}\,dy \tag{107}$$

satisfying Eqs. (102)–(104) is given by

$$\mu_q^{t^\pm}(x,t)=\frac{\Gamma_\pm}{\Gamma_\pm+D_s c_{eq}\Omega^2|q|}\,\mu_q(t)\,e^{\mp qx}, \tag{108}$$

[13] We assume that $|\partial x/\partial y|$ is small and take $\hat{x}$ as the direction normal to the step everywhere.

where μ^{t^+} (μ^{t^-}) is the right (left) terrace chemical potential. From Eq. (95), we have

$$\frac{\partial x_q(t)}{\partial t} = \frac{D_s c_{eq} \Omega |q|}{kT} \left[\frac{\Gamma_+}{\Gamma_+ + D_s c_{eq} \Omega^2 |q|} + \frac{\Gamma_-}{\Gamma_- + D_s c_{eq} \Omega^2 |q|} \right] \mu_q(t). \tag{109}$$

For a TD limit, where the rate-limiting process in mass transport is the diffusion on the terrace ($qD_s \ll \Gamma_\pm$), Eq. (109) becomes

$$\frac{\partial x_q(t)}{\partial t} = \frac{2D_s c_{eq} \Omega |q|}{kT} \mu_q(t) = -\frac{2\tilde{\beta} D_s c_{eq} \Omega^2 |q|^3}{kT} x_q(t). \tag{110}$$

The step velocity for an arbitrary step configuration is therefore given by

$$\frac{\partial x(t)}{\partial t} = -\frac{1}{\sqrt{L_y}} \int \frac{2\tilde{\beta} D_s c_{eq} \Omega^2 |q|^3}{kT} x_q \, dq. \tag{111}$$

In the limit of L_y goes to infinity, Eq. (111) can be written as [132]

$$\frac{\partial x_n(y)}{\partial t} = \frac{4D_s c_{eq} \Omega^2 \tilde{\beta}}{\pi kT} \int_{-\infty}^{\infty} S(y - y') \frac{\partial^2 x(y', t)}{\partial y'^2} \, dy', \tag{112}$$

where $S(y) = (c^2 - y^2)/(c^2 + y^2)^2$, with a convergence factor c which is of the order of the lattice constant in the step-edge direction (a_y). The step velocity of Eq. (112) is a non-local function of the step chemical potential $\mu(y) \propto \partial_y^2 x(y)$ as one expects from the terrace diffusion mechanism.

3.3.4.2. Steps in a quasi-1D step array. Before considering the general case of fluctuating 2D step arrays, let us consider a quasi-1D step array of "straight steps". Now the step chemical potential, μ_n is given by

$$\mu_n = \Omega [V'(w_n) - V'(w_{n-1})] \tag{113}$$

from Eq. (90). Here we emphasize the 1D nature of the step chemical potential by the notation μ_n (rather than $\mu_n(y)$ used in Sections 3.3.4.2 and 3.3.4.3). Since adatom movement in the step-edge direction is not considered, there are two limiting cases of mass transport depending on whether a step exchanges atoms with neighboring terraces only (*local movement*) or with terraces at all distances through a global reservoir (*global movement*).

Before considering these limiting cases, let us discuss a general case with finite step permeability [133]. Steps are called permeable when adatoms can go to the neighboring terrace by direct hopping over the step edge (bypassing attachment/detachment processes). Fig. 20 shows a schematic illustration (a) and an analogous electric circuit (b) for the atomic current on the surface with finite step permeability [133,134]. The adatom flux on the terrace is given by the sum of the direct hopping current from the neighboring terrace and the current from the nearby steps. For example, the adatom current immediately to the left (right) of the nth step j_n^- (j_n^+) is given by

$$j_n^- = j_n^{s-} + j_n^p, \qquad j_n^+ = j_n^{s+} + j_n^p, \tag{114}$$

where j_n^p is the direct hop current over the step n and j_n^{s-} (j_n^{s+}) is the adatom current between the step n and the left (right) neighboring terrace. With a linear kinetic approximation, in which we assume that

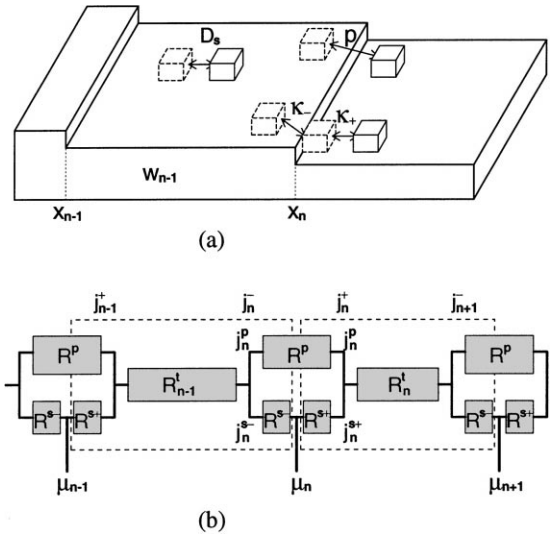

Fig. 20. (a) A schematic illustration and (b) an analogous electric circuit of the adatom current with finite step permeability. Adatoms on the $(n-1)$th terrace go to the nth terrace through direct hopping over the step-edges, associated with the effective resistance $R^p = kT/pc_{\rm eq}$ or through the attachment/detachment process. $R^{s\pm} = \Omega^2 kT/\Gamma_\pm = kT/\kappa_\pm c_{\rm eq}$ is the resistance associated with adatom exchange between the step-edge and the neighboring left $(-)$ or right $(+)$ terrace and $R^t = kTw/D_s c_{\rm eq}$ is the terrace resistance. The step chemical potential μ_n is determined by the step configuration through Eq. (113). The limit of $R^p/R^{s\pm}$ goes to zero (infinity), corresponds to the global (local) movement case. In quasi-static approximation, the current in each dashed box should be the same. The difference in currents between the two dashed boxes is proportional to the step velocity $(\partial_t x_n \propto j_n^- - j_n^+)$.

the net mass current between the two regions is proportional to the difference in chemical potentials, j_n^p and $j_n^{s\pm}$ can be written as

$$j_n^p = (\mu_{n-1}^{\rm tR} - \mu_n^{\rm tL})/R^p, \qquad j_n^{s-} = (\mu_{n-1}^{\rm tR} - \mu_n)/R^{s-}, \qquad j_n^{s+} = (\mu_n - \mu_n^{\rm tL})/R^{s+}, \tag{115}$$

where μ_n is the chemical potential of the step n and $\mu_n^{\rm tR}$ and $\mu_n^{\rm tL}$ are the terrace chemical potentials $\mu_n^{\rm t}(x)$ at the boundaries

$$\mu_n^{\rm tR} = \lim_{\delta x \to 0} \mu_n^{\rm t}(x_{n+1} - \delta x), \qquad \mu_n^{\rm tL} = \lim_{\delta x \to 0} \mu_n^{\rm t}(x_n + \delta x). \tag{116}$$

The effective resistance R^p associated with the direct hop (step permeability p [133,134]) and the resistance associated to the adatom exchange between the step-edge and the neighboring left $(-)$ or right $(+)$ terrace $R^{s\pm}$ are given by

$$R^p = kT/pc_{\rm eq}, \qquad R^{s\pm} = kT/c_{\rm eq}\kappa_\pm, \tag{117}$$

where $\kappa_\pm$ is the kinetic coefficient of attachment and detachment from the step edges as introduced in Section 2.3.2 as a step boundary condition for the BCF model. Within the quasistatic approximation, where the step motions are much slower than the adatom movements, the current at the right-hand side of the nth step j_n^+ and the current at the left-hand side of the $(n+1)$th step, j_{n+1}^- should be the same and equal to the current on the nth terrace

$$j_n^+ = j_{n+1}^- = j_n^{\rm t} = [\mu_n^{\rm tL} - \mu_n^{\rm tR}]/R_n^{\rm t} \tag{118}$$

where the effective terrace resistance with surface diffusion constant D_s is given by

$$R_n^t = kTw_n/D_s c_{eq} \tag{119}$$

as shown in Jeong and Weeks [135]. The equation of motion for the step is given by mass conservation near the step

$$\frac{\partial x_n}{\partial t} = \Omega\,(j_n^+ - j_n^-) = \Omega\,[\mu_n - \mu_n^{tL}]\,/\,R_n^{s+} - \Omega\,[\mu_{n-1}^{tR} - \mu_n]\,/\,R_n^{s-}. \tag{120}$$

To use this equation, one needs to find μ_n^{tL} and μ_n^{tR} from Eq. (118) (for given step chemical potentials determined by Eq. (113) for the specific step profile). There are several limiting cases, including global and local mass transport [117], in which the terrace chemical potential can be solved analytically and the step velocity $\partial_t x_n$ can be expressed in terms of step chemical potentials.

3.3.4.2.1. Global movement. If adatoms can hop between different terraces very easily and diffuse on the surface very fast compared to the attachment/detachment rate ($R^t/R^{s\pm} \ll 1$ and $R^p/R^{s\pm} \ll 1$), all terraces will have the same chemical potential everywhere and hence act as a global reservoir. Since atoms at a step-edge are exchanged with the ''global terrace reservoir'', steps move according to the chemical potential difference between the step and the reservoir

$$\frac{\partial x_n}{\partial t} = \frac{\Gamma_A}{\Omega kT}\,[\mu_n - \mu_{res}] = \frac{\Gamma_A}{kT}\,[V'(w_n) - V'(w_{n-1})], \tag{121}$$

where the mobility of the step-edge, Γ_A, is given as $\Gamma_A = \Gamma_+ + \Gamma_- = \Omega^2 c_{eq}(\kappa_+ + \kappa_-)$. The above equation (121) also describes step motion for the evaporation–condensation case where μ_{res} is the chemical potential in the vapor (rather than on the terrace). Both cases are called global mass movement since an atom from a step can go to any step through the global reservoir.

3.3.4.2.2. Local movement. When adatoms cannot hop between terraces ($R^p/R^{s\pm} = \infty$), the chemical potential on the terrace is determined by the neighboring boundary steps only. The mass movement in this case is called ''local'' since atoms from a step are effectively exchanged with the neighboring steps only and the motions of neighboring steps are strongly coupled. Since the current by direct hopping is zero ($p = 0$), the analogous electric circuit of Fig. 20 becomes a series circuit consisting of three resistors, R^{s+}, R^t and R^{s-} between neighboring steps. Therefore, the step velocity can be written as

$$\frac{\partial x_n}{\partial t} = \frac{1}{\Omega kT}\,(\Gamma_e(w_n)[\mu_n - \mu_{n+1}] + \Gamma_e(w_{n-1})[\mu_n - \mu_{n-1}]\,), \tag{122}$$

where the effective step mobility $\Gamma_e(w)$ which is governed by the combination of the rates of terrace diffusion and the attachment/detachment rate at the step-edge is given by

$$\Gamma_e(w) = [\,R^{s+} + R^t + R^{s-}\,]^{-1} = \left[\frac{1}{\Gamma_-} + \frac{w}{D_s c_{eq}\Omega^2} + \frac{1}{\Gamma_+}\right]^{-1}. \tag{123}$$

In fact, one can use the traditional BCF framework in the $p = 0$ case and derive Eq. (123) by solving the 1D version of Eqs. (95) and (102) with boundary conditions at step n and at $n+1$ similar to Eq. (103).[14] As expected, the step mobility of Eq. (123) becomes terrace width independent [136] when

[14] See appendix of Ref. [135] for the conditions that the derivation is valid.

the rate-limiting process is the attachment/detachment at the step ($w\Gamma_{\pm} \ll D_s c_{eq}\Omega^2$ or $R_t \ll R^{s\pm}$), and we have

$$\frac{\partial x_n}{\partial t} = \frac{1}{\Omega kT}\,\frac{\Gamma_+\Gamma_-}{\Gamma_+ + \Gamma_-}[2\mu_n - \mu_{n+1} - \mu_{n-1}]. \tag{124}$$

In the opposite diffusion limited case, where $w\Gamma_{\pm} \gg D_s c_{eq}\Omega^2$ or $R_t \gg R^{s\pm}$, Eq. (123) becomes

$$\frac{\partial x_n}{\partial t} = \frac{D_s c_{eq}\Omega}{kT}\left[\frac{\mu_n - \mu_{n-1}}{w_{n-1}} + \frac{\mu_n - \mu_{n+1}}{w_n}\right]. \tag{125}$$

3.3.4.2.3. Finite step permeability. If adatom diffusion on the terrace is much faster than inter-terrace hopping and attachment/detachment processes ($R^t/R^{s\pm} \ll 1$ and $R^t/R^p \ll 1$), the terrace chemical potential can be expressed in terms of the step chemical potentials. Since the terrace resistance is much smaller than R^p and $R^{s\pm}$, the terrace chemical potential becomes uniform on each terrace ($\mu_n^{tL} = \mu_n^{tR} = \mu_n^t$) and we can write [134]:

$$\begin{bmatrix} 2(\kappa+p) & -p & 0 & \cdots & -p \\ -p & 2(\kappa+p) & -p & \cdots & 0 \\ 0 & -p & 2(\kappa+p) & \cdots & 0 \\ \vdots & \vdots & \vdots & \ddots & \vdots \\ -p & 0 & 0 & \cdots & 2(\kappa+p) \end{bmatrix} \begin{bmatrix} \mu_1^t \\ \mu_2^t \\ \mu_3^t \\ \vdots \\ \mu_N^t \end{bmatrix} = \kappa \begin{bmatrix} \mu_1 + \mu_2 \\ \mu_2 + \mu_3 \\ \mu_3 + \mu_4 \\ \vdots \\ \mu_N + \mu_1 \end{bmatrix}, \tag{126}$$

from Eqs. (115) and (118) where we have assumed no asymmetry between the step-up and step-down directions and set $\kappa = \kappa_+ = \kappa_-$. Since the matrix on the left-hand side of the equation is a circulant matrix [137], the terrace chemical potential, μ_n^t can be solved analytically and can be expressed as

$$\mu_n^t = \sum_m K_m(\mu_{n+m} + \mu_{n+m+1}). \tag{127}$$

In the limit $N \to \infty$, K_m is given by

$$K_m = \frac{\kappa}{2(\kappa+p)}\,\frac{1}{\sqrt{1-a^2}}\left(\frac{1-\sqrt{1-a^2}}{a}\right)^m, \tag{128}$$

with $a = p/(\kappa+p)$. The step velocity is now calculated from Eq. (120) with $\mu_n^{tL} = \mu_n^{tR} = \mu_n^t$. Note that K_m describes the correlation between the adatom chemical potential at a given terrace with the adatom chemical potential m steps away and it decays exponentially as m increases. If we define N_c as the number of steps over which K_m decreases by half [134] ($K_{N_c} = K_0/2$), it is approximately given by

$$N_c \approx \ln(2)\sqrt{\frac{p}{2\kappa}} \tag{129}$$

for $p \gg \kappa$. Since N_c is the range of correlation between the chemical potential values on different terraces, the mass transport is effectively non-local over a number of steps smaller than N_c, and is local over a number of steps larger than N_c. Recall that we have made a quasistatic approximation in deriving Eq. (127) and assumed that the step chemical potentials are constant. This is only valid when the diffusing adatoms on the terrace move over many terraces so quickly that the step chemical potentials hardly change in this timescale.

3.3.4.3. Fluctuating steps in a 2D step array. In the step approach, the step velocity for a fluctuating step in a 2D step array in first-order kinetics is generally written as

$$\frac{\partial x_n(y)}{\partial t} = \sum_{n'=1}^{N_s} \int_0^{L_y} \mathrm{d}y'\ D(x_n(y); x_{n'}(y'))\ [\mu_n(y) - \mu_{n'}(y')] \tag{130}$$

with an adatom exchange coefficient matrix, $D(x_n(y); x_{n'}(y'))$ and step chemical potential given by Eq. (90). Formally, to test the validity of the above equation and to find the matrix element, $D(x_n(y); x_{n'}(y'))$, one needs to consider an adatom diffusion equation on a terrace with the boundary conditions at steps. However, solving the diffusion equation with boundary conditions at fluctuating steps is difficult for the general kinetic process. Here, we discuss a couple of limiting cases of mass transport which may be good approximations for some experiments.

First, let us consider the global movement case, in which adatom exchange between any two points on steps occurs through a global (constant chemical potential) reservoir. In this case, the adatom exchange coefficient is constant, $D(x_n(y); x_{n'}(y')) = \Gamma_A/(\Omega N_s L_y kT)$, and the step velocity of Eq. (130) becomes

$$\frac{\partial x_n}{\partial t} = \frac{\Gamma_A}{\Omega kT}\left[\mu_n(y) - \frac{1}{N_s L_y}\sum_{n'=1}^{N_s}\int_0^{L_y} \mathrm{d}y' \mu_{n'}(y')\right] = \frac{\Gamma_A}{\Omega kT}\ [\mu_n(y) - \mu_{\mathrm{res}}], \tag{131}$$

where the reservoir chemical potential is given as the overall average step chemical potential, $\mu_{\mathrm{res}} = 1/N_s L_y \sum_{n=1}^{N_s} \int_0^{L_y} \mathrm{d}y \mu_n(y)$ and is identically zero when the step chemical potential of Eq. (90) is used. This effective global adatom exchange mechanism is physically relevant when the attachment/detachment rate at steps is slow compared to surface diffusion including diffusion across steps to distant terraces, so that adatoms can freely diffuse to any place on the surface in a typical attachment/detachment interval.

If the rate-limiting process is attachment/detachment at the step but if adatom hops between different terraces do not occur readily, step dynamics falls into the kinetics with local conservation family [136] and the motions of neighboring steps are coupled. In the resistance picture of Fig. 20, this corresponds to $R^t/R^s \ll 1$ and $R^s/R^p \ll 1$. In this case, the rapid diffusion on a terrace ensures that each terrace has a spatially uniform chemical potential of adatoms, though its values are not the same for different terraces in general. Within the quasistatic approximation, the chemical potential on the nth terrace, μ_n^t can be obtained from adatom conservation on the terrace [136]

$$\mu_n^t = (\Gamma_+ \bar{\mu}_n + \Gamma_- \bar{\mu}_{n+1})/(\Gamma_+ + \Gamma_-), \tag{132}$$

where

$$\bar{\mu}_n = \frac{1}{L_y}\int_0^{L_y} \mu_n(y)\,\mathrm{d}y \tag{133}$$

is the average nth step chemical potential.[15] In writing Eq. (132), we have implicitly assumed that atoms diffusing on the terrace move so quickly that they ''sample'' the chemical potential of the entire

[15] This result can be again easily understood from the analogy with conductance in a series of electrical circuits (Fig. 20). Since the chemical potential difference between two steps $\Delta\mu$ is $\bar{\mu}_{n+1} - \bar{\mu}$ and the total resistance, $R = R_+ + R_-$ is $1/\Gamma_+ + 1/\Gamma_-$, the terrace chemical potential μ_n^t is given by, $\mu_n^t = \bar{\mu} + (R_+/R)\Delta\mu = (\Gamma_+\bar{\mu}_n + \Gamma_-\bar{\mu}_{n+1})/(\Gamma_+ + \Gamma_-)$.

length of the step. Now steps move according to the chemical potential difference between the step, and the terrace and the step velocity is given by

$$\frac{\partial x_n(y)}{\partial t} = \frac{\Gamma_+}{\Omega kT}\ [\mu_n(y) - \mu_n^{\mathrm{t}}] + \frac{\Gamma_-}{\Omega kT}\ [\mu_n(y) - \mu_{n-1}^{\mathrm{t}}]. \tag{134}$$

Since L_y is much larger than the terrace width w in a typical vicinal surface system, the adatoms on the terrace may not diffuse over the entire length of the step L_y in a typical attachment/detachment time interval, which maybe much larger than the diffusion time to the neighboring step across the terrace, i.e., $D_s c_{eq}\Omega^2/w \gg \Gamma_\pm > D_s c_{eq}\Omega^2/L_y$. In this case, the local chemical potential on the terrace should be obtained by averaging the step chemical potential over the diffusion distance, l_d, in the y-direction and will show a weak y-dependence. In this case, Eq (132) should be replaced by

$$\mu_n^{\mathrm{t}}(y) = \frac{\Gamma_-}{\Gamma_+ + \Gamma_-}\bar{\mu}_n^-(y) + \frac{\Gamma_+}{\Gamma_+ + \Gamma_-}\bar{\mu}_{n+1}^+(y), \tag{135}$$

with

$$\bar{\mu}_n^\pm(y) = \int_0^{L_y} \mu_n(y')K(l_d^\pm; y - y')\,\mathrm{d}y', \tag{136}$$

where the normalized smearing kernel $K(l_d^\pm; r)$ has the cutoff distance $l_d^\pm = D_s c_{eq}\Omega^2/\Gamma_\pm$ (for example, $K(l_d; r) \sim \mathrm{e}^{-|r|/l_d}$).

If the surface diffusion is slow enough (or the attachment/detachment rate is fast enough) that the diffusion length on the terrace during a typical attachment/detachment interval becomes of order w or less, i.e., $D_s c_{eq}\Omega^2/w \le \Gamma_\pm$, the adatom exchange rate becomes a function of the distance between the two points of exchange. To obtain a general expression for the step velocity, we should include the mass transport modes between two points with different y-positions as well as the adatom exchanges between the same y-neighboring steps. However, for the step bunching or unbunching dynamics in which steps remain nearly straight, the variation of step chemical potential in the y-direction is much smaller than in the x-direction and we can approximate the step velocity by

$$\frac{\partial x_n(y)}{\partial t} = \frac{\Gamma_e(w_n(y))}{\Omega kT}\ [\mu_n(y) - \mu_{n+1}(y)] + \frac{\Gamma_e(w_{n-1}(y))}{\Omega kT}\ [\mu_n(y) - \mu_{n-1}(y)], \tag{137}$$

with the effective step mobility of Eq. (123). When the potential difference between two neighboring steps is much smaller than the potential difference along the same step ($|\partial\mu_n(y)/\partial y| \gg |\mu_n(y) - \mu_{n-1}(y)|/w_n(y)$), the equal y-approximation for the exchange coefficient matrix of Eq. (130):

$$D(x_n(y); x_{n'}(y')) = \Gamma_e(w_n(y))\delta_{n,n+1}\delta(y - y') + \Gamma_e(w_{n-1}(y))\delta_{n,n-1}\delta(y - y') \tag{138}$$

in Eq. (137) is not a good approximation since step motion will occur mainly by adatom exchange between different points along the same step. This would be also the case when the surface diffusion across the terrace is slow compared to the attachment/detachment rate ($D_s c_{eq}\Omega^2/w \ll \Gamma_\pm$). In these cases, the adatom exchange coefficient matrix is not known even for an approximate form. The continuum step approach for the dynamics of Eq. (130) does not seem to be so powerful here and we may have to consider the adatom diffusion equation on a terrace with the boundary conditions at steps.

4. Application of step models for morphology evolution

In this section, we discuss how the continuum step model has been applied to experimental observations of the dynamics of surfaces. We begin with the simplest example of the relaxation of a quasi-1D step array. This analysis can be extended to investigate the properties of a nearly circular step and therefore the motion of islands (monolayer clusters of atoms encompassed by a step). Then we review the relaxation of the step profile, especially from a quasi-1D step bunch profile [125]. Predictions from the continuum step models in both cases will be compared with experimental results. After reviewing these relaxation dynamics, we turn to the dynamics of (the reconstruction) driven faceting. Reconstruction on the surface changes the step–step interactions, but still the step motion can be described from a driving force of the step chemical potential differences [92,117]. The step approach is then applied to a current-induced step bunching [77, 138]. In this case, the step dynamics cannot be described by the step chemical potential alone, but by integrating out the adatom (and advancancy) motions on the terrace, we get the equation of motion of steps expressed by a velocity function of steps in terms of step configurations only.

4.1. Determining the energetic and kinetic parameters

In Section 3.3 we have discussed extensively how the rate of step motion can be predicted quantitatively for given knowledge of a ''step mobility'' and a step chemical potential gradient. A main strength of the step chemical approach is the ability to make an independent, experimental determination of these parameters. Specifically, only measurements of the spatial and temporal correlation functions of steps in equilibrium are required to completely quantify the problem.

Thus the continuum step model is in distinct contrast to the traditional kinetic approaches in which the parameters are determined (a) from extrapolation based on microscopic models, or (b) from modeling the kinetic process of interest. The later technique is useful for confirming one's understanding of a process, but hardly qualifies as a predictive method. The former approach, prediction from microscopic understanding, is the most desirable. However, as discussed in Sections 2.2 and 3.1, significant progress is required before this approach is practical. The equilibrium experimental parameters that are measured for use in the continuum step model will serve as rigorous standards for testing microscopic predictability.

In the following two sub-sections we will outline the experimental techniques needed to obtain the energetic and kinetic parameters from the measurement of equilibrium steps.

4.1.1. Spatial correlations of step-edge positions

To use the coarse-grained step Hamiltonian of Eq. (89), the input parameters, step stiffness, $\tilde{\beta}$ and step–step interaction, $V(w)$ must be known. Information about these parameters can be extracted from the measurement of mean-square step wandering, $G(y) = \langle (x(y) - x(0))^2 \rangle$ [Eq. (62)] which can be obtained directly from static STM [124,139], REM [123], or LEEM [140] images. For specific models, the relationship between step stiffness and step kink energy can also be easily calculated as discussed in Section 2.2. One can also estimate step kink energy from the measurement of the thermal distribution of kink depths.

The step interactions can also be determined from the step-edge correlations, as outlined in Section 3.3.2.1. However, to date, an alternative approach of measuring the distribution of step–step spacings

has been mainly used for experimental analyses. In Sections 4.1.1.1 and 4.1.1.2, we present one example each of an experimental determination of the energetic step parameters. A synopsis of parameters measured in this way is presented in Table 7.

4.1.1.1. Step stiffness and diffusivity. If one has a static image of a thermally-equilibrated step, such as the one shown in Fig. 1, then it is possible to analyze the thermal wandering of the step using the distribution function ($G(y) = \langle [x(y) - x(0)]^2 \rangle$, Eq. (62)). In making such an analysis it is important to insure that the step was static, e.g. that there was no thermal motion of the step on the timescale required to take the image [141–143]. This is unlikely to be a problem in a true microscopic technique such as REM or LEEM where the image is formed optically. In a scanning technique such as SEM or STM, the question of whether the step could have moved while the image was being made must be considered. In addition, when STM is being used to measure step correlations, there is concern about the effect of tip–surface interactions [144,145]. However, if sufficient care is employed in imaging, then the images can be analyzed to determine the free energy parameters governing step behavior.

The first step in analysis is to digitize the position of the step, that is measure its displacement x from some reference line (usually the average step position), as a function of distance parallel to the step y. Given $x(y)$, one approach is to calculate the rms displacement of the step from its average position, and relate it to the step stiffness using

$$\langle \delta_y^2 \rangle = kTL/m\tilde{\beta}, \tag{139}$$

where L is the length of the step that is analyzed, and $m = 6$ or 12 depending on whether the ends of the step are fixed (as for instance at a pinning site) or free [123,146,147]. Alternatively, one can calculate $G(y)$, the differential displacement of the step over a distance y, using Eq. (62). This has the benefit of improving statistics at small separations, which can be measured at many positions along the step edge. As discussed in Section 3.3.2.1, the differential displacement is predicted to vary linearly with the distance parallel to the step for distances much smaller than the collision distance l_c:

$$G(y) = (b^2/a)\cos^3\theta\, y = kTy/\tilde{\beta} \tag{140}$$

with

$$l_c = \tilde{\beta}w^2/4kT, \tag{141}$$

where b^2 is the step diffusivity, $\tilde{\beta}$ is the step stiffness ($\tilde{\beta} = a_y kT/b^2\cos^3\theta$), θ is the angle between the step and a high symmetry direction (see Fig. 6), and w is the average step–step separation [41].

Sudoh et al. [148] have performed such a measurement for a Si(1 1 3) surface equilibrated very near to a step-bunching transition (see Section 4.3.2.2). By quenching from this temperature, they were able to trap a distribution of steps of different heights shown in Fig. 21(a). As might be expected, the single height steps wander the most freely, and steps of greater height wander correspondingly less, as shown in the measured displacements of the steps in Fig. 21(b). The step stiffnesses determined from the slopes in Fig. 21(b) vary nearly linearly with the step height: for single-height steps $\tilde{\beta}_1 = 57\,\text{meV}/\text{Å}$, for double-height steps $\tilde{\beta}_2 = 85\,\text{meV}/\text{Å}$, for triple-height steps, $\tilde{\beta}_3 = 163\,\text{meV}/\text{Å}$, and for quadruple-height steps $\tilde{\beta}_4 = 220\,\text{meV}/\text{Å}$. This result allows an interesting comparison with the prediction of a simple-lattice model for the step free energy, such as Eq. (6). If we make the simplest assumption that the kink energy for an N-tuple height step is N times that of a single-height step, then we expect that the

Table 7
Measured values of step free energies. The formalism described in Section 4.1.1 has been used in the analysis of real-space images of a variety of stepped surfaces to determine the step free energies. Here are listed measured values of the step diffusivity, b^2/a (Eqs. (62), (64) and (140)) and the terrace width distribution (Eq. (146)), and the corresponding derived quantities, the step interaction energy, A [Eq. (147)] and the step interaction free energy coefficient, g (Eq. (11))

System	Equilibrium temperature	b^2/a, Eq. (140)	Terrace width Distri. (σ/w)	Step inter. energy[a] A	Step inter. free energy[b] $g(T)$	Ref.
Si(1 1 1) -7×7 sngl height steps $[2\,\bar{1}\,\bar{1}]$	830°C	1 ± 0.2 Å	0.26 ± 0.01	0.4 ± 0.1	0.036 ± 0.012[c] ($\tan\theta=0.05$)	[27]
Si(1 1 1) -7×7 sngl height steps $[\bar{2}\,1\,1]$	830°C	N/A	N/A	0.4 ± 0.1	0.022	[27]
Si(1 1 1) -1×1	900°C	$2.2-2.9$ Å	0.34 ± 0.02	$0.39-0.43$	$0.04-0.06$	[27,123, 169,323]
Si(1 1 1) Br -1×1	580°C	0.14 ± 0.03 Å	0.26 ± 0.01	0.06 ± 0.01	0.004 ± 0.001 ($\tan\theta=0.05$)	[324]
Si(1 1 1) Al-$\sqrt{3}\times\sqrt{3}$ $R30°$	770°C	2.2 Å	0.24 ± 0.01	1.2 ± 0.2	0.1 ± 0.01	[150]
Si(1 1 1) Ga-$\sqrt{3}\times\sqrt{3}$ $R30°$	550 °C	3.4 Å	0.26	1.1		[147]
Si(1 1 3) $[1\,\bar{1}\,0]$ steps[d]	[875–900°C][e]	8.3[e] Å	0.066 ± 0.006	930 ± 170	360 ± 70	[156]
Si(1 1 3)						
Single steps[f]		2.7 Å				
Double steps[f]	710°C	1.8 Å				[148]
Triple steps[f]		0.9 Å				
Quad. steps[f]		0.7 Å				
Si(1 1 3) $[\bar{3}\,\bar{3}\,2]$ steps	920°C	143 Å ($\theta=0$)				[242]
Si(0 0 1)[h]	850 K 625 K	~ 15 Å S_B step	~ 0.26 $w=250$ Å not Gaussian		[325]	
Ag(1 1 0)	300 K	5 Å	~ 0.4 not Gaussian		0.009[g]	[223,184]
Ag(0 0 1)		[i]		0.054–0.065		[326]
(0–2°) step[i]	300 K	0.07–0.12 Å	0.27 ± 0.002	0.006–0.017		[327]
(10–15°) step[i]		0.6–1.0 Å	0.34 ± 0.001	0.025–0.04		[41]
Pt(1 1 1)[j]	900 K		0.14	~ 2.4	~ 0.4	[315]
Pb(1 1 1)[k]		440 K				
A-steps		2.1 Å				[328]
B-steps		0.8 Å		0.052	0.079	
Cu(1,1,11)[l]	293 K	0.02 Å	~0.24	~0.063	[m]	[151]

Table 7. (*continued*)

System	Equilibrium temperature	b^2/a, Eq. (140)	Terrace width Distri. (σ/w)	Step inter. energy[a] A	Step inter. free energy[b] $g(T)$	Ref.
Cu(1 1 7)[l]	298 K	0.035 Å	0.209	0.0092		
Cu(1,1,13)[l]	295 K	0.032 Å	0.246	0.0043		[329]
	320 K	0.050 Å	0.265	0.0055	[m]	[330]
	348 K	0.071 Å	0.273	0.0074		
Cu(1,1,19)[l]	320 K	0.049 Å	0.267	0.0051		
	370 K	0.080 Å	0.302	0.0059		
Cu(11,7,7)[n]	296 K	0.055 Å	0.252	0.0063		[329]
	306 K	0.059 Å	0.270	0.0058	[m]	[330]
Cu(19,17,17)[n]	333 K	0.083 Å	0.328	0.0040		
	353 K	0.010 Å	0.311	0.0065		
Cu(23,21,21)[n]	328 K	0.077 Å	0.286	0.0063		

[a] A in Eq. (145) with $n = 2$, unit: eV-Å.
[b] g in Eq. (8), unit: eV/Å^2.
[c] The measurement was done with steps misoriented by about 3° from the high-symmetry direction. In the limit of θ goes to zero, the step-interaction free-energy parameter goes to 0.022 ± 0.005 eV/Å^2.
[d] Step edge 90° away from the high-symmetry direction.
[e] Calculated using the quoted [156] values of a-parallel and a-perpendicular for the room-temperature (3×2) phase.
[f] Step edge 35° from the high-symmetry direction.
[g] The step interactions appear on Ag(1 1 0) to be nearly entropic with the possible addition of an oscillatory term. For the purely entropic interactions, the cubic step interaction parameter, $g(T) = (\pi kT)^2/6h^3\tilde{\beta}$.
[h] For Si(0 0 1), the equilibration temperature for the step distribution, 850 K is deduced to be higher than the equilibrium temperature for the kinks, 625 K. The minimum kink depth is twice the 1×1 unit cell width, or 7.68 Å. Measurements were performed for a structure with steps oriented in the high-symmetry [1 1 0] direction for which alternating single-height step have a different structure, S_A or S_B. Alternating terraces have a 90° rotation of the reconstruction. As a result the step interactions are governed by strain-fields induced by the domain-boundaries [331]. The step-distribution function therefore has a highly non-linear dependence on the terrace width. As the miscut angle approaches 2°, step pairing becomes important, further complicating the distributions and interactions. For low step densities, Bartelt and Tromp [332] suggest expanding the logarithmic interaction potential in the form $U(x') = 3(x/l)^2$eV/Å where l is the average step separation and x' is the distance of the step from the midpoint between 2 neighboring steps [331,333].
[i] Step angles are 0–2° for the second line and 10–15° for the third line. Hoogeman and co-workers [326] determined the kink formation energy to be 0.114 ± 0.001 eV using direct measurement of the kink-length distribution. They measured the step interactions for steps at a separation of 2.5 unit cells by measuring correlations of kink motion on adjacent steps. Hoogeman's value of the kink energy was used by Wang et al. [327] for determining the quoted step diffusivities through the TSK equation (see Table 4 for step angle = 0, and ref. [41] for rotated steps.)
[j] The step edge stiffness was not determined in this study. However, if the extrapolation of Giesen and coworkers [163] (see section 4.1.2 and Table 8) is used, a value of $b^2/a = 0.25$ Å is obtained for 900 K, yielding the values for A and g listed in this table.
[k] These values were determined from direct observations of the ECS of supported Pb particles. A good agreement with the expected ECS based on Eq. (14) is found for B-steps, while the agreement for A-steps is not good.
[l] These surfaces are vicinal to the (1 0 0) orientation.
[m] Calculating the value of $g(T)$ from the values given for T, b^2/a and A is left as an exercise for the reader.
[n] These surfaces are vicinal to the (1 1 1) orientation.

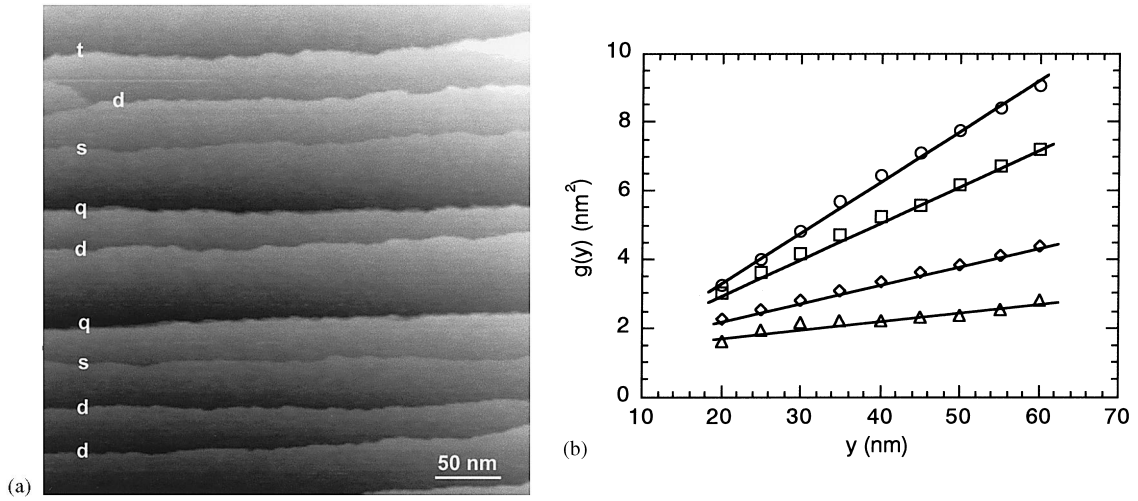

Fig. 21. (a) A 360 nm × 360 nm STM image of the Si(1 1 3) surface quenched after annealing at 710 °C for 10 min. Single-, double-, triple- and quadruple-layer steps are marked as *s*, *d*, *t*, and *q*, respectively. The steps are oriented at an angle of 35° away from the high-symmetry direction. (b) The mean square displacements are plotted versus the separation distance parallel to the average step-edge, *y*, for single- (circles), double- (squares), triple- (diamonds), and quadruple- (triangles) height steps. Each point is an average of data measured for 5–12 steps. The measured slopes are 0.15 ± 0.01, 0.100 ± 0.005, 0.052 ± 0.001 and 0.040 ± 0.005 nm for single-, double-, triple- and quadruple-height steps, respectively (figures from Ref. [148], provided by H. Iwasaki of Osaka University).

step stiffness should depend on step height N in a highly non-linear fashion

$$\tilde{\beta}_N = 2(a_y/a_x^2)kT \sinh^2(N\epsilon/2kT), \tag{142}$$

where ϵ is the kink energy of a single-height step, and a_x and a_y are the depth of a single kink and the smallest possible separation of two kinks, respectively. However, if the binding energy of the N-steps is comparable to the kink energy, then step wandering and step-unbinding will occur in the same temperature range. Sudoh et al. [148,149] model this complication by describing the step interactions with a Hamiltonian

$$H = \sum_{i=1}^{N}\sum_{y=1}^{L} \epsilon|n_i(y)| - \sum_{i=1}^{N-1}\sum_{y=1}^{L} \epsilon_a \delta(x_i(y), x_{i+1}(y)) \tag{143}$$

where $n_i(y)$ is the kink depth, that is the change in step position between position y and $y+1$, and ϵ_a is a binding energy per site of two steps which have the same position (x, y). This Hamiltonian allows the steps within a bunch formed from N steps to fluctuate between bound and unbound configurations along the length of the bunch. As a result, at high temperature the steps within the bunch begin to act independently, yielding a limiting linear behavior on step height

$$\tilde{\beta}_N = N\tilde{\beta}_1. \tag{144}$$

The crossover between the low-temperature limit of Eq. (142) and the high-temperature behavior of Eq. (144) can be quantified by performing a Monte Carlo simulation using the Hamiltonian of Eq. (143).

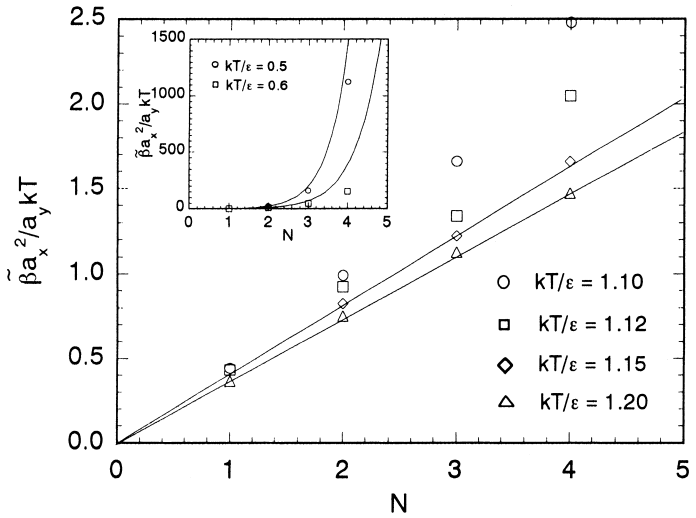

Fig. 22. The variation of step stiffness with step height calculated from Monte Carlo simulations based on the Hamiltonian of Eq. (143) is shown by the symbols for different values of the temperature. (In all calculations the binding energy ϵ_a is set equal to the kink energy ϵ.) In the inset, the solid lines show the low-temperature limit of behavior calculated using Eq. (142), and in the main plot, the solid lines are calculated using Eq. (143) (figures from Ref. [148], provided by H. Iwasaki of Osaka University).

Sudoh et al. plot of the calculated dependence of step stiffness on step height for different values of kT/ϵ is shown in Fig. 22. A linear dependence of step stiffness with step height occurs when the temperature approaches the binding energy, consistent with the original observation that the steps were equilibrated near the bunching transition temperature. This is a nice example of how the simplest sort of atomistic model can be used to provide a physical basis for understanding systems with extremely complex atomic interactions.

4.1.1.2. Step–step interactions. As discussed earlier, even when there is no direct energetic interaction between steps (except the "no-crossing" contact interaction), the distribution of step spacings remains peaked near the average step–step spacing, because this allows the maximum entropy of wandering. Joos et al. [122] have quantified the step distribution function, the probability $P(x)$ of observing a step–step distance x, for the three cases of attractive, zero and repulsive energetic interactions between steps. As shown in Fig. 23, the step distributions for the three cases show characteristic functional shapes which can be used to quantify the three types of interactions. In the case of repulsive energetic interactions of an inverse power law form

$$U = Ax^{-n}, \tag{145}$$

where n is greater than or equal to 2, and x is the distance between a pair of steps measured perpendicular to the average step direction, then the distribution of step-spacings is a Gaussian distribution about the average step spacing w

$$P(x) = \frac{1}{\sqrt{2\pi}\,\sigma}\, e^{-(x-w)^2/2\sigma^2}. \tag{146}$$

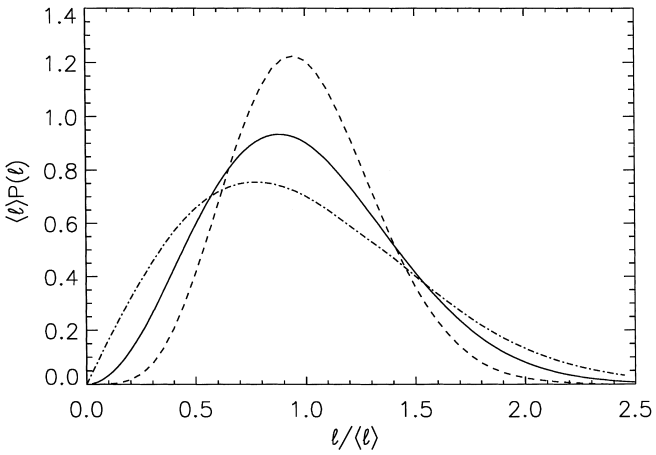

Fig. 23. Distributions of step–step separations calculated using the free-fermion approximation. $P(L)$ is the probability of observing two steps separated by a distance L. $\langle L\rangle$ is the average step spacing. The behavior of freely wandering steps is shown by the solid curve. The distribution for steps with a repulsive energetic interaction in addition to the entropic behavior is shown by the dashed curve. The distribution for steps with an attractive energetic interaction in addition to the entropic interaction is shown by the dash-dot curve (figures from Ref. [1 2 2] provided by T.L. Einstein of University of Maryland).

The width of the distribution σ is related to the step interactions and step diffusivity via

$$\sigma = \left[\frac{kTb^2(T)}{8n(n+1)Aa}\right]^{1/4} w^{(n+2)/4}. \tag{147}$$

Before discussing the application of Eq. (147), it is important to note some limitations in its use. First, it has been assumed in the derivation that steps interact only with their nearest neighbors. An appropriate inclusion of further neighbor effects is accomplished by replacing A in Eq. (147) by $\zeta(4)A$, which is approximately $1.08A$ [150]. Secondly, the approximation of Eq. (147) will fail when the strength of the energetic interactions is small. Specifically, for the case of $n = 2$, A must be much greater than $kTb^2/4a$. Other than these restrictions, on the basis of comparisons with exact results and analytical approximants, Eq. (147) appears to be an excellent approximation [122,153].[16]

The Gaussian shape of step distributions has been observed in a number of cases (see Table 7). A careful analysis of the dependence of the width of the distribution on the average step spacing has been performed by Alfonso et al. [123], who measured the distribution for steps on Si(1 1 1) at an elevated temperature over a range of step spacings between 200 and 1400 Å. The results are most consistent with a value of $n = 2$ in Eq. (145).[17] A value of $n = 2$ is also to be expected on the basis of the expected physical mechanisms for energetic step interactions [154] of which the dominant interaction is most likely to be an elastically-mediated interaction [155].

[16] We can not reconcile the results of Joos, et al. [122] with recent reports by Barbier et al. [151], and Ihele et al. [152], that Eq. (147) overestimates the value of A by nearly a factor of 3. At present, the evidence for Eq. (147) being correct under the assumptions noted in the text, appears compelling.

[17] The data point at the largest step separation in Alfonso's work fits the predicted form for $n = 2$ least well. However, this point may be the result of incomplete equilibration of the step distribution.

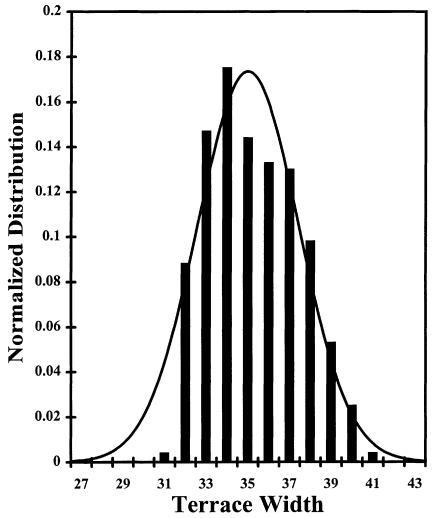

Fig. 24. Terrace width distribution in units of a for the Si(1 1 3) surface with a misorientation of about 0.2° in the [1 $\bar{1}$ 0] direction. The average terrace width, w, corresponds to approximately 35 a where $a = a_y = 11.54$ Å. The best Gaussian fit to the data, shown as a solid line, has a width of $\sigma = 2.3\,a$. The experimentally measured step diffusivity is $0.8\,a^2$ (figure from Ref. [156], provided by H.J.W. Zandlvliet of the University of Twente).

As shown in Table 7, most measured distributions have a typical distribution width to average terrace width ratio (σ/w) of around $1/4 - 1/3$. However, there has been one recent report of an anomalously narrow distribution of step spacings with a terrace width ratio of 0.066 [156], as shown in Fig. 24. This distribution was measured on a Si(1 1 3) surface misoriented in the low-symmetry [1 $\bar{1}$ 0] direction, after it was quenched from above the temperature where step bunching occurs. The ''anomaly'' of the narrow distribution is based on comparison with other measured distributions, such as those in Table 7, as well as on estimates of reasonable interaction strengths based on elasticity theory. Specifically, if step interactions are governed by elastic effects, then the interaction of Eq. (145) will have an exponent of $n = 2$, and an interaction [157,158]

$$A = [2/\pi E_2]\,(s^2h^2 + p_x^2), \tag{148}$$

where h is the step height, s is the surface stress, p_x is the in-plane dipole moment, and E_2 is the 2D analogue of Young's modulus. Since p_x is unknown, it is often just tacitly neglected. For instance, as tabulated and discussed elsewhere [150], there is surprisingly good (factor of two) agreement between the measured strength of the step interactions for single-height steps on clean vicinal Si(1 1 1) surfaces and values of A obtained using Eq. (142) with theoretical estimates of the surface stress, and the value of p_x set to zero. On the other hand Stewart et al. [159] have measured a tangential dipole moment which they estimate to be nearly three times their computed normal dipole moment. The measured step interactions for Al- and Ga-covered surfaces are also larger than that would be predicted based on theoretical values of the surface stress term alone [150], which again might be due to a contribution from the tangential dipole component p_x.

There is no theoretically predicted value for the surface stress for Si(1 1 3). However, if surface stress alone determined the step interactions, then the surface stress of Si(1 1 3) would have to be

Table 8
Selected observations of step fluctuations. The formalism described in Section 4.1.2 has been used in the analysis of time-resolved real-space images of a variety of stepped surfaces to determine the associated kinetic parameters. The stiffness of the steps ($\tilde{\beta}$, Eq. (140)) at the temperature of measurement is listed for each system, because its value is required in interpreting the rate of step fluctuations. Most observations of step fluctuations have been performed using a 1D measurement, as defined in Eq. (149). For these, the time-exponent of the fluctuations is listed for comparison with the predicted behavior of Eqs. (150)−(152). For a small number of systems, the full 2D fluctuations of the steps have been measured, as defined by Eq. (167). For these, the wavelength dependence is also reported for comparison with the predictions of Eqs. (169) and (170). Where analysis of the magnitude of the fluctuations has been performed, the rate parameters, step mobility= Γ_{A}, or terrace diffusion constant are reported, or the corresponding time constants tau (for the relationship between the step mobility and time constant see Eqs. (150) and (151)). In other cases, where the temperature dependence of the relative rate was analyzed, the effective activation energy governing the fluctuations is reported

System [technique]	Temperature	Step stiffness $\tilde{\beta}$	Limiting behavior	Kinetic parameters	Reference
Au(1 1 0)[STM]	350–590 K	Pinned steps[a]	$t^{1/2}$	$E_a = 0.7 \pm 0.1$ eV	[334,142]
Pb(1 1 1)[STM]	300 K		$t^{1/4}$		[142]
Pt(1 1 1)[STM][b]	530 K	0.40 eV/Å		See Eq. (154)	[163]
	540 K*	0.36 eV/Å			
	550 K	0.30 eV/Å	$t^{0.29}$		
	607 K		$t^{0.37}$		
	635 K		$t^{0.25}$		
	800 K		$t^{0.22}$		
	800 K*		$t^{0.24}$		
Ag(1 1 0)[STM][c]	300 K	18 meV/Å, 150 meV/Å	$t^{0.49}$, $\tau_q \sim q^{-2}$	$\tau_a = 350$ ms, $\tau_a = 400$ ms	[335,1]
Ag(1 1 1)[STM]	300 K		$t^{1/4}$	[d]	[336]
Cu(1 0 0)[STM]	293 K	0.64 eV/Å	$t^{1/4}$	$\tau_h = 0.9 - 4.4$ s	[161,151]
Cu(1 0 0)[(e)]	310 K		$t^{0.37}$		[143]
	320 K		$t^{0.41}$		
	340 K		$t^{0.30}$		
	360 K		$t^{0.25}$		
	390 K		$t^{0.26}$		
Cu(1 1 1)[f]	305–500 K		$t^{0.24-0.32}$	[f]	
Si(1 1 1)[REM][g]	950°C	30 meV/Å	$t^{1/2}$, $\tau_q \sim q^{-2}$	$\tau_a = 10^{-6}$ s	[169]
Si(1 1 1)[REM][g]	950°C			$D_s c_{\mathrm{eq}} = 10^{-8}$/s	[146]
Si(0 0 1)[STM][h]	230–350 °C			$E_a = 1.3 \pm 0.3$ eV	[337]
Si(0 0 1)[STM][h]	520–700 K			$E_a = 0.97 \pm 0.12$ eV	[338]
Si(0 0 1)[STM][h]	725 K	∼40 meV/Å(SA) ∼5 meV/Å(SB)	$t^{0.6\pm0.1}$	$\tau_a = \sim 16$ s	[339]
Si(0 0 1)	790°C	12 meV/Å	$t^{1/2}$, $\tau_q \sim q^{-2}$	$\Gamma_A = 2 \times 10^6$ Å^3/s	[340,332]
[LEEM][i,j]	860°C	8.5 meV/Å		$\Gamma_A = 4 \times 10^6$ Å^3/s $\tau_a = 5 \times 10^{-5}$ s	
	920°C	7.0 meV/Å		$\Gamma_A = 8 \times 10^6$ Å^3/s	
	980°C	5.5 meV/Å		$\Gamma_A = 1.8 \times 10^7$ Å^3/s	
	1030°C	3.0 meV/Å		$\Gamma_A = 3 \times 10^7$ Å^3/s	
	1100°C	3.5 meV/Å		$\Gamma_A = 8 \times 10^7$ Å^3/s	

Table 8 (*continued*)

[a] Kuipers and co-workers measured the fluctuations of segments of pinned steps with local forced kink densities of $0 - 0.125$ kinks/site. They conclude that there are no thermally activated kinks in the temperature range of measurement. They attribute the observed $t^{1/2}$ temporal dependence to uncorrelated motion of the intrinsic kinks.

[b] The unitless distances of Ref. [163] were converted to angstroms by assuming $a_x = (\sqrt{3}/2)\, a_y$, $a_y = 2.77$ Å, the interatomic spacing on Pt(111). The two types of high-symmetry step edges were included in the measurements, steps oriented toward the $[\bar{2}11]$ (marked with * in the temperature column), and steps oriented toward the $[2\bar{1}\bar{1}]$ (all the remaining measurements). Both types of step edges gave the same results for the model microscopic parameters deduced from the measurements. The temperature dependence of both the diffusivity and the prefactor of the time correlation function were combined to yield an activation energy for hopping parallel to the step edge of 1.0 ± 0.16 eV, and a kink energy of 0.167 ± 0.005 eV

[c] For Ag(1 1 0), the lower values of step stiffness and τ_a correspond to a step misoriented by 60° away from the close packed $[\bar{1}\,1\,0]$ direction, and the higher values corresponds to a step oriented in the close packed direction.

[d] The authors [336] report the time correlation function to be $G(t) = at^{1/4}$ with $a = 0.7 \pm 0.1(\text{atomic rows})^2$. However, the time scaling constant which must have been used to obtain a prefactor with these units is not apparent in the manuscript. Therefore it is not possible to extract physical information from the quoted number.

[e] Giesen and co-workers [143] estimate the kink energy is 0.13 eV, and the diffusion barrier for an atom moving along a straight segment of the step to be 0.6 eV. They attribute the decrease in the time exponent with increasing temperature to a change from largely uncorrelated kink motion to correlated kink motion.

[f] Giesen and co-workers [341] use a calculated value of the kink energy [342], 0.128 eV to determine the step stiffness as a function of temperature. The measured time correlation functions from 300–500 K then yield

$$F(t)/a^2 = 0.464(1.87 \times 10^{15\pm2}\ \mathrm{s}^{-1})^{1/4}\ \exp[-(\tfrac{3}{4}\epsilon + \tfrac{1}{4}E_a)/kT]t^{1/4},$$

with $E_a = 0.62 \pm 0.06$ eV and $a = 2.21$ Å.

[g] The analyses of Refs. [169,146] for Si(1 1 1) step fluctuations were performed on the same data (from the group of J.J. Métois), with different assumptions about the underlying mass transport mechanisms. In Ref. [169], attachment/detachment limited kinetics were assumed. In Ref. [146], diffusion limited kinetics with direct exchange between steps was assumed. This special case of diffusion-limited kinetics yields wavelength dependence as q^{-2} rather than the q^{-3} obtained form diffusion limited kinetics for an isolated step.

[h] In all three studies of Si(0 0 1), the unit of step fluctuation was determined to be two dimer pairs in the temperature range of measurement.

[i] The stiffness values tabulated are for the SA steps (see Table 3, footnote f). The error bars are approximately $\pm$ 25%. For the SB steps the stiffness values were approximately 10 meV/Å over the measured temperature range, with error bars large enough to accommodate the expected temperature variation.

[j] The measured step mobilities were the same for SA and SB steps. The error bars on the values of the mobilities are approximately $+100\%$, -50%. To determine the attachment/detachment time constant from the measured mobilities, the diffusing species was assumed to be a Si dimer. The temperature variation of the step mobility corresponds to an activation energy of 1.45 ± 0.15 eV.

approximately 40–50 times larger than the stress of Si(1 1 1) to account for the observed step distributions. The novel atomistic feature of Si(1 1 3) is the prevalence of rebonded atoms, with attendant puckering of the surface and many angles far from their ideal tetrahedral values [160]. As a result it might not be considered too surprising to find a dramatic increase in surface stress on Si(1 1 3). On the other hand, the measured step distributions are a result of equilibration at temperatures above the disordering temperature of the surface reconstructions of Si(1 1 3), where the rebonding configurations of the reconstructions should be substantially less important. This case illustrates the difficulties of establishing an understanding of a key thermodynamic parameter – the step interaction free energy – based on atomistic understanding of the surface.

4.1.2. Temporal step fluctuations and the kinetic parameters

The temporal fluctuations of steps that are in equilibrium can be measured and analyzed to provide the kinetic parameters that govern step motion under both equilibrium and non-equilibrium conditions. A synopsis of experimental results is provided in Table 8. The most straightforward approach to such measurements is to consider the time dependence of a single fixed position on a step edge

$$G(t) = \langle [x(y,t) - x(y,0)]^2 \rangle. \tag{149}$$

This measurement can be made for instance in STM by scanning repeatedly across one point on the step-edge (again being careful to assure that the tip itself does not perturb the step position). Once the time dependence of the step position is obtained, the correlation function can be calculated and analyzed to determine its time dependence, which in simple cases should go as $t^{1/n}$ with $n = 4$ in the limiting case of step-edge diffusion, $n = 3$ for terrace diffusion and $n = 2$ for attachment/detachment limited kinetics [93,146]. For step-edge limited kinetics, the overall expression for the time correlation function is [161,162]

$$G(t) = 0.78\,[(kT)^3 \Gamma_h t/\tilde{\beta}^3]^{1/4}, \tag{150}$$

where Γ_h is the step mobility due to step-edge wandering. If the step diffuses by atoms hopping one lattice constant at a time and if the mean time between successive hops in the same direction along the step edge is τ_h, then $\Gamma_h = a_y^3 a_x^2/\tau_h$. For attachment/detachment limited kinetics, the full expression is [1,93,170]

$$G(t) = [4kT\Gamma_{\mathrm{a}} t/\pi\tilde{\beta}]^{1/2}, \tag{151}$$

where the step mobility $\Gamma_{\mathrm{a}} = a_x^2 a_y/\tau_{\mathrm{a}}$, and τ_{a} is the mean time between successive attachment/detachment events at a single element of the step-edge. The full expression for diffusion-limited kinetics is

$$G(t) = 0.86\,(\Omega kT/\tilde{\beta})^{2/3}\,(2D_{\mathrm{s}} c_{\mathrm{eq}} t)^{1/3}, \tag{152}$$

where Ω is the atomic area of the diffusing specie (usually assumed to be $\Omega = a_x a_y$ for a diffusing atom), D_{s} is its diffusion coefficient on the smooth surface, and c_{eq} is the equilibrium concentration of the diffusing specie on the terraces. From Eqs. (150)−(152), it is easy to see that analysis of the 1D time correlation functions to determine the kinetic parameters governing surface mass transport requires an independent knowledge of the step stiffness. A full 2D analysis, as described in Section 4.1.2.2, makes an independent measurement of the stiffness unnecessary. Cross-over between the different limiting cases represented by Eqs. (150)−(152) occurs smoothly over a narrow range of parameter space [153] (which will usually occur physically as a function of temperature).

The real-space time-correlation function of Eq. (149) has been used in a number of STM experiments to analyze step fluctuations as shown in Table 8. The use of this approach to study the step fluctuations on Pt(1 1 1) over a 250 K range of temperature has yielded results readily interpretable in terms of lattice models of the underlying atomic processes [163]. The time correlation functions measured in this experiment are shown in Fig. 25. The amplitude of the fluctuations varies by over an order of magnitude over a temperature range from 550 to 800 K. The time variation of the correlation function appears most consistent with an exponent of 1/4 which corresponds to fluctuations via step-edge diffusion as in Eq. (150).

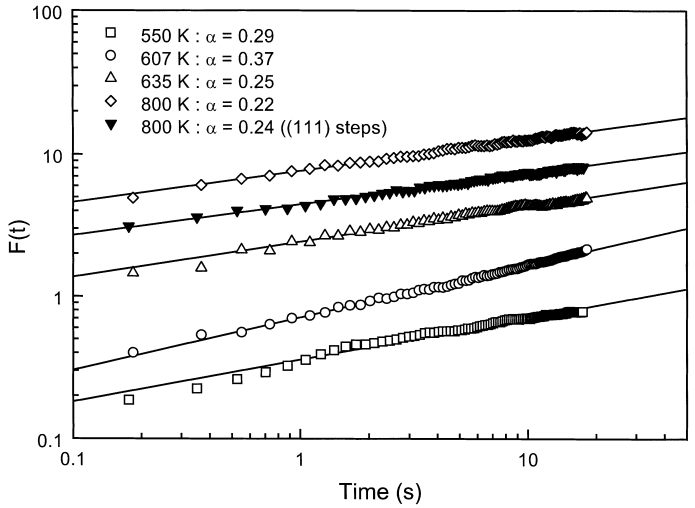

Fig. 25. Thermal fluctuations of steps oriented toward the $[\bar{2}\,1\,1]$ (called (1 1 1) steps) and toward the $[2\,\bar{1}\,\bar{1}]$ (called (1 0 0) steps) were measured using STM on Pt(1 1 1). The time correlation function (here labeled $F(t)$ rather than $G(t)$ as in Eq. (149)) is plotted in dimensionless units of a_x^2 (where $a_x(\mathrm{Pt}(1\,1\,1)) = 2.4\,\text{Å}$) as a function of time. The wide range of temperature of the measurement has allowed tests of lattice models and extraction of the corresponding energetic parameters (figure from Ref. [163], provided by M. Giesen of the Forschungs-Zentrums Jülich).

The measurements were compared with predictions of simple lattice models, using the low-temperature limit for the TSK prediction for the step stiffness (see Table 4)

$$b^2/a \sim 2a\exp(-\epsilon/kT), \tag{153}$$

which was determined from step images measured from 530 to 550 K. The results yield a kink energy of 0.167 ± 0.005 eV, which appears to be the same for both orientations of step. The temperature variation of the measured correlation functions was evaluated yielding the result

$$G(t) = 9.4 \times 10^3 \pm 0.32a^2 s^{-1/4} \exp[(-0.50 \pm 0.04\,\text{eV})/kT]t^{1/4}, \tag{154}$$

which appears to be valid for both types of steps. Using Eq. (150), the measured value of the kink energy ϵ, and a lattice model for the step mobility Γ_h [164], the results indicate an activation energy for diffusion along the step-edge of E_s less than or equal to 1.0 ± 0.16 eV. The inequality arises from lack of information about the relative energy barriers for hopping over kink sites versus hopping over straight step segments. This value of the activation energy is substantially higher than the value calculated using effective medium theory [165], and also higher than the value determined from FIM measurements made at much lower temperature [166]. However, the difference between the two experimental measurements can be rationalized as due to the expected strong temperature dependence of the pre-exponential factor [163].

4.1.2.1. Fourier analysis of step fluctuations. In Section 3.3.4, we considered the equation of step motion in three limiting cases of mass transport, evaporation–condensation (EC), step-edge diffusion

(SED) and terrace diffusion (TD) cases. For an isolated step, assuming up and down terrace symmetry, the velocity of the step, when all three mechanisms are active, can be written as

$$\frac{\partial x(y)}{\partial t} = \frac{\Gamma_{\mathrm{A}}}{\Omega kT}\ [\mu(y) - \mu^{\mathrm{t}}(y)] + \frac{\Gamma_h}{\Omega kT}\frac{\partial^2 \mu(y)}{\partial y^2}, \tag{155}$$

where the step chemical potential, $\mu(y)$, is given by $\tilde{\beta}\,\partial_y^2 x$ and the local *terrace* chemical potential at the boundary, $\mu^{\mathrm{t}}(y)$, which depends on the kinetic coefficients, D_{s} and Γ, is yet to be expressed in terms of $\{\mu(y)\}$. If surface diffusion is much faster than attachment/detachment at the step, the terrace chemical potential will be uniform, and can be defined as zero. In this case, $\partial_{\mathrm{t}} x(y)$ is determined solely by the local step configuration around y. More generally, due to a finite terrace diffusion rate, the terrace chemical potential $\mu^{\mathrm{t}}(y)$ depends on the step configurations of finite range and $\partial_{\mathrm{t}} x(y)$ becomes a non-local function of $\mu(y)$:

$$\frac{\partial x(y)}{\partial t} = \int_0^{L_y} \mathrm{d}y'\ D(y;y')\ [\mu(y) - \mu(y')]. \tag{156}$$

However, the adatom exchange coefficient matrix, D in Eq. (156) can be diagonalized by Fourier transforming [46], yielding

$$\frac{\partial x_q}{\partial t} = -\frac{\Gamma_q}{\Omega kT}\ \mu_q, \tag{157}$$

where $x_q = (1/\sqrt{L_y}) \int \mathrm{d}y x(y)\, \mathrm{e}^{-\mathrm{i}qy}$, $\mu_q = (1/\sqrt{L_y}) \int \mathrm{d}y \mu(y)\, \mathrm{e}^{-\mathrm{i}qy}$ and the qth component of step mobility, Γ_q, is given by [131,167]

$$\Gamma_q = \Gamma_{\mathrm{A}}\left[D_{\mathrm{s}} c_{\mathrm{eq}} \Omega^2 |q| + \Gamma_h q^2\right] / \left[\Gamma_{\mathrm{A}} + D_{\mathrm{s}} c_{\mathrm{eq}} \Omega^2 |q| + \Gamma_h q^2\right], \tag{158}$$

where D_{s} is the surface diffusion constant and c_{eq} is the equilibrium concentration on the terrace far from the step. Since $\mu_q = -\Omega\tilde{\beta} q^2 x_q$ for an isolated step (Eq. (106)), Eq. (157) can be written as

$$\frac{\partial x_q}{\partial t} = -\frac{1}{\tau_q} x_q \tag{159}$$

with the relaxation time

$$\tau_q = \frac{kT}{\tilde{\beta} q^2 \Gamma_q}. \tag{160}$$

For the detachment/attachment (D/A) case, $\Gamma_{\mathrm{A}} \ll [D_{\mathrm{s}} c_{\mathrm{eq}} \Omega^2 |q| + \Gamma_h q^2]$ and Γ_q of Eq. (158) becomes Γ_{A}. Therefore, we have $\tau_q = (kT/\Gamma_{\mathrm{A}}\tilde{\beta})\, q^{-2}$ for the D/A case. For both step-edge diffusion (SED) and surface diffusion (SD) cases, $\Gamma_{\mathrm{A}} \gg [D_{\mathrm{s}} c_{\mathrm{eq}} \Omega^2 |q| + \Gamma_h q^2]$ and Γ_q becomes $D_{\mathrm{s}} c_{\mathrm{eq}} \Omega^2 |q| + \Gamma_h q^2$. For the SD case, $\Gamma_q = D_{\mathrm{s}} c_{\mathrm{eq}} \Omega^2 |q|$ since $D_{\mathrm{s}} c_{\mathrm{eq}} \Omega^2 |q| \gg \Gamma_h q^2$ and we have $\tau_q = (kT/\Omega^2 D_{\mathrm{s}} c_{\mathrm{eq}} \tilde{\beta})\, |q|^{-3}$. For the SED case where $\Gamma_h q^2 \gg D_{\mathrm{s}} c_{\mathrm{eq}} \Omega^2 |q|$, we have $\tau_q = (kT/\Gamma_h \tilde{\beta})\, |q|^{-4}$ since $\Gamma_q = \Gamma_h q^2$. Thus for the three limiting cases of mass transport, D/A, SD and SED, the relaxation time τ_q can be written as $\tau_q \propto |q|^{-n}$ with $n = 2$, 3 and 4, respectively.

We now wish to relate the step mobilities to the experimentally observable thermal fluctuations of the step positions. When thermal fluctuations of step motion are considered, Eq. (159) becomes

$$\frac{\partial x_q(t)}{\partial t} = -\frac{1}{\tau_q} x_q(t) + \zeta_q(t), \tag{161}$$

with the thermal noise ζ_q satisfying

$$\langle \zeta_q(t) \rangle = 0, \qquad \langle \zeta_q(t) \zeta_{q'}(t') \rangle = f_q^2 \, \delta_{q',-q} \, \delta(t - t'), \tag{162}$$

where the amplitude of the thermal noise, f_q is yet to be determined. Since the linear kinetic coefficient and the strength of the noise are related by the fluctuation–dissipation theorem, they can be obtained from the measurement of temporal correlations of step-edge fluctuations. From Eqs. (161) and (162), it is straightforward [106] to show that

$$C_q(t) = \langle x_q(t) x_{-q}(0) \rangle = \tfrac{1}{2} f_q^2 \, \tau_q \, e^{-t/\tau_q} \tag{163}$$

and comparing with the equal time correlation function of Eq. (61), we have

$$f_q^2 = 2kT/(\tilde{\beta} q^2 \tau_q) = 2\Gamma_q \tag{164}$$

as in the fluctuation–dissipation theorem. Now, from Eqs. (160) and (163) we have

$$C_q(t) = \Gamma_q \, \tau_q \, \mathrm{e}^{-t/\tau_q} = \frac{kT}{\tilde{\beta} q^2} \, \mathrm{e}^{-t/\tau_q}. \tag{165}$$

By directly comparing with experimental measurement of C_q with Eq. (165), we get the relaxation time τ_q. The step mobility Γ_q is then obtained from Eq. (160) and the kinetic coefficients, Γ_A, Γ_h, and D_s are obtained in turn through Eq. (158).

Note that the relaxation time τ_q in Eq. (160) was derived using Eq. (106) which is correct only for an isolated step. When we consider the step–step interaction, the μ_q is not so simple as in Eq. (106) but it can be still written as $\mu_q = \epsilon_q x_q$, where ϵ_q now depends on both step stiffness $\tilde{\beta}$ and the step–step interaction parameter g [168]. In this general case, Eq. (165) becomes $C_q(t) = kT/2\epsilon_q \, \mathrm{e}^{-t/\tau_q}$ with $\tau_q = kT/\epsilon_q \Gamma_q$.

4.1.2.2. Application to experiment. We can use the approach described in the previous section to do a more complete analysis given a full 2D image of the fluctuating step. Such images can be obtained using true imaging techniques such as LEEM or REM. Alternatively, with care, they can be obtained using STM, SEM or SREM as long as the rate of step fluctuation is much slower than the time required to form the scanned image. In analyzing the data, we begin with the position of the step edges $x(y,t)$ and determine the different wavelength components of the fluctuations using a Fourier transform to find x_q, via [169]:

$$x(y,t) = \frac{1}{\sqrt{L}} \sum_q x_q(t) \mathrm{e}^{\mathrm{i}qy}. \tag{166}$$

The correlation function for each wavelength is then determined from the data using

$$G_q(t) = \langle |x_q(t) - x_q(0)|^2 \rangle. \tag{167}$$

A general expression for the time correlation function is found using Eq. (165) with Eqs. (158) and (160)

$$G_q(t) = 2\langle |x_q|^2 \rangle - 2\langle x_q(t)x_{-q}(0) \rangle = 2C_q(0)\,(1 - \mathrm{e}^{-t/\tau_q}) = \frac{2kT}{\tilde{\beta}q^2}\,(1 - \mathrm{e}^{-t/\tau_q}), \tag{168}$$

where

$$\tau_q = 2kT/\tilde{\beta}q^2 f(q) \tag{169}$$

with $f(q) = 2\Gamma_q$. For the three limiting cases of mass transport, the function $f(q)$ has the following values [167]:

$$f(q) = \begin{cases} 2\Gamma_{\mathrm{a}}, & \text{for attachment/detachment} \\ 2D_{\mathrm{s}}c_{\mathrm{eq}}\Omega^2|q|, & \text{for terrace diffusion} \\ 2\Gamma_h q^2, & \text{for step-edge diffusion,} \end{cases} \tag{170}$$

where the definitions of the parameters are the same as for Eqs. (150)–(152). As would be expected, here we see that larger wavelength fluctuations have larger amplitude and longer time constants and stiffer steps fluctuate with smaller amplitude and smaller time constants. The overall timescale of the fluctuations is set by the fundamental time constant τ_q, which is different for each of the three fluctuation mechanisms as shown by Eqs. (169) and (170). In addition, each of the three mechanisms gives a different wavelength dependence for the timescale. For the step-edge diffusion mechanism, the time constant increases as the fourth power of the wavelength, consistent with our expectation that long wavelength fluctuations should be difficult when they can only occur via 1D transport along the step edge. For the terrace-diffusion mechanism, the wavelength dependence is intermediate, scaling as the third power. For the attachment–detachment mechanism, the time constant falls off least strongly with wavelength, consistent with the expectation that long wavelength fluctuations are most easily supported when they involve events occurring independently at different location along the step-edge.

Analysis of the thermal fluctuations of steps on Ag(1 1 0), shown in Fig. 1, was performed using both this approach and the 1D approach of Section 4.1.2 [1]. These data were measured for steps well-separated from their neighbors, e.g., for step–step distances greater than 3000 Å. The step positions in the images were identified using a derivative approach and digitized to obtain $x(y,t)$. Then the wavelength dependent components of the step displacement $x_q(t)$ were determined using a Fourier transform, and the Fourier components of the correlation function were calculated using Eq. (166). The resulting curves for wavelengths from approximately 400 to 3000 Å, shown in Fig. 26(a), are shown as open circles, with the fits to Eq. (168) shown as solid curves. From these data the value of the step stiffness is determined to be $\tilde{\beta} = 19\,\mathrm{meV/Å}$. Using this value in Eq. (141) for the collision length, with the step separation $w > 3000$ Å, we obtain a collision length of greater than 100 microns. Thus the analysis of the step fluctuations using Eq. (168) is well within the condition ($q > 2\pi/l_{\mathrm{c}}$) assumed in neglecting step–step interactions in deriving these equations.

The fits to the curves in Fig. 26(a) yield also the values of the Fourier components of the time constant τ_q, as shown in Fig. 26(b). A fit of these data to Eq. (166) with the exponent governing the q-variation as a variable, in principle, will allow the limiting cases of step mobility mechanisms (as listed in Eq. (170)) to be distinguished. As shown in Fig. 26(b) by the solid lines, these data are clearly fit better by a q^2 variation (suggesting attachment–detachment limited kinetics) than by a q^4 variation (which would correspond to step-edge diffusion limited kinetics). It is also clear from these data that

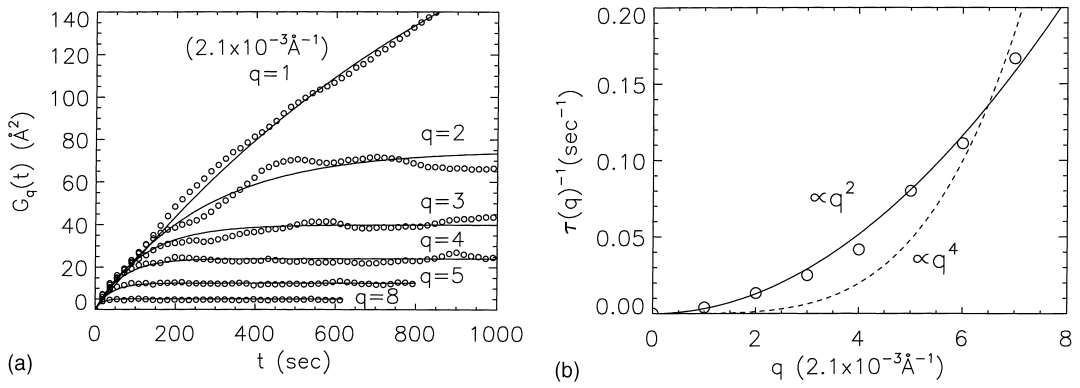

Fig. 26. Analysis of the thermal fluctuations of steps on Ag(1 1 0) at room temperature (see Fig. 1). (a) The autocorrelation functions $G_q(t)$ for different Fourier components of the step displacement are shown as open circles for the measured values. Fits to Eq. (168) are shown as solid curves. The fits allow the value of $\tilde{\beta} = 18\,\mathrm{meV/\AA}$ to be determined along with the wavelength-dependent time constants τ_q for the fluctuations. (b) The inverse of the characteristic wavelength-dependent time constant τ_q determined from the fits in (a) is shown as a function of q. Fits to the expected variation for attachment/detachment limited kinetics ($\tau_q \sim q^{-2}$) and step-edge diffusion limited kinetics ($\tau_q \sim q^{-4}$) are shown as solid curves (figure from Ref. [1], provided by J. Reutt-Robey of University of Maryland).

the acceptable values of the exponent will extend upward from 2 so that a value of 3 (as expected for diffusion-limited kinetics), or some crossover value as would occur from competing mechanisms [170] cannot be ruled out. If one makes the simplest assumption of pure attachment/detachment limited kinetics, then the step mobility and related time constants for that mechanism can be extracted from the fit to the data of Fig. 26(b). The value of the step mobility determined in this way is $\Gamma_a = 1.6\times 10^2 a^3/s$. If one relates this to a time constant for atomic hopping on and off of a step, and assumes that the diffusing species has an atomic volume characteristic of a single Ag atom ($a^3 \sim 64\,\mathrm{\AA}^3$), the value of τ_a is 350 ms. This long time constant is consistent with the slow fluctuations shown in Fig. 1.

This measurement and analysis was performed for steps oriented along a low-symmetry crystallographic direction (30° away from the [1 $\bar{1}$ 0] direction). A repeated measurement for steps in the high-symmetry direction yielded a substantially larger step stiffness, $\tilde{\beta} = 150\,\mathrm{meV/\AA}$, and thus much smaller amplitude step fluctuations. However the time dependence of the fluctuations gave a comparable step mobility, corresponding to an attachment/detachment rate of approximately 400 ms. This result indicates that the high intrinsic kink density on the low-symmetry step does not affect the attachment/detachment rate appreciably. This may mean that attachment/detachment mechanism is not strongly dependent on the presence of kinks. Alternatively, it may suggest that there is sufficient thermal activation of kinks on the low-symmetry step to saturate the exchange.

4.2. *Relaxation of metastable structures*

In the previous section, we discussed how one can get the information on energetics and kinetics of steps needed for the continuum step model from the measurement of equilibrium step fluctuations. In this section, the use of the continuum step model to quantify the experimentally measured decay of metastable morphology is presented.

4.2.1. Decay of a step bunch

Here, we review the relaxation dynamics of quasi-1D step profiles using the models for continuum step dynamics described in Section 3.3.4.2. To avoid the difficulty associated with the step and anti-step annihilation events in step approach discussed in Section 3.1.2, we consider systems with steps in the same direction. The initial non-uniform step configurations thus relax toward the equilibrium uniform state without changing the total number of steps. Although this is one of the simplest systems for a step dynamics study, for a general initial non-uniform step configuration, it is impossible to solve the equations of step motion (in Section 3.3.4.2) analytically and obtain the step profile $x_n(t)$. However, for some special initial non-uniform configurations, the relaxation dynamics toward the uniform profile can be studied analytically [171]. For most studies of the analytical behavior of the relaxation step profile, a common way to attack the problem has been constructing a continuum equation from step equations by considering limiting cases in which the step indexes can be considered as continuous variables [49,51,128,136,171,172]. When we replace differences involving the step indices by derivatives, the equation of step motion becomes a partial differential equation (PDE) (see Eq. (177) for example). In many cases [136,171,172], the solutions have a scaling form, $xt^{-\beta}$, as in the Mullins continuum equations above T_R (see Section 2.3.1), where the time scaling exponent β is related to the mass transport modes. Recently, Fu et al. [125, 136] measured thermal decay of metastable step bunches on Si(1 1 1) and showed that the mass transport occurs via local mass movement by applying this scaling ansatz. First, we review their experiment of the decay of isolated step bunches and then discuss modeling it in terms of a bunch of N steps bounded by two infinite flat terraces.

4.2.1.1. Relaxation of step bunches on Si(1 1 1). Fu and co-workers [125,136] investigated the thermal relaxation of non-uniform surfaces consisting of bunches of closely spaced steps separated by terraces much wider than the equilibrium step separation. The step bunches are produced using direct heating current to create a kinetic instability (Section 2.3.4). The dramatic changes in surface morphology produced by the use of direct current heating on the Si(1 1 1) surface have been well known [173] and will be discussed in detail in Section 4.4. Here we briefly review Fu et al.'s experiment on the decay of the resulting metastable structures. Three different initial step-bunched surfaces were prepared by applying direct current, in the direction known to cause instability, for different amounts of time. This allowed fabrication of bunches of controlled size, ranging from ~50 to 28 Å in height. During the relaxation of these starting surfaces, indirect heating at a temperature of 930°C was used to avoid the effects of a direct current on the decay of the surface structures. Fig. 27(a) shows a 3D STM image of one of the initial step-bunched surfaces. Fig. 27(b) and (c) show the surface after relaxation for 30 and 120 min at 930°C. For each heating preparation, the maximum slope of the bunches was measured for 11–22 bunches on the surfaces. The slopes were then averaged and plotted as a function of time for comparison with the quasi-1D theory of step bunch decay described below.

4.2.1.2. Isolated step bunch and shape-preserving ansatz. As shown in Fig. 27, the steps remain relatively straight through out the experiment and hence the quasi-1D models discussed in Section 3.3.4.2 can be applied to analyze the experiment. In the absence of any driving force (such as reconstruction, adsorption or internal attraction between steps), the physics is dominated by the effects of step repulsions. Since no steps are created or destroyed in the process, the step creation energy is irrelevant here and the effective step–step interaction $V(w)$ in Eq. (113) is given by $V(w) = g/w^2$. The chemical potential of the nth step in a quasi-1D array of straight steps is then given

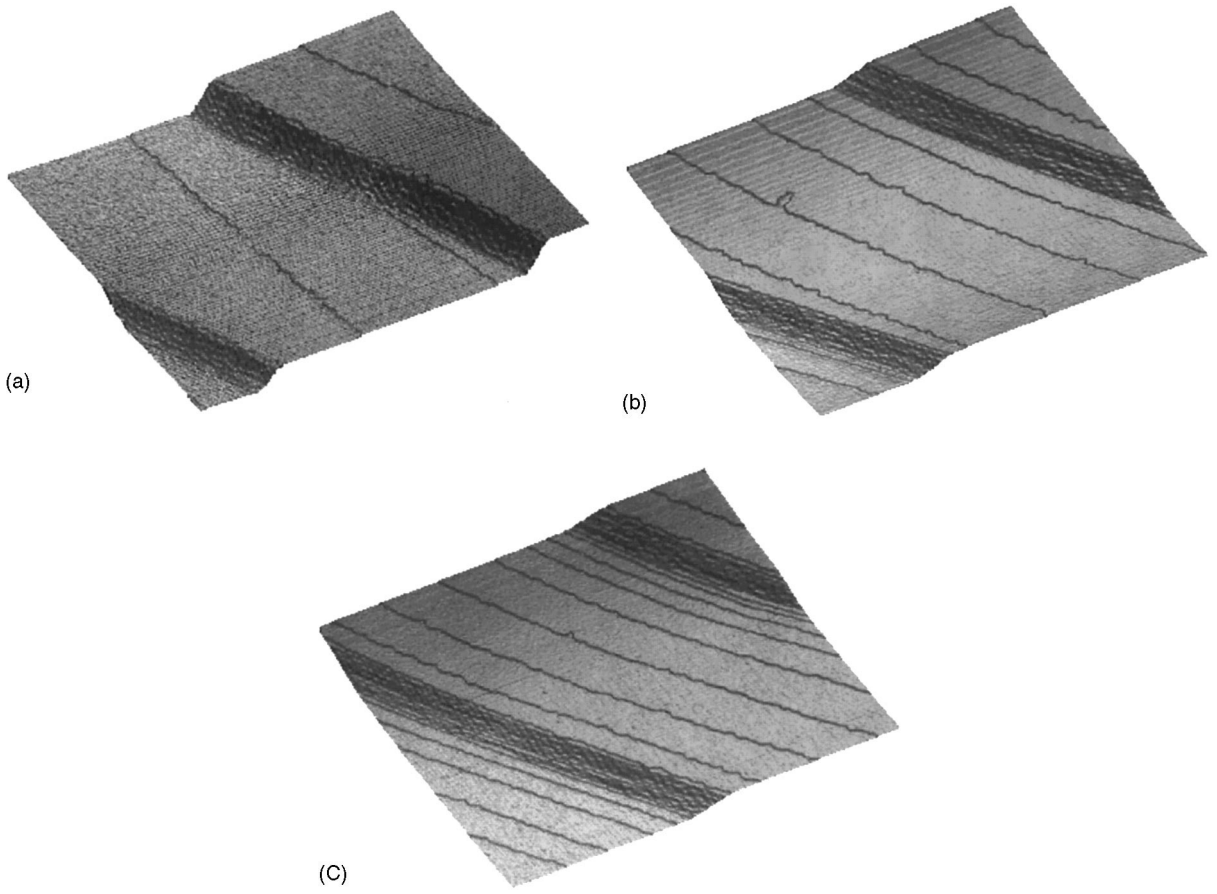

Fig. 27. (a) 50 000 Å × 50 000 Å STM images of an initial surface with a bunch size of 16 steps, a bunch–bunch separation of 22 300 Å, and an initial step-step separation with the bunches of 124 Å (prepared by heating with DC in the step down direction at 1260 °C for 2 min). This was followed by relaxations under direct heating for (b) 30 and (c) 120 min (figures are from Ref. [125]).

by $\mu_n = 2g\Omega\,(w_{n-1}^{-3} - w_n^{-3})$ from Eq. (113). Therefore, the equations of step motion considered in Section 3.3.4.2 in the three limiting cases (Eqs. (121), (124) and (125)) become difference equations of the terrace widths, w_n:

$$\frac{\partial x_n}{\partial t} = \frac{2g\Gamma_A}{kT}\left[\frac{1}{w_{n-1}^3} - \frac{1}{w_n^3}\right] \tag{171}$$

for the global movement case,

$$\frac{\partial x_n}{\partial t} = \frac{2g\Gamma_+\Gamma_-}{kT(\Gamma_+ + \Gamma_-)}\left[\frac{-1}{w_{n-2}^3} + \frac{3}{w_{n-1}^3} - \frac{3}{w_n^3} + \frac{1}{w_{n+1}^3}\right] \tag{172}$$

for the attachment/detachment limited case with local movement, and

$$\frac{\partial x_n}{\partial t} = \frac{2gD_s c_{eq}\Omega^2}{kT}\left[\frac{2w_{n-1}^{-3} - w_{n-2}^{-3} - w_n^{-3}}{w_{n-1}} + \frac{2w_n^{-3} - w_{n-1}^{-3} - w_{n+1}^{-3}}{w_n}\right] \tag{173}$$

for the surface diffusion limiting case. The decay of the step bunches was modeled by considering the motion of an isolated step bunch consisting of N steps bounded by infinite flat terraces. In the attachment/detachment limited case, the adatom chemical potential on the two flat terraces is assumed to be equal to the equilibrium value. As in the Ozdemir and Zangwill [51] study, a ''shape-preserving'' ansatz

$$w_n = A_n \tau^{\beta} \tag{174}$$

with $\tau = t + t_0$, is used to solve the equations of motion, Eqs. (171)–(173). Eq. (174) is called the ''shape-preserving'' ansatz because after the surface has acquired this shape-preserving profile, the profile of the system at any later time can be obtained by multiplying each terrace width by a constant. The existence of this shape-preserving form can be easily seen by substituting it into

$$\frac{\partial w_n}{\partial t} = \frac{\partial x_{n+1}}{\partial t} - \frac{\partial x_n}{\partial t}, \tag{175}$$

where $\partial_t x_n$ is given by Eqs. (171)–(173). For example, for the attachment/detachment limited case with local mass transport, such substituting gives rise to

$$\beta\tau^{\beta-1}A_n = B\tau^{-3\beta}\left[\frac{1}{A_{n-2}^3} - \frac{4}{A_{n-1}^3} + \frac{6}{A_n^3} - \frac{4}{A_{n+1}^3} + \frac{1}{A_{n+2}^3}\right], \tag{176}$$

where $B = 2g\Gamma_+\Gamma_-/kT(\Gamma_+ + \Gamma_-)$ is a constant. Since this equation should hold for any time, we have $\beta = 1/4$. Similarly, we can show that $\beta = 1/4$ for the attachment/detachment limited case with non-local mass transport and $\beta = 1/5$ in the diffusion-limited case [51]. Also, Eq. (176) and its analogs for the other limiting cases give sets of non-linear equations for A_n which can be solved numerically. When the numerical solution A_n is rescaled by the number of steps in the bunch N, and plotted against the rescaled step index n/N, the rescaled amplitude NA_n for systems with different step bunch sizes collapses to a single curve [136] for large N. This can be understood by considering the continuum limit of the problem. For the attachment/detachment limited case, this yields an expression for the slope z_x at the center of the bunch

$$z_x(0,t) = \frac{\partial}{\partial x}\left[\lambda Z_0(x/t^{1/4})\right] = \frac{hZ_0'(0)}{2Z_0(\infty)}Nt^{-1/4} \sim \left[\frac{t}{N^4}\right]^{-1/4}. \tag{177}$$

This result is consistent with the numerical size scaling law, A_nN =const., for the discrete step models. The terrace width at the center of the bunch, $A_{N/2} \sim 1/N$ and the slope at the center scales proportional to N. Therefore, for the attachment/detachment limited case with local mass transport, both the continuum model and the step model predict that the slope at the center of the step bunch scales as

$$s_0(t) \sim \frac{1}{w_{N/2}(t)} \sim \left(\frac{t}{N^4}\right)^{-1/4}. \tag{178}$$

By similar approaches, it can be shown that the decay of the slope at the center of an isolated step bunch obeys the scaling law

$$s_0(N,t) \approx m(t/N^{\alpha})^{-\beta}, \tag{179}$$

for all three cases of step motion, aside from a short initial transient, where m is a constant independent of the bunch size. For the attachment/detachment rate limited mechanism with local mass transport, $\beta = 1/4$ and $\alpha = 4$, as shown above. For the local mass movement in the diffusion limited case, we have $\alpha = 4$ and $\beta = 1/5$, while for global movement, we have $\alpha = 2$ and $\beta = 1/4$. This scaling law is exact for the continuum model (or the step models in the large bunch size limit). It is an approximation for the step models with finite bunch sizes, but the approximation fits the numerical solutions of motions well even for the small step bunch sizes under consideration.

To test the scaling prediction of Eq. (179) with the experiment and to obtain the best value of α, Fu et al. [125,136] performed a three-parameter fit for the data sets involving decay of bunches of three different sizes. They found that the experimental data indeed scale with the number of steps in the bunches and obtained the best value of $\alpha = 4.3$, with a conservative error bar on α of ± 0.5 ($\alpha = 4.3 \pm 0.5$). The measured value of α is consistent with a local mass transport model of step motion, for which α is predicted to be 4. They further made quantitative comparisons between the theoretical mechanisms and the experimental results using the energetic and kinetic parameters from other independent experiments. They used the step–step interaction coefficient from direct observation of the equilibrium distribution of terrace width [121] and reflection electron microscope measurement of a stress-mediated interaction [121,123]. For the adatom attachment coefficient κ and the diffusion coefficient D_s, they used the values from the kinetic parameters determined by direct observations of the equilibrium fluctuations of the steps ($\Gamma = 5 \times 10^7$ Å^3/s, $D_s c_0 \approx 10^8$/s) [169]. These parameters were used in numerical solutions of Eqs. (172) and (173) to make predictions on the characteristics of the decay of the slope. The numerical calculations were done for starting surfaces with bunch sizes matching those of the experimental system, N = 16, 12 and 9. Fig. 28 shows the resulting calculated relaxation curves. The results show quantitative agreement between the measured rates and the predicted rates, well within the experimental uncertainties. The time scaling observed ($\beta = 0.2-0.3$) is consistent with either a diffusion limited case ($\beta = 0.2$) or the attachment/detachment case ($\beta = 0.25$).

4.2.2. Decay of structures with curvature effects

In the example of the previous section, the physical decay could be well described by treating the steps as moving quasi one-dimensionally (e.g., as described in Section 3.3.4.2). However for more complex structures, where the curvature of the steps is an important component of step motion, a treatment including both step interaction and the step stiffness terms of Eq. (90) becomes necessary.

4.2.2.1. Island decay. The application of the continuum step model for structures with step curvature is most simply illustrated for the case of single-layer high island (or a single-layer deep pit). If the structure is not in equilibrium with its Gibbs–Thomson concentration of surface adatoms [Eq. (47)], it will decay (or grow) via a continuous change in its radius [174]. For the simplest case of a circular structure, the problem can be addressed in a 1D form using Eqs. (92)−(94) and (147) with the linear position x replaced by the radius. Using the attachment/detachment rate-limited case as the simplest

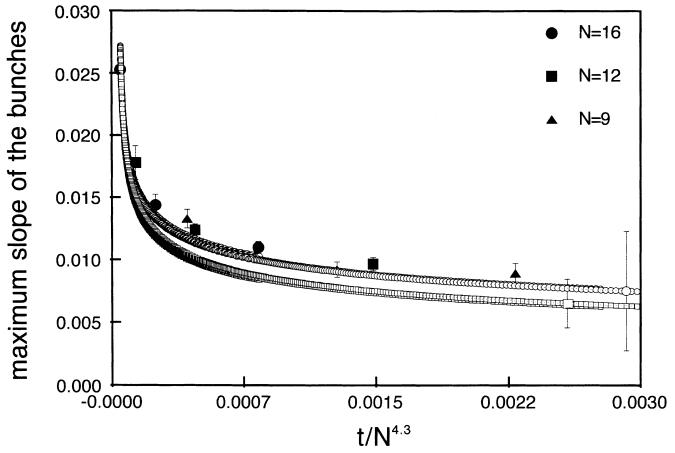

Fig. 28. Plot of scaled slope versus time for the experimental data and results of the numerical solutions. The three experimental data sets are plotted using different symbols, solid circles for $N = 16$, solid squares for $N = 12$, and solid triangles for $N = 9$, and the error bars again represent the standard deviation of the mean. The closely spaced points show the results of the numerical solutions for the two local mass transport relaxation mechanisms (Eqs. (172) and (173)). For each mechanism, relaxation results were obtained for the three initial surface configurations matching the experiment (initial slope of .0253, the starting slope of all the data after appropriate time shifts) and then scaled using the experimental value of $\alpha = 4.3$. The hollow squares denote the results for the attachment/detachment limited case with local mass transport, and the hollow circles denote results for the diffusion limited case. The error bar shown for each mechanism is the error bar for the specific time for which it is plotted and was obtained from the numerical solution results assuming an error in g of 30%, an error in Γ of 50%, and an order of magnitude variation in $D_s c_{eq}$. Alternatively, one can evaluate the agreement by comparing the value of $g\Gamma = 4.5 \times 10^5$ eVÅ/s obtained from the best fit to the data (not shown) to the predicted range of values: (1.1–6.6) $\times 10^6$ eV Å/s.

example, use of $\partial_y^2 x = 1/r$ in Eq. (92) yields the rate of change of the radius from Eq. (93)

$$\frac{\mathrm{d}r}{\mathrm{d}t} = \frac{a^4 c_{eq}\,\tilde{\beta}\kappa_-}{kT\,r}, \tag{180}$$

where we have assumed that only exchange with the lower terrace contributes to the motion of the island edge and chosen the terrace chemical potential $\mu_t = 0$. Relating the radius of the island to the number of atoms in the island yields the result that the number decay rate is constant,

$$\frac{\mathrm{d}N}{\mathrm{d}t} = \frac{2\pi a^2 c_{eq}\,\tilde{\beta}\kappa_-}{kT}, \tag{181}$$

independent of the island radius. Such a constant decay rate has been beautifully demonstrated by Ichimiya et al. [175] for the decay of single-layer islands and pits on Si(1 1 1). They observed structures with several thousand atoms over their entire lifetime over a temperature range 400–600 °C using in situ STM. At each temperature, the decay rate was constant. The thermal variation was activated, following

$$\frac{\mathrm{d}N}{\mathrm{d}t} = (2 \times 10^{11\pm1} s^{-1})\,\mathrm{e}^{-(1.5\pm0.1\,\mathrm{eV})/kT} \tag{182}$$

for island decay. At 465°C, this corresponds to a decay rate of 6 atoms/s, yielding by comparison with Eq. (181)

$$c_{\mathrm{eq}}\,\tilde{\beta}\kappa_{-} = 4.7 \times 10^{-3}/\mathring{\mathrm{A}}^2\mathrm{s}. \tag{183}$$

This information (along with information about step interactions) provides the input needed for predicting the rate of evolution of more complex 3D structures, as in the following section.

4.2.2.2. Decay of a bi-periodic structure. The importance of step curvature effects in the experimental decay of sinusoidal surface profiles was demonstrated by Blakely and co-workers [176,177]. They showed the effect of a small density of steps running perpendicular to the sinusoid (the result of a unavoidable small misorientation during sample preparation). These crossing steps allow layers to be removed from the sinusoid by perpendicular step motion, rather than by the direct annihilation of anti-steps discussed in Section 3.1.2.

Blakely and co-workers [133,178] have recently brought this observation to a logical conclusion by studying the decay of a structure with 2D sinusoidal modulation. The configuration studied is shown in Fig. 29. The initial structure is shown in Fig. 29(a), and a schematic illustration of the corresponding step configuration is shown in Fig. 29(b). Direct imaging of the structure with LEEM, as shown in Fig. 29(c), allows the steps to be visualized as the boundaries in contrast between the 1×2 and 2×1 reconstructed layers of Si(0 0 1). The decay of the metastable structure at 940 °C was followed dynamically using LEEM. Analysis of the image to follow the changes of area of the island and holes observable in Fig 29(c) yielded data such as those in Fig. 30(a).

To model the observed time variation, the step chemical potential was defined as in Eq. (90):

$$\mu_n(y) \equiv -\Omega_{\mathrm{s}}\frac{\delta H}{\delta x_n(y)} = \Omega_{\mathrm{s}}\left[V'(w_n(y)) - V'(w_{n-1}(y)) + \tilde{\beta}\,\frac{\partial^2 x_n}{\partial y^2}\right]. \tag{90}$$

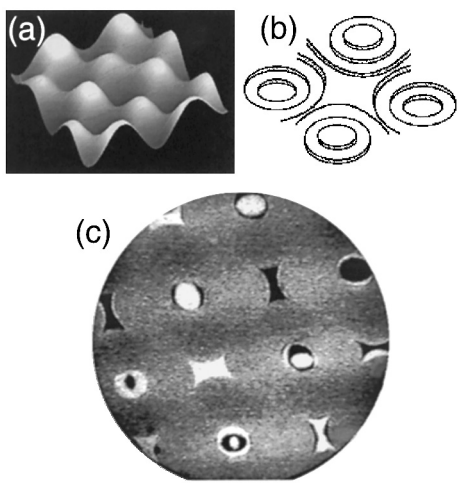

Fig. 29. (a) A 12 micron × 12 micron AFM image showing a biperiodic grating on Si(0 0 1) following initial cleaning and annealing above 1100°C. The amplitude of the grating is 0.4 micron. (b) Schematic illustration of the surface profile of the grating. The number of steps has been reduced for clarity − in the real sample there were several hundred steps between the tops and bottoms of the grating. (c) LEEM image of the grating during annealing at 950 °C (8 micron field of view) (figure from Ref. [133], provided by Prof. J.M. Blakely, Cornell).

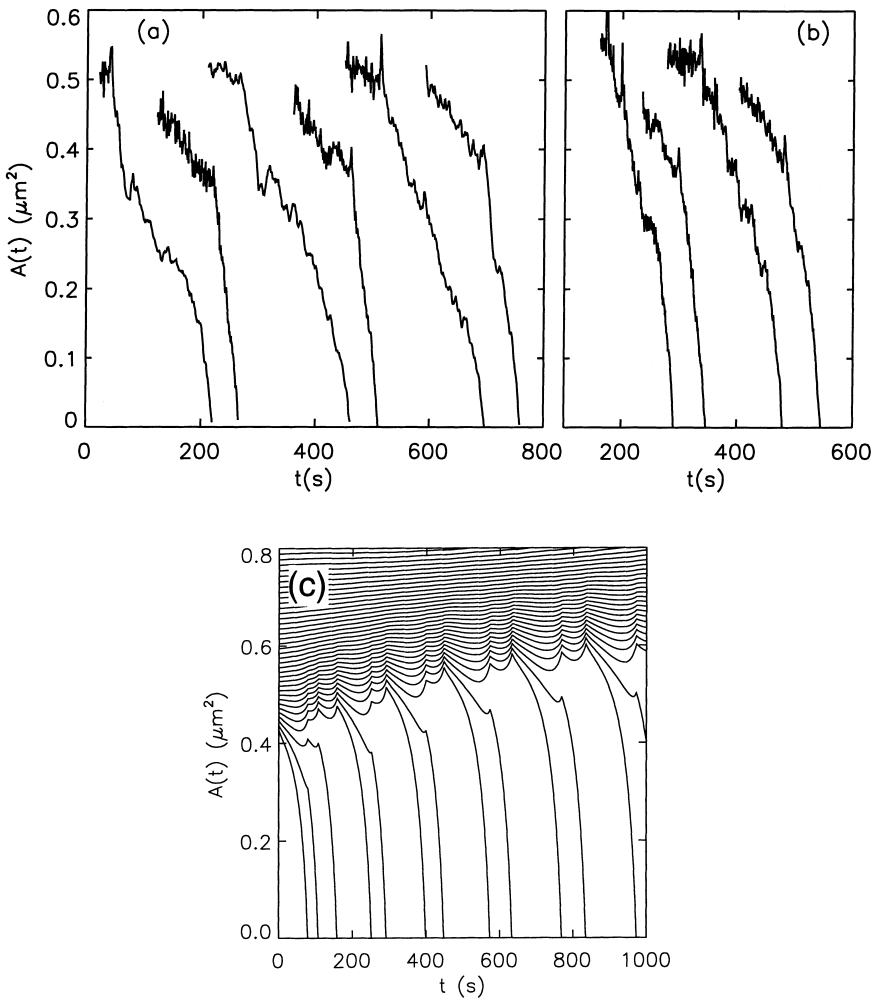

Fig. 30. (a) Experimentally measured time dependence of the area of the holes at the bottoms and (b) tops of the gratings. (c) Calculated time dependence of the areal evolution using a step chemical potential which includes both curvature effects and step–step interactions, as well as a boundary condition which allows adatoms to cross steps without incorporation (permeable steps as described in Section 3.3.4.2.1) (figure from reference [133]).

Here, as the steps form a nearly circular boundary, the step stiffness term is inversely proportional to the radius of the island (or the hole). A first attempt to model the time-variation of the area using only the step stiffness term of Eq. (90) (e.g., μ_n proportional to $1/R$, where R is the radius of curvature) gave results qualitatively different than those of Fig. 30(a). The primary cause of the discrepancy was the strong instability of the steps with respect to kinetic bunching. Addition of an empirical (see Table 7, footnote h) step interaction term with an inverse square dependence gave results qualitatively more similar to the data. Specifically the calculated decay in this case occurs sequentially from layer to layer, with very rapid fall-off of a layer once it begins to shrink. However, the predicted decay lacks the pairing behavior so evident in Fig. 30(a) and (b), where two layers decay in tandem, with the decay of the subsequent layers only beginning when the first two have completely disappeared.

To model the pairing behavior it was necessary to modify the boundary conditions used in defining the equations of motion. Specifically, the original assumption is that all atoms which impinge on a step are either reflected or incorporated [e.g., see Eq. (37)]. Following Ozdemir and Zangwill [179], it is reasonable to assume a third process, adatom crossover (or transmission) to the adjacent terrace, when there is a chemical potential gradient between the terraces (see Section 3.3.4.2.3). By including the *step permeability* process in the boundary conditions, Blakely and co-workers were able to match all the qualitative features of the observed decay, as shown in Fig. 30(c). The best fit is observed for a ratio of transmission to incorporation of approximately forty. If we use this ratio in Eq. (129), we find that the number of terraces which a diffusing atom samples in defining the terrace chemical potential is roughly three terraces on each side of the original step.

4.3. Faceting transitions

As discussed in Section 2.2, the stability of surfaces with respect to faceting can be described either in terms of the orientations present on the equilibrium crystal shape (ECS), or in terms of the convexity of the free energy curve. Similarly, experimental studies of the interfacial stability can be approached either by direct observations of the ECS [180,181], or by systematic studies of the stability of macroscopic surfaces as a function of their orientation [10].

In the following sections, we will review some examples of reversible faceting transitions involving continuous changes in step density. As discussed in Section 2, such transitions require the formation of a non-convex free energy curve as a function of step density. The most obvious way that such a curve (e.g., Fig. 11) could arise is via an attractive step–step interaction. However, the most common interactions between steps are due to the entropy of step wandering and stress-mediated interactions, and are repulsive. As a result, most faceting transitions are not in fact due to attractive step interactions, but to competing free energy curves induced by changes in surface composition due to adsorption, growth or segregation, or to changes in surface structure due to reconstruction or surface melting. In addition, faceting to discrete orientations may occur due to the formation of ''magic vicinals'' for which the step separation at a specific orientation is a favorable match to the unit cell of a surface reconstruction [182]. Recently, some physical mechanisms for attractive step interactions have been proposed [154,183–186], which supply a plausible explanation for the relatively rare observations of changes in morphology which are not directly connected to a phase transition on the surface.

4.3.1. Adsorption and reconstruction-induced faceting

Changes in symmetry and atomic structure due to adsorption and reconstruction of surfaces are common [6], and the associated phase transitions (both first and second order) have been studied extensively [187,188]. The energy differences between different surface reconstructions or adsorbed layers may be relatively small, as shown by some examples in Table 2, compared to the typical surface energy density of around $0.1\,\mathrm{eV/\AA^2}$. These energy differences will show up in the leading term in Eq. (26). However, we can expect that the rebonding that drives the formation of the adsorbed or reconstructed surface layer will also occur at the step-edges, and thus the step free energy, β, is likely to be changed by fractional amounts similar to the changes in the facet energy. Finally, the stress of a surface is generally changed, often by large amounts [155,189,190], and since both the stress-mediated interactions between steps and the step stiffness affect the step-interaction parameter g, we can expect that it too will commonly be changed during adsorption or reconstruction.

Adsorption or reconstruction can make a vicinal surface with a single macroscopic orientation unstable and cause it to facet into surfaces with different orientations [191] as described in Sections 2.2.3 and 2.2.4. Experimental examples include faceting associated with the 7×7 reconstruction on Si(1 1 1) surfaces [116] and with the formation of $(n \times 1)$ oxygen chains on O/Ag(1 1 0) surfaces [192]. Brief reviews on both experiments will be provided in Sections 4.3.1.5 and 4.3.1.6. Before discussing on the experiments, we first generalize the 2D step Hamiltonian of Eq. (89) to include the effect of the surface reconstruction. This generalization is also applicable to adsorption in the case where an overlayer of a specific coverage is formed. The more general case where the coverage is varying with time or as a function of misorientation angle (see Section 2.2 and Fig. 5) will require a more elaborate treatment.

Here we begin with a particular model for reconstruction-induced faceting, as described in Section 2.2.4. In this model, the reconstruction occurs on the low-index reference plane and lowers its free energy relative to that of an unreconstructed surface. However the same reconstruction that produces the lower free energy for the flat face increases the energy of the steps (which disturb the reconstruction). Therefore, reconstruction can occur only on terraces wider than some *critical terrace width* w_c. As discussed in Section 2.2.4 and illustrated in Fig 13(a), the critical width is given by $w_c = 1/\rho_c = \epsilon_s/\epsilon_r$ if $\Delta f_0 = \epsilon_r$ is the energy gain (per unit area) due to reconstruction and $\Delta\beta = \epsilon_s$ is the extra energy cost (per unit length) for forming an isolated step on the reconstructed terrace. When steps are uniformly distributed initially with the average terrace spacing w_a much less than w_c, step fluctuations leading to the formation of a sufficiently wide terrace are required for the reconstruction to begin. Continued growth of the reconstructed region can make the vicinal surface facet into a reference reconstructed surface and a much more sharply inclined unreconstructed surface with closely bunched steps.

4.3.1.1. 2D step hamiltonian incorporating reconstruction. It is reasonable to assume that the kinetics of the reconstruction will be much faster than the kinetics of the step rearrangements in most cases [193]. Therefore, we treat a terrace segment as the unit of reconstruction or deconstruction in describing reconstruction dynamics on the timescale of the movement of a typical step segment. We assign a discrete value, $R_{n,j} = 1$ or 0 to the jth segment of the nth terrace depending on whether it is reconstructed or not. Fig. 31 shows the process of constructing a step continuum model from this discrete model, using the approach presented in Section 3.3.1. A typical step configuration in the

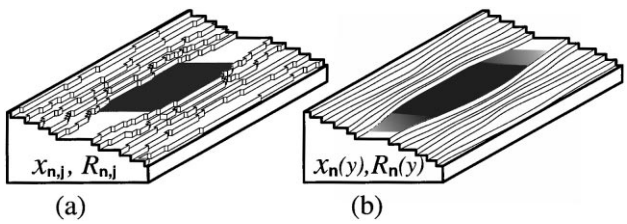

Fig. 31. (a) A typical step configuration in the terrace–step–kink model with a reconstructed facet nucleus when reconstruction occurs only on terraces (shaded) wider than w_c. The surface and reconstruction profiles are specified by discrete variables, $x_{n,j}$ and $R_{n,j}$ where n is the terrace number and j is the discrete position along (parallel to) the step-edge. (b) By coarse-graining along the nominal step edge direction, we get the continuum step and reconstruction configurations described by $x_n(y)$ and $R_n(y)$. The "reconstruction concentration" R on the terrace is proportional to the darkness of the shading.

terrace-step-kink model with a reconstructed facet nucleus on the terrace region wider than w_c is shown in Fig. 31(a). The surface and reconstruction profiles are specified by discrete variables, $x_{n,j}$ and $R_{n,j}$. A continuous description of the terrace reconstruction, described by $R_n(y)$, is obtained by coarse graining parallel to the step: $R_n(y) = \sum_j R_{n,j} K(y - y_j)$ just as for the step positions in Eq. (58). The continuum step position $x_n(y)$ and reconstruction profile $R_n(y)$ are represented in Fig 31(b).

To describe the evolution of reconstruction-driven faceting in terms of the continuum variables, $\{x_n(y)\}$ and $\{R_n(y)\}$, we need to provide an effective Hamiltonian for arbitrary configurations of these coarse-grained variables. To accomplish this, a phenomenological mesoscopic model Hamiltonian has been introduced [135] which incorporates the known results for two simpler systems, a 1D fluctuating interface [194,23] and a 2D array of fluctuating steps with uniform average spacing [21,22] with an additional contribution from reconstruction

$$H(\{x_n\}) = \sum_n \int \mathrm{d}y \left[V(w_n(y), R_n(y)) + \frac{\tilde{\beta}_n}{2} \left(\frac{\partial x_n}{\partial y} \right)^2 + \frac{D_r w_n(y)}{2} \left(\frac{\partial R_n}{\partial y} \right)^2 \right]. \tag{184}$$

Here $w_n(y)$ is the local terrace width as in Eq. (89). The first term, $V(w_n(y), R_n(y))$, describes the effective step–step interactions between the nth step and $(n+1)$th step where $R_n(y)$ represents the "fractional coverage of reconstruction" on the terrace between them. The line stiffness of the nth step, which may depend on the reconstruction coverage of the neighboring terraces, R_{n-1} and R_n, mainly controls the extent of fluctuation of the nth step.[18] The third term of the Hamiltonian represents the interface energy between reconstructed and unreconstructed regions on the nth terrace. This term makes the initial formation of an isolated reconstructed nucleus more difficult than the growth of an existing region of reconstruction (in the y-direction).

As in Section 3.3.2, it is assumed that the appropriate form of the step–step interaction can be obtained from a 1D (projected) free energy density with the step density $\rho = 1/w$ equal to the local width. The standard form [21,22] (for *unreconstructed* vicinal surfaces) is given by $f_u(\rho) = f^0 + \beta\rho + g\rho^3$. (here in all subsequent equations, we have set the step height h equal to a unit distance; see Eq. (26)) as discussed in Section 2.2.4. For the surface with uniform reconstruction coverage R, with $0 \le R \le 1$, we assume that the 1D free energy density still has the same functional form

$$f(\rho, R) = f^0(R) + \beta(R)\rho + g(R)\rho^3, \tag{185}$$

but with R dependent coefficients. The free energy of the fully reconstructed surface, $f(\rho, R{=}1) = (f^0 - \epsilon_r) + (\beta + \epsilon_s)\rho + g\rho^3$, is lower than that of the unreconstructed surface, $f(\rho, R{=}0) \equiv f_u(\rho)$ when the step density ρ is less than $\rho_c \equiv \epsilon_r/\epsilon_s$. With a proper smoothing scheme, the effect of reconstruction is expected to be proportional to R; hence, we use $f^0(R) = f^0 - \epsilon_r R$ and

[18] The line stiffness change due to reconstruction is not considered for the faceting dynamics in the nucleation regime described in the following sub-section (4.3.1.2–4). Although the change in the stiffness is expected to be of the same order as the change in the step energy $\beta(R)$ in Eq. (29), the line stiffness change does not alter the basic results, while the change in the step energy is an essential ingredient in the faceting dynamics.

$\beta(R) = \beta + \epsilon_s R$ in the continuum approach.[19] Following the previous arguments in Section 2.2.4, the interaction term $V(w,R)$ in the 2D model Hamiltonian is approximated by the interaction $f(1/w,R)w$ of a 1D model at the local width w:

$$V(w,R) = (f^0 - \epsilon_R R)w + (\beta + \epsilon_s R) + g/w^2. \tag{186}$$

4.3.1.2. Models for reconstruction and step motion [135,195]. To model the dynamics of reconstruction and step motion, we make a linear kinetics approximation, assuming that the rates of change of the reconstruction and step positions are proportional to the associated changes in free energy as calculated from the effective Hamiltonian in Eq. (184). This naturally makes us consider a local reconstruction field which couples linearly to the local reconstruction coverage. Formally, the local reconstruction field on the nth terrace at y, $B_n(y)$ is defined by

$$B_n(y) \equiv -\frac{1}{w_n(y)}\frac{\delta H}{\delta R_n(y)}, \tag{187}$$

and from the effective Hamiltonian of Eq. (184) we have

$$B_n(y) = \epsilon_r - \epsilon_s/w_n(y) + D_r \frac{\partial^2 R_n(y)}{\partial y^2}. \tag{188}$$

For the uniform coverage ($\partial_y^2 R_n = 0$) on an infinitely wide terrace ($w_n = \infty$), $B_n(y)$ takes the constant value of ϵ_r as expected. On a finite width terrace, there are boundary effects from the steps which provide an effective field, with average value $\epsilon_s/w_n(y)$, opposing the reconstruction. The third term ($\sim \partial_y^2 R_n$) tends to make reconstruction uniform on a terrace to reduce the interface energy in the y-direction. The magnitude of the interface energy is parameterized by D_r. When D_r tends to zero (small interface energy), local terraces with widths $w(y)$ larger than $w_c \equiv \epsilon_s/\epsilon_r$ will increase their reconstruction coverage regardless of the coverage of the neighboring regions in the y-direction. However, for large D_r, the nucleation of reconstruction at a local terrace region is unlikely unless a sufficiently long lateral region of width w_c or wider is formed. In contrast, a local terrace region with width w_c adjacent (in the y-direction) to an already reconstructed region will be more easily reconstructed. In this sense, w_c is the ''critical width for lateral growth'' in the y-direction [92] and is in general smaller than the critical width for the initial nucleation of reconstruction for the model with non-zero D_r.

With a linear kinetics approximation, the kinetic equation for the reconstruction is easy to write down, since the extent of reconstruction is not a conserved quantity. The reconstruction rate is simply

[19] A couple of approximations are made here. First, the reconstruction concentration dependence of the step interaction parameter $g(R)$ is ignored and the g value of the unreconstructed surface is used This does not seem to introduce serious error for the faceting dynamics in the nucleation regime, since the reconstructed terraces are much wider than the other terraces and for these $g(R)/w^3$ is negligible. In general the R dependence of g is expected to be non-trivial since the reconstruction can change the surface stress. This reconstruction effect on the step–step interaction may be important in some applications. Second, in general, there is a local coarse-grained free energy of the reconstruction term $f_l(R)$, which has minima for particular values of R in both $f(R)$ and $\beta(R)$. Such $f_l(R)$ together with the third term in Eq. (184) may have the familiar Landau–Ginzburg form [120]. Here, the role of $f_l(R)$ is taken minimally by setting $f_l(R) = 0$ for $0 \le R \le 1$ and ∞ otherwise, so that the R value can be restricted to $0 \le R \le 1$.

assumed to be proportional to the local reconstruction field

$$\frac{\partial R_n(y)}{\partial t} = \Gamma_R B_n(y) = \Gamma_R \left[\epsilon_r - \epsilon_s / w_n(y) + D_r \frac{\partial^2 R_n(y)}{\partial y^2} \right], \tag{189}$$

where Γ_R is the inverse of the "friction" coefficient relating the "velocity" $\partial_t R$ to the "force" B.

For the dynamics of step motion, as discussed before, it is natural to consider the step chemical potential, since the step motion results from adsorption or emission of atoms at the step-edge. The step chemical potential defined by $\mu_n(y) \equiv -\Omega \delta H / \delta x_n(y)$ is now given by

$$\begin{aligned} \mu_n(y) &\approx -\Omega \left[\left. \frac{\partial V(w,R)}{\partial w} \right|_{\substack{cw_n(y) \\ R_n(y)}} - \left. \frac{\partial V(w,R)}{\partial w} \right|_{\substack{cw_{n-1}(y) \\ R_{n-1}(y)}} + \tilde{\beta} \frac{\partial^2 x_n}{\partial y^2} \right] \\ &= -\Omega \left[\epsilon_R \{ R_{n-1}(y) - R_n(y) \} + 2g \{ w_{n-1}^{-3}(y) - w_n^{-3}(y) \} + \tilde{\beta} \frac{\partial^2 x_n}{\partial y^2} \right], \end{aligned} \tag{190}$$

from Eq. (184), where the functional derivative of the third term, which is of the same order as the previously ignored R dependence of $\tilde{\beta}$, has been ignored for simplicity.

Three limiting mass transport cases are considered; the global mass movement of Eq. (131), local mass movement with attachment/detachment rate-limiting kinetics of Eq. (134), and the case when the diffusion rate is comparable to the attachment/detachment rate (Eq. (95)). We do not consider the possible effect of a Schwoebel barrier [66] and always set $\Gamma_+ = \Gamma_- = \Gamma$. For detailed kinetic and energetic parameters in the simulation see ref. [135] and [195]. For the step dynamics with global mass exchange, a global reservoir is assumed to be formed on the terrace ($\Gamma_A = 2\Gamma$). For the local attachment/detachment case ($D_s c_{eq} \Omega^2 / w \gg \Gamma_\pm$), we consider the case when the length of each terrace L_y is much larger than the diffusion length, $l_d^\pm = D_s c_{eq} \Omega^2$ and use Eq. (135) to calculate the terrace chemical potential.

Starting from the same initial roughly circular nucleus, the equation of step motion, Eq. (131), Eq. (134) or Eq. (95) was numerically integrated together with the equation for the reconstruction Eq. (189). In all cases, after a nucleus is created, it grows much faster in the step-edge direction (where step repulsions are relatively small) than it does in the direction normal to the steps. Thus the nucleus quickly forms an elongated cigar-like shape. However, the subsequent temporal and spatial behavior of the faceting process is very different depending on the mechanism of mass transport on the surface.

Fig. 32(a) shows typical step configurations from all three cases in the early stage of the faceting. With global mass transport, as the reconstructed facet grows it forces neighboring terraces to become smaller. There is a smooth relaxation to the average width far from the facet. Step spacings in the cases with local mass transport, show more interesting behavior because of the correlated step motion as shown in Fig. 32(b).

4.3.1.3. Isolated facet growth. Before discussing this correlated facet growth in more detail, let us first consider the growth rate of an *isolated* facet. The formation of other (induced) nuclei on all other terraces is artificially prevented by setting R_n to zero except on the terrace on which the original nucleation occurred. The time dependence of the facet length and width during growth is then measured. Fast dynamics for reconstruction is assumed and the response for the reconstruction is set to be fifty times faster than step motion. (For the exact values of parameters see [135].) In all three cases

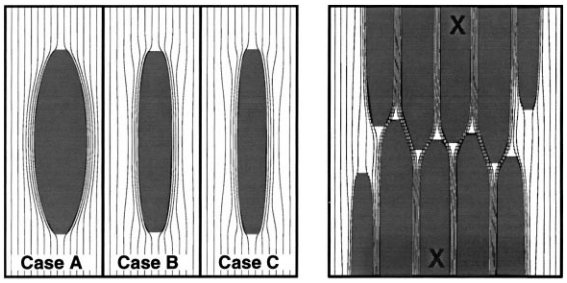

Fig. 32. Top view of step configurations near growing nucleus in the early stage (a) and late stage (b). In (a), initial configurations for case A (global mass transport), case B (local attachment/detachment limited step motion) and case C (diffusion limited step motion) are shown. In (b), a regular pattern in the diffusion limited case (C in panel (a)) arising from interaction between two nuclei through an induced nucleation mechanism is shown. The initial positions of the nuclei (created by hand) are on the terraces marked by X but outside the figure.

the reconstructed region propagates in the y-direction with a *constant* velocity (after an initial transient where it forms the elongated shape). Linear growth along the step direction has been seen in experiment (see Section 4.3.1.5. [116]) and there are general theoretical arguments for constant facet tip velocity [195].

On the other hand, the growth rate of the *normal* width for global movement case is different from that of the local movement cases. Fig. 33 shows the growth of the facet width versus time in a log–log plot. All data in each case fall into a straight line, indicating that the reconstructed terrace width increases as $w \sim t^{\alpha}$. For global mass transport, the facet grows as $t^{1/2}$, while it grows as $t^{1/4}$ for both cases of local mass transport. These results agree with the predictions of the classic 1D continuum model of Mullins [44]. The surface configurations of the diffusion limited case in Fig. 32(a) are similar to those of the local attachment/detachment limited case when two configurations with the same lateral

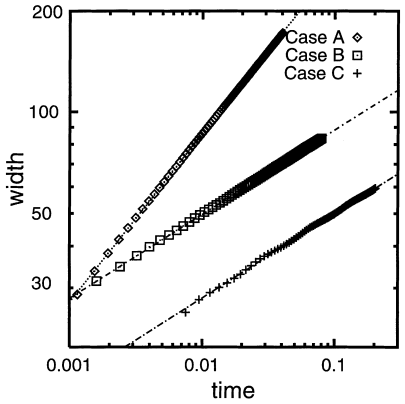

Fig. 33. Measured time dependences of the facet widths for case A (global mass transport), case B (local attachment/detachment limited step motion) and case C (diffusion limited step motion) are shown in a log–log plot. All data in each case fall into a line indicating that the reconstructed terrace width increases as $w \sim at^{\alpha}$. The α values of the fitting lines are $1/2$ for case A and $1/4$ for cases B and C. Time and widths are in arbitrary units (figure from ref. [135]).

size are compared, though it takes about six times longer to grow to the same lateral size in the diffusion limited case.

4.3.1.4. Induced nucleation and 2D pattern formation. Let us now relax the constraint forbidding other nuclei from forming. Even if thermal fluctuations were included, this should produce essentially no change in the case of global mass transport. Since all terraces near the original facet become smaller on an average, other thermally nucleated facets are *less* likely to occur nearby. The story is quite different in the cases with local mass transport, where *induced* nuclei can form and inhibit the further growth of the original facet as shown in Fig. 32(b). In these cases, the motion of a step is directly coupled to the motion of neighboring steps. Initially, as the step bounding the reconstructed terrace moves forward to increase the reconstructed terrace's width, the neighboring step must move backward to conserve adatoms locally. Thus both the original reconstructed terrace and the terrace in front of the step that moves backward get wider. When the two steps that move in opposite directions come sufficiently close to each other for step repulsions to become important (with spacing approaching that of the equilibrium step bunch), they ''collide'' and both begin to move forward together as a bunch because of the driving force from the reconstructed terrace behind. Then the local conservation process repeats itself, causing new steps in front of the advancing step bunch to move backward and making the terraces in front of those steps wider. As the original facet grows, the number of steps in the bunch increases and the widths of the widest terraces in front of the step bunch also increase. Such sufficiently wide terraces can be nuclei for the reconstruction of another facet.

Jeong and Weeks [117] performed a quantitative treatment of this induced nucleation mechanism using a 1D model (the $\tilde{\beta} \to \infty$ limit of Eq. (134)). When the typical distance between steps in a step bunch, $w_b \sim (2g/\epsilon_r)^{1/3}$, is much smaller than the average terrace width w_a, it was shown that only one other terrace, aside from the original facet, is larger than w_a at any given time. In the limit that w_b/w_a goes to zero, the maximum width of the induced wide terrace increases linearly with the number of steps, n_b, in the bunch separating it from the original facet. Moreover, it remains as the widest terrace for an increasing long time interval, $\Delta t \sim n_b^3$. Once it gets larger than w_c, reconstruction will occur. Further growth of the original facet then essentially stops, but the new facet can induce another nucleus on the other side as it continues to grow. Then this new nucleus can induce another one and so on. The velocity of the nucleation front is *linear* in time because it always takes the same amount of time to induce a nucleus. Hence, the faceted surfaces arising from this idealized process have a periodic distribution of reconstructed terraces separated by step bunches.

An interesting 2D pattern arises from induced nucleation when two (thermal) nuclei form that are close in the x-direction but separated by a large distance in the y-direction. Fig. 32(b) shows a step configuration in the diffusion limited case arising from two such nuclei (created by hand). As time goes, each nucleus grows as $t^{1/4}$ in the normal direction until it produces its own induced nucleus. In the lateral direction, nuclei grow essentially linearly in t until they ''collide'' with each other and form a bunch of *crossing steps* between them. After such an encounter, the nuclei stop growing in the y-direction. The number of steps in a crossing bunch is determined by how many steps initially separated the two nuclei when they formed. Once this configuration forms, other nuclei induced by the two original facets will produce new crossing steps at essentially the same y-position as the original crossing steps. Hence, an *alignment* of crossing step bunches is formed as shown in Fig. 32(b). The number of steps in the induced crossing bunches are expected to be the same as that in the original crossing step bunch when the idealized induced nucleation mechanism of the 1D model is accurate. A

strong tendency for alignment of crossing steps has been found in some step bunching experiments on vicinal GaAs(0 0 1) [196], though it is not known yet whether this is an equilibrium or purely kinetic phenomena as considered here.

If thermal fluctuations were taken into account, the regular patterns selected by this kinetic mechanism would be expected to be less sharp. In particular, when w_b/w_a is not so small, the effects of mass conservation are spread out over many terraces and several terraces in front of the step bunch become larger than w_a. These would be particularly advantageous sites where thermal nucleation could occur, even before the induced width of the terrace as predicted by the deterministic models would exceed w_c. Thus nucleation sites and times are less precisely determined in this case, and we expect the number of steps in a bunch, n_b, to be smaller than the value predicted by the 1D model or the deterministic 2D model. Although there are a number of different factors (including particular elastic interactions [197,198]) that can contribute to the facet spacing in particular systems, induced nucleation represents a very general *kinetic* mechanism that should be considered in analyzing experimental data.

4.3.1.5. Faceting driven by 7×7 *reconstruction on Si(1 1 1).* The prototypical system for reconstruction induced faceting as described in Section 4.3.1.1 is Si(1 1 1). The Si(1 1 1) surface is reconstructed in a structure of 7×7 periodicity [199], which disorders in a strongly first-order phase transition at approximately 830°C [200,201]. Above this phase transition, all the vicinal surfaces up to at least 12° of miscut, and all azimuthal orientations are stable. That is, they are observed to have a uniform density of steps consistent with the predictions of entropic wandering [34,123,202], as described in Section 2.2. Upon cooling through the phase transition temperature, however, the surface morphology changes dramatically, with the changes depending on the azimuthal direction of miscut.

4.3.1.5.1. Equilibrium phase diagram. The measured equilibrium phase diagram for Si(1 1 1) is shown in Fig. 2(b) for a temperature below the 7×7 reconstructive temperature [20]. This phase diagram was measured using electron diffraction (LEED) to determine the step densities present on the surface as a function of temperature [43,202–204]. Careful studies of the reversibility of the phase transitions as well as comparison with STM [124], REM [200] and LEEM [201] observations of the structures were used to reach the conclusion that the phases observed actually represent equilibrium structures. Along the high symmetry $[\bar{2}\,1\,1]$ azimuth, and on azimuths of up to 40° on either side of the $[\bar{2}11]$, the surface undergoes faceting to the 7×7-reconstructed (1 1 1) facet and to a bunch of steps whose average step–step separation decreases continuously (step density thus increases continuously) with decreasing temperature [202–204]. Directly along the high symmetry azimuth, the step bunch stabilizes in a (331) facet below 700°C [205,206]. Along the low-symmetry azimuths, no similar stabilization has been reported [202]. This phase separation is attributed to an increase in the step-free energy in the 7×7 reconstructed phase, which causes the free energy curves of the 7×7 phase and the high-temperature 1×1 phase to intersect as the free energy of the 7×7 reconstructed (1 1 1) surface drops below that of the high-temperature phase at the transition [207]. In Fig. 13(a), this would correspond to f_r representing the free energy of the 7×7 phase, and f_u representing the free energy of the unreconstructed phase.

Directly along the high-symmetry $[2\,\bar{1}\,\bar{1}]$ azimuth, the surface is orientationally stable, but undergoes a change in step structure coincident with the reconstructive transition. The change involves the formation of triple-layer-high steps [208] in a mixture of singles and triples, with the density of triple-height steps increasing with increasing azimuthal miscut [204,209]. The formation of triples has been

attributed to competition between a small energy cost for the formation of a triple step from three singles, and the reduction in step–step repulsions which occurs upon step tripling [209,210]. Recent studies using variable temperature STM have shown that the step tripling phase transition does not proceed abruptly at the reconstructive transition, but instead passes through a brief regime of faceting [211].

However, at small angles away from the $[2\,\bar{1}\,\bar{1}]$ azimuth, the steps undergo a continuous rotational phase separation between two phases of non-zero step density . As shown by the tie-bar in Fig. 2(b), in one phase, the steps are straight, perpendicular to the $[2\,\bar{1}\,\bar{1}]$ azimuth, and have the ratio of single- and triple-height steps corresponding to the net step density. In the other phase, the steps are bunched to a higher density, and rotated to a larger angle away from the $[2\,\bar{1}\,\bar{1}]$ than the macroscopic orientation. The result suggests an extremely high kink density for steps perpendicular to the $[2\,\bar{1}\,\bar{1}]$ direction in the presence of the 7×7 reconstruction.

Using the construction of intersecting free energy curves, of the form of Eq. (26), and simple lattice models for the step free energy, it was possible to model the observed phase diagrams quantitatively, as shown by the solid lines in Fig. 2(b) [20,27]. As a result of the fit, estimates of the changes in step and facet energies required to explain the phase diagram were obtained, as shown in Table 9. The absolute magnitude of the increase in step energy required to explain the observed azimuthal phase separation is small, an increase of as little as $14\,\mathrm{meV/\AA}$, but the increase in kink energy required to drive the rotational phase separation is relatively large, the kink energy for single-height steps on the $[2\,\bar{1}\,\bar{1}]$ azimuth must be approximately six times larger in the 7×7 phase than in the high temperature phase to explain the observations.

Table 9
The parameters needed to describe the complete phase diagram of Si(1 1 1) within a nearest-neighbor square lattice model with elastic step–step interactions are the kink energies, ϵ and the step–step interaction strength in the high-("1×1") and low-(7×7) temperature phases, and the temperature variation of the difference in the surface tension $\Delta f_0(T)$ of the two phases on the (1 1 1) facet. These values, along with the resulting derived values for the step formation free energy, $\beta(T)$, and the step-step interaction term, $g(T)$, are shown for $T \approx 830\,^{\circ}\mathrm{C}$. From [27]

	7×7 phase		1×1 phase
	$[\bar{2}\,1\,1]$azimuth (single-height steps)	$[2\,\bar{1}\,\bar{1}]$azimuth (triple-height steps)[b]	$[\bar{2}\,1\,1]$ and $[2\,\bar{1}\,\bar{1}]$ azimuth
Kink energy	$> 1.9\,\mathrm{eV}$[a]	4.4 eV	0.23 eV
Step-interaction strength, A	$0.40\,\mathrm{eV\AA}$	$3.6\,\mathrm{eV\AA}$	$0.15\,\mathrm{eV\AA}$
$\Delta f_0(800^{\circ}\mathrm{C})$	$-0.14\,\mathrm{meV/\AA^2}$		Ref. phase
Step-formation energy, $\beta(0, 800^{\circ}\mathrm{C})$	$> 70\,\mathrm{meV/\AA}$[a]	$165\,\mathrm{meV/\AA}$	$56\,\mathrm{meV/\AA}$
Step-interaction term, $g(0, 800^{\circ}\mathrm{C})$	$22\,\mathrm{meV/\AA^2}$	$7\,\mathrm{meV/\AA^2}$	14[c] $\mathrm{meV/\AA^2}$

[a] The limiting values in the table arise from the inequalities in the requirements for the free energy curves to give rise to phase separation.

[b] The kink energy and step free energies of the triple steps on this azimuth are almost exactly three times as large as for single steps. The step interaction strength, A is nine times that of single steps.

[c] The best experimental value for the step interaction parameter has since been revised [323] to 40–60 $\mathrm{meV/\AA^2}$. Recalculation of an internally consistent set of parameters to explain the measured phase diagrams (Fig. 2) using the higher value of the step interaction parameter would result in concomitantly higher values of the difference in step energies and the difference in facet energies between the two phases.

The consequences of the orientational stability of a surface for the fabrication of small structures is illustrated in Fig. 2(a), which shows the structure of a small circular pit on Si(1 1 1) following high-temperature annealing [212,213]. The anisotropy of the resulting shape clearly follows the predictions of the phase diagram with relatively smooth troughs occurring along the three axes of $\{2\,\bar{1}\,\bar{1}\}$ symmetry, and highly faceted structures along the other orientations.

4.3.1.5.2. Nucleation and growth, spinodal for Si(1 1 1). The equilibrium phase changes described in the previous section take place under the action of a first-order phase transformation in the surface reconstruction, and themselves represent first-order phase separations in the orientation of the surface. As a result, we expect that these processes will be initiated by a nucleation of the low-temperature phase upon cooling. This expectation has been amply fulfilled by direct observations of the faceting process using LEEM [108,116,203] and variable temperature STM [126,214].

As shown in Fig. 34(a)−(c), faceting occurs via nucleation and growth for temperatures down to approximately 10° below the phase transition. (Between 848°C and 857°C, the appearance and growth of faceting is qualitatively the same, except that the rate of appearance of nuclei decreases dramatically close to the reconstructive transition temperature.) The facets nucleate via the formation of the 7×7 reconstruction and grow as originally predicted by Mullins [215] and as described in Section 4.3.1.3. The growth is fast in the direction of miscut, because the repulsions between the steps on either side of

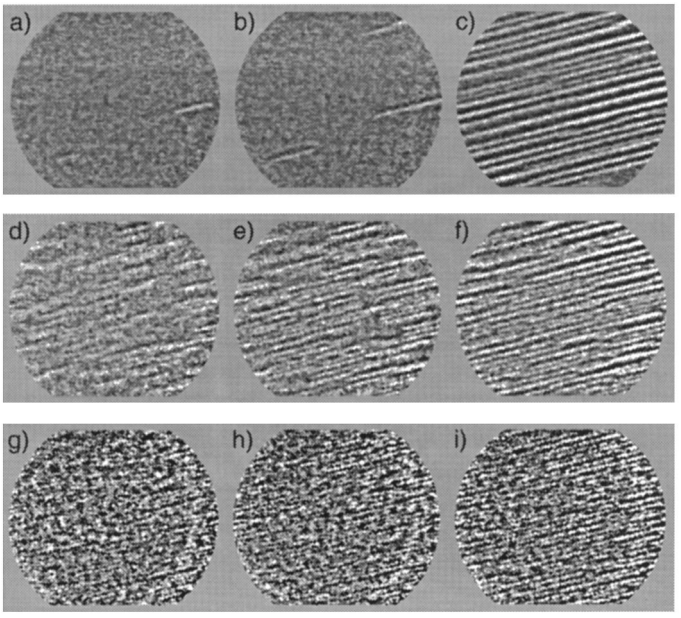

Fig. 34. Sequences of LEEM images of vicinal (4 ° of miscut) Si(1 1 1) quenched to different temperatures below the 7×7 reconstructive transition temperature of 857°C. The field of view in all panels is 4 microns in diameter. Before the quench the surface contains a uniform array of steps which are separated by a distance smaller than the instrumental resolution. Contrast following the quench occurs due to the change in electron scattering due to the formation of the reconstruction. In these images, the bright regions correspond to areas with 7×7 reconstruction and the dark regions to areas which still have the structure of the high-temperature phase. Panels (a)–(c) correspond to a quench to 848.3°C, Panels (d)–(f) correspond to a quench to 847.3°C and Panels (g)–(i) correspond to a quench to 844.5°C. In each sequence the three images were measured at 1s, 3s and 60 s after the quench. (figures are from Ref. [108]).

the facet must be overcome to allow the facet to grow. Very quickly after appearance of the nuclei however, the growth in the perpendicular direction saturates at a value of approximately 600 Å. Effects of surface strain [116], and also induced nucleation effects [117,126], are both likely to play a role in this saturation. In the direction parallel to the steps, the growth of the nuclei proceeds quickly with a linear speed of 1000 ± 200 Å/s. A theoretical description of the parallel growth depends on knowledge of the step energy and the critical nucleus size as well as the step interactions and rate of thermal fluctuations. The formalism to determine the parallel growth rate using this information has been developed [136], yielding a value for the growth speed of 350–2400 Å/s for values of the critical width from 83 to 113 Å [136].

Panels (d)–(f) in Fig. 34 show the result of a quench 1° lower than in panels (a)–(c), and panels (g)–(i) correspond to a quench yet another 2.8° lower in temperature. These data show that over this temperature regime there is a strong and rapid change in the nature of the faceting process. With lower temperatures of quench, the 7×7 begins to appear somewhat randomly all over the surface, and finally at the lowest temperature shown in Fig. 34, the surface is instantly covered with 7×7-facets after the quench. However, the order in this surface is not at all comparable to the facet covered surface of Fig. 34(c), which results from the growth of nuclei. Instead the structure of Fig. 34(g) has narrow (300 Å) facets which have little or no relative correlation in their positions. This poorly ordered structure then coarsens with time, as shown in Figs. 34(h) and (i), eventually yielding a well-defined period in the direction perpendicular to the step edges. This transition from a nucleation process to a process analogous to a spinodal decomposition can be understood in terms of the free energy curve of Fig. 13(a). Facet formation via nucleation is expected to the left of the crossover point for the two free energy curves, and ''spinodal-like'' formation to the right. With decreasing temperature, the crossover point moves to the left, and thus a transition from nucleation to a more abrupt process should occur in a narrow temperature range as observed [108].

4.3.1.6. Oxygen adsorption-induced faceting on Ag(1 1 0) Surface. Because it is commonly assumed that the low-coordination of the substrate atoms at step edges will result in enhanced reactivity to chemical adsorption, it might seem reasonable to predict that chemical adsorption would lead to a lowering of the step energy term in Eq. (8). This, in turn, would lead to different types of intersecting free energy curves based on structures with different chemical composition [216]. (In the extreme case, one would predict coexistence of a ''clean'' phase with no adsorbate, and a second phase with a fixed coverage of adsorbate. However, it is equally reasonable to assume a partition of different concentrations of adsorbate between different orientational phases [10].) The case of O/Ag(1 1 0) therefore presents somewhat of an intuitive surprise, because here in fact atomically resolved STM images show that the adsorption of oxygen occurs solely on the terraces [217], even though formation of the ordered oxygen overlayer proceeds via abstraction of Ag atoms from the step edges to form ordered chains of O–Ag–O structure [217]. With increasing oxygen coverage, the density of the ordered overlayer on the terraces increases without any observable onset of oxygen binding at the steps. In this context, the orientational phase separation which occurs upon oxygen adsorption [192,218], shown in Fig. 35, appears to have a mechanism very similar to the reconstruction-induced faceting of Si(1 1 1).

The sequence of images in Fig. 35 shows, first, the ''frizzled'' steps [219] characteristic of thermal step motion during the time of imaging. Characterization of the time constant of these fluctuations has been described in Section 4.1.2.2 [1], and the equilibrium distribution of step–step spacings has also been determined [184]. Upon introduction of oxygen, the fluctuations of the steps become larger, as

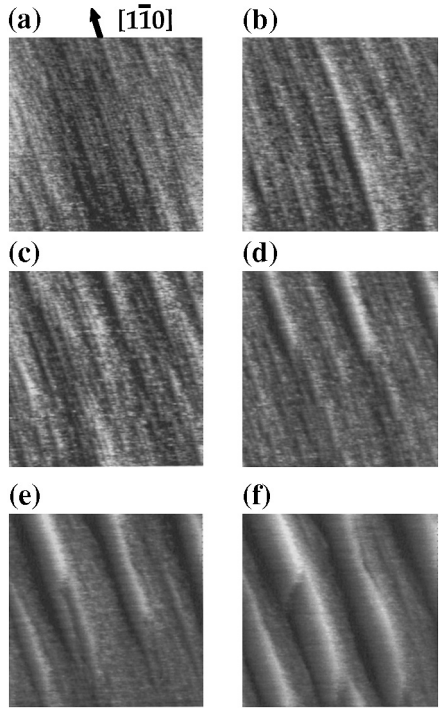

Fig. 35. STM sequence of images at room temperature showing oxygen-induced faceting of a Ag(110) surface misoriented by 2° toward the [0 0 1]. Each panel shows the same area, of size 1500 Å × 1500 Å. (a) The initial clean surface, average step separation is 35Å, (b)–(f) the evolution of structure during exposure to a pressure of 10^{-8} mbar of O_2. The time of exposure for each image is: (b) 66 min (39*L*); (c) 107 min (63*L*); (d) 125 min (73*L*); (e) 160 min (94*L*); (f) 260 min (152*L*). The structure shown in (f) represents saturation – no further changes in structure were observed after this point (figures are from Ref. [218] provided by J. Reutt-Robey, University of Maryland).

shown in Fig. 35(b), where some of the terraces between steps are substantially larger than the average spacing of 35 Å. When the terrace fluctuations reach approximately 100 Å in width, they begin to persist, as shown by the wide terraces which appear at the top of Fig. 35(c) and grow downward in Fig. 35(d). At this point, the oxygen overlayer shows a distinct ordering into a 7 × 1 structure on the wide terraces. The rows of ordered oxygen atoms are oriented perpendicular to the average step edge direction. With continuing exposure to oxygen, the density of the ordered oxygen structure increases, eventually reaching a 3 × 1 symmetry, while the (1 1 0) facets grow in width. The faceted structure saturates with an average step-step separation within the step bunches of approximately 12 Å. The faceting transition can be reversed by reaction of the surface with carbon monoxide, which removes the adsorbed oxygen.

Because there is no evidence of oxygen adsorption within the "step bunched" phase, the phase transition can be understood as a competition between the free energy curves of the clean surface, and a surface covered with oxygen. Oxygen adsorption lowers the free energy of the (1 1 0) facets, but is unfavorable on steps. The resulting free energy of the oxygen covered surface can thus be written as

$$f = (f_0 - \epsilon_t) + (\beta + \epsilon_s)\rho + g'\rho^3, \tag{191}$$

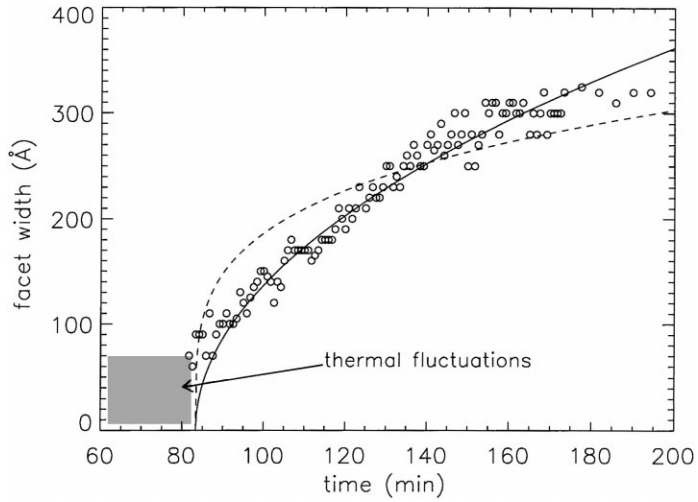

Fig. 36. The width of the central facet from Fig. 35 is shown as a function of time after the onset of O_2 exposure. The facet growth is roughly consistent with a $t^{1/4}$ dependence after the onset of nucleation (figures are from Ref. [192], provided by J. Reutt-Robey, University of Maryland).

where ϵ_t is the oxygen-induced decrease in the free energy of the terrace, ϵ_s the oxygen-induced increase in the step free energy, and g' is the step interaction term in the presence of oxygen. The intersection of this curve with the free energy curve of the oxygen-free surface thus results in a phase separation between oxygen covered facets, and oxygen-free step bunches similar to the phase separation illustrated in Fig. 13. In the case of oxygen adsorption, the free energy of the facets decrease monotonically as the oxygen coverage increases, driving a continuous increase in the orientation of the oxygen-free step bunches. The kinetics of the faceting process should be governed by the exchange of Ag atoms with the steps, which appears to be attachment/detachment limited [1]. This exchange occurs sufficiently quick to provide the excess Ag needed to form the ordered oxygen overlayer as long as the oxygen pressure remains below 10^{-5} mbar [217]. As shown in Fig. 36, following the onset of nucleation, the growth of the terraces does indeed appear consistent with the $t^{1/4}$ behavior that would be predicted from the attachment/detachment limited fluctuations of the steps (see Section 4.3.1.3).

4.3.1.7. Magic vicinals on Pt(0 0 1). In the previous two sections, orientational phase separations driven by a strong interaction between an ordered surface layer (whether a reconstruction or an adsorbate overlayer) were described. It has been predicted theoretically [182] that registry of an ordered superstructure with steps can stabilize those orientations where the step separation matches an integral number of unit cells of the superstructure. For the case of Si(1 1 1), the terraces of the stepped surfaces are observed to be quantized in units of the 7×7 unit cell [220]. However, stabilization of specific orientations corresponding to integral units of the 7×7 cell is not observed [202] because the stepped phase always remains in the high-temperature 1×1 structure. We similarly expect that the phase diagram for oxygen-induced faceting of Ag(1 1 0) will not include stabilization of particular angles, because the stepped phase does not contain the $n \times 1$ superstructure of the oxygen overlayer. In contrast to these phase diagrams, the phase diagram of vicinal Pt(0 0 1) contains an orientational reverse phase separation which demonstrates strong orientation selection with decreasing temperature [221].

Representative data from the measurements, and the resulting overall phase diagram for this system are shown in Fig. 37.

The phase diagram of Pt(0 0 1) contains a number of interesting points. First of all, the transition is driven by a reconstructive transition which occurs between a high-temperature *rough* phase of the (0 0 1) surface and a low-temperature hexagonally reconstructed phase. The phase transition is first-order, so that the intersecting free energy formalism shown in Fig. 13 provides an appropriate description. However, unlike Si(111), since the low-index surface is rough, the high temperature phase is not described by Eq. (8), but instead includes a quadratic term in $\tan(\phi)$ [222]. As a result, the shape of the phase boundary from 1820 to 1630 K follows a $t^{1/2}$ power law rather than the $t^{1/3}$ power law expected when the low-index surface is a facet (non-rough) at high temperature [203,216], where $t = (T - T_c)/T_c$ is the reduced temperature.

Once the reconstructed phase is formed, phase separation proceeds smoothly through the temperature of 1685 K, where the reconstructed unit cell begins to rotate with respect to the high, symmetry direction of the substrate. However, at 1630 K, there is a distinct change in both the step structure and the rotation of the reconstruction. As indicated in Fig. 37, at this temperature there is the appearance of a new orientational phase near 2° which alters the phase diagram. Now surfaces of orientation below 2° phase separate between the (1 0 0) facet and the 2° vicinal. Simultaneously, with the appearance of this new stable facet, the rotation of the reconstruction undergoes an abrupt jump from approximately ±0.4° away from the [1 1 0] direction to ±0.8°. Finally, and perhaps most remarkably, the directions of the step edges themselves rotate to a new direction ±4.8° away from the [1 1 0] direction. A similar set of changes occur approximately 40° lower, with another stable vicinal phase near 6° of misorientation.

It appears quite clear that the formation of the two stable vicinals correspond to the "magic" stabilization predicted by Bartolini et al. [182]. The 2° phase corresponds to between 3.5 and 4.5 reconstructive unit cells, and the ±4.8 ° rotation of the steps (which appears to occur over domains over 0.5 micron in width) aligns the steps with corrugations of the surface resulting from the interference pattern formed by the mismatch between the size of the reconstructed unit cell and the substrate. In terms of a free energy diagram, we qualitatively envision that the formation of the magic vicinal is the result of a downward cusp in the free energy diagram appearing at a miscut angle of 2°. As also previously noted in the discussion for Si(1 1 1), the magnitude of the free energy changes required to cause these dramatic transformations in morphology can be extremely small. In this case, Yoon and co-workers estimate that the difference in free energy between the (0 0 1) facet and the 2° phase is only 0.35 meV/Å^2.

4.3.2. Attractive step interactions

In all the discussion above, we have explicitly considered cases when steps interact repulsively. Under these conditions, the formation of closely grouped step structures requires the intervention of some external factor, such as reconstruction, melting or adsorption, which introduces a competing free energy curve. However, as suggested by Fig. 11, the presence of true attractive step interactions, which can cause the free energy to decrease with increasing step density, can also serve to induce orientational phase separation.

The existence of long-range attractive interactions between steps as a result of oscillatory electronic interactions as a function of step separation has been predicted [154] and suggested experimentally [223]. In addition a short range interaction can arise when multiple-height steps have a favorable

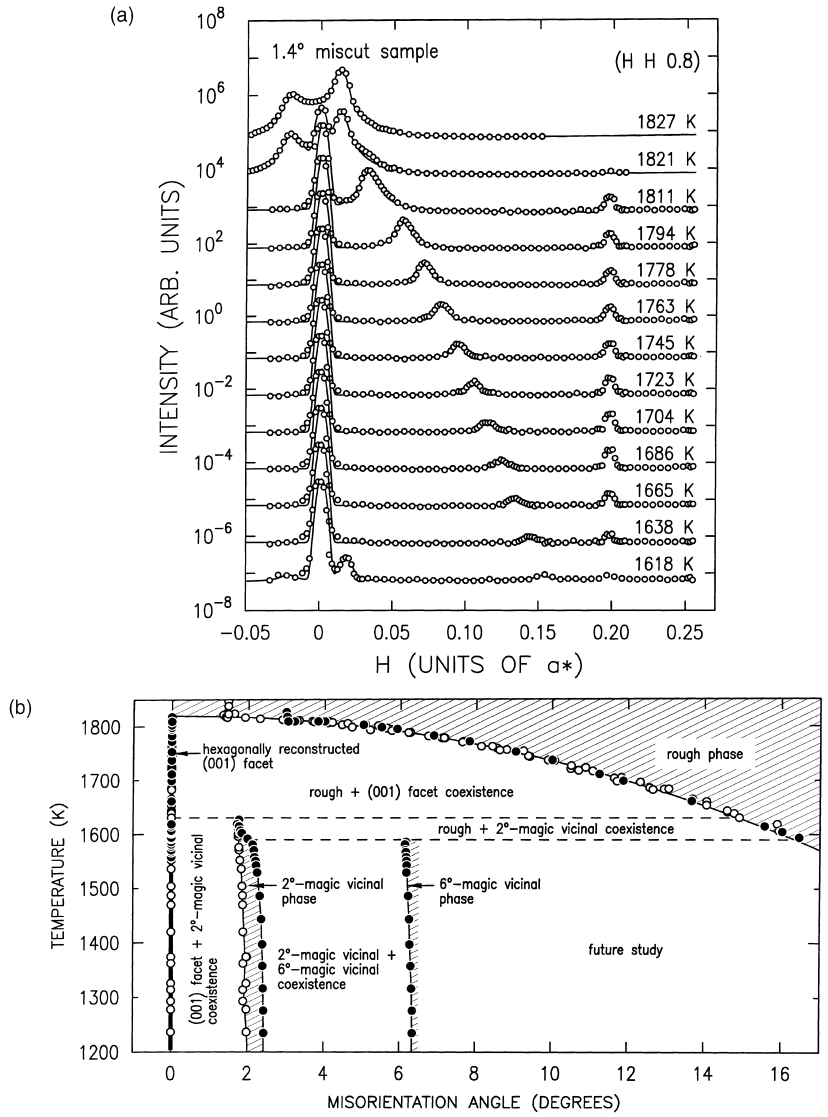

Fig. 37. (a) X-ray profiles of the diffraction pattern from the 1.4° misoriented surface along the direction of macroscopic misorientation. Above the reconstructive transition temperature, only a pair of diffraction beams corresponding to the macroscopic miscut direction is observed. Just below the transition, a peak at $H = 0.2$, corresponding to the periodicity of the reconstruction, appears. Simultaneously, a strong peak at $H = 0$, corresponding to the (0 0 1) facet, appears. The original high temperature beam shifts continuously to a higher value of H, indicating an increase in the corresponding polar angle. (The interpretation of the data shown is based on extensive additional measurement of profiles as a function of perpendicular reciprocal vector value [221]). Finally, below 1630 K, the shifted beam disappears and is replaced by a new beam near $H = 0.02$, the $H = 0$ beam is dramatically reduced in intensity. (b) Orientational phase diagram of the Pt surface near the [0 0 1] direction for misorientation angles towards the [1 1 0] direction. The phase diagram was measured using X-ray diffraction. Two different samples of macroscopic miscut angles of 1.4° (open circles) and 3.0° (solid circles) were measured. The single phase regions of the phase diagram are shown hatched, and the two-phase regions are un-hatched. Solid lines are boundaries between two phases. Dashed lines emphasize the phase coexistence at triple points (figure from Ref. [221], provided by S. Mochrie, MIT).

formation energy compared to single-height steps, e.g.,

$$\beta_n < n\beta_1, \tag{192}$$

as discussed in Section 4.1.1.1. In this case, one expects that the multiple-height steps will be favored at lower temperature, and will tend to break into single-height steps at higher temperature [224]. Such a mechanism underlies the formation of triple-height steps on Si(1 1 1) [43,209], as well as being a likely factor in many of the cases of adsorbate-induced step height changes which have been observed experimentally (see Table 5). In the following sections, we will present two examples of interesting reversible surface structural changes which appear to be driven by different types of attractive step interactions.

4.3.2.1. Step doubling on W(4 3 0) [225]. As tungsten has a bcc crystal habit, the (4 3 0) surfaces consists of terraces of the close-packed (1 1 0) orientation separated by steps. At low temperatures, an electron diffraction analysis shows that the steps on this surface are, on average, 16 Å apart. This is consistent with the predicted spacings for steps that are a single layer in height.

However, upon heating, the diffraction profiles change dramatically. A new peak characteristic of period doubling appears, while the original diffraction peaks decrease in intensity (but do not disappear). Analysis of the diffraction profiles shows that, similar to the case of step-tripling on Si(1 1 1) [204], the new phase consists of a mixture of different height steps. In this case, the mixture consists of single- and double-height steps with approximately 2/3 of the steps being singles and approximately 1/3 being doubles.

The observation of step doubling with increasing temperature is surprising because normally one would expect single-height steps to wander more readily than doubles (see Table 4 and Eq. (142)), and thus to be stabilized by the entropy of wandering at higher temperatures [224]. Conrad and co-workers emphasize the balance of stability for steps of different heights by considering the low level approximation for the step free energy contribution to the overall surface free energy (see Eq. (8))

$$\left[\frac{\beta_{1,2}(T)}{h_{1,2}}\right]\tan\phi \sim \left[\frac{\beta_{1,2}(0) - 2kT/a}{h_{1,2}}\right]\exp(-\epsilon_{1,2}/kT)\tan\phi, \tag{193}$$

where the subscripts 1 and 2 refer to single and double height steps, respectively, and h is the step height, where $h_2 = 2h_1$. In the simplest models, one would expect that both the zero-temperature step energy, $\beta_2(0)$ and the kink energy ϵ_2 would be approximately twice as large as the values for single steps:

$$2\beta_1(0) = \beta_2(0) + \delta\beta, \qquad 2\epsilon_1 = \epsilon_2 + \delta\epsilon.$$

At $T = 0$, the surface containing steps with the lower step energy will be stable. With increasing temperature, the step with the smaller kink energy will eventually achieve a lower step free energy and become stable (the influence of the step interaction term, e.g., Eq. (10) or (11) will be discussed below). For the case of W(4 3 0), it is reasonable to assume that the double step energy is slightly more than twice the single step energy ($\delta\beta < 0$), as only singles are observed at low temperature. Then the appearance of double steps at higher temperature would require that the double height kink energy, ϵ_2, is smaller than the single height kink energy, ϵ_1 (e.g., $\delta\epsilon > \epsilon_1$!). This surprising suggestion has in fact been predicted theoretically with the estimated formation energy of the double height steps

approximately 2.5 times that of the singles, but with the kink energy on the singles being approximately 2.4 times the kink energy on the doubles [225].

The observation of a mixture of step heights at high temperature cannot be understood simply in terms of the effect of the competition in the step energies. If these gave the only contribution to the surface free energy, a transition from a surface containing all single steps to one containing all double steps would occur abruptly at a temperature determined by $\beta_1(T)/h_1 = \beta_2(T)/h_2$. However, with the addition of the non-linear term due to step interactions, mixed phases can represent the lowest energy configuration. Because the step repulsion free energy term decreases with increasing step height (because at fixed miscut angle, increasing h also increases step separation, see Eqs. (11) and (148)), we expect multiple layer steps to form a larger fraction of the mixture at higher step densities, where the step interactions make the largest contribution to the surface free energy [209]. The combination of this step-density dependence with the strong temperature dependence predicted by the competition of the step free energies seems the simplest explanation of the experimentally observed change in the fraction of double steps with temperature. The effect of the theoretically predicted oscillatory interaction with an attractive interaction minimum near the observed single–double step-height configuration [183] could also help to stabilize the mixed phase.

4.3.2.2. Faceting of vicinal Si(1 1 3). The complex structure and stability of high index and vicinal Si were investigated in the pioneering work of Olshanetsky and co-workers [226,227]. Their work, in particular for surfaces along the azimuth from (1 1 1) to (0 0 1), has been expanded by REM studies [228,229], X-ray diffraction measurements [230–232], and detailed STM characterizations [233]. A summary of Baski and co-workers' quantification of the structures is shown in Fig. 38. Interesting areas of phase coexistence occur between the (1 1 4) and (1 1 3) and between the (1 1 3) and

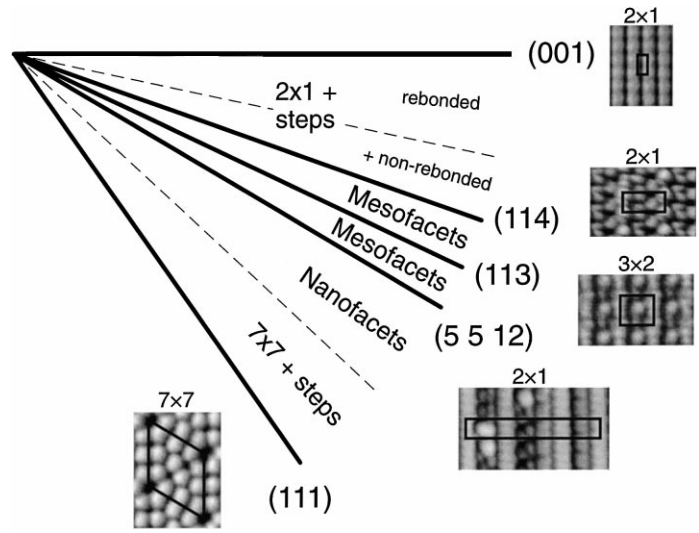

Fig. 38. The surfaces on the azimuth from the (0 0 1) to the (1 1 1) can be described by a rotation angle ($\phi = 0$–54.7°) around the [1 $\bar{1}$ 0] direction, and a corresponding density of steps with edges parallel to the [1 $\bar{1}$ 0] direction. The solid lines in the figure denote orientations with stable planar reconstructions. STM images of these reconstructions are shown with their corresponding unit cells outlined. The dashed lines indicate approximate orientations dividing regions of different structural types (figure from Ref. [233], provided by A. Baski, Virginia Commonwealth University).

(5,5,12) orientations. The large scale orientational phase separation is clearly illustrated in Figs. 39(a) and (d), where (1 1 3) facets are separated by step bunches running parallel to the [1 $\bar{1}$ 0] direction. An interesting difference between the two phase-separated surfaces is the way in which the slight azimuthal miscut is accommodated. On the surface misoriented towards the (0 0 1) [Fig. 39(a)], there is

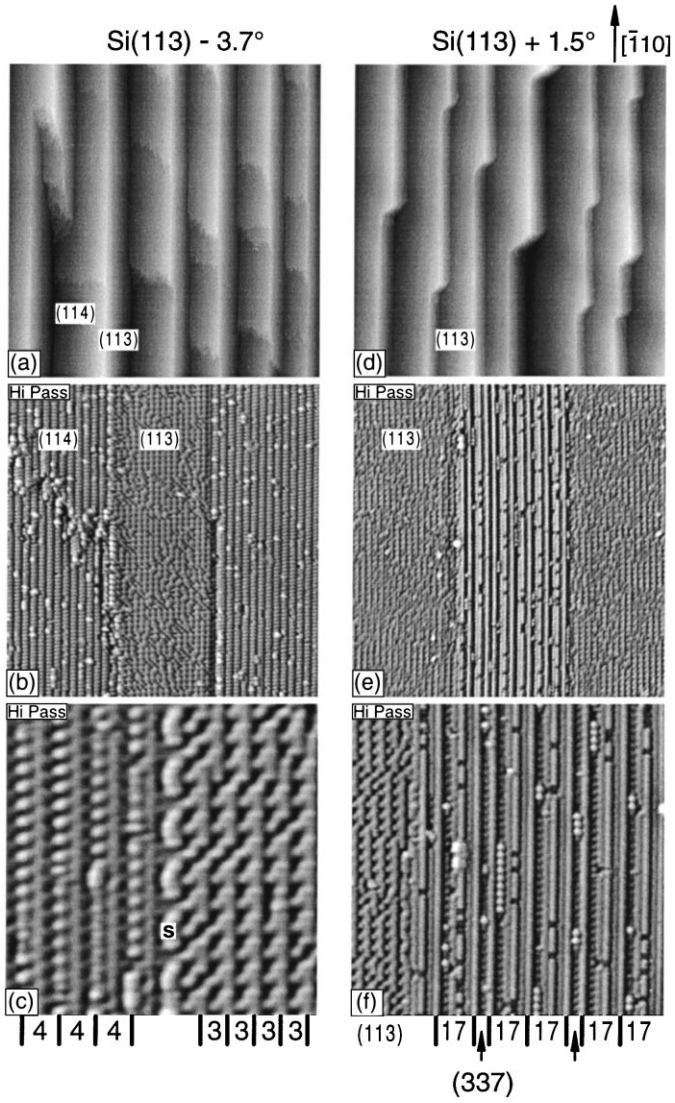

Fig. 39. STM images of surfaces vicinal to Si(1 1 3). Figures (a)–(c) are from a surface misoriented from (1 1 3) by 3.7° toward the (0 0 1) {the vector [$\bar{3}$ $\bar{3}$ 2] which runs from right to left in this figure defines the direction downhill and perpendicular to the average step edge}. Figures (d)– (f) are from a surface misoriented from the (113) by 1.5° toward the (1 1 1) {the vector [3 3 $\bar{2}$] which runs from left to right in this figure defines the direction downhill and perpendicular to the average step edge}. Areas of the images are: (a) and (d) 3720 Å × 3720 Å (b) and (e) 650 Å × 650 Å (c) 140 Å × 140 Å, and (f) 300 Å × 300 Å. Images (b), (c), (e) and (f) have been high pass filtered to make the atomic-scale features more apparent. In the atomic resolution image (bottom) the unit cells of the reconstruction on each surface are labeled 3 = (1 1 3), 4 = (1 1 4) and 17 = (7, 7, 17), which is the subunit of the (5,5,12) surface (figure from Ref. [233], provided by A. Baski, Virginia Commonwealth University).

a small density of steps running nearly perpendicular to the [1 $\bar{1}$ 0] direction on the (1 1 3) facets. On the surface misoriented towards the (1 1 1) [Fig. 39(d)], the miscut is accommodated by large "kinks" at the boundary of the (1 1 3) and (5,5,12) facets.

4.3.2.2.1. Reversible phase separation. The obvious question is how this orientational phase separation is related to the formation of the complex reconstructions observed on these surfaces. Specifically, it is known that the reconstruction of the (1 1 3) surface disorders in a second-order phase transition around 900 K [234–236]. This transition temperature is far different from the temperatures at which vicinal Si(1 1 3) surfaces become unstable with respect to faceting as observed using REM [22,228,229,237] and X-ray diffraction [230–232]. The transitions in morphology occur reversibly with temperature as shown in Fig. 40. However, unlike the cases of Si(1 1 1) and Pt(0 0 1) discussed in earlier sections, there is no correlation between the onset of the reconstruction and the phase boundaries of the orientational phase separation.

Instead, the phase diagram of Fig. 40, which has been measured in detail using X-ray diffraction [230–232], shows that phase separation occurs at a much higher temperature than the reconstructive transition. At high temperatures, the diffraction data shows both the periodicity of a

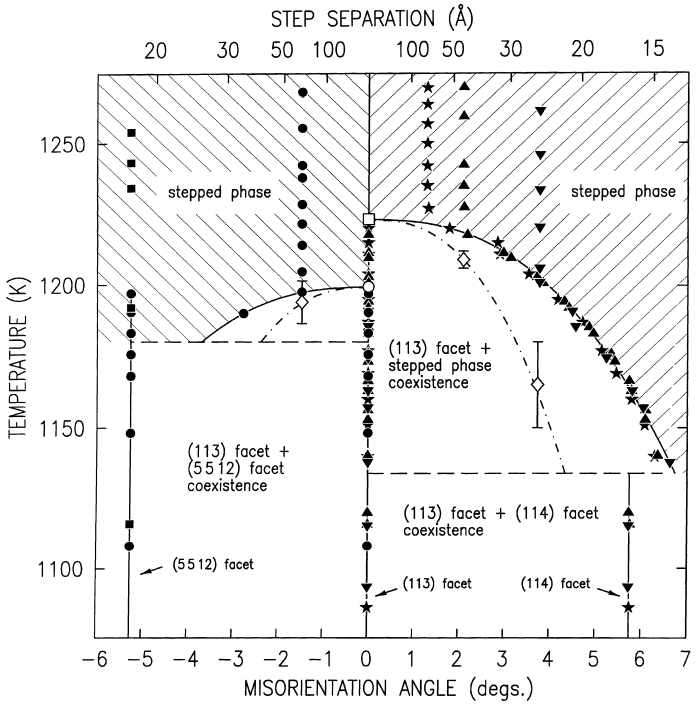

Fig. 40. Orientational phase diagram, measured using X-ray diffraction, of stepped Si(1 1 3) surfaces for orientations between (1 1 4) and (5,5,12) plotted versus temperature and misorientation angle toward the [0 0 1] direction. On the left half of the diagram (negative orientation angles) the step-edges are perpendicular to the [3 3 $\bar{2}$] direction, and on the right half, the step-edges are perpendicular to the [$\bar{3}$ $\bar{3}$ 2] direction. Four macroscopic misorientation angles were measured as indicated by the solid symbols: triangles correspond to a net 2.1° miscut, inverted triangles to a 3.7° miscut, circles to a −1.43° miscut, and squares to a −5.2° miscut. The one-phase regions are shown hatched, two phase regions are unhatched. Solid lines show the phase boundaries (figure from Ref. [231], provided by S. Mochrie, MIT).

uniformly stepped phase consistent with the angle of miscut, and the diffraction line shape expected for thermally wandering steps (a rough surface). However, upon cooling towards the phase boundary, an increase in diffuse scattering intensity near the specular beam indicated strong fluctuations of the step separation. At the phase boundary, the surface begins to phase separate into (1 1 3) facets and step bunches which increase in orientation angle with decreasing temperature. At low enough temperature, the step bunches "lock-in" to a particular facet orientation, the (1 1 4) and (55,12), respectively, for the two misorientation directions, consistent with the STM observations of Fig. 39. Mochrie and co-workers [232] have also measured the phase diagram for vicinal (1 1 3) surfaces miscut in low symmetry directions. For a surface miscut toward the $[\bar{3}\,0\,1]$ direction, the onset of phase separation at zero miscut occurs at 1050 K, and proceeds smoothly with no "lock-in" to a specific facet orientation at lower temperature. For a surface miscut toward the $[\bar{1}\,1\,0]$ direction, the net step orientation is perpendicular to the high symmetry direction, and the phase diagram is qualitatively different from the other misorientation directions. Specifically, at the onset of phase separation at 1215 K, a 1.8° miscut sample phase separates into regions of high and low step density, with the density in each phase varying continuously down to 1075 K. At that point, steps are expelled from the low-density phase, creating (1 1 3) facets, and the high density phase undergoes an azimuthal phase separation, creating (2 1 4) and (2 1 5) facets. The overall surface morphology then consists of an array of pyramids, rather than the hill-and-valley structure characteristic of phase separation between two orientations. For all of the measured phase diagrams, the boundary with the high-density step region has been found to vary roughly as the square root of the reduced temperature [$\delta\phi \sim (T - T_c)^{0.42-0.54}$] [230,232].

The intersecting free-energy curve description, which was natural for Si(1 1 1) and Pt(0 0 1), cannot be applied to the Si(1 1 3) surface because there is no physical basis for defining a second free energy curve related to changes in morphology. Alternatively, one must then consider the possibility of long-range attractive interactions [230] as the origin of the phase separation. This possibility is supported by the observation of strong fluctuations in the step separation just above the phase separation. Such fluctuations are expected in the temperature range where there is strong competition between the entropic repulsions between the steps and an attractive interaction, and would result in the definition of the transition at zero angle as a tricritical point (open symbols in Fig. 40) [22,230]. However, there is no physical mechanism known that will give rise to monotonic long-range interactions between the steps. Furthermore, an approximate theoretical description of an orientational phase separation including long-range attractions leads to a predicted value of 1 for the exponent governing the phase boundary, rather than the observed value of approximately 1/2 [22,230].

The alternative physical mechanism for the phase separation is based on a short-ranged attractive interaction between steps [238], which are likely to arise due to favorable atomic binding configurations allowed by specific step separations. Formation of step bunches proceeds by collisions of steps during thermal fluctuations [239]. Such a binding mechanism, and the correlated "zipping" and "unzipping" of step pairs has been described by Khare and co-workers [224]. Specific applications of this idea to the phase separation of Si(1 1 3) have been proposed recently by Bhattacharjee [185] and Lassig [186]. In their continuum approach, they independently describe a phase coexistence consistent with the measured phase diagram. However, agreement can only be achieved with a special value of the step interactions. Shenoy et al. [240] have refined this description by using an atomistic (TSK) model mapped onto a 1D model of interacting spinless fermions. They conclude that the phase separation can be more accurately described as the formation of bunches of steps of size n. (This is in contrast to the continuum description in which the bunched phase coalesces and would grow in size without limit in

the absence of kinetic effects.) The value of n is governed by the specific nature of the short ranged interactions and the ratio of the repulsive to the attractive step interaction energies. Shenoy et al. consider the observation of step groupings of $n = 1 - 4$ described in Section 4.1.1.1 [148] as evidence for the formation of small n bunch phases predicted by this theoretical description, and the phase diagram of Fig. 40 to correspond to a larger value of $n \sim 22$.

4.3.2.2.2. Kinetics of phase separation. In the cases of reconstruction and adsorption induced faceting described earlier, the onset of faceting proceeds via nucleation of a new phase on a terrace. This is followed by growth of the facet and correlated motion of the steps on either side much as originally envisioned by Mullins [215]. In the case of phase separation of Si(1 1 3), where attractive step interactions provide the motive for the process, the kinetic processes should be quite different. Mochrie and co-workers have made extensive measurements of the kinetics of the phase separation using X-ray diffraction line widths to monitor the size and separation of the step bunches [239,241,242]. This approach provides data over a wide dynamic range in both time and length as shown in Fig. 41. The step bunches are found to increase in separation distance L as $t^{0.16\pm0.02}$, thus with a time exponent distinctly different from the value of approximately 1/4 expected for faceting via nucleation [192,215, 216]. To understand this exponent, Mochrie and co-workers have developed a model in which step

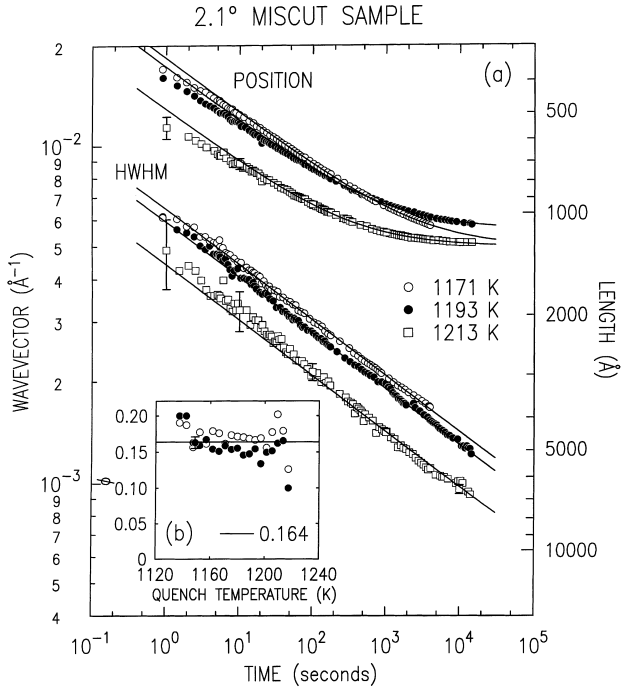

Fig. 41. (a) Kinetics of the phase separation of a vicinal Si(1 1 3) sample with a macroscopic miscut of 2.1° toward the [0 0 1] direction. The position of the diffraction peak corresponding to the periodicity of the step bunches, and the width of the peak which reflects the long-range order of the bunches are shown as a function of time following quenches from 1248 K (the one-phase region in Fig. 40) to 1171, 1193 and 1213 K (the two-phase region in Fig. 40). The length scale (bunch separation) corresponding to the peak position is shown on the right-hand axis. (b) The inset shows the time exponent ϕ deduced from a fit of the peak shift to a form $t^{-\phi}$ (figure from Ref. [239], provided by S. Mochrie, MIT).

bunching occurs via collisions of wandering steps (and step bunches). They make the simple assumption that the stiffness of a bunch of n steps $\tilde{\beta}_n$ will be n times the stiffness of a single step (see Section 4.1.1.1), and that the mobility of a bunch of n steps Γ_n will be $1/n$ times the mobility of a single step. They then combine the expected collision length $l_c(L) \sim \tilde{\beta}_n L^2/kT$ of the bunches of steps for the groove period L with the relaxation time of an over-damped mode of wavelength $l_c(L)$ to obtain an estimate of the time for the groove period to double

$$\tau \sim \frac{kT\, l_c^2}{\Gamma_n \tilde{\beta}_n} \sim \frac{1}{kT}\left(\frac{\tilde{\beta}_n}{\Gamma_n}\right) L^4 \propto n^2 L^4 \propto L^6, \tag{195}$$

which leads to a prediction of an exponent of $1/6$ for the time evolution of the average bunch spacing. The mechanism of the evolution of step bunching via ''zipping'' of colliding steps has been supported by STM images of the evolution of the bunching following quenches through the phase transition [149], as shown in Fig. 42. The average facet size here was also found to grow approximately as $t^{1/6}$ in these experiments. Sudoh and co-workers also compared the evolution of the structure with predictions of a kinetic Monte Carlo calculation based on a TSK model with short range interactions (see Eq. (152)). These simulations yielded an time exponent of 0.2 ± 0.01. Continuing effort on the theoretical

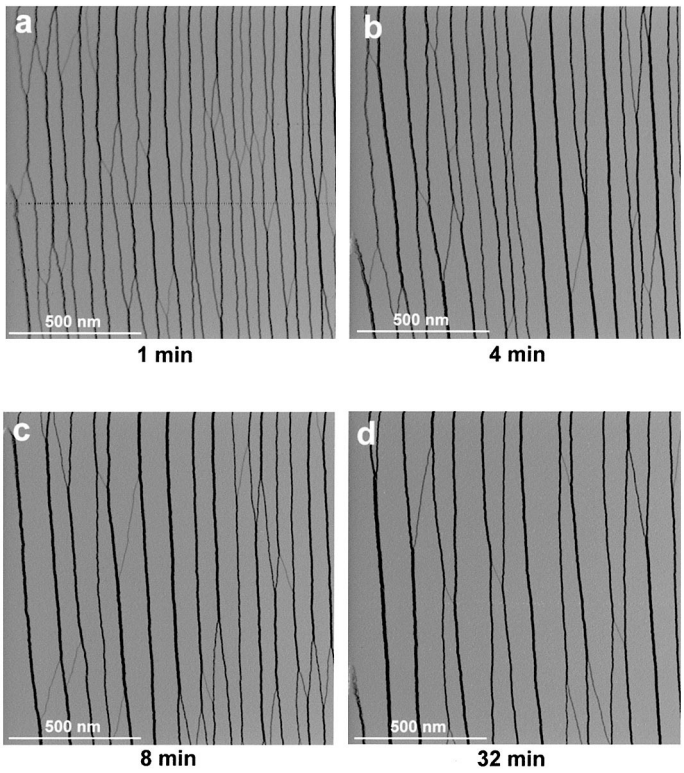

Fig. 42. A vicinal Si(1 1 3) surface misoriented by 1.7° along an azimuth 33° away from the $[\bar{1}\,1\,0]$ toward the $[\bar{3}\,\bar{3}\,2]$ direction has been quenched from 900°C to 650°C and there annealed for the times indicated under each image. The images are 1300 nm × 1300 nm in size (figure from Ref. [149], provided by H. Iwasaki, University of Osaka).

description of this phase separation has clear potential to yield significant understanding of the nature of the attractive interactions which underlie the macroscopic behavior.

4.4. Current-induced step bunching

In the previous sections we have described applications of the continuum step model to problems in which structures evolve to the equilibrium configuration, beginning either with a metastable structure, or during a transition between two different equilibrium structures. Another very interesting and challenging application for the continuum step model is the spontaneous evolution of metastable structures during a kinetic instability. Such instabilities have long been postulated as a natural evolution of the idea of step flow growth, as described in Section 2.3.2. Here we will discuss the kinetic instabilities in surface morphology that occur when heating Si samples using a direct current through the bulk of the sample. Latyshev [173] first recognized and quantified this effect, showing that non-equilibrium step bunching can be created by direct current heating in the direction perpendicular to the step edges, with at least three distinct temperature regimes of behavior. In the range from the disappearance of the 7×7 reconstruction (at approximately 830°C) to approximately 1000°C, step bunching is created when direct current is passed through the sample in the step-down direction. From approximately 1000°C to approximately 1200–1250°C, there is a reversal, and step bunching occurs when direct current is in the step-up direction. Another reversal occurs at approximately 1200°C, and above this temperature step bunching occurs when direct current is in the step-down direction [243–247]. In addition, there appears to be another reversal in the effect of current direction that occurs with decreasing temperature at the 7×7 reconstruction [243], and another that occurs about 100°C below the melting temperature of Si [173].

These striking and remarkable changes in step morphology on Si(1 1 1), along with similar observations concerning step morphology on other vicinal Si surfaces [214,248,249] have generated extensive theoretical interest in understanding the origins of the observed phenomena. Qualitatively, kinetic instabilities leading to step bunching arise from diffusional anisotropy during sublimation or growth, as proposed by Frank [78] and Schwoebel [66]. The observation of current-induced step bunching indicates that in the case of Si(1 1 1), the diffusional anisotropy is caused by a surface electromigration force [250]. The changes in the direction of current associated with bunching at different temperatures on Si(1 1 1) would then most simply suggest a temperature-dependent effective charge for surface electromigration [251]. However, a consideration of the processes governing the evolution of step structure shows that there are other possible mechanisms for the temperature-dependent reversals as well [55,86,252,253].

We will not attempt here to provide a detailed review of the entire literature on the subject of this instability. Instead we will describe a few points that illustrate the power of the continuum step model. As a starting point, we can consider Latyshev's remarkable observations of the evolution of step morphology under the driving current, shown in Fig. 43. Proceeding from top to bottom in this image, we see the initial uniform step structure with an average step spacing of approximately 500 Å. Upon heating with direct current, the step bunching instability arises with evolution of step structure via the formation of ''arcs'' which break loose from one step bunch, and cross the terrace to attach to the neighboring step bunch. These steps then zip up along the neighboring bunch, leaving crossing steps which recede in the direction parallel to the step bands, yielding arrays of crossing steps of well-defined separation. These crossing arrays feel the action of the external electric field roughly parallel to their

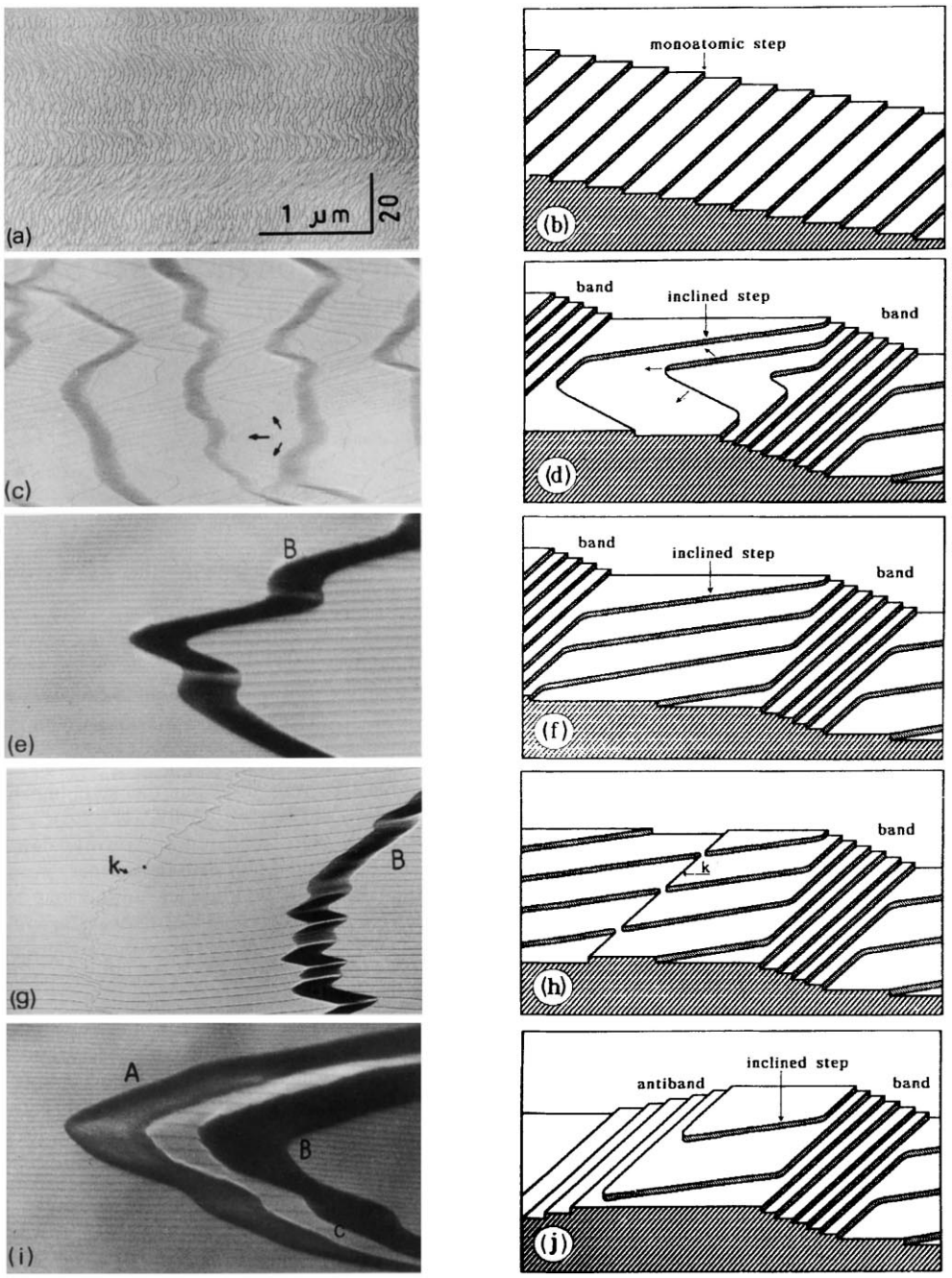

Fig. 43. Reflection electron microscope images of the evolution of step structure on a nominally flat Si(1 1 1) surface at 1260°C. Schematic illustration of the step morphology in the images is shown to the right of each REM image. The direction of current flow is from left to right, e.g. in the step down direction with respect to the initial step orientation (figure from Ref. [344], provided by A. Latyshev, Institute of Semiconductor Physics, Novosibirsk).

edges, eventually resulting in a new type of instability shown in Fig. 43$(g)-(j)$. The new instability is initiated as a series of correlated ''kinks'' in the step-edge which grow to form an anti-band (e.g., a step bunch with the step-down direction 180° from the step-down direction of the neighboring surface) running parallel to the original step band.

We can think about the underlying physics of this process in terms of a weak electromigration force [251,254,255] acting on the atoms which are thermally activated for diffusion at the temperatures of interest. Because the force is so weak that it only acts to impose a small bias on the diffusion, its effects can be treated as a weak perturbation on the equations governing surface mass transport. In terms of the BCF description of Section 2.3.2, this force shows up as an extra term $(D_s F/kT)\mathrm{d}c(x)/\mathrm{d}x$ in Eq. (36) [55], and as a source of anisotropy for the step-edge attachment coefficients $\kappa_{\pm}$ of Eq. (37). In terms of the step chemical potential approach, the electromigration force contributes a potential energy gradient and thus an additional term $-qE_x$ in the equation for the step chemical potential [125]. Kandel and Weeks [77] have developed a physical continuum model to describe the kinetic evolution of the step structure under such a weak perturbing force. They incorporate all of the underlying physical phenomena into the equation for the step velocity

$$v = k_+ w_+ + k_- w_- + \gamma \frac{\partial^2 x}{\partial y^2}, \tag{196}$$

where w_+ and w_- are the widths of the terraces in front of and behind the moving step, k_+ and k_- are the attachment/detachment rates for the corresponding steps, and the curvature parameter γ is related to the step stiffness and step mobility by $\gamma = \Gamma_a \tilde{\beta}/kT$. Numerical simulation of the step evolution using this equation yields predictions of step bunch evolution in remarkable qualitative agreement with the REM data, as shown in Fig. 44(a). STM images of surfaces quenched from the temperature at which the stability occurs show the same characteristic step arcs and crossing arrays [256]. A quantitative analysis of the step curvature in these structures in terms of Kandel and Weeks theory shows that the instability is driven by an anisotropy in step attachment rates of a factor of five. This surprisingly large number, even more surprisingly corresponds to an very small electromigration force corresponding to an

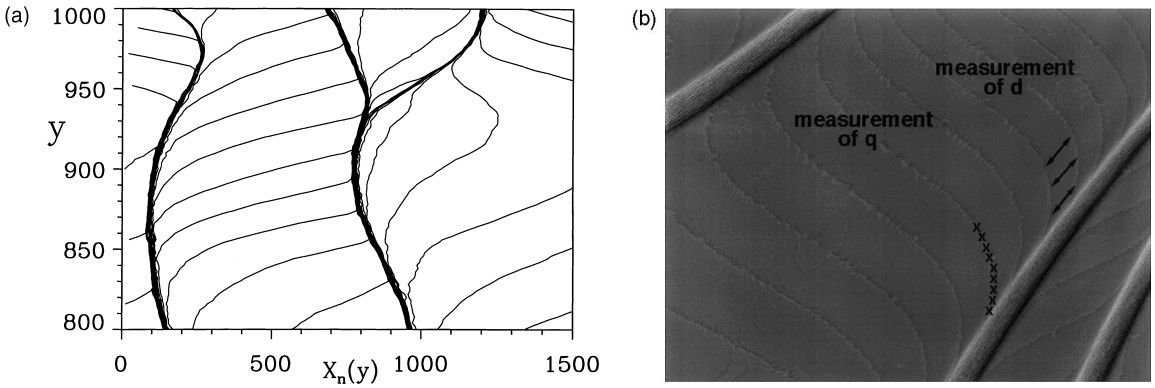

Fig. 44. (a) Snapshot of a system of 30 steps from a Monte Carlo simulation using the model of Kandel and Weeks. Steps move from left to right and are marked by solid lines. Heavy solid lines correspond to step bunches. (b) STM image of a step bunch formed by direct current heating of Si(1 1 1) and the array of crossing steps, illustrating measurement of the curvature and spacing of the steps in the crossing array (figure from Ref. [256]).

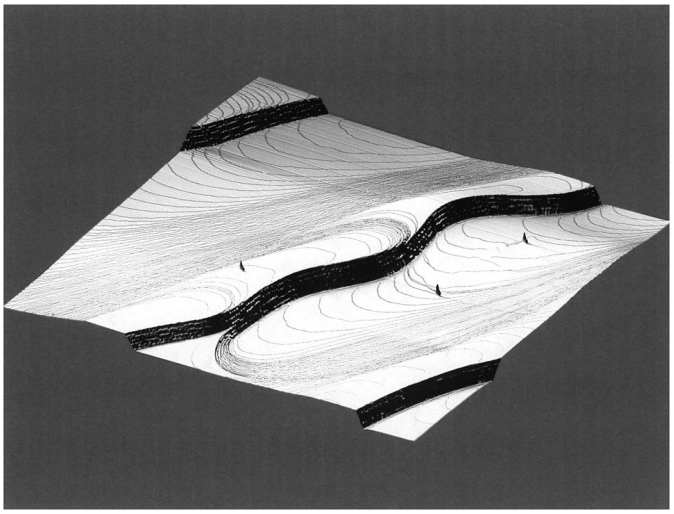

Fig. 45. 10 micron × 10 micron STM image of Si(1 1 1) measured at room temperature after heating at 1300°C with direct current in the step downhill direction. The bending of crossing steps to form the antibands is clearly shown.

effective charge of approximately 0.1 electron unit, as determined by using the Stoyanov formalism [55] to relate the measured anisotropy to the 1D equations of motion. Although this estimate of the effective charge involves severe physical assumptions, it correctly indicates the small order of magnitude of the value, as has subsequently been confirmed by a number of other measurements of the value [246,247,257].

Subsequent quantitative work on the nature of the electromigration force and its impact on step bunch evolution and decay has allowed the competition between terrace diffusion and step attachment detachment rates on Si(1 1 1) to be quantified [257,125]. The results support Latyshev's original intuition that the second instability, the formation of step anti-bands arises due to the effect of an adatom concentration gradient across the wide terraces between bands. STM images of the instability, as shown in Fig. 45, allow quantitative measurements of the curvature of the steps involved in forming the anti-band, which in turn can be related to the underlying parameters of the continuum step model.

5. Conclusions

Ultimately, one would like to have the ability to predict large scale macroscopic behavior quantitatively given an atomic scale understanding of the surface properties. In this review, we have shown how length scales can be effectively bridged to accomplish this. The key is the ability to relate atomic scale properties to the equilibrium behavior of steps, in particular, step fluctuations. Then given the step properties, the evolution of structure to the macroscopic scale can be accomplished with the continuum step model. In this review we have summarized the equations for several simple limiting cases, which can be readily employed for analysis of experimental data. Such analysis requires only a small number (2 or 3 for single-component surface) of experimentally measured equilibrium step parameters. The ability to predict or extrapolate the step parameters for different conditions would be extremely useful.

However, at present, the ability to predict step properties from atomistic properties is limited to simple lattice models. Extending this capability to real atomic interactions should be a major effort of continuing work in surface studies. Other remaining challenges in developing a predictive capability for surface morphology include extending the continuum step model to systems with strong step curvatures (fully 2D structural evolution), and incorporating the effects of strongly coupled external fields.

Acknowledgements

This work has been supported by the NSF-MRSEC at the University of Maryland under grant number DMR-96-32521, and by the DoD through the Laboratory for Physical Science. We gratefully acknowledge many useful discussions with Profs. T.L. Einstein and J.D. Weeks concerning the preparation of this manuscript.

Note added in proof

Additional recent calculations of step kinetic parameters can be found in P.J. Feibelman, Phys. Rev. Lett. 81 (1998) 168; S. Jeong, A. Oshiyama, Phys. Rev. Lett. 81 (1998) 5366.

References

[1] W.W. Pai, N.C. Bartelt, J.E. Reutt-Robey, Phys. Rev. B(1996) 15991.
[2] J.W. Gibbs, in: The Scientific Papers of J. Willard Gibbs, Dover, New York, 1961.
[3] P. Nozìeres, in: C. Godrèche (Ed.), Solids Far From Equilibrium, Cambridge University Press, Cambridge, 1992, pp. 1–154.
[4] C. Herring, Phys. Rev. 82 (1951) 87.
[5] M. Wortis, in: R. Vanselow, R.F. Howe (Eds.), Chemistry and Physics of Solid Surfaces VII, Springer, Berlin, 1988, pp. 367–428.
[6] P.J. Rous, in: D.G. Pettifor (Ed.), Cohesion and Structure of Surfaces, Elsevier Science, Amsterdam, 1995.
[7] N. Moll, A. Kley, E. Pehlke, M. Scheffler, Phys. Rev. B 54 (1996) 8844.
[8] M. Flytzani-Stephanopoulos, L. Schmidt, Progr. Surf. Sci. 9 (1979) 83.
[9] G.A. Somorjai, M.A.Van Hove, Surf. Sci. 30 (1989) 201.
[10] E.D. Williams, N.C. Bartelt, Ultramicroscopy 31 (1989) 36.
[11] R.C. Nelson, T.L. Einstein, S.V. Khare, P.J. Rous, Surf. Sci. 295 (1993) 462.
[12] S.T. Chui, J.D. Weeks, Phys. Rev. B 14 (1976) 4978.
[13] J. Lapujoulade, Surf. Sci. Rep. 20 (1994) 191.
[14] J. Villain, D.R. Grempel, J. Lapujoulade, J. Phys. F: Met. Phys. 15 (1985) 809.
[15] W.K. Burton, N. Cabrera, F.C. Frank, Philos. Trans. Roy. Soc. London, Ser. A 243 (1951) 299.
[16] A.F. Andreev, Sov. Phys. JETP 53 (1981) 1063.
[17] A.A. Chernov, Sov. Phys. Usp. 4 (1961) 1116.
[18] B. Voigtländer, T. Weber, Phys. Rev. Lett. 77 (1996) 3861.
[19] J.E. Avron, H. van Beijeren, L.S. Schulman, R.K.P. Zia, J. Phys. A 15 (1982) L81.
[20] E.D. Williams, R.J. Phaneuf, J. Wei, N.C. Bartelt, T.L. Einstein, Surf. Sci. 294 (1993) 219.
[21] E.E. Gruber, W.W. Mullins, J. Phys. Chem. Solids 28 (1967) 875.
[22] C. Jayaprakash, C. Rottman, W.F. Saam, Phys. Rev. B 30 (1984) 6549.

[23] M.P.A. Fisher, D.S. Fisher, J.D. Weeks, Phys. Rev. Lett. 48 (1982) 368.
[24] M.E. Fisher, D.S. Fisher, Phys. Rev. B 25 (1982) 3192.
[25] Y. Akutsu, N. Akutsu, T. Yamamoto, Phys. Rev. Lett. 61 (1988) 424.
[26] T. Yamamoto, Y. Akutsu, N. Akutsu, J. Phys. Soc. Jpn. 63 (1994) 915.
[27] E.D. Williams, R.J. Phaneuf, J. Wei, N.C. Bartelt, T.L. Einstein, Surf. Sci. 310 (1994) 451.
[28] Y. Carmi, S.G. Lipson, E. Polturak, Phys. Rev. B 36 (1987) 1894.
[29] C. Rottman, M. Wortis, J.C. Heyraud, J.J. Metois, Phys. Rev. Lett. 52 (1984) 1009.
[30] J.J. Saenz, N. Garcia, Surf. Sci. 155 (1985) 24.
[31] S. Surnev, K. Arenhold, P. Coenen, B. Voigtlander, H.P. Bonzel, J. Vac. Sci. Technol. A 16 (1998) 1059.
[32] J.L. Goldberg, X.-S. Wang, N.C. Bartelt, E.D. Williams, Surf. Sci. 249 (1991) L285.
[33] J.C. Heyraud, J.M. Bermond, C. Alfonso, J. Métois, J. Phys. I (France) 5 (1995) 443.
[34] D.Y. Noh, K.I. Blum, M.J. Ramstad, R.J. Birgeneau, Phys. Rev. B 48 (1993) 1612.
[35] N.C. Bartelt, T.L. Einstein, E.D. Williams, Surf. Sci. 276 (1992) 308.
[36] J.M. Blakely, Introduction to the Properties of Crystal Surfaces, Pergamon Press, New York, 1973.
[37] J.W. Cahn, in: W. Johnson, J. Blakely (Eds.), Interfacial Segregation, American Society of Metals, Metals Park, OH, 1977.
[38] J.E. Metois, J.C. Heyraud, Ultramicroscopy 31 (1989) 73.
[39] N.C. Bartelt, T.L. Einstein, C. Rottman, Phys. Rev. Lett. 66 (1991) 961.
[40] M. Uwaha, P. Nozières, in: I. Sunagawa (Ed.), Morphology and Growth Unit of Crystals, Terra Scientific Publishing Co, Tokyo, 1989, pp. 17–35.
[41] E.D. Williams, N.C. Bartelt, in: W.N. Unertl (Ed.), Handbook of Surface Science, North-Holland, Amsterdam, 1996, pp. 51–99.
[42] J.W. Cahn, J. Physique Colleoq. 43 (C6 suppl.) (1982) 199.
[43] J. Wei, X.-S. Wang, N.C. Bartelt, E.D. Williams, R.T. Tung, J. Chem. Phys. 94 (1991) 8384.
[44] W.W. Mullins, J. Appl. Phys. 28 (1957) 333.
[45] W.W. Mullins, J. Appl. Phys. 30 (1959) 77.
[46] W.W. Mullins, in: W.D. Robertson, N.A. Gjostein (Eds.), Metal Surfaces, American Society of Metals, Metals Park, OH, 1962, pp. 17–66.
[47] H. Spohn, J. Stat. Phys. 71 (1993) 1081.
[48] N.C. Bartelt, J.L. Goldberg, T.L. Einstein, E.D. Williams, Surf. Sci. 273 (1992) 252.
[49] A. Rettori, J. Villain, J. Phys. (France) 49 (1988) 257.
[50] F. Lançon, J. Villain, Phys. Rev. Lett. 64 (1990) 293.
[51] M. Ozdemir, A. Zangwill, Phys. Rev. B 42 (1990) 5013.
[52] L.-H. Tang, in: P.M. Duxbury, T. Pence (Eds.), Dynamics of Crystal Surfaces and Interfaces, Plenum Press, New York, 1997, pp. 169–184.
[53] A.A. Chernov, E.D. Dukova, Kristallografiya 5 (1960) 627.
[54] R. Ghez, S.S. Iyer, IBM J. Res. Dev. 32 (1988) 804.
[55] S. Stoyanov, Jpn. J. Appl. Phys. 30 (1991) 1.
[56] G.S. Bales, A. Zangwill, Phys. Rev. B 41 (1990) 5500.
[57] A.V. Latyshev, A.L. Aseev, A.B. Krasilnikov, S.I. Stenin, Physica Status Solidi A113 (1989) 421.
[58] J. Villain, A. Pimpinelli, D. Wolf, Cond. Mat. Phys. 16 (1992) 1.
[59] A. Pimpinelli, D.E.W. J.Villain, Phys. Rev. Lett. 69 (1992) 985.
[60] J.A. Venables, in: D.A. King, D.P. Woodruff (Eds.), Surface Processes in Epitaxial Growth, Elsevier, 1997, pp. 1–45.
[61] G.L. Kellog, Surf. Sci. Rep. 21 (1994) 1.
[62] Bruner, Surf. Sci. Rep. 31 (1998) 121.
[63] P.J. Feibelman, Phys. Rev. Lett. 65 (1990) 729.
[64] P.J. Feibelman, S. Esch, T. Michely, Phys. Rev. Lett. 77 (1996) 2257.
[65] G. Ehrlich, F. Hudda, J. Chem. Phys. 44 (1966) 1039.
[66] R.L. Schwoebel, E.J. Shipsey, J. Appl. Phys. 37 (1966) 3682.
[67] F. Reif, Fundamentals of Statistical and Thermal Physics, McGraw-Hill, New York, 1965.
[68] Y.-N. Yang, E.D. Williams, Phys. Rev. Lett. 72 (1994) 1862.
[69] J. Lyklema, Fundamentals of Interface and Colloid Science, Academic Press, London, 1991, p. 295ff.

[70] A.W. Adamson, Physical Chemistry of Surfaces, Wiley, New York, 1982, p. 54ff.
[71] M. Uwaha, Y. Saito, Phys. Rev. Lett. 68 (1992) 224.
[72] A.V. Latyshev, H. Minoda, Y. Tanishiro, K. Yagi, Phys. Rev. Lett 76 (1996) 94.
[73] K. Morgenstern, G. Rosenfeld, E. Laegsgaard, F. Beseubacher, Phys. Rev. Lett. 80 (1998) 556.
[74] J.G. McLean, B. Krishnamachari, D.R. Peale, E. Chason, J.P. Sethna, B.H. Cooper, Phys. Rev. B 55 (1997) 1811.
[75] P. Bennema, G.H. Gilmer, in: P. Hartman (Ed.), Crystal Growth: An Introduction, North Holland, Amsterdam, 1973, p. 263.
[76] M. Uwaha, Phys. Rev. B 46 (1992) 4364.
[77] D. Kandel, J.D. Weeks, Phys. Rev. Lett. 74 (1995) 3632.
[78] F.C. Frank, in: R.H. Doremus, B.W. Roberts, D. Turnbull (Eds.), Growth and Perfection of Crystals, Wiley, New York, 1958, pp. 411–419.
[79] D. Kandel, J.D. Weeks, Phys. Rev. B 49 (1994) 5554.
[80] G. Ehrlich, K. Stolt, Ann. Rev. Phys. Chem. 31 (1980) 603.
[81] S.C. Wang, G. Ehrlich, Phys. Rev. Lett. 70 (1993) 41.
[82] G. Rosenfeld, R. Servaty, C. Teichert, B. Poelsema, G. Comsa, Phys. Rev. Lett. 71 (1993) 895.
[83] S.C. Wang, T.T. Tsong, Phys. Rev. B 62 (1982) 6470.
[84] S.S. Stoyanov, M. Ichikawa, T. Doi, Jpn. J. Appl. Phys. 32 (1993) 2047.
[85] S.S. Stoyanov, H. Nakahara, M. Ichikawa, Jpn. J. Appl. Phys. 33 (1994) 254.
[86] A. Natori, Jpn. J. Appl. Phys. 33 (1994) 3538.
[87] P. Avouris, R. Wolkow, IBM Research Report No. RC (1988) 13884.
[88] A.V. Latyshev, A.L. Aseev, A.B. Krasilnikov, S.I. Stenin, Surf. Sci. 227 (1990) 24.
[89] T. Suzuki, J.J. Metois, K. Yagi, Surf. Sci. 339 (1995) 105.
[90] E. Bauer, W. Telieps, G. Turner, J. Vac. Sci. Technol. A 6 (1988) 573.
[91] K.G. Wilson, Rev. Mod. Phys. 47 (1975) 773.
[92] J.D. Weeks, D.-J. Liu, H.-C. Jeong, in: P. Duxbury, T. Pence (Eds.), Dynamics of Crystal Surfaces and Interfaces, Plenum Press, New York, 1997, pp. 199–216.
[93] N.C. Bartelt, T.L. Einstein, E.D. Williams, Surf. Sci. 312 (1994) 411.
[94] L. Jorgenson, R. Harris, Phys. Rev. B 47 (1993) 3504.
[95] G. Bilalbegovíc, F. Eroclessi, E. Tosatti, Europhys. Lett. 18 (1992) 163.
[96] W. Selke, J. Oitmaa, Sur. Sci. 198 (1988) L346.
[97] J. Straley, E.B. Kolomeisky, unpublished.
[98] H.P. Bonzel, E. Preuss, Surf. Sci. 336 (1995) 209.
[99] M.V.R. Murty, B.H. Cooper, unpublished.
[100] C. Duport, A. Chame, W.W. Mullins, J. Villain, in: P. Duxbury, T. Pence (Eds.), Dynamics of Crystal Surfaces and Interfaces, Plenum Press, New York, 1997, pp. 71–81.
[101] K. Binder, D.W. Heerman, Monte Carlo Methods in Statistical Physics, Springer, Berlin, 1988.
[102] C.L. Henley, in: D.P. DiVincenzo, P.J. Steinhardt (eds.), Quasicrystals, The State of Art, World Scientific, Singapore, 1991, pp. 429–524.
[103] H.-C. Jeong, P.J. Steinhardt, Phys. Rev. B 48 (1993) 9394.
[104] D.A. Huse, W. van Saarloos, J.D. Weeks, Phys. Rev. B 32 (1985) 233.
[105] M. Kardar, G. Parisi, Y.C. Zhang, Phys. Rev. Lett. 56 (1986) 889.
[106] J. Villain, J. Phys I 1 (1991) 19.
[107] J. Krug, H. Spohn, in: C. Godrèche (Ed.), Solids Far From Equilibrium, Cambridge University Press, Cambridge, 1992, pp. 1–154.
[108] R.J. Phaneuf, N.C. Bartelt, E.D. Williams, W. Swiech, E. Bauer, Phys. Rev. Lett. 71 (1993) 2284.
[109] P.M. Chaikin, T.C. Lubensky, Principles of Condensed Matter Physics, Cambridge, New York, 1995.
[110] B.A. Dubrovin, A.T. Fomenko, S.P. Noviko, Modern Geometry, Methods and Applications, Springer, New York, 1992.
[111] D.-J. Liu, J.D. Weeks, Phys. Rev. Lett. 79 (1997) 1694.
[112] J.M. Blakely, H. Nykura, Acta. Metall. 10 (1962) 565.
[113] K. Yamashita, H. Bonzel, H. Ibach, Appl. Phys. 25 (1981) 231.
[114] W. Selke, P. Duxbury, Phys. Rev. B 52 (1995) 17468.
[115] P.C. Searson, R. Li, K. Sieradzki, Phys. Rev. Lett. 74 (1995) 1395.

[116] R.J. Phaneuf, N.C. Bartelt, E.D. Williams, W. Świech, E. Bauer, Phys. Rev. Lett. 67 (1991) 2986.
[117] H.-C. Jeong, J.D. Weeks, Phys. Rev. Lett. 75 (1995) 4456.
[118] J. Stewart, N. Goldenfeld, Phys. Rev. A 46 (1992) 6505.
[119] F. Liu, H. Metiu, Phys. Rev. B 48 (1993) 5808.
[120] J. Langer, in: C. Godrèche (Ed.), Solids Far From Equilibrium, Cambridge University Press, Cambridge, 1992, pp. 297–363.
[121] N.C. Bartelt, T.L. Einstein, E.D. Williams, Surf. Sci. 240 (1990) L591.
[122] B. Joós, T.L. Einstein, N.C. Bartelt, Phys. Rev. B 43 (1991) 8153.
[123] C. Alfonso, J.M. Bermond, J.C. Heyraud, J.J. Métois, Surf. Sci. 262 (1992) 371.
[124] X.-S. Wang, J.L. Goldburg, N.C. Bartelt, T.L. Einstein, E.D. Williams, Phys. Rev. Lett. 65 (1990) 2430.
[125] E.S. Fu, M.D. Johnson, D.-J. Liu, J.D. Weeks, E.D. Williams, Phys. Rev. Lett 77 (1996) 1091.
[126] H. Hibino, Y. Homma, T. Ogino, Phys. Rev. B 51 (1995) 7753.
[127] R. Evans, in: D. Henderson (Ed.), Fundamentals of Inhomogeneous Fluids, Dekker, New York, 1992.
[128] P. Nozières, J. Phys. (France) 48 (1987) 1605.
[129] S.S. Stoyanov, Appl. Surf. Sci. 60/61 (1992) 55.
[130] M. Uwaha, J. Crystal Growth 128 (1993) 92.
[131] H.P. Bonzel, W.W. Mullins, Surf. Sci. 350 (1996) 285.
[132] S.V. Khare, Ph.D. Thesis, University of Maryland, College Park, MD, 1996.
[133] S. Tanaka, N.C. Bartelt, C.C. Umbach, R.M. T.J.M. Blakely, Phys. Rev. Lett. 78 (1997) 3342.
[134] D.-J. Liu, J.D. Weeks, Phys. Rev. B 57 (1998) 14891.
[135] H.-C. Jeong, J.D. Weeks, Phys. Rev. B 57 (1998) 3949.
[136] D.-J. Liu, E.S. Fu, M.D. Johnson, J.D. Weeks, E.D. Williams, J. Vac. Sci. Technol. B 14 (1996) 2799.
[137] R. Bellman, in Introduction to Matrix Analysis, McGraw-Hill Book, New York, 1960, chap.12, p. 234.
[138] D.-J. Liu, J.D. Weeks, D. Kandel, Surf. Rev. Lett. 4 (1997) 107.
[139] B.S. Swartzentruber, Y.-W. Mo, R. Kariotis, M. Lagally, M. Webb, Phys. Rev. Lett. 65 (1990) 1913.
[140] M. Mundschau, E. Bauer, W. Telieps, W. Świçech, Surf. Sci. 223 (1989) 413.
[141] J.C. Girard, S. Gauthier, S. Rousset, W.S.S. deCheveigne, J. Klein, Surf. Sci. 301 (1994) 245.
[142] L. Kuipers, M.S. Hoogeman, J.W.M. Frenken, H. van Beijeren, Phys. Rev. B 52 (1995) 11387.
[143] M. Giesen-Seibert, F. Schmitz, R. Jentjens, H. Ibach, Surf. Sci. 329 (1995) 47.
[144] J. Li, R. Berndt, W.-D. Schneider, Phys. Rev. Lett. 76 (1996) 1888.
[145] M. Böhringer, W.-D. Schneider, R. Berndt, Surf. Sci. 408 (1998) 72.
[146] A. Pimpinelli, J.J.M. J.Villain, D. E.Wolf, J.C. Heyraud, I. Elkinani, G. Uimin, Surf. Sci. 295 (1993) 143.
[147] K. Fujita, Y. Kusumi, M. Ichikawa, Phys. Rev. B 58 (1998) 1126.
[148] K. Sudoh, T. Yoshinobu, H. Iwasaki, E. Williams, Phys. Rev. Lett. 80 (1998) 5152.
[149] K. Sudoh, T. Yoshinobu, H. Iwasaki, E.D. Williams, Scanning Microscopy 8 (1998) 9.
[150] C. Schwennicke, X.-S. Wang, E. Williams, Surf. Sci. 418 (1998) 22.
[151] L. Barbier, L. Masson, J. Cousty, B. Salanon, Surf. Sci. 345 (1996) 197.
[152] T. Ihele, C. Misbah, O. Pierre-Louis, Phys. Rev. B 58 (1998) 2289.
[153] T. Einstein, S. Khare, O. Pierre-Louis, Mat. Res. Soc. Symp. Proc. 528 (1998) 237.
[154] T.L. Einstein, in: W.N. Unertl (Ed.), Physical Structure, North Holland, Amsterdam, 1996, pp. 579–650.
[155] H. Ibach, Surf. Sci. Rep. 29 (1997) 193.
[156] S. van Dijken, H.J.W. Zandlvliet, B. Poelsema, Phys. Rev. B 55 (1997) 7864.
[157] V.I. Marchenko, A.Y. Parshin, Zh. Eksp. Teor. Fiz. 79, 257 (1980) [Sov. Phys. JETP 52 (1980) 129].
[158] J.M. Rickman, D.J. Srolovitz, Surf. Sci. 284 (1993) 211.
[159] J. Stewart, O. Pohland, J. Gibson, Phys. Rev. B 49 (1994) 13848.
[160] J. Wang, A.P. Horsfield, M.C. Payne, Phys. Rev. B 54 (1996) 4092.
[161] L. Masson, L. Barbier, J. Cousty, B. Salanon, Surf. Sci. 317 (1994) L1115.
[162] M. Poensgen, J. Wolf, J. Frohn, M. Giesen, H. Ibach, Surf. Sci. 274 (1992) 430.
[163] M. Giesen-Seibert, G.S. Icking-Konert, K. Stapel, H. Ibach, Surf. Sci. 366 (1996) 229.
[164] A. Natori, R.W. Godby, Phys. Rev. B 47 (1993) 15816.
[165] J. Jacobsen, K.W. Jacobsen, P. Stoltze, J. Norskov, Phys. Rev. Lett. 74 (1995) 2295.
[166] D.W. Bassett, P.R. Webber, Surf. Sci. 70 (1978) 520.

[167] T.L. Einstein, S.V. Khare, in: P.M. Duxbury, T. Pence (Eds.), Dynamics of Crystal Surfaces and Interfaces, Plenum Press, New York, 1997, pp. 83–96.
[168] H.-C. Jeong, J.D. Weeks, unpublished.
[169] N.C. Bartelt, J.L. Goldberg, T.L. Einstein, E.D. Williams, J.C. Heyraud, J.J. Métois, Phys. Rev. B 48 (1993) 15453.
[170] S.V. Khare, T.L. Einstein, Phys. Rev. B 57 (1998) 4782.
[171] N. Israeli, D. Kandel, Phys. Rev. Lett. 80 (1998) 3300.
[172] H.-C. Jeong, J.D. Weeks, Scan. Micro. 8 (1998) 17.
[173] A.V. Latyshev, A.L. Aseev, A.B. Krasilnikov, S.I. Stenin, Surf. Sci. 213 (1989) 157.
[174] Y. Homma, H. Hibino, T. Ogino, N. Aizawa, Phys. Rev. B 58 (1998).
[175] A. Ichimiya, Y. Tanaka, K. Ishiyama, Phys. Rev. Lett. 76 (1996) 4721.
[176] C.C. Umbach, M.E. Keeffe, J.M. Blakely, J. Vac. Sci. Technol B 9 (1991) 721.
[177] M.E. Keeffe, C.C. Umbach, J.M. Blakely, J. Phys. Chem. Solids 55 (1994) 965.
[178] S. Tanaka, C. Umbach, J. Blakely, R.M. Tromp, M. Mankos, Appl. Phys. Lett. 69 (1996) 1235; J. Vac. Sci. Tech. A 15 (1997) 1345.
[179] M. Ozdemir, A. Zangwill, Phys. Rev. B 45 (1992) 3718.
[180] J.C. Heyraud, J.J. Metois, J.M. Bermond, J. Cryst. Growth 98 (1989) 355.
[181] S. Surnev, P. Coenen, H.P. Bonzel, W.W. Mullins, Surf. Sci. (1996).
[182] A. Bartolini, F. Ecrolessi, E. Tosatti, Phys. Rev. Lett. 63 (1989) 872.
[183] W. Xu, J.B. Adams, T.L. Einstein, Phys. Rev. B 54 (1996) 2910.
[184] W.W. Pai, J.S. Ozcomert, N.C. Bartelt, T.L. Einstein, Surf. Sci. 307–309 (1994) 747.
[185] S.M. Bhattacharjee, Phys. Rev. Lett. 76 (1996) 4568.
[186] M. Lässig, Phys. Rev. Lett. 77 (1996) 526.
[187] T. Einstein, Chem. Phys. Solid Surf. VII 307 (1988).
[188] M. Bernasconi, E. Tosatti, Surf. Sci. Rep. 17 (1993) 363.
[189] R. Cammarata, Prog. Surf. Sci. 46 (1994) 1.
[190] C.E. Bach, M. Giesen, H. Ibach, T.L. Einstein, Phys. Rev. Lett. 78 (1997) 4225.
[191] E.D. Williams, Surf. Sci. 299/300 (1994) 502.
[192] J.S. Ozcomert, W.W. Pai, N.C. Bartelt, J.E. Reutt-Robey, Phys. Rev. Lett. 72 (1994) 258.
[193] F. Katsuki, K. Kamei, Appl. Surf. Sci. 94/95 (1996) 485.
[194] D.B. Abraham, Phys. Rev. Lett. 51 (1983) 1279.
[195] D.-J. Liu, J.D. Weeks, M.D. Johnson, E.D. Williams, Phys. Rev. B 55 (1997) 7653.
[196] K. Hata et al., Appl. Phys. Lett. 76 (1994) 5601.
[197] M. Yoon, S.G.J. Mochrie, D.M. Zehner, G.M. Watson, D. Gibbs, Surf. Sci. 338 (1995) 225.
[198] F. Pourmir, S. Rousset, S. Gauthier, M. Sotto, J. Klein, J. Lecoeur, Surf. Sci. 324 (1995) L337.
[199] K. Takayanagi, Y. Tanishiro, M. Takahashi, S. Takahashi, J. Vac. Sci. Technol. A 3 (1985) 1502.
[200] N. Osakabe, Y. Tanishiro, K. Yagi, G. Honjo, Surf. Sci. 109 (1981) 353.
[201] W. Telieps, E. Bauer, Surf. Sci. 162 (1985) 163.
[202] R.J. Phaneuf, N.C. Bartelt, E.D. Williams, Phys. Rev. B 38 (1988) 1984.
[203] R.J. Phaneuf, E.D. Williams, Phys. Rev. Lett. 58 (1987) 2563.
[204] R.J. Phaneuf, E.D. Williams, Phys. Rev. B 41 (1990) 2991.
[205] H. Hibino, Y. Shinoda, Y. Kobayashi, K. Sugii, Jpn. J. Appl. Phys. 30 (1991) 1337.
[206] H. Hibino et al., Phys. Rev. B 47 (1993) 13027.
[207] E.D. Williams, N.C. Bartelt, Science 251 (1991) 393.
[208] V.I. Mashanov, B.Z. Ol'shanetskii, JETP Lett. 36 (1982) 355.
[209] J. Wei, X.-S. Wang, J.L. Goldberg, N.C. Bartelt, E.D. Williams, Phys. Rev. Lett. 69 (1992) 3885.
[210] E.D. Williams, N.C. Bartelt, in: R. Jullien (Ed.), Surface Disordering: Growth, Roughening, and Phase Transitions, Nova Science Publishers, Les Houches, 1996, pp. 103–112.
[211] H. Hibino, T. Ogino, Phys. Rev. Lett. 72 (1994) 657.
[212] T. Ogino, H. Hibino, Y. Homma, Jpn. J. Appl. Phys. 34 (1995) L668.
[213] T. Ogino, H. Hibino, K. Prabhakaran, J. Vac. Sci. Technol B 14 (1996) 4134.
[214] M. Suzuki et al., J. Vac. Sci. Technol. A 11 (1993) 1640.
[215] W.W. Mullins, Phil. Mag. 6 (1961) 1313.

[216] N.C. Bartelt, E.D. Williams, R.J. Phaneuf, Y. Yang, S.D. Sarma, J. Vac. Sci. Technol. A 7 (1989) 1898.
[217] W.W. Pai, N.C. Bartelt, J.E. Reutt-Robey, Surf. Sci. 330 (1995) L679.
[218] J.S. Ozcomert, W.W. Pai, N.C. Bartelt, J.E. Reutt-Robey, J. Vac. Sci. Technol. A 12 (1994) 2224.
[219] M. Giesen, J. Frohn, M. Poensgen, J. Wolf, H. Ibach, J. Vac. Sci. Technol. A 10 (1992) 2597.
[220] J.L. Goldberg, X.-S. Wang, J. Wei, N.C. Bartelt, E.D. Williams, J. Vac. Sci. Technol. A 9 (1991) 1868.
[221] M. Yoon, S.G.J. Mochrie, D.M. Zehner, G.M. Watson, D. Gibbs, Phys. Rev. B 49 (1994) 16702.
[222] J.D. Weeks, in T. Riste (Ed.), Ordering in: Strongly Fluctuating Condensed Matter Systems, Plenum Press, New York, 1980, pp. 293–317.
[223] J.S. Ozcomert, W.W. Pai, N.C. Bartelt, J.E. Reutt-Robey, Surf. Sci. 293 (1993) 183.
[224] S.V. Khare, T.L. Einstein, N.C. Bartelt, Surf. Sci. 339 (1995) 353.
[225] S. Dey, S. Kiriukhin, J. West, E. Conrad, Phys. Rev. Lett. 77 (1996) 530.
[226] B.Z. Olshanetsky, A.A. Shklyaev, Surf. Sci. 82 (1979) 445.
[227] B.Z. Olshanetsky, V.I. Mashanov, Surf. Sci. 111 (1981) 414.
[228] T. Suzuki, Y. Tanishiro, H. Minoda, K. Yagi, M. Suzuki, Surf. Sci. 298 (1993) 473.
[229] T. Suzuki, Y. Tanishiro, H. Minodaa, K. Yagi, ICEM 13 (1994) 1033.
[230] S. Song, S.G.J. Mochrie, Phys. Rev. Lett. 73 (1994) 995.
[231] S. Song, M. Yoon, S.G.J. Mochrie, Surf. Sci. 334 (1995) 153.
[232] M. Yoon, S.G.J. Mochrie, M.W. Tate, S. Gruner, E.F. Eikenberry, Surf. Sci. 411 (1998) 70.
[233] A.A. Baski, L.J. Whitman, Surf. Sci. 392 (1997) 69.
[234] Y.-N. Yang, E.D. Williams, R.L. Park, N.C. Bartelt, T.L. Einstein, Phys. Rev. Lett. 64 (1990) 2410.
[235] D.L. Abernathy, S. Mochrie, Phys. Rev. Lett. 69 (1992) 941
[236] R.M. Tromp, W. Theis, N. Bartelt, Phys. Rev. Lett. 77 (1996) 2522.
[237] T. Suzuki, K. Yagi, Phys. Stat. Sol. 146 (1994) 243.
[238] S.T. Chui, J.D. Weeks, Phys. Rev. B 23 (1981) 2438.
[239] S. Song, M. Yoon, S.G.J. Mochrie, G.B. Stephenson, S.T. Milner, Surf. Sci. 372 (1997) 37.
[240] V.B. Shenoy, S. Zhang, W. Saam, Phys. Rev. Lett. 81 (1998) 3475.
[241] S. Song, S.G.J. Mochrie, G.B. Stephenson, Phys. Rev. Lett. 74 (1995) 5240.
[242] M. Yoon, S.G.J. Mochrie, M.W. Tate, S. Gruner, E.F. Eikenberry, Phys. Rev. Lett. 80 (1998) 337.
[243] Y. Homma, R.J. McClelland, H. Hibino, Jpn. J. Appl. Phys. 29 (1990) L2254.
[244] A. Yamanaka, N. Ohse, H. Kahata, K. Yagi, in: S.Y. Tong (Ed.), The Structure of Surfaces III, Springer, Berlin, 1991, pp. 502–506.
[245] Y.-N. Yang, E.S. Fu, E.D. Williams, Surf. Sci. 356 (1996) 101.
[246] T. Senoh, H. Minoda, Y. Tanishiro, K. Yagi, Surf. Sci. 357–358 (1996) 518.
[247] J.-J. Metois, M. Audriffen, Int. J. Mod. Phys. B 11 (1997) 3691.
[248] M. Ichikawa, T. Doi, Appl. Phys. Lett. 60 (1992) 1082.
[249] K. Yagi, Surf. Sci. Rep. 17 (1993) 305.
[250] H. Yasunaga, A. Natori, Surf. Sci. Rep. 15 (1992) 205.
[251] D. Kandel, E. Kaxiras, Phys. Rev. Lett. 76 (1996) 1114.
[252] C. Misbah, O. Piere-Louis, A. Pimpinelli, Phys. Rev. B 51 (1995) 17283.
[253] S.S. Stoyanov, Surf. Sci. 370 (1997) 345.
[254] P.J. Rous, T.L. Einstein, E.D. Williams, Surf. Sci. 315 (1994) L995.
[255] P.J. Rous, D.N. Bly, Phys. Rev. B, in press (1999).
[256] E.D. Williams, E. Fu, Y.-N. Yang, D. Kandel, J.D. Weeks, Surf. Sci. 336 (1995) L746.
[257] E.S. Fu, D.-J. Liu, M.D. Johnson, J.D. Weeks, E.D. Williams, Surf. Sci. 385 (1997) 259.
[258] G.A. Wolff, J.G. Gualtieri, The American Mineralogist 47 (1962) 562.
[259] W.R. Tyson, W.A. Miller, Surf. Sci. 62 (1977) 267.
[260] V.K. Kumikov, K.B. Khokonov, J. Appl. Phy. 54 (1983) 1346.
[261] H.P. Bonzel, Surf. Sci. 328 (1995) L571.
[262] C.L. Liu, J.M. Cohen, J.B. Adams, A.F. Voter, Surf. Sci. 334–344 (253) 1991.
[263] M. Methfessel, D. Hennig, M. Scheffler, Phys. Rev. B 46 (1992) 4816.
[264] J.R. Smith, T. Perry, A. Banerjea, J. Ferrante, G. Bozzolo, Phys. Rev. B 44 (1991) 6444.
[265] J.F. Nicholas, An Atlas of Models of Crystal Surfaces, Gordon and Breach, New York, 1965.

[266] M.A.V. Hove, G.A. Somorjai, Surf. Sci. 92 (1980) 489.
[267] D.R. Eisner, T.L. Einstein, Surf. Sci. 286 (1993) L559.
[268] M. Dreschler, Surf. Sci. 266 (1992) 1.
[269] C. Messmer, J.C. Bilello, J. Appl. Phys. 52 (1981) 4263.
[270] J.J. Gilman, J. Appl. Phys. 31 (1960) 2208.
[271] R. Jacodine, J. Electrochem. Soc. 110 (1963) 524.
[272] D.J. Eaglesham, A.E. White, L.C. Feldman, N. Moriya, D.C. Jacobson, Phys. Rev. Lett. 70 (1993) 1643.
[273] R.D. Meade, D. Vanderbilt, Phys. Rev. B 40 (1989) 3905.
[274] I. Stich, M.C. Payne, R.D. Kinjg-Smith, J.-S. Lin, L.J. Clarke, Phys. Rev. Lett. 68 (1992) 1351.
[275] K.D. Brommer, M. Needels, B.E. Larson, J.D. Joanopoulos, Phys. Rev. Lett. 68 (1992) 1355.
[276] R. Stumpf, M. Scheffler, Phys. Rev. B 53 (1996) 4958.
[277] S.V. Khare, T.L. Einstein, Surf. Sci. 314 (1994) L857.
[278] C.-L. Liu, J.B. Adams, Surf. Sci. 294 (1993) 211.
[279] S. Kodiyalam, K.E. Khor, N.C. Bartelt, E.D. Williams, S.D. Sarma, Phys. Rev. B 51 (1995) 5200.
[280] D.J. Chadi, Phys. Rev. Lett. 43 (1979) 43.
[281] S. Tang, A.J. Freeman, B. Delley, Phys. Rev. B 45 (1992) 1776.
[282] C. Roland, G. Gilmer, Phys. Rev. B 46 (1992) 13428.
[283] D.J. Chadi, Phys. Rev. Lett. 59 (1987) 1691.
[284] C. Roland, G. Gilmer, Phys. Rev. B 46 (1992) 13437.
[285] B.D. Yu, M. Scheffler, Phys. Rev. Lett. 77 (1996) 1095.
[286] J.R. Heffelfinger, M.W. Bench, C.B. Carter, Surf. Sci. 343 (1995) L1161.
[287] J.R. Heffelfinger, C.B. Carter, Surf. Sci. 389 (1997) 188.
[288] K.-J. Song, C.Z. Dong, T.E. Madey, in: e.a. S.Y.Tong (Ed.), The Structure of Surfaces III, Springer, Berlin, 1991, p. 378.
[289] T.E. Madey, J. Guan, C.-Z. Dong, Surf. Rev. Lett. 3 (1996) 1315.
[290] J. Guan, R.A. Campbell, T.E. Madey, J. Vac. Sci. Technol. A 13 (1995) 1484.
[291] H. Hibino, Y. Shinoda, Y. Kobayashi, K. Sugii, (1990) 1135.
[292] H. Tokumoto et al., Ultramicroscopy 42–44 (1991) 816.
[293] K. Yagi et al., Progr. Theorer. Phys. Suppl. 106 (1991) 303.
[294] H. Tanaka, Y. Watanabe, I. Sumita, Appl. Surf. Sci. 60/61 (1992) 474.
[295] M. Suzuki, Y. Homma, Y. Kudoh, R. Kaneko, Appl. Surf. Sci. 60/61 (1992) 460.
[296] J. Wei, X.-S. Wang, N.C. Bartelt, E.D. Williams, Phys. Rev. Lett. 69 (1992) 3885.
[297] T.R. Ohno, E.D. Williams, Appl. Phys. Lett. 55 (1989) 2628.
[298] T.R. Ohno, E.D. Williams, J. Vac. Sci. Technol. B 8 (1990) 874.
[299] A.V. Latyshev, H. Minoda, K. Yagi, Surf. Sci. 401 (1998) 22.
[300] L. Seehofer, S. Huhs, G. Falkenberg, R. Johnson, Surf. Sci. 329 (1995) 157.
[301] Y. Takahashi, H. Minoda, Y. Tanishiro, K. Yagi, Surf. Sci. 433–435 (1999) 512.
[302] P.R. Pukite, P.I. Cohen, Appl. Phys. Lett. 50 (1987) 1739.
[303] T.R. Ohno, E.D. Williams, Jpn. J. Appl. Phys. 28 (1989) L2061.
[304] L. Yi, Y. Wei, I.S.T. Tsong, Surf. Sci. 304 (1994) 1.
[305] S. Folsch, G. Meyer, M. Henzler, Surf. Sci. 394 (1997) 60.
[306] T. Shimakura, H. Minoda, K. Yagi, Surf. Sci. 407 (1998) L657.
[307] Z. Gai, H. Ji, Y. He, C. Hu, R.G. Zhao, W.S. Yang, Surf. Sci. L851–L856 (1995) 338.
[308] R.A. Marbrow, R.M. Lambert, Surf. Sci. 71 (1978) 107.
[309] J.S. Ozcomert, W.W. Pai, N.C. Bartelt, J.E. Reutt-Robey, Mater. Res. Soc. Symp. Procs. 335 (1995) 115.
[310] A.M. Molenbroek, J.W.M. Frenken, Surf. Sci. 366 (1996) 587.
[311] H.M. van Pinxteren, J.W.N. Frenken, Surf. Sci. 275 (1992) 383.
[312] G.M. Watson, Phys. Rev. Lett. 71 (1993) 3166.
[313] H.M. van Pinxteren, B. Pluis, J.W.N. Frenken, Phys. Rev. B 49 (1994) 13798.
[314] G. Comsa, G. Mechtersheimer, B. Poelsema, Surf. Sci. 119 (1982) 172.
[315] E. Hahn, H. Scief, V. Marsico, A. Fricke, K. Kern, Phys. Rev. Lett. 72 (1994) 3378.
[316] J. Batteas, J. Dunphy, G. Somorjai, M. Salmeron, Phys. Rev. Lett. 77 (1996) 534.
[317] L. Niu, D. Koleske, S. Sibener, Surf. Sci. 356 (1996) 144.

[318] G.M. Watson, D. Gibbs, D. Zehner, M. Yoon, S. Mochire, Surf. Sci. 407 (1998) 59.
[319] G.M. Watson, D. Gibbs, S. Song, A.R. Sandy, S. Mochire, Phys. Rev. B 52 (1995) 12329.
[320] L. Schwenger, H.-J. Ernst, Surf. Sci. 347 (1996) 25.
[321] S. Kodiyalam, K.E. Khor, S.D. Sarma, Phys. Rev. B (1996).
[322] S. Kodiyalam, K.E. Khor, S.D. Sarma, J. Vac. Sci. Technol. B 14 (1996) 2817.
[323] J.M. Bermond, J.J. Métois, J.C. Heyraud, F. Floret, Surf. Sci. 416 (1998) 430.
[324] X.-S. Wang, E. Williams, Surf. Sci. 400 (1998) 220.
[325] B.S. Swartzentruber, Phys. Rev. B 47 (1993) 13432.
[326] M.S. Hoogeman, D.C. Schlosser, J.W.M. Frenken, Phys. Rev. B 53 (1996) 13299.
[327] P. Wang, H. Pfnür, T.L.E. S.V. Khare, E. Williams, Preprint, 1998.
[328] K. Arenhold, S. Surnev, H.P. Bonzel, P. Wynblatt, Surf. Sci. (1998), submitted for publication.
[329] M. Giesen, Surf. Sci. 370 (1997) 55.
[330] T. Einstein, M. Giesen, (1999) in preparation.
[331] O.L. Alerhand, D. Vanderbilt, R.D. Meade, J.D. Joannopoulos, Phys. Rev. Lett. 61 (1988) 1973.
[332] N.C. Bartelt, R.M. Tromp, Phys. Rev. B 54 (1996) 11731.
[333] A. Garcia, J. Northrup, Phys. Rev. B 48 (1993) 17350.
[334] L. Kuipers, M.S. Hoogeman, J.W.M. Frenken, Phys. Rev. Lett. 71 (1993) 3517.
[335] H. Over, O. Knotek, E. Lugscheider, Z. Metallkde 73 (1982) 552.
[336] F. Mugele, A. Rettenberger, J. Boneberg, P. Leiderer, Surf. Sci. 400 (1998) 80.
[337] B.S. Swartzentruber, M. Schacht, Surf. Sci. 322 (1995) 83.
[338] C. Pearson, B. Borovsky, M. Krueger, R. Curtis, E. Ganz, Phys. Rev. Lett. 74 (1995) 2710.
[339] H.J.W. Zandvliet, B. Poelsema, Phys. Rev. B 51 (1995) 5465.
[340] N.C. Bartelt, R.M. Tromp, E.D. Williams, Phys. Rev. Lett. 73 (1994) 1656.
[341] M. Giesen, G. Icking-Konert, Surf. Sci. 412/413 (1998) 645.
[342] B. Loisel, D. Gorse, V. Pontikis, J. Lapujoulade, Surf. Sci. 221 (1989) 365.
[343] M. Kalff, G. Comsa, T. Michely, Phys. Rev. Lett. 81 (1998) 1255.
[344] A.V. Latyshev, A.B. Krasilnikov, A.L. Aseev, Surf. Sci. 311 (1994) 395.